Engineering pH-responsive biomaterials for cancer immunotherapy

Meilyn Sylvestre

A dissertation
submitted in partial fulfillment of the
requirements for the degree of

Doctor of Philosophy

University of Washington
2021

Reading Committee:
Suzie H. Pun, Chair
Marta Scatena
Patrick Stayton

Program Authorized to Offer Degree:
Bioengineering

University of Washington

Abstract

Engineering pH-responsive biomaterials for cancer immunotherapy

Meilyn Sylvestre

Chair of the Supervisory Committee:
Suzie H. Pun
Department of Bioengineering

Recent advances in immunotherapy have transformed cancer treatment, while highlighting the complex interactions between the immune system and tumors. For delivery of unstable molecules or immunogenic agents, these therapies often employ nanoformulations to deliver therapeutics to diseased tissue while minimizing off-target toxicity. However, delivery of these carriers is severely limited by numerous biological barriers, preventing therapies from reaching sufficient therapeutic concentrations. Carrier accumulation can be enhanced by incorporation of passive and active targeting, and/or stimuli-responsive elements to help steer the carrier to the appropriate diseased tissues, cells, and intracellular compartments. In this work, we seek to engineer new therapies to enhance targeting and delivery of cancer therapeutics by combining both active and passive targeting strategies. Part I motivates tumor-associated macrophages as immunotherapy targets (**Chapter 1**), leading into our first approach in which we identified a novel targeting ligand that binds to human tumor-associated macrophages and monocytes (**Chapter 2**). Part II discusses the challenges of peptide delivery in oncology applications (**Chapter 3**), prefacing our designed peptide-polymer conjugates that passively accumulate in tumors and respond to external pH to facilitate intracellular peptide delivery upon cellular internalization. Using this strategy, we designed a polymeric delivery system to safely deliver (**Chapter 4**) a variety of immunogenic peptides (**Chapters 5, 6, and 7**). Part III outlines the challenges in delivering therapeutics past the blood-brain barrier (**Chapter 8**), and reports the progress on the development of targeted nanoparticles for brain cancer treatment (**Chapter 9**).

List of Contents

List of Contents iv
List of Figures x
List of Tables xii
Acknowledgements xiii

Part I Targeting tumor-associated myeloid cells 1
Chapter 1 Progress on Modulating Tumor-Associated Macrophages with Biomaterials 2
1.1 Abstract 2
1.2 Introduction 2
1.2.1 Mononuclear phagocytic system (MPS) 3
1.2.2 Macrophage polarization: the M1/M2 paradigm 4
1.2.3 Tumor-associated macrophages in cancer 6
1.3. Synthetic biomaterials to target TAMs in cancer by systemic delivery 7
1.3.1 TAM-targeted therapeutic strategies 7
1.3.2 Passive targeting 10
1.3.2.2. Liposomes 12
1.3.2.3. Inorganic Nanoparticles 13
1.3.2.4. Polymer, polymeric nanoparticles, and polymer depots 14
1.3.2.5. Limitations in passive targeting 15
1.3.3 Active targeting 16
1.3.3.1. Monoclonal Antibodies 17
1.3.3.2. Peptides 19
1.3.3.3. Carbohydrates 20
1.3.3.4. Oligonucleotides 22
1.3.3.5. Limitations in active targeting 22
1.4. Localized TAM modulation by biomaterials: lessons from wound healing 24
1.4.1 Macrophages in wound healing 24
1.4.2 Macrophage response to engineered biomaterials 25
1.4.2.1. Implantable scaffolds 26

1.4.2.2. Pore size 27
1.4.2.3 Fiber diameter and modifications 28
1.4.3 Injectable hydrogels 28
1.4.4 Application of wound healing principles to cancer 29
1.5. Engineered macrophages and biomaterials 31
1.5.1 Genetically engineered macrophages 32
1.5.2 Macrophages as drug delivery vehicles 34
1.5.2.1 Polymeric backpacks 35
1.5.2.2 Macrophage 'Trojan horses' 36
1.5.3 Macrophage shells 37
1.6 Future Directions 37
1.7 Acknowledgements 38
References 38
Chapter 2 Identification of a DNA aptamer that binds to human monocytes and macrophages 44
2.1 Abstract 44
2.2 Introduction 44
2.3. Results 46
2.3.1 Identification of aptamer A2 by cell-SELEX 46
2.3.2 Characterization of aptamer A2 binding to macrophages. 49
2.3.3 Characterization of aptamer A2 binding to PBMCs 50
2.4 Discussion 54
2.5 Experimental Procedures 56
2.6 Acknowledgements 61
2.7 Conflict of Interest 61
2.8 Supplemental Information 61
References 66

Part II Developing immunogenic polymer-peptide conjugates 68
Chapter 3 Rational design of polymeric carriers for improved peptide delivery 69
3.1 Abstract 69
3.2 Introduction 69

3.2.1 Increase in vivo stability 71
3.2.2 Improve accumulation and cell uptake 74
3.2.2.1. Tumor accumulation and penetration 74
3.2.2.2. Cell uptake 77
3.2.2.2.1. Charge-mediated uptake 77
3.2.2.2.2. Receptor-mediated uptake 77
3.2.2.2.3. Environment-triggered uptake 79
3.2.3 Strategies to facilitate cytosolic delivery of peptides 83
3.2.3.1 Proton sponge effect 86
3.2.3.2 Anionic membrane-destabilizing polymers 90
3.2.3.3 Pore formation 91
3.2.3.4 Cell membrane fusion 93
3.2.3.5 External stimuli 94
3.2.3.6 Methods to monitor intracellular peptide delivery 96
3.2.3.7 Challenges in cytosolic delivery 97
3.3 Conclusions and Perspectives 99
References 101
Chapter 4 Replacement of L-amino acid peptides with D-amino acid peptides mitigates anti-PEG antibody generation against polymer-peptide conjugates in mice 109
4.1 Abstract 109
4.2 Introduction 110
4.3 Results 112
4.3.1 Synthesis of melittin micelles 112
4.3.2 In vitro activity of L- and D-melittin peptides and micelles is comparable 115
4.3.3 Incorporation of D-melittin increases maximum tolerated dose (MTD) 118
4.3.4 Incorporation of D-melittin enables safe, repeated dosing of micelles 120
4.3.5 The adaptive immune response is attenuated in DMM-treated mice 121
4.3.6 PAF receptor antagonist extends survival but does not rescue mice 125
4.4 Discussion and Conclusion 126
4.5 Experimental Procedures 129
4.6 Acknowledgements 132

4.7 Competing Interests 132
4.8 Supplemental Information 132
References 135
Chapter 5 Development of D-melittin polymeric nanoparticles for anti-cancer treatment 139
5.1 Abstract 139
5.2 Introduction 140
5.3. Results 142
5.3.1 Polymer synthesis of melittin micelles 142
5.3.2 Lytic activity in vitro 143
5.3.3 Characterization of immunogenic cell death (ICD) 147
5.3.4 Safety of free peptide and micelles in vivo 148
5.3.5 Safety of particles upon repeat injection 149
5.3.6 Anti-tumor efficacy of D-melittin peptide and micelles in vivo 151
5.3.7 Anti-tumor efficacy of combinatorial DMM&ICB treatment 152
5.4 Discussion and Conclusion 154
5.5 Materials and methods 160
5.6 Acknowledgements 163
5.7 Competing Interests 163
5.8 Supplemental Information 164
References 168
Chapter 6 Development of Candidalysin polymer-peptide conjugates 171
6.1 Abstract 171
6.2 Introduction 171
6.3 Results 173
6.3.1 Design of polymer-peptide conjugates 173
6.3.2 Peptide activity in vitro 174
6.3.3 Micelle activity in vitro 175
6.3.4 Tumor reduction with CP-Candidalysin micelles 178
6.4 Discussion 179
6.5 Experimental Procedures 181
6.6 Acknowledgements 184

6.7 Competing interests 184
6.8 Supplemental Information 185
References 186
Chapter 7 Polymer-mediated delivery of peptide R3 for cancer immunotherapy 188
7.1 Abstract 188
7.2 Introduction 188
7.3 Results 191
7.3.1 Polymer synthesis and characterization 191
7.3.2 Toxicity in vitro 192
7.3.3 Lytic activity in vitro 194
7.3.4 Immunogenic cell death 195
7.3.5 Anti-tumor efficacy in vivo 196
7.4 Discussion 198
7.5 Methods & Materials 201
7.6 Acknowledgments 204
7.7 Conflicting Interests 204
7.8 Supplemental Information 205
References 208

Part III Crossing the blood-brain barrier 210
Chapter 8 Challenges in crossing the blood-brain barrier in cancer treatment 211
8.1 Abstract 211
8.2 Need for new therapies 211
8.3 Blood-brain barrier biology 211
8.3.1 Anatomical composition 212
8.3.2 Transport across the BBB 213
8.3.3 Macromolecule exclusion and implications for therapy 215
8.4 Current strategies to cross the BBB 215
8.4.1 Physical disruption 215
8.4.2 Transient disruption 216
8.4.3 Receptor mediated transcytosis 217

8.5 Transferrin targeted delivery across the BBB 218
8.5.1 Transferrin and transferrin receptor binding 219
8.5.2 Influence of binding affinity and avidity on Tf-targeted transcytosis 220
8.5.3 Acid-labile transferrin targeted particles 221
References 222
Chapter 9 Delivering nanodrugs across the blood-brain barrier for glioblastoma treatment 224
9.1 Abstract 224
9.2 Introduction 224
9.3 Results 226
9.3.1 Synthesis of targeted pro-drug nanoparticles 226
9.3.2 Development of transcytosis assay 228
9.3.3 Brain accumulation of nanoparticles 230
9.3.4 Development of brain tumor model 232
9.3.5 Tumor reduction with targeted nanoparticles 234
9.4 Discussion 236
9.5 Methods 239
9.6 Acknowledgements. 241
9.7 Conflicting Interests 241
9.8 Supplemental Information 241
References 244
Chapter 10 Future directions 247
10.1 VIPER-D-R3 for peptide delivery to solid tumors 247
10.1.1 Pathway specific cell death 247
10.1.2 Incorporation of targeting ligands 248
10.1.3 Investigation of different delivery routes 248
10.1.4 Incorporation of alternative immunogenic peptide cargos 248
10.2 Targeted nanoparticles for chemotherapeutic delivery to brain tumors 249
10.2.1 Incorporation of alternative targeting ligands 250
10.2.2 Incorporation of alternative core chemistries 250
References 251

List of Figures

Figure 1.1: Macrophage distribution and polarization 6
Figure 1.2: Tumor-associated macrophages as drivers of tumor growth 7
Figure 1.3: TAM-targeted clinical and pre-clinical strategies 8
Figure 1.4: Nanoparticle properties influence macrophage internalization 12
Figure 1.5. Active targeting ligands recognize cellular markers and facilitate internalization 17
Figure 1.7: Adoptive cellular transfer therapies for cancer treatment 32
Figure 2.1: Cell-SELEX schematic that led to the identification of aptamer A2 48
Figure 2.2: Aptamer binding to human M0-, M1-, and M2-like macrophages 50
Figure 2.3: Aptamer binding to $CD14^+$ cells in complete PBMCs 52
Figure 3.1: Challenges in polymer-mediated delivery of peptide therapeutics 70
Figure 3.2. Structure of Janus dendrimer with protein binding and antifouling features 73
Figure 3.3: Schematic representation of the fabrication of melittin/Cypate@HA complexes 76
Figure 3.4: Targeted co-delivery of an antigen and dual agonists by mannose targeting NPs 78
Figure 3.5: Nanoparticles hydrolyze in tumor microenvironment to increase internalization 80
Figure 3.6 Design of a surface charge-switchable system for codelivery of KLA and p53 82
Figure 3.7: Peptide-PAMAM conjugate with MMP2-sensitive PEG and TAT 83
Figure 3.8. Mechanisms of endosomal escape 85
Figure 3.9: Fluorination of polymers to mediate cytosolic protein delivery 88
Figure 3.10: Lytic peptides to mediate endosomal escape 92
Figure 3.11: Incorporation of photosensitizers can improve internalization and targeting 95
Figure 4.1: Polymer synthesis of micelles 115
Figure 4.2: In vitro activity of L- and D-melittin peptides and micelles 118
Figure 4.3: MTD determination of LMM and DMM 119
Figure 4.4: Survival and weight of mice receiving repeat injections of LMM and DMM 121
Figure 4.5: LMM injections in normal and NSG mice 121
Figure 4.6: IgG and IgM antibodies against micelles, polymer, and peptide 124
Figure 4.7: Liver toxicity after micelle injection was evaluated by H&E, ALT/AST 125
Figure 5.1: Design of D-melittin conjugate for systemic delivery of melittin 142
Figure 5.2: Synthesis and characterization of D-melittin conjugate 143

Figure 5.3: Peptide and micelle activity in vitro 146
Figure 5.4: Evaluation of immunogenic cell death in CT26 cancer cells 148
Figure 5.5: H&E staining of major organs after repeat injection of peptide and particles 150
Figure 5.6: Serum ALT/AST activity 151
Figure 5.7: Evaluation of anti-tumor effects of free peptide and micelles in CT26 tumors 152
Figure 5.8: Tumor reduction with combinatorial ICB in 4T1 and CT26 tumors 154
Figure 6.1: Synthesis of Candidalysin micelles 174
Figure 6.2: In vitro activity of peptide 175
Figure 6.3: Toxicity of Candidalysin micelles and peptide 177
Figure 6.5: In vivo activity of Candidalysin 179
Figure 7.1: Design of polymer-peptide conjugates bearing melittin and R3 190
Figure 7.2: Characterization of micelles 192
Figure 7.4: Cytotoxicity of R3 peptide and micelles 193
Figure 7.5: Lytic activity of micelles in vitro 195
Figure 7.6: Immunogenic cell death 196
Figure 7.7: Tumor inhibition in vivo 197
Figure 8.1: Anatomical composition of the blood brain barrier 213
Figure 8.2: Transport routes across the endothelial cells of the BBB 214
Figure 8.3: Schematic of RMT mechanism. 218
Figure 8.4: Endocytic recycling of Tf 220
Figure 8.5: Schematic of acid-cleavable decoupling of Tf 222
Figure 9.1: Schematic of acid-cleavable transferrin nanoparticles 227
Figure 9.2: Schematic of synthesis of particles 228
Figure 9.3: Development of a transwell assay. 230
Figure 9.4: Nanoparticle accumulation in normal mice 232
Figure 9.5: Measuring tumor burden in vivo 234

List of Tables

Table 1.1: Summary of current clinical and pre-clinical therapies 9
Table 1.2: Properties of implantable scaffolds modulate local macrophage response..... 27
Table 4.1: Characterization of micelles..... 115
Table 4.2: Cytotoxic and hemolytic activity of melittin 118
Table 4.3: Death of mice after LMM or DMM injection..... 120
Table 5.1: Toxicity of D-melittin peptide and micelles against tumor cells 146
Table 5.2: Hemolytic activity of D-melittin peptide and micelles..... 146
Table 6.1. Toxicity of Candidalysin against murine macrophages and cancer cells. 175
Table 6.2: Cytotoxicity of peptide and micelles in murine and human tumor cell lines 177
Table 6.3: Hemolytic activity of CP-Candidalysin 177

Acknowledgements

This work would not have been possible without my amazing team of mentors, friends, and colleagues that have supported me during my journey. With them, I've experienced the joy of a successful experiment, and commiserated over the pain of a failed one. Working alongside my team of personal cheerleaders (and personal trainers) has shaped me into the scientist that I am today.

I am most grateful to my Ph.D. advisor and supervisor, **Suzie Pun**: For believing in me and supporting me, even when I didn't believe in myself; for providing me with the mentors and environment that nurtured me and asked all the right questions; for encouraging me to be proud of myself and my accomplishments; for showing me how to handle difficult situations with composure, humility, and virtue; and for embodying the kind of scientist and mentor that I aspire to be. Thank you for giving me a chance and taking me into your lab, and thank you for all the patience and encouragement you have given me. Even before coming to UW, I had a feeling that your lab was a place I wanted to be. And I was right – it was easily one of the best decisions I've ever made.

I would like to thank my reading committee, **Suzie Pun**, **Marta Scatena**, and **Patrick Stayton**, as well as my Supervisory Committee, **Suzie Pun**, **Marta Scatena**, **Patrick Stayton**, and **Elizabeth Nance**, for their guidance during my Ph.D.

My mentor, friend, and "GWL" **Gary Liu**: For always taking an interest in me – my science, my wellbeing, and my social life; for patiently answering all my questions (science and not-science related); and for shaping me into a stronger writer, scientist, and card player. Working with you smoothed my transition from clueless-second year to competent scientist. I will always treasure the workspace we created and I dearly miss your enthusiasm and zest. I'm thankful that Mean Girls, inventory duty, and chocolate chip cookies brought us together.

My mentor **Shixian Lyu**: For your tireless enthusiasm for science and always telling me to "take a rest." It has been an immense pleasure working with you and I have learned so much from you,

and it is because of you that I have *finally* mastered tail vein injections. I am so glad that we will have a strong joint-publication record so we can remember our time working together! I will miss you dearly when you're off becoming a famous PI in China!

My roommate, friend, and co-cat-parent **Sara Keller**: For your steadfast support, compassion, and encouragement. While my labmates shaped me into a scientist, you helped shape me into a more empathetic, thoughtful, and adventurous person. I am so grateful we roomed together for these past 5 years – it will be weird living in Seattle without you!

My lunchmate and friend **Jamie Hernandez**: For your vivacity, high tolerance of my rambling stories, and shared enthusiasm for silly nonsense. I've loved our daily lunches together (pre-COVID), whirlwind shopping experiences at the Southcenter Mall and Costco, and late-night happy hour shopping trips! Your gusto for life inspires me to appreciate what I have while also keeping an eye out for my next big adventure.

My hiking/backpacking friends **Sara Keller**, **Jamie Hernandez**, **Audrey Olshefsky**, **Alex Prossnitz**, **Alison Williams,** and **Anthony Dario**: For always being down for a new adventure, and encouraging me to do the same! When I moved to Seattle, I had hardly any hiking experience; and now thanks to you all, I have fallen in love with the lakes and mountains! You all showed me how much fun graduate school can be, and that there's more to life than science!

My cohort- and lab mates **Ian Cardle**, **Emmeline Cheng**, and **Alex Prossnitz**: For commiserating alongside me and inspiring me everyday since we started this journey together! **Ian** – it's always a joy working with you, as you are always cheerful, good-natured, and generous. Thanks for all your help and endless patience with flow. **Emmeline** – you are so kind hearted and accepting; your gentle patience has always lifted me in times of need. I fondly remember our late nights in the cubicles our first year! **Alex** – your exuberant personality and emotional intelligence make you an amazing friend and colleague. You always have a kind word to encourage me and remind me not to be too hard on myself, and I cherish our friendship through the years.

My bench buddy and mentor **Drew Sellers**: For being my friend, mentor, and part-time therapist. I'm so fortunate we could be bench-buddies and gripe about life together. I'm glad you finally admit that we're best friends, even though it took you 5 years!

My lab manager **Nataly Kacherovsky**: For being a steadfast source of pragmatism, fun, and advice (science, mushroom, and garden-related). We make a great team managing the lab together!

All of the current **Pun Lab members**: For creating an amazing work environment that I was lucky to be a part of for the past 5 years! **Audrey –** I always love working together! You are the only person that appreciates my Christmas cheer/fervor/fanaticism and I'll miss playing Christmas jingles in July. I hope all my future colleagues share your good-natured spirit and optimism. **Clinton** and **Trey** – your visits to Foege were also a nice treat! **Lucy** – I'll miss our lunch adventures together! **Kefan, Ben,** and **Melissa** – I'm very excited that you all are joining the lab! I am excited to see all the amazing things I am sure you will accomplish.

Past Punions **Gary Liu**, **Brynn Olden**, **Bob Lamm**, **Daniel Lee**, and **Albert Yen**: For your support, inspiration, and encouragement. I've admired all of you immensely – your work ethic and productivity; generosity and patience; and humility and virtue. I am so fortunate to have had the opportunity to work alongside you all!

My boyfriend **Ian Hull**: For your support, encouragement, and love. Thanks for always being on my team, but also for not being afraid to stand up to me and tell me when I'm wrong. My PhD adventure has come to end, but ours is just beginning, and I look forward to exploring it with you.

My mom **Marilyn Sylvestre**: For leading by example and showing me that a strong, independent, and successful woman can still ask for help. I wouldn't be here without your encouragement and reminders to take a couple deep breaths every now and again.

Part I

Targeting tumor-associated myeloid cells

Chapter 1

Progress on Modulating Tumor-Associated Macrophages with Biomaterials[1]

Meilyn Sylvestre, Courtney Crane, and Suzie H. Pun

1.1 Abstract

Tumor-associated macrophages are a complex and heterogeneous population of cells within the tumor microenvironment. In many tumor types, tumor-associated macrophage contribute toward tumor malignancy and are therefore a therapeutic target of interest. This progress report highlights three major strategies for regulating tumor-associated macrophage, emphasizing the role of biomaterials in these approaches. First, systemic methods for targeting tumor-associated macrophage are summarized and limitations to both passive and active targeting approaches considered. Second, lessons learned from the significant literature on wound healing and macrophage response to implanted biomaterials are discussed with the vision of applying these principles to localized, biomaterials-based modulation of tumor-associated macrophage. Finally, the developing field of engineered macrophages, including genetic engineering and integration with biomaterials or drug delivery systems, is examined. The report includes analysis of major challenges in the field along with exciting opportunities for the future of macrophage-based therapies in oncology.

1.2 Introduction

Macrophages are fundamental cells of the mononuclear phagocytic system and hold diverse roles in homeostasis, inflammation, and wound healing. In cancer, tumor-associated macrophages (TAMs) drive disease progression and have been correlated with worse patient prognoses.[1,2] Compared to other inflammatory cell types in cancer, TAMs have emerged as therapeutic targets of interest. In many solid tumors, TAMs comprise a significant portion of infiltrating leukocytes and are a major source of secreted growth factors, cytokines, and chemoattractants.[3,4]

[1] *Reprinted with permission from Sylvestre, M., Crane, C.A., et al. Progress on modulating tumor-associated macrophages with biomaterials. Adv. Mat.* ***32****, 1902007 (2019). Copyright 2019 WILEY-VCH Verlag GmbH & Co. KGaA Weinheim.*

Furthermore, they are fundamentally involved in every stage of cancer progression, promoting tumor cell survival and preparing distant sites for metastatic seeding.[5]

In addition to their significant impact in cancer, macrophages are also crucial players in wound healing, orchestrating the transition from inflammation to tissue remodeling.[6] In this review, we discuss systemic and localized approaches to target and modulate macrophage activity in disease, and cell-based therapies that engineer macrophages for cancer. Nanoparticle and polymer biomaterials have been used extensively as systemic drug delivery vehicles to TAMs, employing both passive and active targeting strategies. Here, we define passive targeting as particle accumulation due to physical properties (e.g. charge, size, and shape), and active targeting as particle accumulation mediated by molecular recognition. However, particle-based strategies for TAM-targeting are challenged by the macrophages' high intrinsic phagocytosis and non-specific clearance of circulating particles, resulting in high off-target uptake and toxicity. To overcome some of the challenges associated with systemic strategies, localized tumor treatments have also been used to modulate TAM activity. While localized treatments have been used primarily in wound healing application, we will derive key principles across macrophage-based therapies. Finally, we discuss the burgeoning field of engineered macrophage and the application of biomaterials in enhancing macrophage cell therapies. Understanding how biomaterial properties influence local immune populations can profoundly improve therapeutic outcomes.

1.2.1 Mononuclear phagocytic system (MPS)

At the front-line of immune defense are mononuclear phagocytes, comprising monocytes, macrophages, and dendritic cells in the spleen, liver, and lymph nodes. These cells colonize every organ in the body and can perform specialized functions dependent on location (**Figure 1.1A**). Monocytes are derived from hematological precursors in the bone marrow and enter blood circulation for 1-3 days where they can be recruited into tissues throughout the body in response to appropriate signals, such as injury or inflammation, and mature into macrophages. There is some controversy about whether blood circulating monocytes replenish tissue-resident macrophages, or if tissue-resident macrophages are self-replenishing populations.[7,8]

Tissue-resident macrophages are derived from precursors in the yolk sac during embryogenesis, are seeded throughout the body, and mature into specialized resident macrophages with broad roles in waste clearance, metabolism, and immune surveillance. These heterogeneous cells, which go by tissue-specific names, perform distinct functions and are critical for maintaining tissue homeostasis.[9] For example, red pulp macrophages in the spleen recycle iron and clear old erythrocytes, and Kupffer cells in the liver clear pathogens and waste from the blood. Osteoclasts (bone macrophages) resorb bone and alveolar macrophages in the lungs clear surfactant. Most notably, macrophages perform immune surveillance and recognize a wide array of pathogen-associated molecular patterns and danger-associated molecular patterns. Upon recognition, macrophages mount an immune response, driving the influx of inflammatory leukocytes. Furthermore, macrophages exhibit critical roles in resolution, tissue repair, and regeneration.[10]

While macrophage play key roles in maintaining homeostasis, their dysregulation and dysfunction have been implicated in disease pathologies throughout the body.[11,12] For example, macrophage accumulation in white adipose tissue has been associated inflammation, insulin resistance, and obesity.[13] In atherosclerosis, macrophages promote a pro-inflammatory environment that can result in the formation of foam cells and unstable plaques.[14] Accumulation of pro-inflammatory macrophages is linked with inflammatory bowel disease severity and progression.[15] Clearly, macrophages are a complex, heterogeneous population of leukocytes that hold diverse yet fundamental roles in homeostasis and disease.

1.2.2 Macrophage polarization: the M1/M2 paradigm

Macrophages exhibit different functional programs in response to environmental cues and, when triggered, are classified into two main subsets: *(1)* classically activated, M1-macrophages, or *(2)* alternatively activated, M2-macrophages (**Figure 1.1B**). Classically-activated macrophage perform pro-inflammatory functions and are polarized by lipopolysaccharide (LPS) and cytokines such as IFN-γ or GM-CSF to exhibit strong effector functions against pathogens and cancer cells. In addition to high phagocytic ability, M1-macrophages produce increased levels of pro-inflammatory cytokines, including IL-12, IL-23, and TNF-α, which facilitate leukocyte recruitment and activation during injury. In contrast, polarization by IL-4 and IL-13 can result in alternatively activated M2-macrophages that perform anti-inflammatory functions. M2-

macrophages contribute to wound healing and repair through debris clearance and release of TGF-β, PDGF, and VEGF. Furthermore, they participate in the resolution of inflammation by producing immunosuppressive cytokines such as IL-10.[16,17] While the M1/M2 macrophage model is broadly used, macrophages are complex and do not form clear-cut activation subsets. The simplified M1/M2 paradigm ignores the source and context of stimulation – M1/M2 stimuli do not exist alone in tissues. In reality, macrophage polarization is multi-dimensional with overlapping functions and markers between subsets, and may therefore be better considered as a continuum of functional states.[16,18]

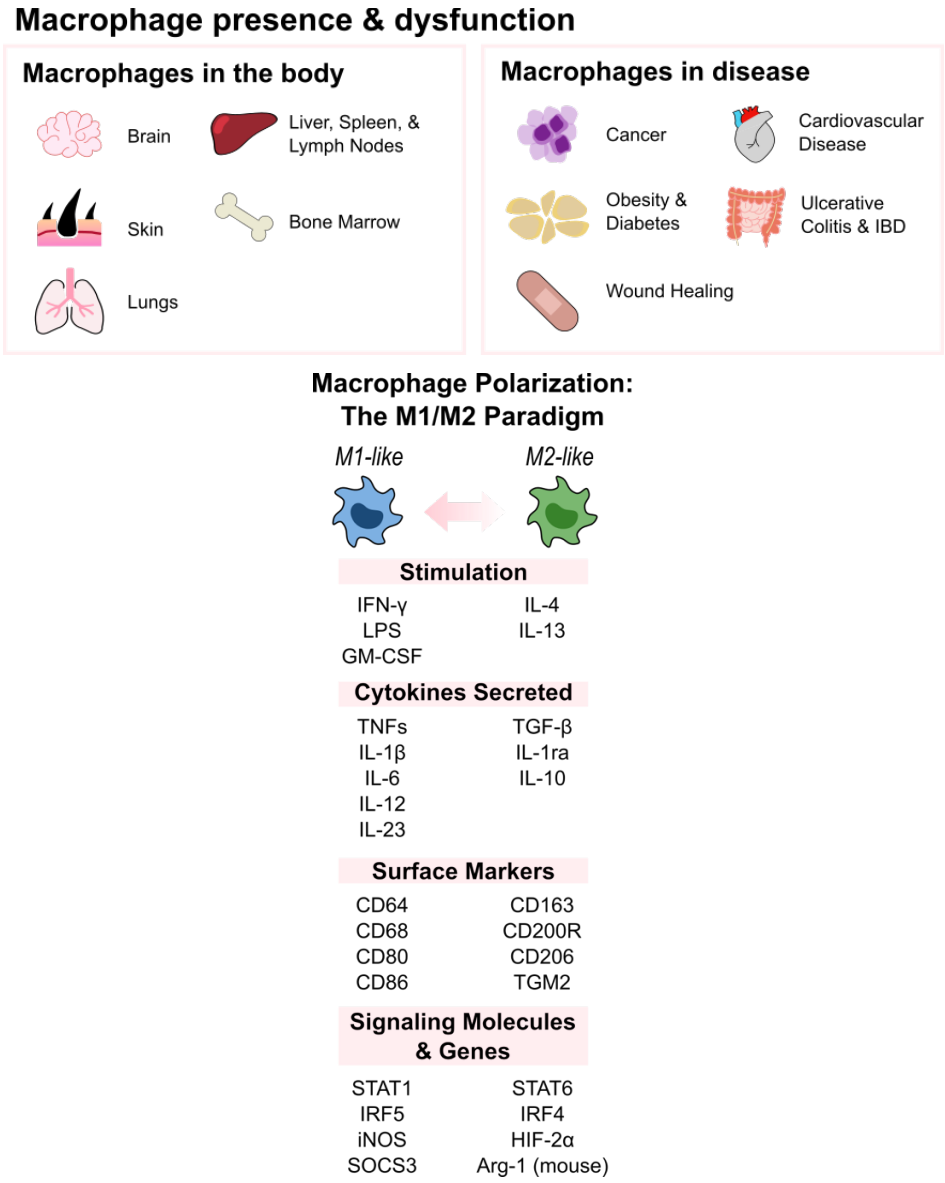

Figure 1.1: Macrophage distribution and polarization.A) Macrophages are present in all organs throughout the body, such as the brain, skin, and liver, and hold key roles in immune defense and in regulating homeostasis. Their dysfunction and dysregulation is linked with many diseases, such as cancer, obesity, and cardiovascular disease. B) Activated macrophages are broadly classified into two subsets: M1-like and M2-like macrophages. These different phenotypes are activated via different stimuli, express different cellular markers, and perform different functions. However, this simplified paradigm does not fully cover the complexity of macrophage polarization, which is multi-dimensional with overlapping functions and markers.

1.2.3 Tumor-associated macrophages in cancer

Clinically, high tumor-associated macrophage infiltration is linked with worse patient prognoses in various tumors, including breast cancer, lung cancer, and lymphomas.[17] TAMs have accordingly emerged as a promising therapeutic target in cancer treatment. Despite the phenotypic plasticity and diversity in the tumor microenvironment, TAMs often exhibit an "M2-like" phenotype, displaying characteristic markers such as the hemoglobin scavenger receptor (CD163) and mannose receptor (CD206). Furthermore, these cells play an anti-inflammatory role, inducing immune suppression and promoting tumor progression through a range of mechanisms including producing immunosuppressive cytokines, suppressing cytotoxic T cell activity while promoting regulatory T cells, and inhibiting B cell signaling (**Figure 1.2**).[1,2,19,20] TAMs further potentiate tumor progression by promoting tumor cell proliferation, angiogenesis, and invasion by releasing growth factors and enzymes that digest the extracellular matrix and basement membrane. Furthermore, TAMs induce cancer cells to migrate through paracrine signaling (CCL18), as well as prepare distant metastatic sites for seeding.[21]

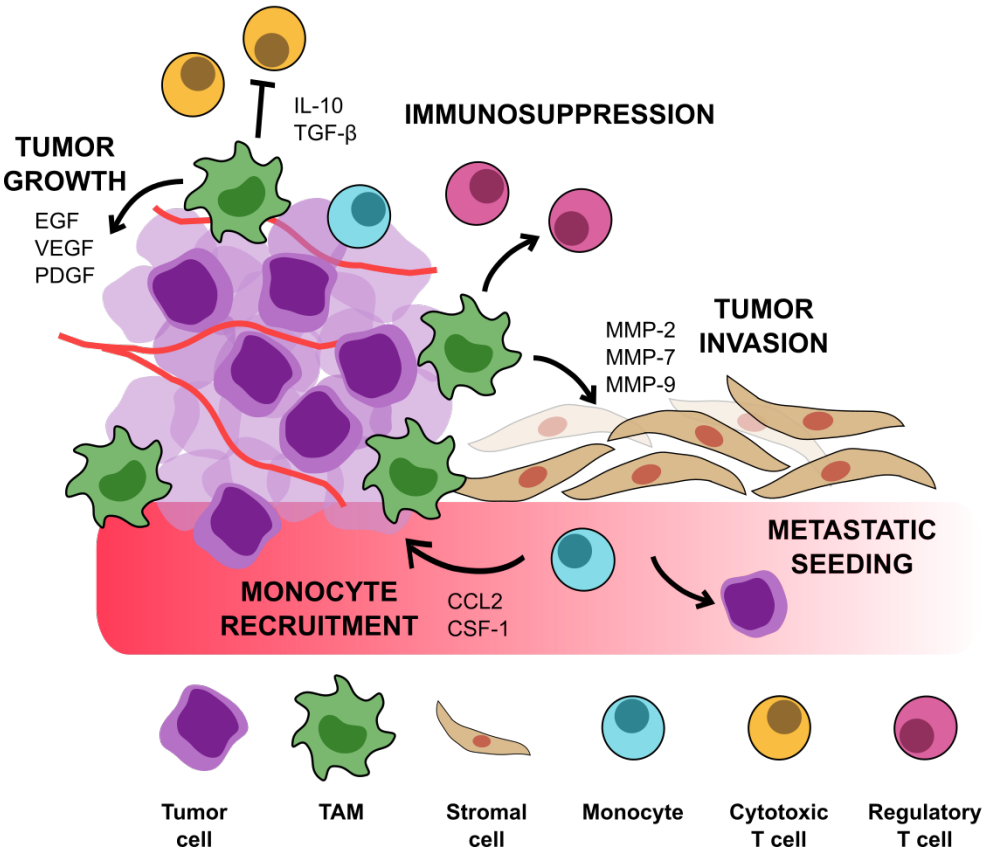

Figure 1.2: Tumor-associated macrophages as drivers of tumor growth. Tumor-associated macrophages drive tumor growth through several mechanisms, such as immunosuppression, monocyte recruitment, and preparation of distant metastatic niches. TAMs further support tumor invasion by releasing enzymes that break down the basement membrane and secreting angiogenic growth factors. They comprise a large proportion of infiltrating immune cells and are involved with every stage of cancer progression. Because of their role in potentiating tumor growth and invasion, TAMs have emerged as an interesting therapeutic target for cancer treatment.

1.3. Synthetic biomaterials to target TAMs in cancer by systemic delivery

1.3.1 TAM-targeted therapeutic strategies

As drivers of tumor progression, TAMs are promising therapeutic targets. Current macrophage-targeted therapies under development aim to *(1)* inhibit monocyte/macrophage recruitment, *(2)* deplete macrophages, or *(3)* activate macrophage anti-tumor functions (**Figure 1.3**).[22–24] There exists some controversy about whether TAMs are derived from blood-circulating monocytes or

from infiltrating peripheral tissue macrophages.[23] However, inhibiting monocyte recruitment and their subsequent maturation into TAMs by blocking the CCL2-CCR2 axis has indeed improved survival in tumor-bearing mice.[25,26] A drawback of this strategy is that cessation of CCL2 inhibition in these model systems can accelerate death via a rebound in monocyte populations and enhanced tumor angiogenesis and metastasis.[27]

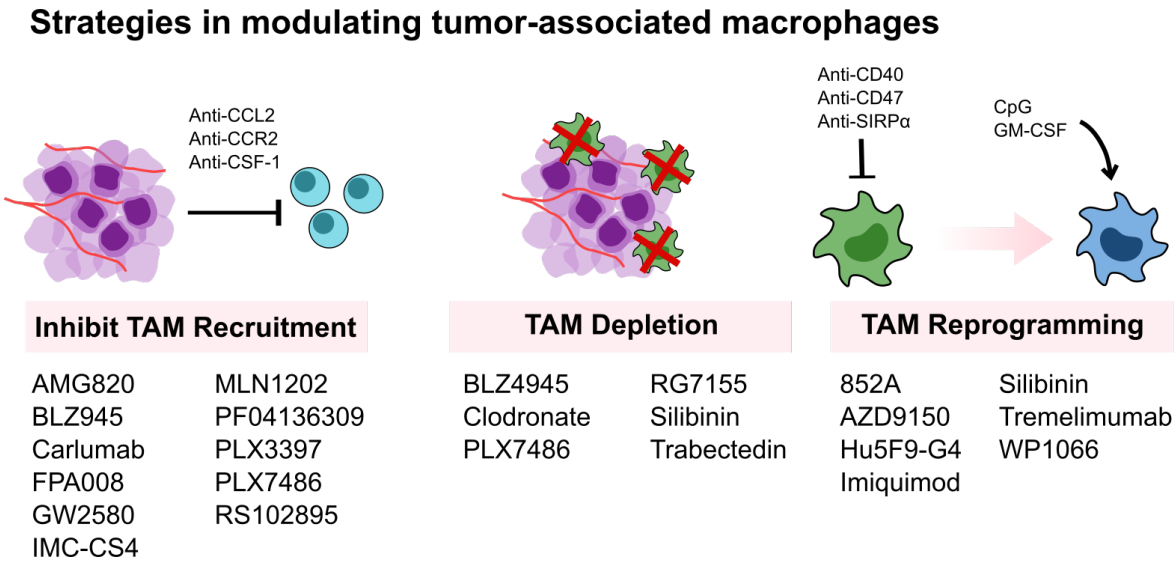

Figure 1.3: TAM-targeted clinical and pre-clinical strategies. Current clinical and pre-clinical macrophage-based strategies aim to (1) inhibit monocyte and macrophage recruitment, (2) deplete TAMs, or (3) reprogram TAMs to an anti-tumor phenotype. Many small molecule or monoclonal antibodies treatments target the CSF-1/CSF-1R or CCL2/CCR2 axis to inhibit monocyte recruitment and macrophage maturation. However, treatment cessation results in a rebound in monocyte population. Second, while TAM depletion has demonstrated efficacy in many animal models, indiscriminate TAM depletion may actually exacerbate tumor progression, emphasizing the complexity of macrophage populations and activity. Lastly, macrophage re-education toward an M1-like anti-tumor phenotype has been shown to reduce tumor progression, but can result in off-target side effects. Overall, all of these strategies can benefit from improved targeting to specific macrophage populations.

Drug	Pathway	Type	Ref.
852A	TLR7	Small molecule	[143]
AMG820	CSF-1R	Monoclonal antibody	NCT02713529, ref. [144]
AZD9150	STAT3	Small molecule	NCT03421353, ref. [145]
BLZ945	CSF-1R	Small molecule	NCT02829723, ref. [66]
Cabiralizumab (FPA008)	CSF-1R	Monoclonal antibody	NCT03336216
Carlumab	CCL2/CCR2	Monoclonal antibody	NCT00992186 (completed), ref. [146]
Clodronate	Apoptosis	Small molecule	[28]
GW2580	CSF-1R	Small molecule	[147]
Hu5F9-G4	CD47/SIRPa	Monoclonal antibody	NCT02953509, NCT02953782
IMC-CS4	CSF-1R	Monoclonal antibody	NCT01346358 (completed), NCT02265536 (completed)
Imiquimod	TLR7	Small molecule	[148,149]
MLN1202	CCR2	Monoclonal antibody	NCT01015560 (completed), NCT01413022 (completed)
PF04136309	CCR2	Small molecule	NCT02732938 (terminated),
PLX3397	CSF-1R	Small molecule	NCT01349049 (completed), ref. [150]
PLX7486	CSF-1R	Small molecule	NCT01804530 (terminated)
RG7155	CSF-1R	Monoclonal antibody	NCT01494688 (completed), ref. [151]
RS102895	CCR2	Small molecule	[152,153]
Silibinin	Apoptosis	Small molecule	[154,155]
Trabectedin	Apoptosis	Small molecule	NCT03884972, NCT03397186, ref. [156,157]
Tremelimumab	CTLA-4	Monoclonal antibody	NCT03298451, NCT02536794
WP1066	STAT3	Small molecule	NCT01904123, ref. [158]

Table 1.1: Summary of current clinical and pre-clinical therapies

Macrophage depletion has been used clinically for the treatment of metastatic breast cancer and other solid tumors (**Table 1.1**).[28] In animal models, systemic delivery of bisphosphonate-loaded liposomes induces apoptosis in macrophages, inhibiting tumor progression and angiogenesis. However, recent evidence suggests that this indiscriminate, systemic depletion of macrophages may exacerbate tumor progression. For example, accumulation of $CD169^{+}$ macrophage has been associated with improved prognosis in hepatocellular and colorectal carcinomas.[29,30] Another

macrophage depletion strategy targets the colony stimulating factor (CSF)-1—CSF-1R axis. CSF-1 is the major growth and differentiation factor produced by many types of cancer cells that induces macrophage maturation, and its cognate receptor CSF-1R is abundantly expressed by monocytes and macrophages. Blocking CSF-1R activation and signaling reduces TAM densities by depleting TAMs and monocytes, and increases $CD8^+/CD4^+$ T cell ratios.[31] However, as with CCL2 blockade, cessation of treatment results in enhanced CSF-1 signaling and rebound monocyte and macrophage populations.[32]

Lastly, TAM re-education activates macrophage anti-tumor functions. Intraperitoneal injection of IFN-γ, a macrophage-activating cytokine that induces a M1-like phenotype, was demonstrated to activate anti-tumor cytotoxicity in mononuclear phagocytes and reduce tumor progression.[33] Similarly, treatment with a CD40 agonist rapidly activates macrophages and facilitated depletion of the tumor stroma and restored tumor immune-surveillance.[34] Kaneda, et. al. reported that macrophage PI 3-kinase γ (PI3kγ) controls the switch between macrophage immune suppression and activation; PI3kγ inhibition activates NFκB-dependent immune-stimulatory polarization and significantly increases $CD8^+$ T cell recruitment and cytotoxicity.[35] Yet, because macrophages are present throughout the entire body, indiscriminate macrophage modulation can result in off-target side effects.[22] Here, we will discuss several strategies to target TAMs using synthetic biomaterials, with the goal of improving drug delivery and reducing on-target off-tumor toxicity. Further discussion on liposome, polymer, and organic TAM-targeted immuno-nanomedicines can be found in this review.[36]

1.3.2 Passive targeting

The mononuclear phagocytic system (MPS) is responsible for clearance of foreign particles in the body and is thus a major hurdle to nanomedicine drug delivery systems. However, for macrophage-targeted therapies, their high phagocytic capability can be utilized for targeting and drug delivery. In particular, macrophages in the liver and spleen, the primary clearance organs, rapidly sequester and degrade 30-99% of injected nanoparticles (NPs) immediately after injection.[37–39] Passive targeting, preferential accumulation due to physical properties like size and charge, and the rate and extent of macrophage uptake, are significantly affected by NP modifications.[40] Worth noting is the passive targeting strategy that relies on the "enhanced permeation and retention" (EPR) effect

which is believed to enhance NP accumulation in tumors due to leaky vasculature. This targeting strategy dominated cancer nanomedicine principles for years, yet the benefits of the EPR effect varies considerably between patients and tumor types.[38,41] As the importance of TAM-tumor interactions gained appreciation, TAMs have been explored as drug targets of interest that can be reached through the passive targeting methods described in this section.

1.3.2.1 Effect of particle properties on macrophage uptake

Because nanoparticles are tunable and readily internalized by phagocytes, they are excellent drug carriers to macrophages. Particle size, charge, and shape affect macrophage uptake (**Figure 1.4**). Particle uptake is optimal between 30 nm–3 μm; outside of this range, phagocytosis decreases.[17,42,43] While highly cationic or anionic particles are internalized by macrophages at a higher rate compared to particles with neutral or slightly negative zeta potentials, size is a stronger determinant of internalization instead of charge.[43] Particle shape influences macrophage uptake as well, with spherical particles being preferentially phagocytosed over ellipsoidal, rod-like, or cylindrical particles. Microparticles with curvature greater than 45 degrees are unable to be completely internalized.[44,45] Shape also affects how stiffness influences internalization: for rod-shaped particles, decreasing stiffness significantly increases internalization, but decreases spherical particle uptake.[46] Controlling these physical parameters can improve drug delivery to target populations. However, when designing an injectable particulate system, it is also important to consider how particle parameters affect other aspects of pharmacokinetics. For example, particles around 100 nm demonstrate the longest circulation time, while nanoparticles less < 5 nm are rapidly excreted through the kidney. Particles 200-500 nm are filtered by the spleen and particles 2-5 μm accumulate in the lung capillaries. Depending on tumor vasculature, particles around 50-100 nm accumulate in the tumor due to the EPR effect.[37] A review of nanoparticulate carrier systems and their interactions with macrophage is well covered by other published work (biological carriers, viral particles, carbon nanotubes, etc.).[38]

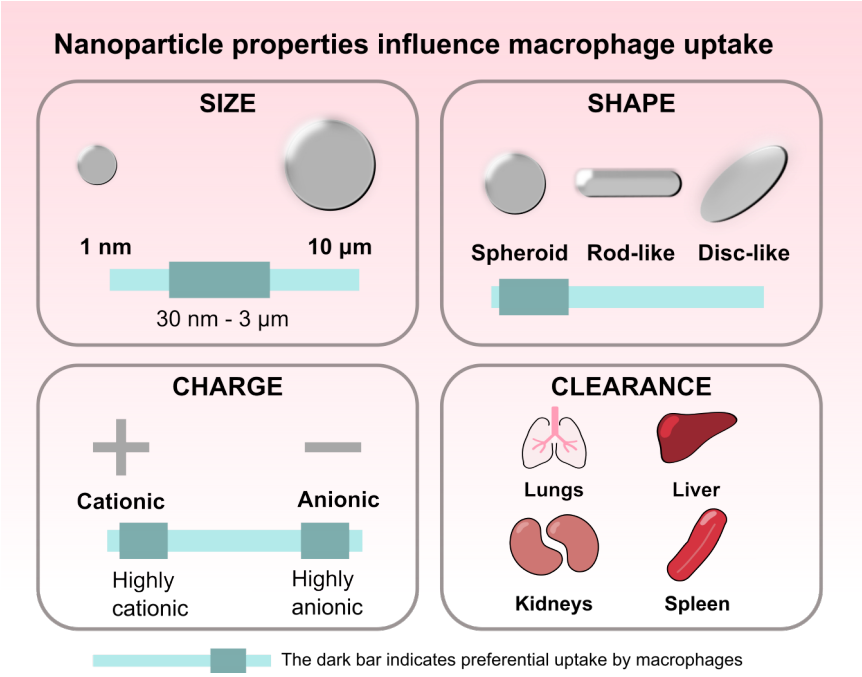

Figure 1.4: Nanoparticle properties influence macrophage internalization. Property parameters that increase macrophage uptake are indicated with the darker bar. Particles between 30 nm and 3 µm in size induce optimal particle uptake. Spheroid particles demonstrate higher uptake compared to rod-like or disc-like shaped particles. Both highly anionic or highly cationic particles undergo high uptake. Nanoparticles are primarily cleared by the lungs, liver, kidney, and spleen. Understanding the effect of these parameters on macrophage uptake can improve particle design to target desired cell populations and reduce clearance.

1.3.2.2. Liposomes

Liposomes are considered to be among the most successful drug delivery systems developed, with several formulations in clinical trials or on the market.[47] Liposomes without surface shielding are inherently recognized by MPS cells, and alterations to their physicochemical properties can further improve uptake by monocytes and macrophages. Overall, small (85 nm), negatively charged liposomes facilitate MPS internalization, whereas large, positively charged particles induce activation and toxicity.[40]

Liposomal formulations of bisphosphonates (e.g. clodronate & alendronate), compounds that induce apoptosis upon internalization, are used as agents for macrophage depletion in animal

models.[47,48] In a murine teratocarcinoma and human rhabdomyosarcoma model, liposomal clodronate effectively depleted monocytes and macrophages, suppressing tumor growth and angiogenesis by up to 92%.[28] A modified clodronate liposome formulation using cationic lipid DOTAP and PEG phospholipid improved clodronate encapsulation. Intravenous (IV) injection resulted in significant tumor and pulmonary nodule reduction in a metastatic melanoma model.[49] The route of injection affects which macrophage populations are depleted. IV injection depletes Kupffer, spleen, and bone marrow macrophages; intraperitoneal (IP) injection depletes peritoneal macrophages; and subcutaneous administration depletes macrophages in the draining lymph nodes.[47]

1.3.2.3. Inorganic Nanoparticles

Gold nanoparticles have been applied *in vivo* as drug carriers, contrast agents, and phototherapy agents. Lin, et. al. relied on macrophage uptake to facilitate delivery of cytosine-phosphate-guanine (CpG) to intracellular toll-like receptor 9 (TLR-9).[50] CpG is a potent stimulant of TLR-9, triggering cell activation, production of pro-inflammatory cytokines, and inducing $CD8^+$ T-cell responses. Small gold NPs (15 nm) functionalized with CpG induced higher TLR-9 stimulation, as measured by TNF-α, IL-6, and G-CSF secretion, than 30 or 80 nm gold particles. Intratumoral injection of NPs improved survival and immune cell infiltration (macrophages, dendritic cells, $CD8^+$ T cells) in B16-OVA tumors. In another example, gold NPs modified with polyethylene glycol (PEG) were engineered with a high-aspect ratio to increase cell exocytosis by macrophages compared with low-aspect ratio or spherical counterparts.[51] Over a 7-day period, NPs that were initially captured by Kupffer cells in the liver and TAMs in the tumor were then exocytosed and transferred to tumor cells. Irradiation of 4T1 tumor-bearing mice 7 days after NP injection significantly inhibited tumor volume and induced greater tumor cell apoptosis compared to irradiation 1 day after injection. The authors hypothesize that the 7 day window was necessary to enable NP transfer from macrophage to tumor cells. Together, this study shows how NP properties can be modified to direct macrophage activity in the tumor environment and enhance therapeutic benefit.

In addition to NP properties influencing uptake, macrophage phenotype plays a significant role in internalization as well. In primary human monocyte-derived macrophages and liver Kupffer cells,

M2-like macrophages preferentially internalized hard nanoparticles, with a hierarchy among the subtypes: M2c > M2 > M2a > M2b > M1.[52] In Kupffer cells, nanoparticle uptake correlated with increasing M2-marker expression (CD163, CD209). Furthermore, nanoparticle internalization decreased inflammatory cytokine secretion. These trends were corroborated by Binnemars-Postma et. al., who investigated the effect of protein coronas on silica nanoparticle uptake by M1 or M2 macrophages.[53]

1.3.2.4. Polymer, polymeric nanoparticles, and polymer depots

Polymer-based drug delivery systems benefit from tunable and controllable architecture, providing control over release kinetics and delivery profiles, and conferring responsiveness to environmental stimuli. In some cases, polymer alone is sufficient to target TAMs or to direct changes in the tumor environment. Zhang, et. al. demonstrated that hydroxyl-functionalized, generation-4 poly(amidoamine) PAMAM dendrimers passively target TAMs in a 9L gliosarcoma model.[54] In another strategy, Huang, et. al. used cationic polymers polyethyleneimine (PEI) and cationic dextran to stimulate TAM anti-tumor activity, likely through TLR-4 signaling.[55] Intratumoral injection of these polycations increased macrophage pro-inflammatory gene expression (NOS2, MHCII) and cytokine secretion (IL-12), and promoted T and nature killer cell infiltration, decreasing tumor size and improving survival in an S180 sarcoma model.

Polymeric nanoparticles have also been used for drug delivery to macrophages. For cancer therapies, these "smart polymers" can be designed to respond to the tumor microenvironment, such as acidic pH or proteases, increasing specific drug delivery to TAMs or cancer cells. In one recent example, Wang, et. al. developed microenvironment-responsive nanoparticles with an IL-12 payload, a cytokine that can induce anti-tumor effects, to re-educate TAMs toward a pro-inflammatory phenotype.[56] Poly(β-amino ester) nanoparticles, capable of dissociating in weakly acidic conditions (pH 6-7), preferentially accumulated in B16-F10 tumors with prolonged IL-12 release over 48 hours. In NP-treated mice, tumor growth was significantly inhibited and macrophage infiltration was higher. Isolated TAMs from treated tumors had substantially higher iNOS, CCR7, and M1-marker expression, compared to controls. Similarly, "ultra-pH-sensitive cluster nanobombs" (SCNs), composed of poly(ethylene glycol)-*b*-poly(2-azepane ethyl methacrylate)-modified PAMAM dendrimers (PEG-*b*-PAEMA-PAMAM), released cargo

specifically in the low tumor pH environment.[57] At the low tumor pH, the SCNs disintegrated and rapidly released their cargo: (*1*) platinum (Pt) prodrug small particles (~10 nm) and (*2*) BLZ-945, a CSF-1R small molecule inhibitor. Compared to larger particles, the Pt prodrugs particles demonstrated improved tumor penetration and distribution, and upon internalization, released cisplatin. The synergistic effects of this therapy reduced TAM infiltration, increased $CD8^+$ T cell/Treg cell ratio, and improved median survival in a metastatic B16 melanoma model. However, this therapy was not sufficient to completely ablate tumors, and mice still presented with lung metastases. In a strategy utilizing responsive polymers, Wang et. al. designed a two-layer nanoparticle for tumor-triggered drug release and TAM depletion, ultimately altering the tumor immune environment.[58] The PEG-PLGA polymer complexes (P^3AB) had an outer "shell" that enabled matrix metalloprotease (MMP) triggered drug release, and an inner "core" for TAM-depletion. In the tumor environment, elevated MMP concentrations released the inner core conjugate, an alendronate-glucomannan (BSP) polymer. BSP targeted macrophages, increasing TAM uptake of alendronate and efficiently inducing apoptosis. In a liver tumor model, P^3AB elevated IFN-γ and reduced IL-10 levels, indicative of a more pro-inflammatory immune environment, and prolonged survival.

Due to their intrinsic phagocytic capability, macrophages can be used as "cellular drug reservoirs." Miller et. al. delivered poly(D,L-lactic-co-glycolic acid)-b-poly(ethylene glycol) (PLGA-b-PEG) NPs loaded with a platinum (Pt) pro-drug to HT1080 tumors.[59] Although TAMs comprised only 4% of the total tumor mass, 30% of total injected NPs accumulated in TAMs. Yet, although TAMs initially had the highest accumulation, surrounding tumor cells exhibited more than twice the amount of Pt-payload compared with TAMs. Analysis of supernatant revealed that TAMs served as drug depots for NPs and released their cytotoxic Pt-payload to surrounding tumor cells. The benefit of TAMs was further confirmed following macrophage depletion via clodronate liposomes, which substantially reduced the efficacy of NPs to inhibit tumor growth.

1.3.2.5. Limitations in passive targeting

Increased tumor and TAM accumulation can be achieved by modulating particle properties such as size, shape, charge, and surface modifications. However, the extent of passive targeting to tumors is highly dependent on tumor vascularization and interstitial fluid pressure. In humans, the

EPR effect is poorly reproduced and highly variable between tumors and patients. Furthermore, passive targeting is limited by an inability to differentiate between diseased and healthy tissues with fenestrated endothelium.[60,61] This distinction is critical for effective TAM-targeted therapies due to high MPS uptake in the liver and spleen, which can lead to therapeutic toxicity. Overall, the contribution of enhanced accumulation by passive targeting is limited to organs at the MPS level.[62]

1.3.3 Active targeting

Active targeting, accumulation due to molecular recognition or interaction, relies on ligand-receptor affinity that is usually combined with the ability to trigger endocytosis.[63] In targeted therapies, the main goal is to direct the payload to the appropriate tissue and cell, with decreased accumulation in healthy tissues. TAM-targeted therapies introduce an additional challenge, aiming to target a specific subset of macrophages. In particular, because macrophage surface receptor expression varies across phenotypes, anti-cancer TAM targeting requires preferential drug delivery to M2-like TAMs over tissue resident macrophages or M1-like TAMs. However, this is challenged by the significant overlap in receptor expression among macrophages, which are distributed throughout the body, as well as the unclear distinction between macrophage phenotypes and functions. This section summarizes active targeting strategies for TAM delivery or modulation (**Figure 1.5**).

Active targeting ligands facilitate cellular recognition and internalization

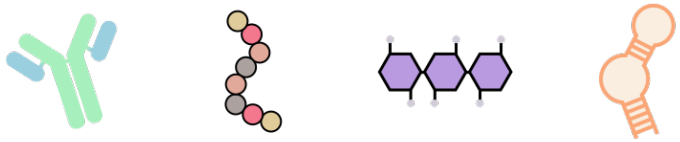

Property	Antibody	Peptide	Carbohydrate	Aptamer
Affinity	High (pM-nM)	Moderate (uM)	High (increases with valency)	High (pM-nM)
Specificity	High	High	High (but promiscuous)	High
Modification	Difficult	Easy	Difficult	Easy
Cost	High	Medium	Low	Medium
Serum stability	Very stable	Requires modification	Stable	Requires modification
Tissue penetration	Low	Moderate	Moderate	High

Figure 1.5. Active targeting ligands recognize cellular markers and facilitate internalization. The ability to differentiate between macrophage phenotypes can improve therapy specificity and reduce off-target effects. However, specific macrophage targeting is still limited by variable surface expression, significant overlap of expression between macrophage phenotypes, and a lack of understanding of macrophage phenotype and function. Currently, antibodies, peptides, carbohydrates, and aptamers are used to increase accumulation in specific macrophage populations. The decision of which ligand to use is a balance between biological considerations (target affinity, specificity, stability, and penetration) and chemical considerations (ease of modification and cost).

1.3.3.1. Monoclonal Antibodies

Therapeutic antibodies are the fastest growing class of biologic drugs, with a 115% increase in new clinical trials between 2007-2016.[64] In TAM-targeted therapies, antibodies are used to (*1*) block macrophage signaling, *(2)* activate macrophage signaling, or (*3*) as a targeting ligand to increase specific drug delivery.

As discussed, the CSF-1/CSF-1R axis is critical for macrophage maturation and survival; disruption of this axis can modulate macrophage populations and improve outcomes in preclinical cancer models. Ries et. al. generated a humanized anti-CSF-1R antibody, RG7155, that blocks both ligand-dependent and ligand-independent receptor activation.[31] Treatment depleted CSF-1R$^+$ TAMs, which was accompanied by increased CD8$^+$ T cell infiltration. Small-molecule CSF-1R inhibitors (PLX3397, BLZ945) can also prolong survival and induce tumor regression, likely through removal of the TAM-mediated immune suppression.[65,66] However, this CSF-1-targeted strategy impacts all macrophages throughout the body, as well as other CSF-1R expressing leukocytes, resulting in systemic toxicities such as elevated liver enzymes, hepatotoxicity, or peripheral edema.[67] Interestingly, observed toxicity differs between small molecule versus antibody inhibitors. Another macrophage-targeting monoclonal antibody treatment against pattern recognition receptor 'macrophage receptor with collagenous structure' (MARCO) also induced anti-tumor activity in mammary and colon carcinoma and melanoma by re-polarizing TAMs to a pro-inflammatory phenotype.[68]

The CD47/signal regulatory protein alpha (SIRPα) axis is another therapeutic target.[69] This immune checkpoint is composed of (*1*) CD47, a molecular "don't eat me signal" that identifies cells as "self," and is often overexpressed in transformed cells, and (2) SIRPα, an inhibitory immune receptor on phagocytes. Anti-CD47 antibody blockade increases macrophage phagocytosis of cancer cells. Although anti-CD47 approaches have modest effects as a monotherapy, synergistic effects with tumor-opsonizing antibodies (rituximab, trastuzumab, cetuximab) or SIRPα antagonists improve anti-tumor response, resulting in cancer elimination in a non-Hodgkin or Raji cell lymphoma models.[70,71] At the time of this review, anti-CD47 antibody Hu5F9-G4 is undergoing Phase 1/2 clinical trials as a monotherapy and in combination with other anti-cancer drugs.[72] Interestingly, a recent study reported that macrophages can circumvent CD47 "don't-eat-me" signaling and phagocytose tumor cells after activation with CpG, a TLR-9 agonist.[73] Kulkarni et. al. designed a supramolecular assembly in an example of antibody-based targeting of lipid nanoparticles, comprising (*1*) a lipid nanoparticle functionalized with an anti-SIRPα antibody to block the SIRPα/CD47 axis, and (*2*) a lipid-modified CSF-1R inhibitor for high drug loading into the nanoparticle.[74] Treatment robustly ablated tumor growth due to increased phagocytosis of cancer cells by macrophages, and increased percentage of M1-like

macrophages ($CD11b^+CD86^+$). The bifunctional supramolecule induced a strong anti-tumor response compared to sequential treatments of anti-SIRPα and anti-CSF-1R (BLZ-945) alone due to improved intratumoral accumulation and circulation, highlighting the critical role a drug delivery system can play in tissue accumulation, pharmacokinetics, and ultimately, therapeutic efficacy.

Antibodies against macrophages surface proteins such as CD169, CD36, CD86, or CD206, have also been used to facilitate targeted delivery of NPs to macrophages.[75–77] Antibodies are the most commonly used active targeting ligand because of their broad range of uses, such as direct anti-tumor effects, facilitation of cellular targeting, or neutralization of soluble ligands or receptors.[78,79] Antibodies can provide the quickest route for clinical proof-of-concept and benefit from a history of safety and tolerability in humans as well as the necessary infrastructure for commercialization. However, while these targeting ligands can offer some cellular and M1/M2 specificity, their efficacy is reduced by overlap with other cells that express the same receptors and by high non-specific macrophage uptake via Fc recognition. For example, CD206 is a pattern recognition receptor that is upregulated on M2-like macrophages, but is also expressed by tissue resident macrophages and dendritic cells. While therapeutic antibodies have achieved impressive results in cancer treatments, their use as targeting ligands to TAMs is limited by several drawbacks. Macrophages express an Fc receptor which can result in non-specific antibody interactions depending on conjugation chemistry. Also, due to their large size (~150 kDa), antibodies suffer from conjugation challenges and poor tissue penetration. Antibodies are currently the most costly form of targeting ligands, compared to small molecules or peptides.[80] The development of nanobodies addresses some of these limitations. Nanobodies are the smallest antigen binding fragment (~15 kDa) and lack the Fc region of conventional antibodies, eliminating non-specific Fc-binding and improving tumor penetration. Targeted delivery using mannose nanobodies was able to induce efficient internalization by $CD45^+MHCII^{low}$ TAMs.[81] However, nanobodies still require extensive optimization as they are challenged by poor solubility and stability, and rapid clearance.[82] As such, significant effort has been exerted to discover other ligand alternatives to antibodies for macrophage targeting.

1.3.3.2. Peptides

Peptide ligands can offer specific recognition of their cognate receptors, and are generally smaller, less immunogenic, and cheaper to manufacture than antibodies. Our group has identified M2pep, a unique peptide sequence that binds preferentially to M2 macrophages over M1/M0 macrophages and other leukocytes.[83] Delivery of a pro-apoptotic peptide depleted macrophage populations and prolonged survival in CT26 tumor-bearing mice. Further optimization improved serum stability and affinity, and conferred intrinsic fluorescence and pH-sensitivity to enable improved specific binding in the acidic tumor environment.[84–87] Conde et. al. conjugated M2pep onto gold nanoparticles to deliver small interfering RNA (siRNA) for VEGF knockdown, demonstrating high selectivity for TAMs in the lung tissue and lavage fluid, and Qian et. al. applied M2pep for TAM-targeted siRNA delivery of anti-CSF-1R resulting in anti-tumor activity in mouse tumor models.[88,89]

Another peptide, UNO, binds CD206 (mannose) receptor on TAMs with high specificity (> 95%) across five tumor models of breast carcinoma, melanoma, glioma, and gastric carcinoma.[90] Significantly, UNO did not home to non-malignant tissues, even those with $CD206^+$ macrophages, or accumulate non-specifically in regions with vascular leakiness. This system is advantageous over other CD206 peptides (i.e. RP-182) or mannose analogues (e.g. Manocept™), which binds to a variety of other receptors, such as SIRPα or CD209. Similarly, the macrophage-binding peptide CRV rapidly extravasated to tumors and bound extracellular retinoid X receptor beta (RXRB) on $CD11b^+F4/80^+$ macrophages.[91] CRV distinguished between macrophages in pathological and healthy tissues, facilitating TAM-specific accumulation of porous silicon NPs in solid tumors. However, peptide delivery systems are limited by reduced binding affinity and increased susceptibility to proteolytic degradation compared to their antibody counterparts.[92]

1.3.3.3. Carbohydrates

Carbohydrate targeting ligands offer high specificity, binding affinity that increases with increasing ligand valency, high water solubility, and low cost. As discussed above, the macrophage mannose receptor (MMR/CD206) is of particular interest in TAM-targeted therapies. MMR is abundantly expressed on M2-like macrophages and efficiently mediates internalization. Zhu et. al. developed a mannose-modified nanoparticle platform to target TAMs in a pH-sensitive manner.[93] PLGA nanoparticles were decorated with an acid-sensitive PEG-coating that was shed in the acidic

tumor microenvironment (~pH 6.8), exposing mannose for binding to the mannose receptor on TAMs. The PEG coating was sufficient to reduce mannose-mediated uptake in the liver and spleen, likely by reducing opsonization of particles. PEGylated nanoparticles showed higher tumor accumulation and circulation, as well as clear TAM-colocalization.

Glucomannan *Bletilla striata* (BSP) is another carbohydrate used to target the mannose receptor on macrophages.[94] A BSP-alendronate conjugate demonstrated induced an 84.5% reduction in $F4/80^+$ cells and in a S180 sarcoma tumor, treatment decreased VEGF, MMP-9, and the number of blood vessels by 83.9%, 65.3%, and 86.3%, respectively. IFN-γ expression, necessary for a Th1 immune response, was markedly increased by 3-fold. Together, these results suggest that TAM-depletion reduced angiogenesis and overcame immune suppression in the tumor microenvironment. Similar results were demonstrated using mannose-decorated manganese dioxide (MnO_2) nanoparticles to relieve hypoxia in tumors.[95] Combined delivery of hyaluronic acid re-programmed M2-like TAMs into an M1-like phenotype. Similarly, β-cyclodextrin nanoparticle-mediated delivery of TLR-7/TLR-8 agonist R848 and anti-PD-1 checkpoint inhibitor improved immunotherapy response.[96] Treatment induced macrophage re-education toward an M1-like phenotype and triggered T cell infiltration, reducing tumor growth and improving survival in MC38 colorectal and B16F10 melanoma models. Muraoka et. al. highlighted the critical role that macrophages play in antigen presentation, the capacity to stimulate cytotoxic T cells, and tumor eradication.[97] Mice were treated with (*1*) cholesteryl pullulan nanogels to deliver long peptide antigen 9m epitope to stimulate a $CD8^+$ T cell response, and (*2*) CpG, a TLR-9 agonist to restore antigen presentation capacity and other pro-inflammatory functions in TAMs. Combined with adoptive T cell transfer of $CD8^+$ T cells, treatment eradicated tumors. Macrophage depletion with clodronate liposomes limited therapeutic efficacy, highlighting the role of macrophage antigen presentation in tumor ablation.

However, carbohydrates can be recognized by multiple lectins, whereas their antibody counterparts offer high specificity to their cognate receptors. For example, mannose moieties can be recognized by other mannose binding receptors, such as DC-SIGN, L-SIGN, Endo180, or mannose binding lectins.[98] In a direct comparison of antibody and carbohydrate targeting ligands for dendritic cell-specific C-type lectin receptor (DC-SIGN), antibodies were more efficient in

driving binding and uptake of NPs. Although carbohydrate-decorated NPs benefitted from higher ligand valency, this advantage did not outcompete the higher affinity binding of the anti-DC-SIGN antibody.[99]

1.3.3.4. Oligonucleotides

Aptamers are short RNA or DNA oligonucleotides that form unique secondary structures, offering high affinity binding and high selectivity between targets. As synthetic ligands, aptamers benefit from relatively low production costs and a broad range of conjugation chemistries. Compared to antibodies, aptamers can offer comparative binding affinities with a much smaller size, improving tissue penetration and allowing them to bind harder-to-reach targets.[100,101]

Aptamers have been used to re-educate TAMs and create a pro-inflammatory tumor immune environment. Roth et. al. generated an RNA aptamer blocking IL-4Rα (CD124) signaling, which has been implicated in pro-tumor TAM polarization.[102] The IL-4Rα aptamer preferentially targeted myeloid-derived suppressor cells (MDSC) and TAMs, reducing downstream STAT6 signaling and inducing apoptosis. In 4T1 tumor-bearing mice, IL-4Rα aptamer treatment significantly inhibited tumor progression and altered the tumor immune environment: MDSC, TAM, and regulatory T cell populations were reduced, while activated, effector T cell populations ($CD8^+$ and $CD69^+$) were increased. However, aptamer treatment alone was insufficient to eradicate the tumor and only temporarily arrested tumor growth.

While the aptamer field is still being explored, it is important to recognize the following *in vivo* limitations for aptamers: susceptibility to nuclease degradation and rapid renal excretion. Aptamers used *in vivo* therefore require chemical modifications to improve serum stability and circulation time.[103]

1.3.3.5. Limitations in active targeting

Although active targeting can improve macrophage uptake, therapeutic efficacy is challenged by limited retention, broad macrophage distribution, and macrophage plasticity. First, carrier biodistribution is controlled by the properties of the carrier itself, such as size, shape, and charge, and is ultimately determined by circulation and extravasation, resulting in passive accumulation.

As carriers accumulate in the tissue, targeting ligands facilitate cellular localization and internalization. Of note, the conjugation of targeting ligands can create a 'binding site barrier' because high affinity antibody interactions occur at the tumor periphery, impeding efficient tumor penetration and creating non-uniform spatial distributions.[104] Overall, an extremely low percentage of nanoparticles end up in target cells.[105] For example, in the tumor, only 0.07% of injected NPs are delivered to the solid tumor, of which only 2% are delivered to cancer cells. The majority of intratumoral NPs are internalized by perivascular macrophages, which dominate uptake even in the presence of targeting ligands: TAMs took in up to 90% of cancer-targeted nanoparticles. This is in part due to higher macrophage concentration near tumor blood vessels: 70% of tumor blood vessels had 1-3 macrophages in the periphery, over half of which were within 10 μm from the vessel. Together, macrophages' high intrinsic phagocytic behavior and spatial location by vasculature favor increased macrophage uptake.[106] While increased macrophage uptake can be advantageous for TAM-therapies, this illustrates the challenge of designing targeted drug delivery systems.

Second, macrophages are distributed throughout the body, posing a challenge for TAM-targeted carriers. Spleen and liver macrophages readily uptake nanoparticles, which can prevent sufficient drug accumulation in target tissues and lead to high toxicity. Even lung macrophages play a role in clearance of IV-injected NPs: Wilbroe et. al. showed that adverse cardiopulmonary reactions were due to robust clearance by resident pulmonary intravascular macrophages, resulting in massive release of thromboxane and prostaglandins.[107] Lastly, TAMs are extremely heterogeneous and can adapt their phenotype and function in response to environmental stimuli. Macrophage extracellular surface expression can fluctuate, and it also overlaps between tissues, macrophage subpopulations, and other immune cells. For example, CD206 is highly expressed on M2a and M2c TAMs, but is also expressed on immature dendritic cells. Monocyte-derived dendritic cells in particular share significant marker overlap with TAMs and express MHCII, F4/80, CD14, and IL-10. To add to the challenge of targeting macrophages within specific tissues, it is also necessary to target specific macrophage subpopulations. For example, Ohnishi et. al. demonstrated that $CD169^+$ TAMs are linked with favorable prognosis.[30,75] Currently, there is an inadequate understanding of the relationship between macrophage phenotype and function, resulting in an inability to preferentially deliver therapeutics to tumor-supporting TAMs *in vivo*.

As such, it is critical that we improve our understanding of macrophage function, diversity, and interactions with tumors in order to develop better therapies.

1.4. Localized TAM modulation by biomaterials: lessons from wound healing

Activated macrophages are essential cells in the natural wound healing process, and have therefore been extensively studied in the context of host response to implanted biomaterials. The principles governing the impact of biomaterials on macrophages in a wound environment might therefore be applied in the future toward TAM modulation in the chronic wound-like environment of solid tumors.[108] Drug-loaded implants are both clinically approved (Gliadel wafer) and in development for localized tumor therapy. Future designs of localized anti-cancer delivery platforms might offer dual chemotherapy and immunotherapy activity by considering the effects of biomaterial properties on macrophage polarization. In this section, we briefly summarize the role of macrophages in wound healing, the effect of biomaterial properties on macrophage activation, and finally biomaterials used for local TAM modulation.

1.4.1 Macrophages in wound healing

Macrophages are essential for complete wound healing, orchestrating cellular responses during the overlapping stages of healing: inflammation, proliferation, and remodeling (**Figure 1.6**). Macrophages mature with the wound, adapting their functions as the wound environment changes and heals.[10,109] In the early stages of hemostasis, infiltrating macrophages adopt an M1-like phenotype, driving inflammation to recruit and activate leukocytes, and clearing debris and apoptotic cells. At this stage, the wound has high levels of IL-1, IL-6, IL-12, TNF-α, and CCL-2. Once the wound is stabilized, macrophages transition toward an M2-like phenotype to promote tissue healing, proliferation, and remodeling. Macrophages encourage angiogenesis and ECM remodeling by secreting growth factors (PDGF, VEGF, FGF) and proteases (serine proteases, MMP-2, MMP-9) and also exert immunosuppressive activities by secreting IL-10 and TGF-β and up-regulating PD-L1 and PD-L2. This M2-like activity mirrors that of TAMs.

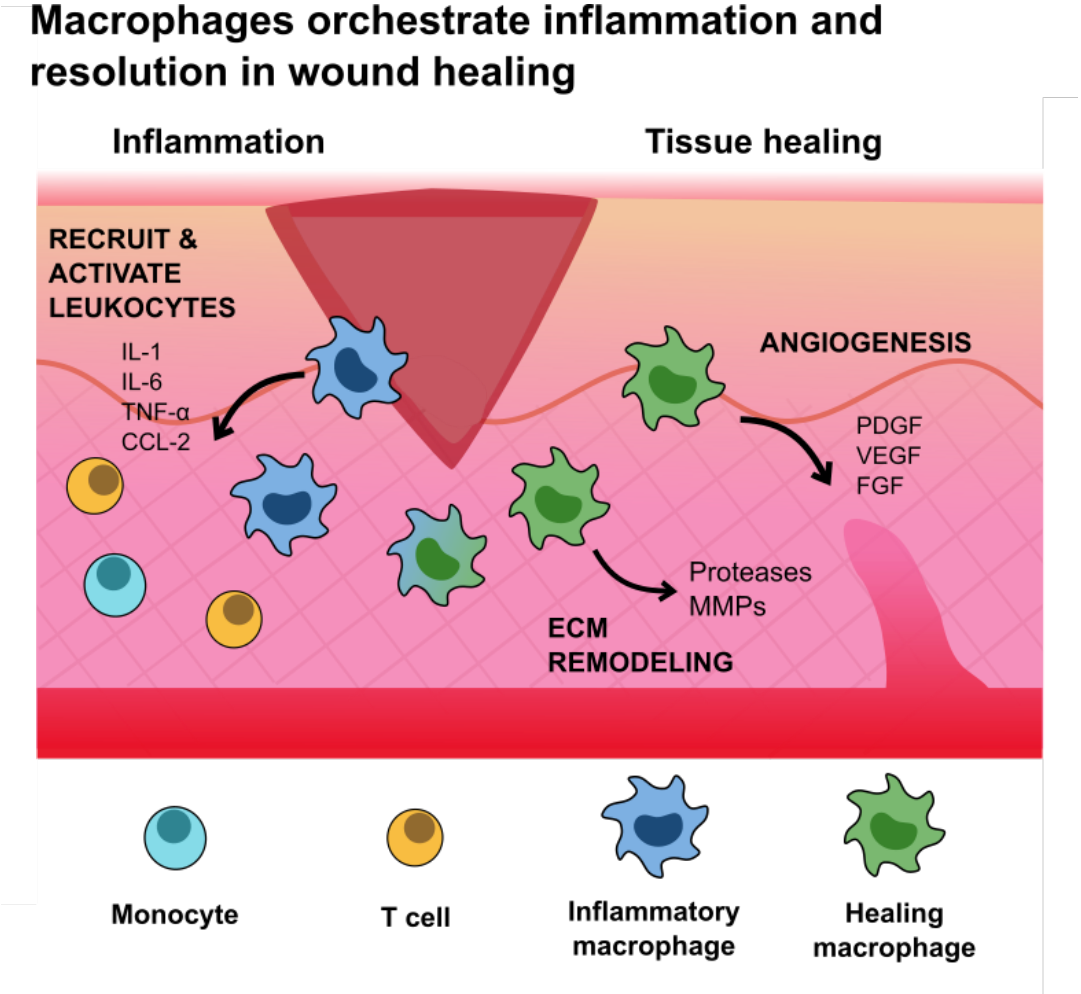

Figure 1.6: Macrophages in wound healing. Macrophages hold an essential role in wound healing, orchestrating the cellular transitions from inflammation, proliferation, and remodeling. Macrophages release cytokines to recruit and activate leukocytes to the wound site, and promote ECM remodeling and new vessel growth. After the initial inflammatory phase, macrophages exert immunosuppressive activities to restore homeostasis and suppress T cell proliferation and activity. These behaviors mirror that of M2-like TAMs in cancer.

1.4.2 Macrophage response to engineered biomaterials

Biomaterials afford tunable systems to modulate macrophage activity. Modifications of architecture (size, geometry, porosity), surface conjugations, or mechanical factors in biomaterials can significantly impact macrophage activation. The macrophage response to implanted biomaterials can be the difference between a successful or failed device. As discussed above, macrophages are master phagocytes, quickly recognizing and internalizing foreign substances.

Small particles are readily ingested, whereas larger particles (> 10 μm) can frustrate macrophages, inducing inflammatory M1-like phenotype and secretion of pro-inflammatory cytokines, proteases, and reactive oxygen species. Larger implants (> 100 μm) induce the foreign body reaction (FBR) and the formation of foreign body giant cell (FBGC), a fusion of multiple macrophages around the implant. FBGCs and fibroblasts deposit a thick, collagen capsule around the implant, which jeopardizes the function of the biomaterial and can necessitate its removal.[110,111]

Geometry and aspect ratio also affect macrophage activation and phagocytosis. Implants with smoother curvature and longer aspect ratios are viewed as "deactivating" because macrophages are unable to phagocytose them.[110] Implant stiffness also influences macrophage activation: PEG-RGD hydrogels with reduced stiffness decreased macrophage activation, as evaluated by cytokine secretion and gene profiling, and resulted in a less severe FBR reaction.[112] Even implant surface architecture and internal porosity elicits different macrophage responses. Rougher surfaces with deeper grooves increase inflammatory macrophage activation compared to smoother surfaces, and higher porosity increases macrophage infiltration.[110] In addition to the physical characteristics of implants, biochemical modifications can be added to influence macrophages and the FBR. Surface modifications with methyl promoted the highest inflammatory macrophage infiltration compared to surfaces modified with hydroxyl groups. Interestingly, hydroxyl modifications induced a significantly lower FBR response. Comprehensive discussions about implant interactions with macrophage are reviewed elsewhere.[110,113]

1.4.2.1. Implantable scaffolds

The chemistry, mechanics, and physical properties of implanted scaffolds all affect the local macrophage response to the foreign material (**Table 1.2**). In the future, implanted biomaterials might also provide another tactic for TAM modulation. This section summarizes what has been reported regarding the effect of scaffold properties of local macrophages, and may provide guidance on properties to either target or avoid in cancer applications.

Parameter	M1-like	M2-like
Pore size	Larger	Smaller
	90–160 μm	30–40 μm
Fiber diameter	Thinner	Wider
	150 nm	500 nm
Stiffness	Less stiff	More stiff
	0.3 kPa	40 kPa

Table 1.2: Properties of implantable scaffolds modulate local macrophage response. Larger pore size, thinner fibers, and less stiff materials promote M1-like macrophage polarization. Smaller pore size, wider fibers, and stiffer materials promote M2-like macrophage polarization. Understanding how implant architecture affects macrophage polarization and activity can guide the design of new cancer therapeutics.

1.4.2.2. Pore size

Implant architecture impacts macrophage activation and the FBR. For implantable scaffolds, appropriate pore size is essential for cellular infiltration, ECM deposition, and angiogenesis necessary for tissue integration. The Ratner group synthesized poly(2-hydroxyethyl methacrylate-co-methacrylic acid) (pHEMA-co-MAA) hydrogel scaffolds to promote cellular integration with myocardial tissues while decreasing fibrotic encapsulation and demonstrated that a pore size of 40 μm decreased the FBR, induced M2-like macrophage polarization, and improved blood vessel density.[114] In comparison, larger pores (90-160 μm) induced a stronger fibrotic response and decreased vascularization. While both M1-like ($NOS2^+$) and M2-like ($CD206^+$) macrophages were present, porous scaffolds increased the number of $CD206^+$ macrophages, suggesting a transition toward a wound healing phenotype. Further investigation into macrophage phenotype in the scaffolds revealed that macrophages immediately within the 34 μm pores exhibited a 63% increase in M1-like (NOS2, IL-1R1) markers.[115] However, macrophages immediately outside the scaffold in foreign body capsule were enriched for M2-like (CD206, SR-BI/II) markers. In contrast, Sugiura et. al., who compared 5 and 30 μm pores in Poly(1-lactic-co-ε-caprolactone) copolymer (PLCP) scaffolds reinforced with poly(1-lactic acid) (PLA) nanofibers, found that large pore (30

μm) scaffolds did not improve vascular regeneration, neotissue formation, or cellular infiltration, and found no significant difference between infiltration of M1-like ($F4/80^+iNOS^+$) or M2-like macrophages ($F4/80^+CD206^+$).[116] While the authors admit that the scaffold pore size was heterogeneous in the large graft, this study illustrates how sensitive macrophages are to their external environment.

1.4.2.3 Fiber diameter and modifications

Similarly, studies have demonstrated that fiber diameter and alignment in electrospun scaffolds affect macrophage activation. Poly-L-lactic acid (PLLA) scaffolds were synthesized with varied fiber alignment (aligned or random) or diameter (~1.5 μm or ~0.5 μm).[117] Aligned fibers increased macrophage adherence compared to random fibers, regardless of fiber diameter; yet, the authors suggested that adherence did not always correlate with macrophage activation. Furthermore, nanofibrous scaffolds reduced inflammatory cytokine (TNF-α, IFN-γ) levels and increased pro-wound healing cytokine (VEGF) levels, regardless of fiber alignment. Overall, fiber diameter had a more significant impact on the inflammatory response: smaller fibers induced M1-like phenotype, while larger fibers induced an M2-like phenotype. Abebayehu et. al. incorporated galectin-1, an immunosuppressive protein, into small and large fiber polydioxanone scaffolds.[118] This modification was sufficient to shift macrophage commitment to an M2-like phenotype on the small diameter fibers. Likewise, functionalization with chondroitin sulfate (CS), a glycosaminoglycan, decreased macrophage inflammation by impeding CD44 binding, preventing the LPS/CD44/NF-κB inflammatory cascade.[119] CS conjugation to a collagen scaffold decreased pro-inflammatory gene (*TNF-α, iNOS*) expression, while increasing anti-inflammatory gene (*TGF-β, Arg, MRC1, IL-10*) markers. Following LPS challenge and *in vivo* implantation, the CS scaffold significantly reduced macrophage expression of pro-inflammatory genes (iNOS, *TNF-α, IL-1β, IL-12β, MMP-1*), and downregulated CD44 expression.

1.4.3 Injectable hydrogels

Hydrogels have garnered interest for their capacity to deliver cellular, drug, or protein therapeutics. Similar to scaffolds, their architecture and physicochemical properties are highly tunable.[120] For wound healing applications, hydrogels have emerged as interesting delivery systems to stimulate macrophage pro-healing activity. Feng et. al. fabricated a carbohydrate-based hydrogel composed

of Konjac glucomannan (KGM) and heparin, which stimulated macrophage secretion of pro-angiogenic growth factors and sequestered them locally, promoting new blood vessel formation.[121] KGM is a carbohydrate in the mannose family and has high affinity for CD206, allowing for rapid macrophage recognition. The crosslinked hydrogels formed pores with an average size of 50 μm, which coincides with reported literature about optimal pore size to induce pro-healing macrophages. THP-1 cells cultured on KGM/heparin gels highly expressed CD206 and secreted high levels of bFGF, EGF, angiogenin, and VEGF-A, growth factors that support blood vessel formation. Furthermore, cells on the gel surface expressed lower levels of pro-inflammatory cytokines IL-1β and TNF-α. Subcutaneous injection into mice revealed increased blood vessel density (184 per mm^2), hemoglobin, and CD31 and α-smooth muscle actin positive cells, indicative of new blood vessel formation, compared to KGM controls.

Hydrogels have also been used in a different type of wound healing. Cystic cavities are devastating to spinal cord injury recovery, inhibiting axonal regeneration and leading to cell death. Hong et. al. developed an imidazole-poly(organophosphazenes) (I-5) hydrogel that successfully eliminated these cavities, as well as potentiated ECM remodeling by stimulating local macrophages to produce MMP-9 enzymes, recruit perivascular fibroblasts, and promote fibronectin matrix assembly.[122] Specifically, the imidazole group on the hydrogel interacted with the histamine receptor on macrophages, enhancing macrophage-hydrogel interactions and maintaining prolonged macrophage presence. I-5 also increased ECM density of $CD11b^+CD206^+$ macrophages with significantly increased MMP-9 expression, which the authors hypothesized contributed to fibrotic ECM remodeling. Overall, I-5 hydrogel enhanced coordination between the fore- and hind paws, improved myelin basic protein immunoreactive signal intensity, and contributed to improved locomotor function.

1.4.4 Application of wound healing principles to cancer

Although wound healing and cancer seem to be on opposite ends of the spectrum in respect to desired macrophage phenotype, we can derive key biomaterials principles from macrophages in wound healing and apply them to improve cancer therapies. For example, scaffolds in wound healing established 30-40 μm as the optimal pore size to stimulate M2-like macrophage phenotype, while larger pores 90-160 μm promote an M1-like macrophage phenotype.[114,115] In electrospun

scaffolds, smaller diameter fibers promote inflammatory activity. Therefore, scaffold-based cancer therapeutics could incorporate larger pores or smaller fiber diameters to activate inflammatory macrophage phenotype in the tumor environment. Substrate rigidity also alters cell transcriptome, phenotype, and behavior: increased rigidity increases macrophage phagocytosis and decreases the inflammatory response.[123] In cancer, this effect is illustrated as macrophages leave the soft, matrix-deficient bone marrow and enter the matrix-rich tumor environment. Alvey et. al. correlated substrate micro-stiffness (kPa) with an increased *Sirpa:cd47* ratio.[124] Understanding this relationship between substrate stiffness and macrophage expression can help design future therapies: softer implantable scaffolds could perhaps downregulate the inhibitory effects of the CD47:SIRPα axis.

Engineered implantable scaffolds could be used to modulate local immune cells and improve cancer treatments. Guerra et. al. used hydrogels to deliver M1-like macrophages directly to the tumor to utilize their anti-tumor activity and overcome acute inflammation associated with systemic injection of M1-like macrophages.[125] Poly(ethylene glycol) diacrylate (PEGdA) was crosslinked with thiolated gelatin poly(ethylene glycol) (Gel-PEG-Cys) and subsequently loaded with THP-1 monocytes, polarized to M1-like macrophages with LPS and IFN- γ. The macrophage-loaded hydrogel was injected adjacent to solid MHCC97L HCC tumors and reduced tumor volume by 6.9-fold. The authors hypothesized that the M1-macrophages created a pro-inflammatory tumor microenvironment with elevated TNF-α and nitrite levels, inducing caspase-3 dependent apoptosis in cancer cells. However, the authors did not characterize macrophage phenotype within the tumor, or whether macrophages within the tumor were derived from the hydrogel.

Another biomaterials-based strategy utilized scaffolds to influence immune cell distribution, reducing TAM populations in the primary tumors and attenuating their tumor supporting activities. Rao et. al. implanted microporous poly(ε-caprolactone) (PCL) scaffolds, which recruited immune cells and reduced tumor burden at metastatic sites.[126] At the site of the scaffolds, increases in inflammatory ($Ly6C^+F4/80^-$) and non-inflammatory monocytes ($CD11b^+Gr\text{-}1^{hi}Ly6C^-$) were detected; both cell populations have been implicated in preparing pre-metastatic niches. Macrophage ($CD11b^+F4/80^+$), DCs ($CD11c^+F4/80^-$), and $CD8^+$ cytotoxic T cell populations were lower at the implant site. Furthermore, mice with PCL implants had reduced tumor burden in the

liver (64%) and brain (75%). The authors hypothesized that the scaffold redistributed monocyte ($CD11b^+Gr\text{-}1^{hi}Ly6C^-$) populations from the tumor and spleen, key niches for metastatic seeding, to the scaffold. This hypothesis was supported by Gr-1 antibody depletion of $CD11b^+Gr\text{-}1^{hi}Ly6C^-$ cells, which also improved survival for mock surgery (control) mice. This study demonstrates how biomaterials can be used to influence immune cell distribution. Accumulation of monocytes in the scaffolds reduced the percent of tumor-associated macrophages at the tumor site, which contributed to improved survival in a MDA-MB-231 tumor model. In another example, Aguado et. al. implanted microporous poly(lactide-co-glycolide) (PLG) scaffolds and confirmed an increase in $CD11b^+Gr\text{-}1^{hi}Ly6C^-$ cells in the scaffolds of tumor bearing mice.[127] Macrophage ($CD11b^+F4/80^+Ly6C^-$), monocyte ($F4/80^-Ly6C^+$), and $CD11c^+$ DC distribution, as well as relative leukocyte recruitment, was consistent across scaffold implanted and mock treated mice. However, recruited macrophages in scaffold treated mice expressed a distinct functional phenotype compared to mock treated mice, suggesting that the scaffold influenced macrophage phenotype. Recruited macrophages ($F4/80^+Vcam1^+$) in the scaffold treated mice displayed an increase in *CCR2*, *CCR7*, and arginase (*Arg*), and decrease in Vcam1 expression relative to mock treated mice. The decreased Vcam1 expression suggested that TAMs were less adhesive, leading to reduced retention in the tumor environment. Furthermore, when conditioned media from $CD45^+$ cells from scaffold-bearing mice was applied to tumor cell cultures, the authors observed decreased tumor cell mobility, CCL2, and increased decorin, a proteoglycan linked to reduction of metastatic spreading. These studies have influenced the development of a hydrogel-scaffold pre-metastatic niche model to investigate activation of disseminated tumor cells, as well as recruitment and modulation of local immune populations.[128] Overall, the immunomodulatory potential of scaffolds can help us understand the cancer environment, development, and dissemination, and ultimately improve cancer therapeutics.

1.5. Engineered macrophages and biomaterials

Because the tumor microenvironment recruits circulatory monocytes and MDSCs via secreted cytokines, researchers have engineered therapeutic macrophages for tumor homing and immunotherapy (**Figure 1.7**). These exogenously-delivered macrophages have been engineered as a cancer therapy, either as a genetically engineered macrophage (GEM) to overcome immune suppression, or to express a chimeric antigen receptor (CAR) for phagocytosis of tumor cells.

Furthermore, they have been used as drug delivery vehicles. Macrophages are clever drug carriers because they are preferentially recruited to the tumor niche and have demonstrated improved tumor penetration, challenges faced by many drug delivery systems. Additionally, these cells are privileged to cross the nearly-impermeable blood brain barrier. Overall, this critical cell can be engineered and equipped with biomaterials to improve therapeutic efficacy.

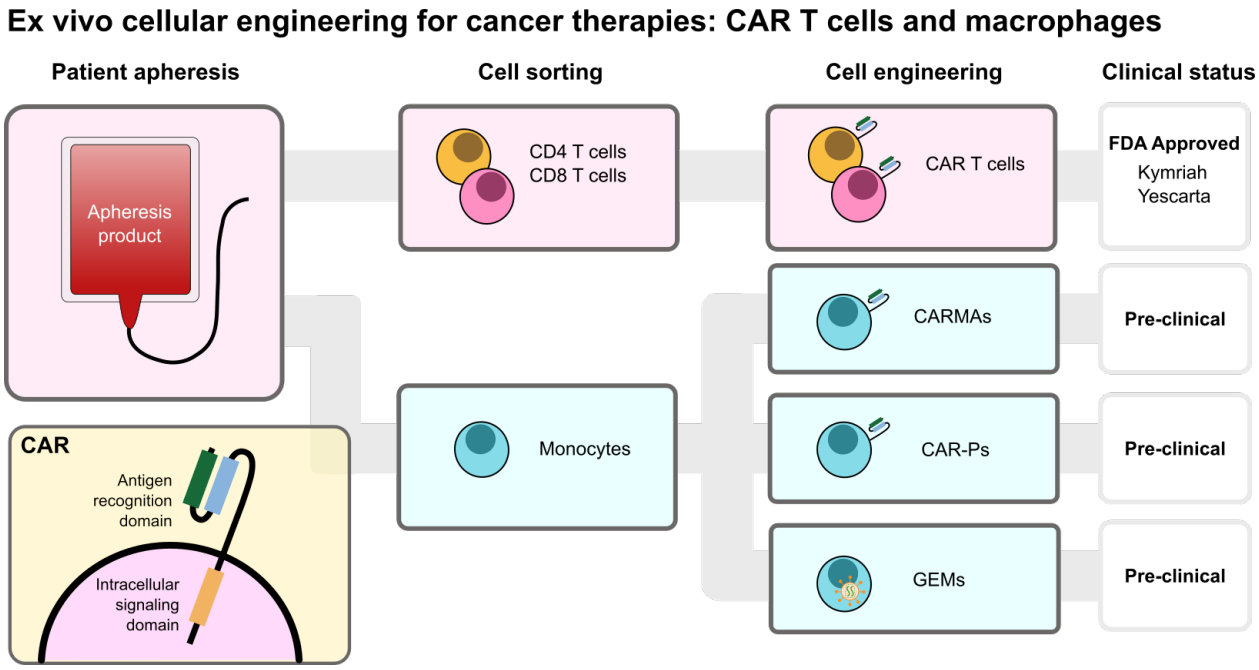

Figure 1.7: Adoptive cellular transfer therapies for cancer treatment. Adoptive cellular therapies are an effective anti-cancer therapy that genetically modifies a patient's own cells as an anti-cancer immunotherapy. Chimeric antigen receptor (CAR) T therapies collect a patient's leukocytes by apheresis and separate $CD4^+$ and $CD8^+$ T cells, which are engineered to express CARs. Kymriah and Yescarta are FDA approved therapies currently available to patients. Parallel to CAR T cells, several groups have demonstrated that monocytes derived from the same apheresis product can be differentiated and modified to express CARs (CAR-macrophages (CARMA) and CAR for phagocytosis (CAR-P)). Genetically engineered macrophages (GEMs) are modified to express proteins that overcome immune evasion and support anti-tumor immune cell activity.

1.5.1 Genetically engineered macrophages

In 1974, Fidler published a pioneering study showing that *ex vivo*-stimulated macrophages reduced pulmonary metastasis in a B16 melanoma model.[129] Disappointingly, in clinical trials, *ex vivo*-

stimulated macrophages failed to show a survival benefit in solid tumor treatment. It was hypothesized that this was due to macrophage diversion to a pro-tumoral phenotype and lack of persistent pro-inflammatory cytokine secretion.[130] To address this, we have recently developed genetically engineered macrophages (GEMs), endowed with resistance to tumor immunosuppressive signals, with the goal of transforming the tumor microenvironment by promoting persistence and activation of natural killer and T cells.[131] In the same vein as adoptive cellular therapies, GEMs would be generated from blood monocytes. Using a novel, highly effective lentivirus for macrophage transduction, the GEMs can be influenced to express proteins that overcome immune evasion, including disruption of IL-10 and PD-L1 gene expression through genome editing, and support of anti-tumor immune cell activity through sTβRII and IL-21 expression. Soluble TβRII secretion interferes with and disrupts TGF-β signaling, and IL-21 activates cytotoxic lymphocytes, and shifts macrophage polarization to an inflammatory phenotype. GEMs were injected into intracranial U87 tumors and no detrimental effects on survival were observed, despite GEM persistence for the duration of the study (30-45 days). Although no added therapeutic benefit was observed following GEM injection, these studies were performed using GEMs expressing bioluminescent proteins as opposed to an immunomodulatory protein, as NOD-SCID gamma mice lack functional B and T cells, and a therapeutic benefit almost certainly depends on an intact endogenous immune system. Future studies in immune-competent mice are needed to understand the safety and potential clinical benefit of GEMs. Overall, GEMs benefits from several key advantages over adoptive T cell transfer. Direct intratumoral injection increases safety compared to systemic intravenous injection and maximizes engineered cell-tumor interactions. Also, GEMs do not divide, so insertional mutagenesis will not affect future immune cell generations *in vivo*. Lastly, GEMs are generated from the currently-discarded monocyte population that is isolated during T cell preparations, reducing the burden on necessary infrastructure for developing a clinical product. Importantly, a manufacturing process for monocyte-derived macrophages has been developed and tested in patients, suggesting feasibility of scale up and clinical administration of engineered macrophages to patients.

In a direct parallel to CAR T cells, several attempts at engineering CAR macrophages have been made. Most notably, chimeric antigen receptor macrophages (CARMA) have been demonstrated as an efficient immunotherapy for solid tumors.[132] CARMA contains (*1*) an extracellular single-

chain antibody variable fragment (scFv) against CD19 or HER-2, (*2*) a CD8 hinge and transmembrane domain, and (*3*) an intracellular cytoplasmic domain (CD3ζ, FcsRIγ, Dectin-1). The CAR was successfully expressed in both THP-1 monocytes and primary macrophages. CARMAs showed high specificity for their cognate targets and successfully engulfed and degraded tumor cells. Furthermore, phagosome repair was observed, indicating macrophage survival of this process, and potential serial tumor cell killing. Combination therapy with CD47/SIRPα blockade enhanced CARMA phagocytosis. Furthermore, transduction stimulated M1-like phenotype (HLA-DR, CD86, CD80, PDL1) and suggested at least temporary and moderate resistance to M2 subversion, indicated by the failure of IL-4 stimulation to induce CD206 expression in CARMAs. In both metastatic breast and ovarian cancer models, a single dose of CARMAs induced a 2,400-fold reduction in tumor burden compared to untreated mice. The CARMA platform is marketed by Carisma Therapeutics.

Similarly, Morrissey et. al. introduced chimeric antigen receptors for phagocytosis (CAR-P) into macrophages.[133] As with CARMAs, the CAR-P contained (*1*) an scFv against CD19 or CD22, (*2*) a CD8 transmembrane domain, and (*3*) an intracellular cytoplasmic domain (CD3ζ, Megf10, or FcRγ) to trigger phagocytosis. Macrophages expressing CAR-Ps were specific for their antigen of interest and able to engulf variably sized targets, ranging from 2.5 to 20 μm in diameter. Incubation with $CD19^+$ Raji B cells revealed that CAR-P macrophages internalized "bites" of the target cells, similar to trogocytosis, a "nibbling of live cells." Interestingly, CAR-P expression in non-professional phagocytes, such as human 3T3 fibroblasts, also promoted antigen-dependent trogocytosis. However, CAR-P macrophages were unable to engulf whole-cells, even after additional CD19 antibody opsonization. Introduction of tandem PI3K signaling, which enables engulfment of large targets, onto the CD19 cytoplasmic domain induced minimal whole cell engulfment (6 cancer cells per 100 macrophages). In a macrophage-Raji co-culture, both CAR-P macrophages with the FcRγ or tandem PI3K-FcRγ significantly reduced Raji cell numbers, through either trogocytosis or whole cell engulfment.

1.5.2 Macrophages as drug delivery vehicles

Monocytes and macrophages have been utilized as targeting and drug delivery vehicles due to their ability to penetrate tissues and cross biological barriers, such as the blood brain barrier (BBB) or

tumor core. Furthermore, monocytes are preferentially recruited to sites of inflammation and cancer, increasing the concentration of therapeutic payload. As such, several groups have equipped these immune cells with external or internal payload *ex vivo,* and demonstrated targeting, tissue penetration, and drug delivery *in vivo.*

1.5.2.1 Polymeric backpacks

Drug-loaded polymeric backpacks (BPs) have been attached to the surface of monocytes or macrophages to take advantage of their preferential recruitment and accumulation to diseased areas. Because monocytes and macrophages are highly phagocytic, it is critical that attached backpacks circumvent cellular internalization, which could result in endosomal degradation or failure to deliver drugs to the target tissue. Attached BPs also should not affect monocyte function (i.e. extravasation) or differentiation into macrophages. Anselmo et. al. designed polymeric BPs, attached them to the surface of monocytes, and investigated cellular migration and differentiation in inflammation models.[134] The backpacks were fabricated layer-by-layer, consisting of poly(methacrylic acid), poly(vinylpyrrolidone), poly(allylamine hydrochloride) (PAH), anionic iron oxide magnetic nanoparticles, and poly(acrylic acid) (PAA). The top layer was decorated with biotinylated mouse-IgG, enabling cellular surface attachment via abundant Fc receptors expressed by monocytes. The final BPs were ~7 μm in diameter and less than 500 nm thick. Following BP attachment, monocytes maintained their ability to transmigrate through an endothelial cell monolayer and to differentiate into macrophages, as characterized by adherence and spreading. However, the authors did not further investigate the effect of BPs on monocyte and macrophage immune modulatory gene or protein expression. In both skin and lung inflammation *in vivo* models, monocytes honed to and carried BPs to inflamed tissues: compared to freely injected BPs, 'hitchhiked' BPs showed a 2- to 6-fold increased accumulation in inflamed tissues and a 2-fold reduction in clearance. The authors hypothesized that inflammation increased ICAM and VCAM expression, enhancing monocyte recruitment. Future work includes drug-loading and tuning an extended release profile.

In a similar approach, Klyachko et. al. fabricated BPs to deliver an anti-oxidant payload across the BBB via macrophage carriers to deactivate released free radicals in brain inflammation.[135] Using layer-by-layer assembly, BPs were fabricated with PAA, PAH, and magnetic nanoparticles (as

above), as well as bovine submaxillary mucin and lectin jacalin. BPs were loaded with the anti-oxidant catalase and attached to macrophages via CD11b antibody. The disc-shaped BPs were 7 μm in diameter and ~600 nm thick. In an LPS-induced brain inflammation model, BP-loaded macrophages were detected in the brain, while freely injected BPs were not, indicating that macrophages facilitated BP delivery across the BBB. Although the BP did effect macrophage mobility, as BP-laden macrophages migrated slower than free macrophages, the BPs enabled high drug loading and a controlled release profile (<50% drug release over 18 hours). About 43% of the BP contained catalase, which was sufficient drug loading to neutralize free radicals released by activated microglia, the brain resident mononuclear phagocytes. Additionally, the multi-layer assembly approach protected catalase from protease degradation. Future work is needed to characterize if sufficient BP-laden macrophages cross the BBB to achieve therapeutic efficacy *in vivo.*

1.5.2.2 Macrophage 'Trojan horses'

In another strategy, monocytes and macrophages have been used to deliver internalized payloads, serving as 'Trojan horses' for nanoparticle transport to solid tumors, including those in the brain. Monocytes loaded with gold (Au) NPs penetrated tumors into the necrotic core, where they succumbed to Au NP photo-induced death upon near infrared irradiation.[136] Similarly, macrophages loaded with chemotherapeutic nanoparticles successfully delivered their payloads to tumors.[137,138] However, in both studies, therapeutic efficacy was limited with only modest reduction in tumor growth.

While there has been an increase in published literature using macrophages as Trojan horse drug delivery vehicles, this strategy is limited by several key challenges.[139] First, there is a significant risk that the payload is toxic to the carrier. Secondly, drug release is relatively slow; while this may be desired to allow for cellular extravasation and targeting, it can also reduce therapeutic efficacy. Lastly, intracellular cargos are highly susceptible to lysosomal degradation. While the use of extracellular BPs addresses the latter issue, these systems have yet to demonstrate sufficient drug loading for *in vivo* efficacy. Similarly, limited therapeutic efficacy has been demonstrated using cellular Trojan horses. Overall, the use of macrophages as drug delivery vehicles is limited until internal cargo trafficking and drug release is better controlled.

1.5.3 Macrophage shells

In addition to being used as active delivery vehicles, macrophage cell membranes (MCM) have been used as shells to camouflage nanoparticles. This coating extended blood circulation by denoting these nanoparticles as "self," and improved tumor cell targeting and uptake. This biostealth strategy offers several advantages over PEGylation, which still results in significant clearance and is limited due to increasing prevalence of anti-PEG antibodies. For example, MCM coated gold nanoparticles were used as a photothermal cancer therapy and significantly enhanced therapeutic efficacy. Importantly, the MCM did not interfere with near infrared (NIR) optical properties, enabling photothermal conversion. Compared to bare NPs, MCM-coated NPs were endocytosed by cancer cells 2-fold higher *in vitro*, circulated nearly twice as long, and exhibited nearly 5-fold higher tumor accumulation *in vivo*. Combined with NIR irradiation, MCM-NP treatment efficiently inhibited tumor growth.[140] In a drug delivery strategy, Cao et. al. coated emtansine liposomes with MCM and showed improved cancer cell engulfment via the $\alpha_4\beta_1$-VCAM-1 axis. Coated liposomes improved specific targeting to metastatic foci, inhibiting lung metastasis formation by 87.1%, compared to free drug and uncoated liposomes.[141] Beyond cancer applications, MCM-NPs have also been used in sepsis management, efficiently sequestering endotoxins and inflammatory cytokines, demonstrating the versatility of MCM coating.[142]

1.6 Future Directions

Tumor-associated macrophages play a critical role in cancer progression, facilitating tumor growth, progression, and immunosuppression. High TAM infiltration correlates with poor patient prognosis clinically, highlighting the therapeutic potential of targeting these immune cells. Indeed, strategies to inhibit TAM recruitment or deplete TAM populations have shown some clinical success. Significant progress in elucidating the mechanisms by which TAMs support tumor growth has enabled the development of new therapies to modulate macrophage activity and tumor growth. However, additional work is needed to improve specific targeting of TAMs and to reduce non-specific macrophage interactions. Interactions with healthy macrophages results in high off target effects, which is a major hurdle for TAM therapies. This is in part due to poor understanding of macrophage phenotype; additional investigation of macrophage subsets and activities will hopefully clarify macrophage-tumor interactions and aid in developing more specific targeting

strategies. Furthermore, we expect to see an emergence of combinatorial therapies with dual-modulation of other immune cells, such as T and natural killer cells, to induce robust tumor regression. The importance and complexity of macrophages is further illustrated by their roles in promoting progression of other diseases, such as chronic wounds, diabetes, and ulcerative colitis. Emerging therapies seek to modulate macrophage activity or correct macrophage dysfunction. We are only now beginning to understand the diverse roles that macrophages play throughout the body and in different diseases. As we elucidate the activities of this complex immune cell, we can better understand macrophage activities in disease and develop better therapeutics.

1.7 Acknowledgements

This work was supported by NIH 1R01CA177272 and 1R21CA232430.

References

[1] R. Noy, J. W. Pollard, *Immunity* **2014**, *41*, 49.
[2] A. Mantovani, F. Marchesi, A. Malesci, L. Laghi, P. Allavena, *Nat. Rev. Clin. Oncol.* **2017**, *14*, 399.
[3] A. Mantovani, P. Allavena, A. Sica, F. Balkwill, *Nature* **2008**, *454*, 436.
[4] L. M. Coussens, Z. Werb, *Nature* **2002**, *420*, 860.
[5] T. Kitamura, B. Z. Qian, J. W. Pollard, *Nat. Rev. Immunol.* **2015**, *15*, 73.
[6] P. J. Murray, T. A. Wynn, *Nat. Rev. Immunol.* **2011**, *11*, 723.
[7] C. V. Jakubzick, G. J. Randolph, P. M. Henson, *Nat. Rev. Immunol.* **2017**, *17*, 349.
[8] D. Hashimoto, A. Chow, C. Noizat, P. Teo, M. B. Beasley, M. Leboeuf, C. D. Becker, P. See, J. Price, D. Lucas, M. Greter, A. Mortha, S. W. Boyer, E. C. Forsberg, M. Tanaka, N. van Rooijen, A. García-Sastre, E. R. Stanley, F. Ginhoux, P. S. Frenette, M. Merad, *Immunity* **2013**, *38*, 792.
[9] L. C. Davies, S. J. Jenkins, J. E. Allen, P. R. Taylor, *Nat. Immunol.* **2013**, *14*, 986.
[10] T. A. Wynn, K. M. Vannella, *Immunity* **2016**, *44*, 450.
[11] T. A. Wynn, A. Chawla, J. W. Pollard, *Nature* **2013**, *496*, 445.
[12] L. Yang, Y. Zhang, *J. Hematol. Oncol.* **2017**, *10*, 58.
[13] M. J. Kraakman, A. J. Murphy, K. Jandeleit-Dahm, H. L. Kammoun, *Front. Immunol.* **2014**, *5*, 1.
[14] K. J. Moore, I. Tabas, *Cell* **2011**, *145*, 341.
[15] R. A. Isidro, C. B. Appleyard, *Am. J. Physiol. - Gastrointest. Liver Physiol.* **2016**, *311*, G59.
[16] P. J. Murray, J. E. Allen, S. K. Biswas, E. A. Fisher, D. W. Gilroy, S. Goerdt, S. Gordon, J. A. Hamilton, L. B. Ivashkiv, T. Lawrence, M. Locati, A. Mantovani, F. O. Martinez, J. L. Mege, D. M. Mosser, G. Natoli, J. P. Saeij, J. L. Schultze, K. A. Shirey, A. Sica, J. Suttles, I. Udalova, J. A. Van Ginderachter, S. N. Vogel, T. A. Wynn, *Immunity* **2014**, *41*, 14.
[17] C. Ngambenjawong, H. H. Gustafson, S. H. Pun, *Adv. Drug Deliv. Rev.* **2017**, *114*, 206.
[18] F. O. Martinez, S. Gordon, *F1000Prime Rep.* **2014**, *6*, DOI 10.12703/P6-13.
[19] Q. Guo, Z. Jin, Y. Yuan, R. Liu, T. Xu, H. Wei, X. Xu, S. He, S. Chen, Z. Shi, W. Hou, B. Hua, *J. Immunol. Res.* **2016**, *2016*, DOI 10.1155/2016/9720912.
[20] E. Timosenko, A. V. Hadjinicolaou, V. Cerundolo, *Immunotherapy* **2017**, *9*, 83.
[21] C. B. Williams, E. S. Yeh, A. C. Soloff, *NPJ Breast Cancer* **2016**, *2*, 15025.
[22] F. T. Andón, E. Digifico, A. Maeda, M. Erreni, A. Mantovani, M. J. Alonso, P. Allavena, *Semin. Immunol.* **2017**, *34*, 103.
[23] Y. Singh, V. K. Pawar, J. G. Meher, K. Raval, A. Kumar, R. Shrivastava, S. Bhadauria, M. K. Chourasia, *J. Control. Release* **2017**, *254*, 92.
[24] K. Sawa-Wejksza, M. Kandefer-Szerszeń, *Arch. Immunol. Ther. Exp. (Warsz).* **2018**, *66*, 97.

[25] B.-Z. Qian, J. Li, H. Zhang, T. Kitamura, J. Zhang, L. R. Campion, E. A. Kaiser, L. A. Snyder, J. W. Pollard, *Nature* **2011**, *475*, 222.
[26] K. Mizutani, S. Sud, N. A. McGregor, G. Martinovski, B. T. Rice, M. J. Craig, Z. S. Varsos, H. Roca, K. J. Pienta, *Neoplasia* **2009**, *11*, 1235.
[27] L. Bonapace, M.-M. M. Coissieux, J. Wyckoff, K. D. Mertz, Z. Varga, T. Junt, M. Bentires-Alj, *Nature* **2014**, *515*, 130.
[28] S. M. Zeisberger, B. Odermatt, C. Marty, A. H. M. Zehnder-Fjällman, K. Ballmer-Hofer, R. A. Schwendener, *Br. J. Cancer* **2006**, *95*, 272.
[29] Y. Zhang, J. Q. Li, Z. Z. Jiang, L. Li, Y. Wu, L. Zheng, *J. Pathol.* **2016**, *239*, 231.
[30] K. Ohnishi, Y. Komohara, Y. Saito, Y. Miyamoto, M. Watanabe, H. Baba, M. Takeya, *Cancer Sci.* **2013**, *104*, 1237.
[31] C. H. Ries, M. A. Cannarile, S. Hoves, J. Benz, K. Wartha, V. Runza, F. Rey-Giraud, L. P. Pradel, F. Feuerhake, I. Klaman, T. Jones, U. Jucknischke, S. Scheiblich, K. Kaluza, I. H. Gorr, A. Walz, K. Abiraj, P. A. Cassier, A. Sica, C. Gomez-Roca, K. E. deVisser, A. Italiano, C. LeTourneau, J. P. Delord, H. Levitsky, J. Y. Blay, D. Rüttinger, *Cancer Cell* **2014**, *25*, 846.
[32] D. A. Hume, K. P. A. Macdonald, *Blood* **2012**, *119*, 1810.
[33] N. Colombo, F. Peccatori, C. Paganin, S. Bini, M. Brandely, C. Mangioni, A. Mantovani, P. Allavena, *Int. J. Cancer* **1992**, *51*, 42.
[34] G. L. Beatty, E. G. Chiorean, M. P. Fishman, B. Saboury, R. Teitelbaum, W. Sun, R. D. Huhn, W. Song, D. Li, L. L. Sharp, D. A. Torigian, P. J. O'Dwyer, R. H. Vonderheide, *Sci.* **2011**, *331*, 1612.
[35] M. M. Kaneda, K. S. Messer, N. Ralainirina, H. Li, C. J. Leem, S. Gorjestani, G. Woo, A. V. Nguyen, C. C. Figueiredo, P. Foubert, M. C. Schmid, M. Pink, D. G. Winkler, M. Rausch, V. J. Palombella, J. Kutok, K. McGovern, K. A. Frazer, X. Wu, M. Karin, R. Sasik, E. E. W. Cohen, J. A. Varner, *Nature* **2016**, *542*, 124.
[36] M. Ovais, M. Guo, C. Chen, *Adv. Mater.* **2019**, *31*, 1.
[37] E. Blanco, H. Shen, M. Ferrari, *Nat. Biotechnol.* **2015**, *33*, 941.
[38] K. Binnemars-Postma, G. Storm, J. Prakash, *Int. J. Mol. Sci.* **2017**, *18*, DOI 10.3390/ijms18050979.
[39] Y. N. Zhang, W. Poon, A. J. Tavares, I. D. McGilvray, W. C. W. Chan, *J. Control. Release* **2016**, *240*, 332.
[40] C. Kelly, C. Jefferies, S.-A. Cryan, *J. Drug Deliv.* **2011**, *2011*, DOI 10.1155/2011/727241.
[41] J. Shi, P. W. Kantoff, R. Wooster, O. C. Farokhzad, *Nat. Rev. Cancer* **2017**, *17*, 20.
[42] Y. Tabata, Y. Ikada, *Biomaterials* **1988**, *9*, 356.
[43] S. S. Yu, C. M. Lau, S. N. Thomas, W. Gray Jerome, D. J. Maron, J. H. Dickerson, J. A. Hubbell, T. D. Giorgio, *Int. J. Nanomedicine* **2012**, *7*, 799.
[44] H. H. Gustafson, D. Holt-casper, D. W. Grainger, S. L. City, S. L. City, P. Chemistry, S. L. City, *Nano Today* **2016**, *10*, 487.
[45] J. A. Champion, S. Mitragotri, *Proc. Natl. Acad. Sci.* **2006**, *103*, 4930.
[46] A. Garapaty, J. A. Champion, *Bioeng. Transl. Med.* **2017**, *2*, 92.
[47] M. Ponzoni, F. Pastorino, D. Di Paolo, P. Perri, C. Brignole, *Int. J. Mol. Sci.* **2018**, *19*, DOI 10.3390/ijms19071953.
[48] N. Van Rooijen, A. Sanders, *J. Immunol. Methods* **1994**, *174*, 83.
[49] F. Piaggio, V. Kondylis, F. Pastorino, D. Di Paolo, P. Perri, I. Cossu, F. Schorn, C. Marinaccio, D. Murgia, A. Daga, F. Raggi, M. Loi, L. Emionite, E. Ognio, M. Pasparakis, D. Ribatti, M. Ponzoni, C. Brignole, *J. Control. Release* **2016**, *223*, 165.
[50] A. Y. Lin, J. P. Mattos Almeida, A. Bear, N. Liu, L. Luo, A. E. Foster, R. A. Drezek, *PLoS One* **2013**, *8*, DOI 10.1371/journal.pone.0063550.
[51] N. Oh, Y. Kim, H. S. Kweon, W. Y. Oh, J. H. Park, *ACS Appl. Mater. Interfaces* **2018**, *10*, 28450.
[52] S. A. MacParland, K. M. Tsoi, B. Ouyang, X. Z. Ma, J. Manuel, A. Fawaz, M. A. Ostrowski, B. A. Alman, A. Zilman, W. C. W. Chan, I. D. McGilvray, *ACS Nano* **2017**, *11*, 2428.
[53] K. A. Binnemars-Postma, H. W. Ten Hoopen, G. Storm, J. Prakash, *Nanomedicine* **2016**, *11*, 2889.
[54] F. Zhang, P. Mastorakos, M. K. Mishra, A. Mangraviti, L. Hwang, J. Zhou, J. Hanes, H. Brem, A. Olivi, B. Tyler, R. M. Kannan, *Biomaterials* **2015**, *52*, 507.
[55] Z. Huang, Y. Yang, Y. Jiang, J. Shao, X. Sun, J. Chen, L. Dong, J. Zhang, *Biomaterials* **2013**, *34*, 746.
[56] Y. Wang, Y. X. Lin, S. L. Qiao, H. W. An, Y. Ma, Z. Y. Qiao, R. P. Y. J. Rajapaksha, H. Wang, *Biomaterials* **2017**, *112*, 153.
[57] S. Shen, H. J. Li, K. G. Chen, Y. C. Wang, X. Z. Yang, Z. X. Lian, J. Z. Du, J. Wang, *Nano Lett.* **2017**, *17*, 3822.
[58] Y. Wang, G. Guo, Y. Feng, H. Long, D. L. Ma, C. H. Leung, L. Dong, C. Wang, *J. Mater. Chem. B* **2017**, *5*,

7307.
[59] M. A. Miller, Y. R. Zheng, S. Gadde, C. Pfirschke, H. Zope, C. Engblom, R. H. Kohler, Y. Iwamoto, K. S. Yang, B. Askevold, N. Kolishetti, M. Pittet, S. J. Lippard, O. C. Farokhzad, R. Weissleder, *Nat. Commun.* **2015**, *6*, 1.
[60] F. Danhier, O. Feron, V. Préat, *J. Control. Release* **2010**, *148*, 135.
[61] S. D. Steichen, M. Caldorera-Moore, N. Peppas, *Eur. J. Pharm. Sci.* **2013**, *48*, 416.
[62] I. Brigger, C. Dubernet, P. Couvreur, *Adv. Drug Deliv. Rev.* **2012**, *64*, 24.
[63] R. R. Wakaska, *Int J Drug Dev Res* **2017**, *9*, 37.
[64] "New clinical trials of monoclonal antibodies have grown 115% in the last ten years," can be found under https://www.globaldata.com/new-clinical-trials-monoclonal-antibodies-grown-115-last-ten-years/, **2017**.
[65] J. H. Stafford, T. Hirai, L. Deng, S. B. Chernikova, K. Urata, B. L. West, J. M. Brown, *Neuro. Oncol.* **2016**, *18*, 797.
[66] S. M. Pyonteck, L. Akkari, A. J. Schuhmacher, R. L. Bowman, L. Sevenich, D. F. Quail, O. C. Olson, M. L. Quick, J. T. Huse, V. Teijeiro, M. Setty, C. S. Leslie, Y. Oei, A. Pedraza, J. Zhang, C. W. Brennan, J. C. Sutton, E. C. Holland, D. Daniel, J. A. Joyce, *Nat. Med.* **2013**, *19*, 1264.
[67] M. A. Cannarile, M. Weisser, W. Jacob, A. Jegg, C. H. Ries, D. Rüttinger, *J. Immunother. Cancer* **2017**, *5*, 1.
[68] A. M. Georgoudaki, K. E. Prokopec, V. F. Boura, E. Hellqvist, S. Sohn, J. Östling, R. Dahan, R. A. Harris, M. Rantalainen, D. Klevebring, M. Sund, S. E. Brage, J. Fuxe, C. Rolny, F. Li, J. V. Ravetch, M. C. I. Karlsson, *Cell Rep.* **2016**, *15*, 2000.
[69] H. L. Matlung, K. Szilagyi, N. A. Barclay, T. K. van den Berg, *Immunol. Rev.* **2017**, *276*, 145.
[70] M. P. Chao, A. A. Alizadeh, C. Tang, J. H. Myklebust, B. Varghese, S. Gill, M. Jan, A. C. Cha, C. K. Chan, B. T. Tan, C. Y. Park, F. Zhao, H. E. Kohrt, R. Malumbres, J. Briones, R. D. Gascoyne, I. S. Lossos, R. Levy, I. L. Weissman, R. Majeti, *Cell* **2010**, *142*, 699.
[71] K. Weiskopf, A. M. Ring, C. C. M. Ho, J. P. Volkmer, A. M. Levin, A. K. Volkmer, E. Özkan, N. B. Fernhoff, M. Van De Rijn, I. L. Weissman, K. C. Garcia, *Science (80-.).* **2013**, *341*, 88.
[72] NIH: National Cancer Institute, "Clinical Trials Using Anti-CD47 Monoclonal Antibody Hu5F9-G4," can be found under https://www.cancer.gov/about-cancer/treatment/clinical-trials/intervention/anti-cd47-monoclonal-antibody-hu5f9-g4, **n.d.**
[73] M. Liu, R. S. O'Connor, S. Trefely, K. Graham, N. W. Snyder, G. L. Beatty, *Nat. Immunol. 2019* **2019**, 1.
[74] A. Kulkarni, V. Chandrasekar, S. K. Natarajan, A. Ramesh, P. Pandey, J. Nirgud, H. Bhatnagar, D. Ashok, A. K. Ajay, S. Sengupta, *Nat. Biomed. Eng.* **2018**, *2*, 589.
[75] W. C. Chen, N. Kawasaki, C. M. Nycholat, S. Han, J. Pilotte, P. R. Crocker, J. C. Paulson, *PLoS One* **2012**, *7*, 1.
[76] A. Al Faraj, A. S. Shaik, S. Afzal, B. Al Sayed, R. Halwani, *Int. J. Nanomedicine* **2014**, *9*, 1491.
[77] M. J. Lipinski, J. C. Frias, V. Amirbekian, K. C. Briley-Saebo, V. Mani, D. Samber, A. Abbate, J. G. S. Aguinaldo, D. Massey, V. Fuster, G. W. Vetrovec, Z. A. Fayad, *JACC Cardiovasc. Imaging* **2009**, *2*, 637.
[78] R. O. Dillman, *Curr. Pharm. Biotechnol.* **2001**, *2*, 293.
[79] D. M. Ecker, S. D. Jones, H. L. Levine, *MAbs* **2015**, *7*, 9.
[80] P. Chames, M. Van Regenmortel, E. Weiss, D. Baty, *Br. J. Pharmacol.* **2009**, *157*, 220.
[81] L. Nuhn, E. Bolli, S. Massa, I. Vandenberghe, K. Movahedi, B. Devreese, J. A. Van Ginderachter, B. G. De Geest, *Bioconjug. Chem.* **2018**, *29*, 2394.
[82] T. De Meyer, S. Muyldermans, A. Depicker, *Trends Biotechnol.* **2014**, *32*, 263.
[83] M. Cieslewicz, J. Tang, J. L. Yu, H. Cao, M. Zavaljevski, K. Motoyama, A. Lieber, E. W. Raines, S. H. Pun, *Proc. Natl. Acad. Sci.* **2013**, *110*, 15919.
[84] C. Ngambenjawong, H. H. Gustafson, J. M. Pineda, N. A. Kacherovsky, M. Cieslewicz, S. H. Pun, *Theranostics* **2016**, *6*, 1403.
[85] C. Ngambenjawong, H. H. Gustafson, M. Sylvestre, S. H. Pun, *ChemBioChem* **2017**, *18*, 2395.
[86] C. Ngambenjawong, M. Sylvestre, H. H. Gustafson, J. M. B. Pineda, S. H. Pun, *ACS Chem. Biol.* **2018**, *13*, 995.
[87] C. Ngambenjawong, S. H. Pun, *ACS Biomater. Sci. Eng.* **2017**, *3*, 2050.
[88] J. Conde, C. Bao, Y. Tan, D. Cui, E. R. Edelman, H. S. Azevedo, H. J. Byrne, N. Artzi, F. Tian, *Adv. Funct. Mater.* **2015**, *25*, 4183.
[89] Y. Qian, S. Qiao, Y. Dai, G. Xu, B. Dai, L. Lu, X. Yu, Q. Luo, Z. Zhang, *ACS Nano* **2017**, *11*, 9536.
[90] P. Scodeller, L. Simón-Gracia, S. Kopanchuk, A. Tobi, K. Kilk, P. Säälik, K. Kurm, M. L. Squadrito, V. R. Kotamraju, A. Rinken, M. De Palma, E. Ruoslahti, T. Teesalu, *Sci. Rep.* **2017**, *7*, 1.

[91] T. Tang, Y. Wei, J. Kang, Z.-G. She, D. Kim, M. J. Sailor, E. Ruoslahti, H.-B. Pang, *J. Control. Release* **2019**, DOI 10.1016/j.jconrel.2019.03.009.
[92] L. Otvos, J. D. Wade, *Front. Chem.* **2014**, *2*, 8.
[93] S. Zhu, M. Niu, H. O'Mary, Z. Cui, *Mol. Pharm.* **2013**, *10*, 3525.
[94] X. Zhan, L. Jia, Y. Niu, H. Qi, X. Chen, Q. Zhang, J. Zhang, Y. Wang, L. Dong, C. Wang, *Biomaterials* **2014**, *35*, 10046.
[95] M. Song, T. Liu, C. Shi, X. Zhang, X. Chen, *ACS Nano* **2016**, *10*, 633.
[96] C. B. Rodell, S. P. Arlauckas, M. F. Cuccarese, C. S. Garris, R. Li, M. S. Ahmed, R. H. Kohler, M. J. Pittet, R. Weissleder, *Nat. Biomed. Eng.* **2018**, *2*, 1.
[97] D. Muraoka, N. Seo, T. Hayashi, Y. Tahara, K. Fujii, I. Tawara, Y. Miyahara, K. Okamori, H. Yagita, S. Imoto, R. Yamaguchi, M. Komura, S. Miyano, M. Goto, S. Sawada, A. Asai, H. Ikeda, K. Akiyoshi, N. Harada, H. Shiku, *J. Clin. Invest.* **2019**, DOI 10.1172/JCI97642.
[98] J. M. Irache, H. H. Salman, C. Gamazo, S. Espuelas, *Expert Opin. Drug Deliv.* **2008**, *5*, 703.
[99] L. J. Cruz, P. J. Tacken, J. M. Pots, R. Torensma, S. I. Buschow, C. G. Figdor, *Biomaterials* **2012**, *33*, 4229.
[100] J. Zhou, J. Rossi, *Nat. Rev. Drug Discov.* **2017**, *16*, 181.
[101] A. D. Keefe, S. Pai, A. Ellington, *Nat. Rev. Drug Discov.* **2010**, *9*, 537.
[102] F. Roth, A. C. De La Fuente, J. L. Vella, A. Zoso, L. Inverardi, P. Serafini, *Cancer Res.* **2012**, *72*, 1373.
[103] S. Ni, H. Yao, L. Wang, J. Lu, F. Jiang, A. Lu, G. Zhang, *Int. J. Mol. Sci.* **2017**, *18*, DOI 10.3390/ijms18081683.
[104] K. Fujimori, D. G. Covell, J. N. Weinstein, J. E. Fletcher, *Cancer Res.* **1989**, *49*, 5656.
[105] Y. H. Bae, K. Park, *J. Control. Release* **2011**, *153*, 198.
[106] Q. Dai, S. Wilhelm, D. Ding, A. M. Syed, S. Sindhwani, Y. Zhang, Y. Y. Chen, P. MacMillan, W. C. W. W. Chan, *ACS Nano* **2018**, *12*, 8423.
[107] P. P. Wibroe, A. C. Anselmo, P. H. Nilsson, A. Sarode, V. Gupta, R. Urbanics, J. Szebeni, A. C. Hunter, S. Mitragotri, T. E. Mollnes, S. M. Moghimi, *Nat. Nanotechnol.* **2017**, *12*, 589.
[108] M. Schäfer, S. Werner, *Nat. Rev. Mol. Cell Biol.* **2008**, *9*, 628.
[109] P. Krzyszczyk, R. Schloss, A. Palmer, F. Berthiaume, *Front. Physiol.* **2018**, *9*, 1.
[110] J. Rayahin, R. Gemeinhart, *Results Probl. Cell Differ.* **2017**, *62*, 317.
[111] Z. Sheikh, P. J. Brooks, O. Barzilay, N. Fine, M. Glogauer, *Materials (Basel).* **2015**, *8*, 5671.
[112] A. K. Blakney, M. D. Swartzlander, S. J. Bryant, *J. Biomed. Mater. Res. - Part A* **2012**, *100A*, 1375.
[113] R. Sridharan, A. R. Cameron, D. J. Kelly, C. J. Kearney, F. J. O'Brien, *Mater. Today* **2015**, *18*, 313.
[114] L. Madden, D. Mortisen, E. Sussman, S. Dupras, J. Fugate, J. Cuy, K. Hauch, M. Laflamme, C. Murry, B. Ratner, *Proc. Natl. Acad. Sci.* **2010**, *107*, 15211.
[115] E. M. Sussman, M. C. Halpin, J. Muster, R. T. Moon, B. D. Ratner, *Ann. Biomed. Eng.* **2014**, *42*, 1508.
[116] T. Sugiura, S. Tara, H. Nakayama, H. Kurobe, T. Yi, Y. U. Lee, A. Y. Lee, C. K. Breuer, T. Shinoka, *Ann. Thorac. Surg.* **2016**, *102*, 720.
[117] E. Saino, M. L. Focarete, C. Gualandi, E. Emanuele, A. I. Cornaglia, M. Imbriani, L. Visai, *Biomacromolecules* **2011**, *12*, 1900.
[118] D. Abebayehu, A. Spence, B. D. Boyan, Z. Schwartz, J. J. Ryan, M. J. Mcclure, *J. Biomed. Mater. Res.* **2017**, *105A*, 2562.
[119] F. Taraballi, B. Corradetti, S. Minardi, S. Powel, F. Cabrera, J. L. Van Eps, B. K. Weiner, E. Tasciotti, *J. Tissue Eng.* **2016**, *7*, DOI 10.1177/2041731415624667.
[120] T. Thambi, Y. Li, D. S. Lee, *J. Control. Release* **2017**, *267*, 57.
[121] Y. Feng, Q. Li, D. Wu, Y. Niu, C. Yang, L. Dong, C. Wang, *Biomaterials* **2017**, *134*, 128.
[122] L. T. A. Hong, Y. M. Kim, H. H. Park, D. H. Hwang, Y. Cui, E. M. Lee, S. Yahn, J. K. Lee, S. C. Song, B. G. Kim, *Nat. Commun.* **2017**, *8*, 1.
[123] N. R. Patel, M. Bole, C. Chen, C. C. Hardin, A. T. Kho, J. Mih, L. Deng, J. Butler, D. Tschumperlin, J. J. Fredberg, R. Krishnan, H. Koziel, *PLoS One* **2012**, *7*, 1.
[124] C. M. Alvey, K. R. Spinler, J. Irianto, L. Smith, M. Tewari, D. E. Discher, C. M. Alvey, K. R. Spinler, J. Irianto, C. R. Pfeifer, B. Hayes, Y. Xia, S. Cho, P. C. P. D. Dingal, J. Hsu, L. Smith, M. Tewari, D. E. Discher, *Curr. Biol.* **2017**, *27*, 2065.
[125] A. D. Guerra, O. W. H. Yeung, X. Qi, W. J. Kao, K. Man, *Theranostics* **2017**, *7*, DOI 10.7150/thno.20251.
[126] S. S. Rao, G. G. Bushnell, S. M. Azarin, G. Spicer, B. A. Aguado, J. R. Stoehr, E. J. Jiang, V. Backman, L. D. Shea, J. S. Jeruss, *Cancer Res.* **2016**, 14.
[127] B. A. Aguado, R. M. Hartfield, G. G. Bushnell, J. T. Decker, S. M. Azarin, D. Nanavati, M. J. Schipma, S. S. Rao, R. S. Oakes, Y. Zhang, J. S. Jeruss, L. D. Shea, *Adv. Healthc. Mater.* **2018**, *7*, 1.

[128] R. A. Carpenter, J. Kwak, S. R. Peyton, J. Lee, *Nat. Biomed. Eng.* **2018**, *2*, 915.
[129] I. J. Fidler, *Cancer Res.* **1974**, *34*, 1074.
[130] R. Andreesen, B. Hennemann, S. W. Krause, *J. Leukoc. Biol.* **1998**, *64*, 419.
[131] K. W. Moyes, N. A. P. Lieberman, S. A. Kreuser, H. Chinn, C. Winter, G. Deutsch, V. Hoglund, R. Watson, C. A. Crane, *Hum. Gene Ther.* **2017**, *28*, 200.
[132] S. Gill, M. Klichinsky, *Modified Monocytes/Macrophage Expressing Chimeric Antigen Receptors and Uses Thereof*, **2017**, US20 16/044440.
[133] M. A. Morrissey, A. P. Williamson, A. M. Steinbach, E. W. Roberts, N. Kern, M. B. Headley, R. D. Vale, *Elife* **2018**, *7*, 1.
[134] A. C. Anselmo, J. B. Gilbert, S. Kumar, V. Gupta, R. E. Cohen, M. F. Rubner, S. Mitragotri, *J. Control. Release* **2015**, *199*, 29.
[135] N. L. Klyachko, R. Polak, M. J. Haney, Y. Zhao, R. J. Gomes Neto, M. C. Hill, A. V. Kabanov, R. E. Cohen, M. F. Rubner, E. V. Batrakova, *Biomaterials* **2017**, *140*, 79.
[136] M. R. Choi, K. J. Stanton-Maxey, J. K. Stanley, C. S. Levin, R. Bardhan, D. Akin, S. Badve, J. Sturgis, J. P. Robinson, R. Bashir, N. J. Halas, S. E. Clare, *Nano Lett.* **2007**, *7*, 3759.
[137] J. Choi, H. Y. Kim, E. J. Ju, J. Jung, J. Park, H. K. Chung, J. S. Lee, J. S. Lee, H. J. Park, S. Y. Song, S. Y. Jeong, E. K. Choi, *Biomaterials* **2012**, *33*, 4195.
[138] S. Li, S. Feng, L. Ding, Y. Liu, Q. Zhu, Z. Qian, Y. Gu, *Int. J. Nanomedicine* **2016**, *11*, 4107.
[139] J. G. Visser, A. Du, P. Van Staden, C. Smith, *Front. Pharmacol.* **2019**, *10*, DOI 10.3389/fphar.2019.00022.
[140] M. Xuan, J. Shao, L. Dai, J. Li, Q. He, *ACS Appl. Mater. Interfaces* **2016**, *8*, 9610.
[141] H. Cao, Z. Dan, X. He, Z. Zhang, H. Yu, Q. Yin, Y. Li, *ACS Nano* **2016**, *10*, 7738.
[142] S. Thamphiwatana, P. Angsantikul, T. Escajadillo, Q. Zhang, J. Olson, B. T. Luk, S. Zhang, R. H. Fang, W. Gao, V. Nizet, L. Zhang, *Proc. Natl. Acad. Sci.* **2017**, *114*, 11488.
[143] M. Singh, H. Khong, Z. Dai, X. Huang, J. A. Wargo, Z. A. Cooper, J. P. Vasilakos, P. Hwu, W. W. Overwijk, *J. Immunol.* **2014**, *193*, 4722.
[144] K. P. Papadopoulos, L. Gluck, L. P. Martin, A. J. Olszanski, A. W. Tolcher, G. Ngarmchamnanrith, E. Rasmussen, B. M. Amore, D. Nagorsen, J. S. Hill, J. Stephenson, *Clin. Cancer* **2017**, *23*, 5703.
[145] M. J. Reilley, P. Mccoon, C. Cook, P. Lyne, R. Kurzrock, Y. Kim, R. Woessner, A. Younes, J. Nemunaitis, N. Fowler, M. Curran, Q. Liu, T. Zhou, J. Schmidt, M. Jo, S. J. Lee, M. Yamashita, S. G. Hughes, L. Fayad, S. Piha-paul, M. V. P. Nadella, X. Xiao, J. Hsu, A. Revenko, B. P. Monia, A. R. Macleod, D. S. Hong, *J. Immunother. Cancer* **2018**, *6*, 1.
[146] I. Brana, A. Calles, P. M. Lorusso, L. K. Yee, T. A. Puchalski, S. Seetharam, B. Zhong, C. Boer, J. Tabernero, E. Calvo, *Target. Oncol.* **2014**, DOI 10.1007/s11523-014-0320-2.
[147] J. G. Conway, B. Mcdonald, J. Parham, B. Keith, D. W. Rusnak, E. Shaw, M. Jansen, P. Lin, A. Payne, R. M. Crosby, J. H. Johnson, L. Frick, M. J. Lin, S. Depee, S. Tadepalli, B. Votta, I. James, K. Fuller, T. J. Chambers, F. C. Kull, S. D. Chamberlain, J. T. Hutchins, *Proc. Natl. Acad. Sci.* **2005**, *102*, 16078.
[148] A. Kakizaki, T. Fujimura, S. Furudate, Y. Kambayashi, T. Yamauchi, H. Yagita, S. Aiba, *Oncoimmunology* **2015**, *4*, 1.
[149] S. Furudate, T. Fujimura, Y. Kambayashi, A. Y. A. Kakizaki, T. Hidaka, S. Aiba, *Anticancer Res.* **2017**, *37*, 3461.
[150] R. B. Holmgaard, D. Zamarin, A. Lesokhin, T. Merghoub, J. D. Wolchok, *EBioMedicine* **2016**, *6*, 50.
[151] L. P. Pradel, C. Ooi, S. Romagnoli, M. A. Cannarile, C. H. Ries, H. Sade, R. Dominik, *Mol. Cancer Ther.* **2016**, *15*, 3077.
[152] P. F. Lindholm, N. Sivapurapu, B. Jovanovic, B. Core, *J. Clin. Cell Immunol.* **2015**, *6*, DOI 10.4172/2155-9899.1000308.Monocyte-Induced.
[153] R. Han, S. Gu, Y. Zhang, A. Luo, X. Jing, L. Zhao, X. Zhao, *Sci. Rep.* **2018**, 1.
[154] P. Forghani, M. R. Khorramizadeh, E. K. Waller, *Cancer Med.* **2014**, *3*, 215.
[155] A. Tyagi, R. P. Singh, K. Ramasamy, K. Raina, E. F. Redente, L. D. Dwyer-nield, R. A. Radcliffe, A. M. Malkinson, R. Agarwal, *Cancer Prev. Res.* **2009**, *2*, 74.
[156] G. Germano, R. Frapolli, C. Belgiovine, A. Anselmo, S. Pesce, M. Liguori, E. Erba, S. Uboldi, M. Zucchetti, F. Pasqualini, M. Nebuloni, N. Van Rooijen, R. Mortarini, L. Beltrame, S. Marchini, I. F. Nerini, R. Sanfilippo, P. G. Casali, S. Pilotti, C. M. Galmarini, A. Anichini, A. Mantovani, M. D. Incalci, P. Allavena, *Cancer Cell* **2013**, *23*, 249.
[157] M. D. Incalci, N. Badri, C. M. Galmarini, P. Allavena, *Br. J. Cancer* **2014**, *111*, 646.
[158] S. F. Hussain, L. Kong, J. Jordan, C. Conrad, T. Madden, I. Fokt, W. Priebe, A. B. Heimberger, *Cancer Res.* **2007**, *67*, 9630.

Chapter 2

Identification of a DNA aptamer that binds to human monocytes and macrophages[2]

Meilyn Sylvestre, Chris Saxby, Nataly Kacherovsky, Heather Gustafson, Stephen J. Salipante, and Suzie Pun

2.1 Abstract

As cancer strategies shift toward immunotherapy, the need for new binding ligands to target and isolate specific immune cell populations has soared. Based on prior work identifying a peptide specific for murine M2-like macrophages, we sought to identify an aptamer that could bind human M2-like macrophages. Tumor-associated macrophages (TAMs) adopt an M2-like phenotype and support tumor progression and dissemination. Here, we employed cell-SELEX to identify an aptamer ligand that targets this cell population over tissue resident (M0-like) or tumoricidal (M1-like) macrophages. Instead, we identified an aptamer that binds both human M0- and M2-like macrophages and monocytes, with highest binding affinity to M2-like macrophage (K_d ~ 20 nM) and monocytes (K_d ~ 45 nM) and minimal binding to M1-like macrophages or other leukocytes. The aptamer binds to $CD14^+$ but not $CD16^+$ monocytes, and is rapidly internalized by these cells. We also demonstrate that this aptamer is able to bind human monocytes when both are administered *in vivo* to mice. Thus, binding to these cell populations (monocytes, M0-like and M2-like macrophages), this aptamer lends itself toward monocyte-specific applications, such as monocyte-targeted drug delivery or column selection.

2.2 Introduction

Manipulation of immune cell populations, either *ex vivo* or *in situ*, has emerged as a powerful technique in cancer therapy. With the ascent of immunotherapies, technologies that facilitate targeting of immune cells that populate the tumor environment has risen in importance. Immunotherapies related to lymphoid cells, such as chimeric antigen receptor (CAR) T-cells

[2] *Reprinted with permission from Sylvestre, M., Saxby, C., et al. Identification of a DNA aptamer that binds to human monocytes and macrophages. Bioconj. Chem.* ***31****, 1899-1907 (2020). Copyright 2020 American Chemical Society.*

(Yescarta and Kymriah) and checkpoint inhibitors (e.g. antibodies against PD-1 or CTLA-4) have shown striking clinical success.[1-4] There is now significant interest in developing immunotherapies related to myeloid cells. Myeloid progenitor cells are derived from the bone marrow and can commit to the monocyte lineage, cells that circulate in the blood and extravasate into tissues where they terminally differentiate into macrophages.[5] Parallel to lymphoid immunotherapies, macrophages have been equipped with cancer-fighting CARs (Charisma) or blocked with immune-checkpoint inhibitors (e.g. antibodies against CD47 or SIRPα).[6-8] Other therapies focus on targeting macrophages within the tumor, but there remains a need to expand the repertoire of targeting ligands for myeloid-derived cells with potential applications in engineered cell manufacturing and targeted drug delivery to these cells.

We started this work with the goal to identify novel tumor-associated macrophage (TAM) ligands. TAMs are associated with poor patient prognosis and have been demonstrated to facilitate disease progression by promoting tumor proliferation, metastasis, and immunosuppression.[8-10] Accounting for up to 50-70% of a solid tumor mass in many cancers (e.g. breast cancer, melanoma, and glioblastoma), TAMs have been linked with worse clinical outcome and resistance to conventional therapies, and there are several TAM-targeted strategies under development for cancer treatment.[8,11-14] However, an important consideration is to limit effects to tissue resident macrophages, which are critical for immune defense and anti-tumor activities.[15] In a simplified binary polarization paradigm, inflammatory macrophages exhibit an M1-like phenotype and have cytotoxic functions, whereas TAMs more closely resemble an M2-like phenotype, which is associated with tissue healing and remodeling.[16] In the context of cancer, this M2-like phenotype supports tumor angiogenesis, growth, and dissemination.[9]

In previous work, we demonstrated that targeted depletion of this M2-like population can prolong survival in tumor bearing mice.[17] Using a subtractive phage panning strategy against murine bone marrow derived macrophages (BMDMs) polarized to M1- and M2-like phenotypes, we identified a peptide sequence, M2pep, that preferentially binds murine M2-like macrophages with low affinity for other leukocytes. Utilizing M2pep for targeted delivery of a pro-apoptotic peptide to M2-like TAMs reduced tumor growth rate and prolonged survival. However, M2pep does not bind human macrophages, limiting clinical applicability. Extensive efforts to identify a human

equivalent of M2pep were unsuccessful, prompting our search for an aptamer ligand against human M2-like TAMs. Aptamers are single-stranded DNA or RNA oligonucleotides that form unique secondary structures capable of specific molecular recognition of cognate targets.[18] These synthetic ligands offer high binding affinity (K_d in pM-nM range), long shelf-life, and fast production.

Here, we sought to identify a DNA aptamer ligand that specifically binds human M2-like macrophages because of their resemblance to TAMs, and demonstrates minimal binding to tissue resident M0-like macrophages or circulating monocytes. Despite receptor overlap between phenotypes, we hypothesized that aptamers would be able to provide enough specificity due to their ability to differentiate proteins with single amino acid mutations.[19] We employed cell-based systematic enrichment of ligands using exponential enrichment (SELEX), an emerging method to identify aptamer ligands against whole-cell targets.[20] We characterized binding by flow cytometry, droplet digital (dd) PCR, and fluorescent microscopy. Ultimately, we identified a novel aptamer that exhibits high binding to monocytes, M0- and M2-like macrophages, yet shows minimal binding to M1-like macrophages. Despite binding to these varied populations, this aptamer could be used for *in situ* binding to monocytes in disease models with monocyte dysregulation (e.g. cancer and infectious disease) or for *in vitro* applications, such as column selection of monocytes from white blood cells for production of engineered monocyte or macrophage cell therapies.[21,22]

2.3. Results

2.3.1 Identification of aptamer A2 by cell-SELEX

To identify an aptamer that binds human M2-like macrophages, we employed cell-SELEX as previously described, using a 52 base-pair (bp) random region DNA aptamer library (10^{16} unique sequences) and human macrophages derived from monocytes, isolated from human leukoreduction system (LRS) chambers.[20] Macrophages were polarized toward M0-, M1-, and M2-like phenotypes by M-CSF, LPS + IFN-γ, and IL-4 respectively; polarization was confirmed by upregulated CD64 and HLA/DR expression (M1-like macrophages) and CD36 and CD180 expression (M2-like macrophages) by flow cytometry (**Figure S2.1**). SELEX was performed against M2-like macrophages for positive selection, and monocytes and M0-like macrophages for negative selection (**Figure 2.1A-B**). These cells were selected by a desire to target TAMs, which

resemble an M2-like phenotype, and to avoid binding to (*i*) tissue resident macrophages, resembling an M0-like phenotype, and (*ii*) circulating monocytes, which would be critical to bypass for intravenous delivery. Although macrophage polarization exists along a spectrum of phenotypes, we used cultured macrophages to produce more homogenous populations for selection. After 9 rounds of iterative selection with increasing stringency, next generation sequence (NGS) was used to catalog resultant aptamer sequences. These were subsequently analyzed using FASTAptamer, phylogenetic trees, and motif analysis (**Figure S2.2**).[23,24] Top aptamers were identified based on (*i*) abundance (reads per million), (*ii*) motif (conserved patterns between sequences), (*iii*) enrichment between starting library, final aptamer pools, and consecutive rounds, and (*iv*) family representation in phylogenetic trees. Binding of resulting pools and selected top aptamers was validated by droplet digital (dd) PCR (**Figure S2.3**). Droplet digital PCR was used to assess efficiency of retained aptamers from each round of selection because it has higher sensitivity than other methods, such as flow cytometry or quantitative PCR.[25] Selected aptamers from the top 10 ranking sequences (ranked per abundance in the final pool) were ordered based on rank, family representation, and motif, and tested for binding against M0-, M1-, and M2-like macrophages. Aptamer A2, named based on rank in the final aptamer pool, demonstrated the highest binding to M2-like macrophages (**Figure S2.4**). To our surprise, A2 also demonstrated high binding to M0-like macrophages as well. Despite binding to this negative cell selection population, we further characterized its binding to macrophages and peripheral blood mononuclear cells (PBMCs).

A

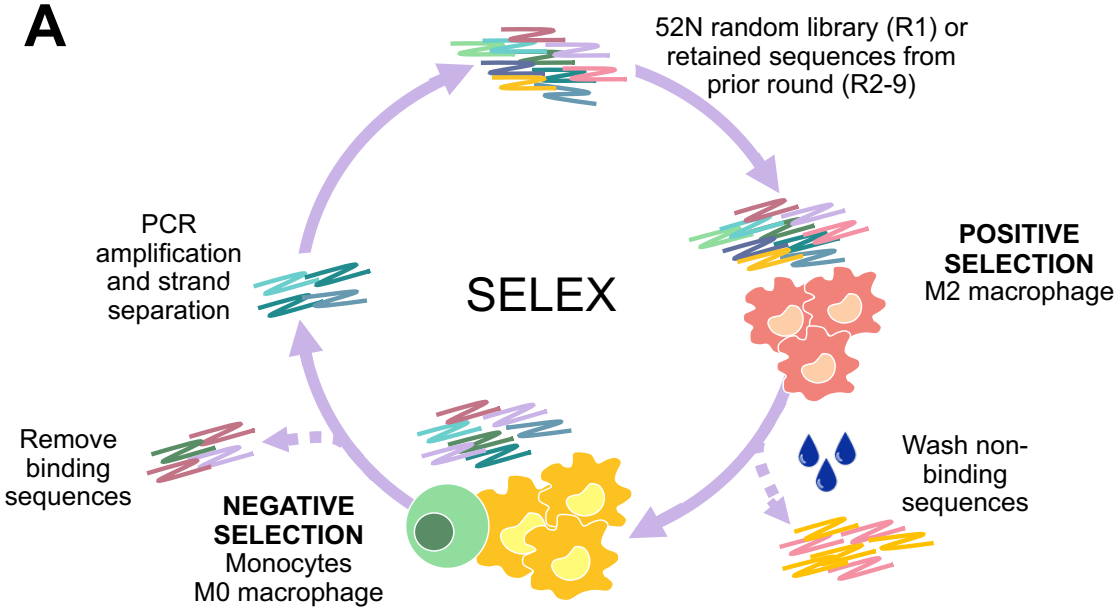

B

Cell-SELEX schematic							
	Positive Selection (M2 Macrophages)					**Negative Selection**	
Round	**# cells**	**Aptamer Conc.**	**Duration**	**BSA/ DHS**	**# washes**	**Cell type**	**# cells**
1	~6M	500 nM	1 hr	0.1% BSA	3	Plastic	
2	~3M	500 nM	1 hr	0.1% BSA	3	Monocytes	10M
3	~3M	500 nM	45 min	0.5% BSA	4	Monocytes	10M
4	~3M	350 nM	45 min	1% BSA	4	M0	~3M
5	~3M	268 nM	30 min	2.5% BSA	4	M0	~6M
6	~3M	333 nM	30 min	2.5% BSA	4	M0	~6M
7	~2M	250 nM	30 min	5% BSA	4	M0	~8M
8	~1.6M	250 nM	30 min	5% DHS	4	M0	~7M
9	~1.6M	200 nM	30 min	10% DHS	4	M0	~7M

Figure 2.1: Cell-SELEX schematic that led to the identification of aptamer A2. A) Cell-SELEX was employed using a 52N-random region DNA aptamer library. Aptamer pools were incubated with positive selection cells and non-binding sequences were removed; aptamer sequences that bound positive selection cells (M2-like macrophages) were recovered and incubated with negative selection cells (M0-like macrophages and monocytes). These sequences that did not bind negative selection cells were recovered, amplified, and used in the next round of selection. B) Stringency was increased in each subsequent round by (i) decreasing the number of positive selection cells, (ii) increasing the number of negative selection cells, (iii) decreasing incubation time with positive selection cells, (iv) increasing serum content, and/or (v) increasing the number of washes following incubation with aptamer pools.

2.3.2 Characterization of aptamer A2 binding to macrophages.

Our initial screening revealed that aptamer A2 bound both M0- and M2-like macrophages, likely due to overlapping receptor expression and closely related phenotypes of those cells. Based on this binding behavior, we hypothesized that A2 would bind less to M1-like macrophages, which are more phenotypically disparate with different receptor expression compared to M0- and M2-like macrophages.[26] Binding studies via flow cytometry confirmed that A2 preferentially binds M0- and M2-like macrophages, with apparent dissociation constants (K_d) of 44.12 ± 8.0 and 22.81 ± 5.6 nM to M0- and M2-like macrophages, respectively (**Figure 2.2A, C**). The maximum binding intensity of A2 to M0- and M2-like macrophages was higher than for M1 macrophages, which suggests higher density of A2-binding receptor expression on M0- and M2-like macrophages versus M1-like macrophages. Binding was compared to a scrambled sequence aptamer control (SCRM), which exhibited no specific binding behavior to M0-, M1-, or M2-like macrophages (**Figure 2.2B, C**). To confirm that binding is specific and not donor-dependent, we assessed binding across unique donors (**Figure 2.2D**). Across donors, aptamer binding to M0-like macrophages was significantly higher than binding to M1-like macrophages (*$p = 0.03$). There was no significant difference in binding of aptamer A2 over SCRM to M1-like macrophages. In contrast, aptamer A2 binding was significantly higher than SCRM binding to M0- (***$p = 0.0002$) and M2-like (**$p = 0.006$) macrophages. Based on aptamer A2's binding behavior against cultured macrophages, we next tested aptamer binding to human triple-negative breast cancer (TNBC) tumor sections, which were selected as a target because of their high macrophage infiltration (**Figure 2.2E**). Tumors were sectioned and stained for human CD206, an M2-like macrophage marker (green), DAPI for nuclei (blue), and aptamer (red). Areas with abundant macrophages were imaged, and aptamer A2 showed higher signal in those cells in comparison with SCRM. Furthermore, A2 samples had a staining pattern consistent with that of CD206 staining, while SCRM did not show a consistent pattern (Spearman's rank correlation$_{A2}$ = 0.69 vs. Spearman's rank correlation$_{SCRM}$ = 0.51).

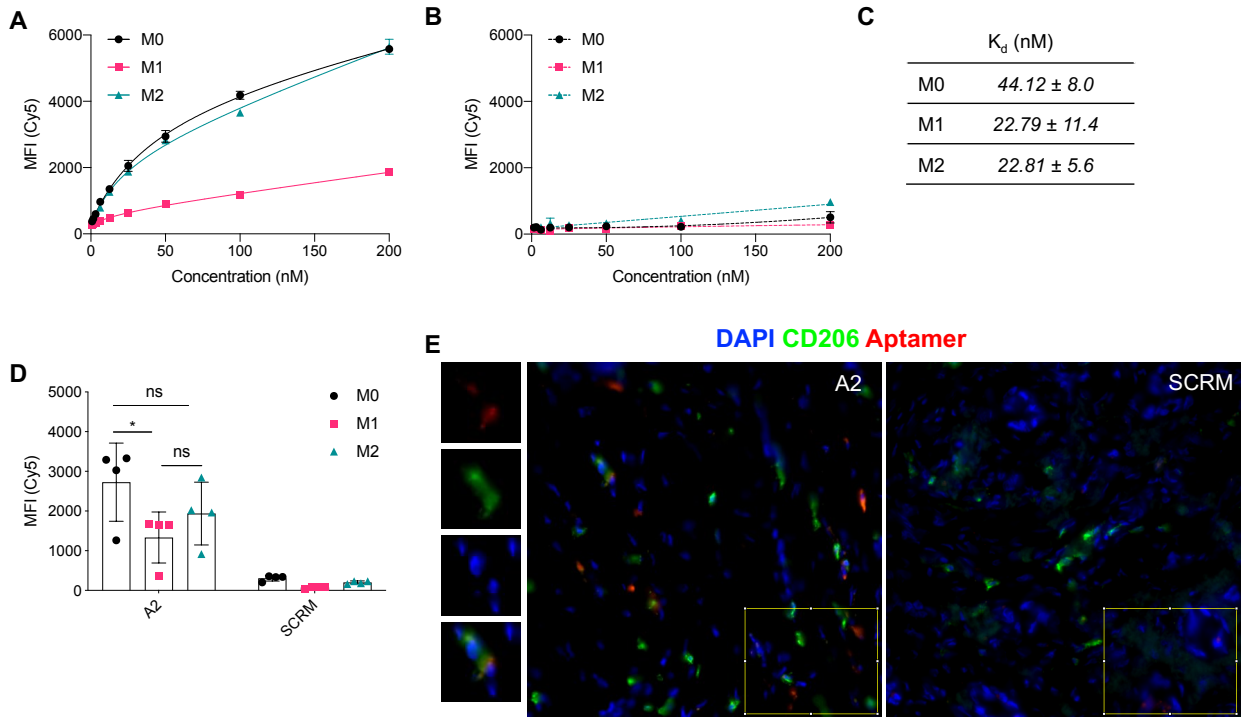

*Figure 2.2: Aptamer binding to human M0-, M1-, and M2-like macrophages. A-B) Aptamers A2 (A) and SCRM (B) was bound to human M0-, M1-, and M2-like macrophages, and apparent dissociation constants (K_d) were calculated. C) Calculated dissociation constants for aptamer A2 binding to M0-, M1-, and M2-like human macrophages. D) Aptamer binding to macrophages was confirmed across unique donors. Aptamer A2 binding to M0-like macrophages was significantly higher than binding to M1-like macrophages (*p = 0.03). A2 binding was significantly higher than SCRM binding to M0- (***p = 0.0002) and M2-like (**p = 0.006) macrophages. There was no significant difference between A2 and SCRM binding to M1-like macrophages. E) Representative images of aptamer binding to human TNBC sections with DAPI nuclear stain (blue), CD206 macrophage stain (green), and aptamer (red). Analyzed region-of-interest (ROI) is outlined in yellow and is equivalent between images. Aptamer A2 correlation with CD206 was significantly higher than SCRM correlation with CD206 (**p = 0.005). Images on the left column show single cell magnification.*

2.3.3 Characterization of aptamer A2 binding to PBMCs

We next sought to characterize the binding profile of aptamer A2 with PBMCs. For TAM targeting applications, A2 would ideally have low non-specific binding to circulating leukocytes to prevent

off-target binding and toxicity. While macrophages are derived from monocytes and thus have some overlapping surface marker expression, we hypothesized that aptamer A2 would not bind monocytes due to their use as negative selection cells. Nevertheless, aptamer A2 bound $CD14^+$ cells (monocytes) with high specificity ($K_d \sim 45 \pm 9.1$ nM), with negligible binding to remaining PBMC cell populations ($CD3^+$ T cells, $CD19^+$ B cells, and $CD56^+$ natural killer cells) (**Figure 2.3A, C**). While aptamer A2 binding to $CD14^+$ monocytes did depend on donor to some extent, binding was consistently above that of SCRM (****$p < 0.0001$) (**Figure 2.3B**). It is likely that variability in donor-to-donor binding can be attributed to varied protein and receptor expression across donors.[27]

To evaluate the potential of using aptamer A2 to deliver cargo intracellularly, we next investigated aptamer internalization. Monocytes were incubated with aptamer for 10 and 20 minutes and then treated with trypsin to remove aptamer bound to external receptors (**Figure 2.3D**). Remaining aptamer fluorescence was analyzed via flow cytometry. While trypsin treatment did significantly reduce overall fluorescent signal (****$p < 0.0001$), the majority of fluorescent signal remained, indicating that the aptamer is rapidly internalized into cells. Aptamer internalization was further validated by confocal microscopy at 20 minutes after incubation, which revealed aptamer presence in punctate staining patterns within monocytes, consistent with vesicular internalization (**Figure 2.3F**). Last, we investigated the monocyte subset to which the aptamer bound. Monocytes are classified as classical ($CD14^{hi}CD16^{lo}$) or non-classical ($CD14^{lo}CD16^{hi}$) monocytes, which comprise 70-95% and 2-11% of monocytes, respectively. We stained PBMCs with anti-human CD14 and anti-human CD16 antibodies, and observed that aptamer A2 only bound to $CD14^+$ classical monocytes, with no binding to $CD16^+$ monocytes (**Figure 2.3E**).

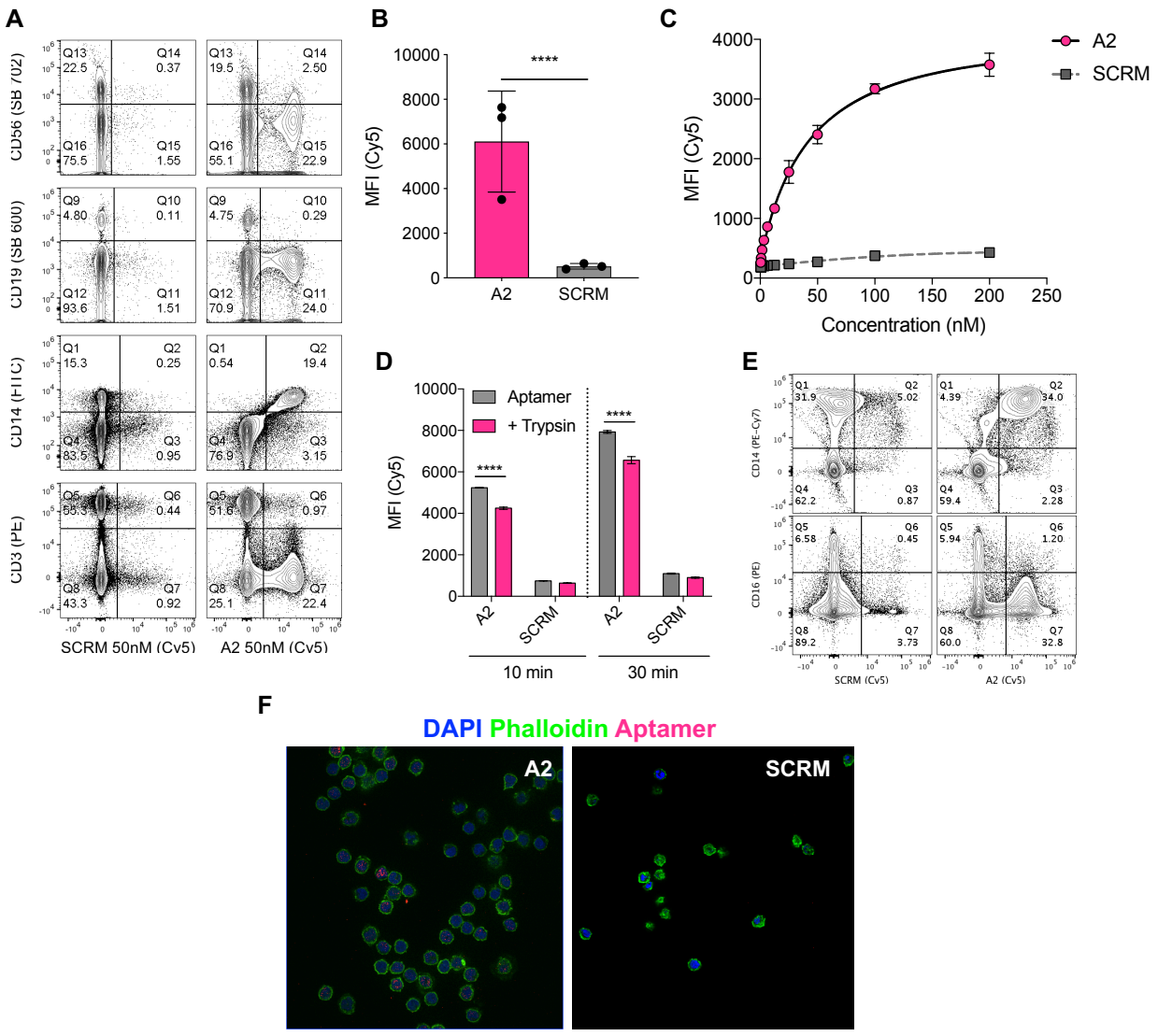

*Figure 2.3: Aptamer binding to CD14⁺ cells in complete PBMCs. A) Aptamer A2 binding (right) was compared to a scrambled aptamer control (left) in PBMCs, staining with antibodies against CD14 (monocytes), CD19 (B-cells), CD3 (T-cells), or CD56 (natural killer cells). B) Aptamer binding (A2 vs. SCRM) was assessed across unique human blood donors (****p < 0.0001). C) Aptamer A2 bound to CD14⁺ population of PBMCs with an apparent dissociation constant ~ 45 ± 9.1 nM. D) Aptamer internalization was assessed by incubation with monocytes, followed by removal of external receptors by trypsin 0.25%. Aptamer fluorescence was determined by flow cytometry (****p < 0.0001). E) Aptamer A2 binding to monocyte CD14⁺ and CD16⁺ populations was assessed. F) Aptamer internalization was assessed by confocal microscopy. Cells were stained with DAPI (blue, nucleus), phalloidin (green, actin), and aptamer (magenta).*

3.4 Aptamer A2 retains binding to monocytes in vivo.

Given the accessibility of monocytes in the blood, we next investigated aptamer binding to monocytes *in vivo*. We focused on monocyte, rather than macrophage, targeting due to challenges in developing humanized mouse models, which still suffer from impaired engrafted macrophage function.[28] To determine whether aptamer A2 retained binding to monocytes *in vivo*, human monocytes cells and aptamer (either A2 or SCRM) were injected intraperitoneally (i.p.) into NOD-scid gamma (NSG) mice, as previously described (**Figure 2.4A**).[29] NSG mice were used because they are immunodeficient, allowing for engraftment of human cells. Cells were recovered by peritoneal lavage and stained with human anti-CD14 antibody. Aptamer A2 retained binding to $CD14^+$ cells over a SCRM control (*****p* < *0.0001*) (**Figure 2.4B-D**). However, it was noted that there was some binding to an unidentified $CD14^-$ cell population; we hypothesize that this could be due to nonspecific charge interactions of DNA oligonucleotides with cells. *In vitro*, we did not observe significant binding to murine macrophages or PBMCs (**Figure S2.5**).

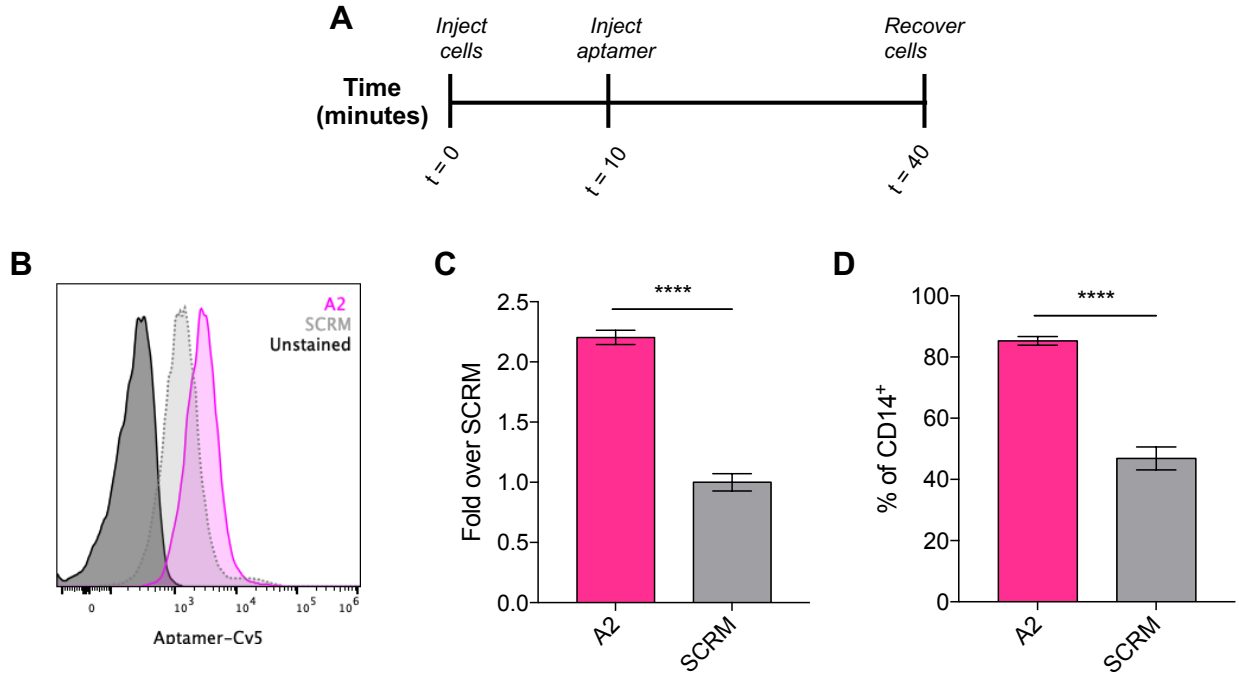

Figure 2.4: Aptamer A2 retains binding to $CD14^+$ cells in vivo. A) Monocytes were injected i.p. (t = 0 minutes), followed by aptamer injection i.p. (t = 10 minutes). After 30 minutes (t = 40 minutes), cells were recovered from the peritoneal cavity and assessed by flow cytometry for anti-CD14 antibody and aptamer staining. B-C) Recovered cells were gated on anti-CD14 antibody staining and assessed for aptamer fluorescence. Results are shown as a histogram (B) or bar graph (C),

*normalized to fluorescence of SCRM aptamer (****p < 0.0001). D) Percent of CD14$^+$ cells that stained for aptamer (****p < 0.0001).*

2.4 Discussion

In this work, we have identified and characterized the binding behavior of aptamer A2 to human monocytes and macrophages. Previously, we demonstrated improved therapeutic efficacy with a murine TAM-targeted peptide, M2pep, to deliver a pro-apoptotic peptide to M2-like TAMs, reducing TAM populations and extending survival in tumor bearing mice.[17] However, M2pep did not bind human M2 macrophages, prompting our search for an aptamer that can bind human M2-like TAMs. We had originally set out to identify an aptamer that could preferentially target M2-like macrophages because of their resemblance to TAMs, and to bypass tissue resident macrophages (M0-like macrophages). We ordered individual aptamer sequences and assessed binding against human macrophages. Although aptamer A1 represented 20% of total sequences, it did not bind to human macrophages (**Figure S2.4**). Propagation of parasitic sequences is not uncommon for the SELEX process and could perhaps be explained by PCR amplification bias.[30] Aptamer A2 had an abundance of 3% in the final pool, but did not have sequence similarities to other identified motifs.

Aptamer A2 did bind M2-like macrophages with high affinity, but also bound monocytes and M0-like macrophages, albeit with lower affinity. While the K_d of aptamer binding to M1-like macrophages was similar to the K_d to M0- and M2-like macrophages, the maximum binding was lower, suggesting lower receptor density on the cell surface. Aptamer binding to monocytes and M0-like macrophages was initially surprising because these cell populations were used as negative selection screens, and aptamers that bound these cells should consequently have been removed during the selection process. However, consideration about receptor overlap between macrophage phenotypes and precursors could explain this binding.[16] M0- and M2-like macrophages are more similar to each other than to M1-like macrophages and have a high degree of receptor overlap. We next characterized aptamer binding to human monocytes. Despite use as negative selection screens, aptamer A2 bound with comparable affinity to monocytes and M0- and M2-like macrophages. This could perhaps be due to high receptor overlap, such as CCR2, CX3CR1, and CSF-1R. This finding further demonstrates the complexity of macrophage polarization, and how

it is best viewed as a continuum rather than as a binary outcome.[15,31] Overall, *in vitro* polarization provides an incomplete picture of macrophage functional states, which are complicated and requires precise environmental cues that are unable to be replicated *in vitro*. Another likely reason that our aptamer bound to negative selection cells is because of the use of several donors for selection. Originally, this strategy was chosen to enable universal application despite variabilities across donor receptor expression. However, donor characteristics (age and gender) can significantly impact cytokine response, ultimately impacting macrophage polarization, receptor expression, and phenotype of the cells.[27] Because different donors have different degrees of receptor expression, the use of multiple, random donors ultimately impacted receptor expression and thus aptamer selection.

We also sought to identify the receptor to which our aptamer bound, but initial pull down attempts were unsuccessful. One barrier for us in pulldown assays is that this method requires extremely high cell numbers.[32] Due to the high cost of isolating human monocytes, we attempted to identify an immortalized cell line to which our aptamer bound. However, aptamer A2 did not bind significantly to murine macrophages or PBMCs, or the immortalized monocyte THP-1 or U937 cell lines (**Figure S2.6**). Based on A2 binding behavior to monocytes, we hypothesized that our aptamer bound to the CD14 receptor, which is expressed by both monocytes and macrophages. We investigated aptamer binding to purified CD14 protein by biolayer interferometry (BLI) and by transfecting Jurkats, a T-cell line, to express CD14. However, no significant binding over SCRM was observed (**Figure S2.7**).

Lastly, we investigated *in vivo* binding to monocytes, given the accessibility of monocytes and the challenges in establishing humanized mouse models to support human macrophage populations. Monocytes are circulating blood cells, whereas macrophage engraftment would require tumor re-population, sufficient aptamer pharmacokinetics and stability to remain intact following injection, and adequate aptamer-tumor localization and targeting. While humanized mouse models have made impressive advancements in replicating human lymphoid cells, the engraftment of human myeloid cells in commercially available immunodeficient mice is technically challenging, costly, and time consuming.[33] Furthermore, engrafted cells have impaired macrophage function and do not exactly replicate their behavior in tumors.[28] Aptamer targeting in the intraperitoneal (i.p.)

cavity of mice, while not exactly replicating an intravenous model, demonstrated binding at relevant physiologic conditions.[29]

Because aptamer A2 binds to both M0- and M2-like macrophages, it holds potential for *in vivo* or *in vitro* applications aimed at monocytes, such as column selection from PBMCs or drug delivery to monocytes in disease states. Indeed, we found that the majority of A2 is rapidly internalized within 10 minutes (**Figure 2.3D**), which could enable efficient intracellular drug delivery. Because monocytes are macrophage precursors, the ability to specifically target these cells could have large implications for future cancer therapies. Researchers have investigated blocking monocyte recruitment to tumors, which temporarily inhibited tumor growth, and have employed monocytes for drug delivery to immune privileged sites (e.g. central nervous system).[34-36] Monocyte are also implicated in viral infection, such as Zika and influenza A, and new therapies could utilize *in situ* targeting for drug delivery or depletion.[37,38] Additionally, aptamer A2 could be applied to magnetic columns for monocyte capture and subsequent release, isolating $CD14^+$ monocytes from PBMCs; this application has been reported by our group for $CD8^+$ T cell isolation.[21] Use of this aptamer for column selection could decrease cost, which could have significant impact as the field moves toward engineered macrophages for adoptive therapies.[7,39,40] Furthermore, A2 could be used to isolate a highly pure population of classical $CD14^+$ monocytes, which offer distinct functional properties (e.g. differentiation, receptor expression, migration) compared to $CD16^+$ monocytes.[41,42] This pure starting populations can provide more homogenous results compared to isolations with mixed $CD14^+$ and $CD16^+$ monocytes.

For use *in vivo*, further modifications would be necessary to extend aptamer circulation time and stability.[43,44] Future work includes investigation into the $CD14^-$ cell population that aptamer A2 bound *in vivo*, and adaptation for column selection.

2.5 Experimental Procedures

Oligonucleotides and cell-SELEX. All oligonucleotides were synthesized by Integrated DNA Technologies (IDT). The ssDNA library (~10^{16} individual sequences) used in the cell-SELEX process was purchased from IDT and consisted of a 52 base-pair (bp) random sequence flanked by two 18 bp constant regions. The primers used for library amplification are as follows: forward

5’-FAM-ATCCAGAGTGACGCAGCA-3’ and reverse 5’-biotin-ACTAAGCCACCGTGTCCA-3’. The SELEX protocol was adapted from a previously reported method [20]. A schematic of the SELEX procedure is shown in Figure 1, including cell number, washes, incubation time, and aptamer concentration. Broadly, positive selection was performed against plated human macrophages polarized to an M2-like phenotype. Bound aptamers were extracted by lifting cells with a cell scraper and heating the suspension to 95°C to denature DNA and separate aptamers from cells. The supernatant containing aptamer sequences was collected, and protein (BSA or DHS) and tRNA (100 μg/ml) was added. For negative selection, these sequences were then bound against monocytes or plated human macrophages polarized to an M0-like phenotype. The supernatant containing unbound aptamer sequences was collected and amplified by PCR using Phusion High Fidelity DNA Polymerase (NEB) with forward and reverse primers. Strand separation was performed with High Capacity Neutravidin Agarose Resin (Thermo), and the FAM-labeled ssDNA aptamer pool was used in the next round.

NGS and data analysis. The resulting ssDNA pools from each round of SELEX were PCR amplified using the MiSeq Reagent Kit v2 (300 cycles) and MiSeq System (Illumina) according to manufacturer’s instructions. Exported FASTA files were analyzed with FASTAptamer v1.0.3, as described previously [21]. Specifically, FASTAptamer-Count was used to rank sequences by reads per million. FASTAptamer-Compare was used to calculate enrichment of sequences between inputted rounds. Neighbor joining phylogenetic trees were constructed for the top 100 sequences from rounds 6-9 using Ninja v1.2.2 and visualized by FigTree v1.4.3. Consensus sequence and conserved motifs across the top 50-100 sequences from each round were predicted using MEME Suite v4.12.0. The NUPACK web application was used to predict secondary structures.

Cell culture and PBMC isolation. Human PBMCs were isolated from Leukocyte Reduction System cones (Bloodworks Northwest) using Ficoll-Paque (GE) density gradient centrifugation. Monocytes isolated using the Monocyte Isolation Kit II (Miltenyi) or Pan Monocyte Isolation Kit (Miltenyi). Human macrophages were cultured by plating monocytes in RPMI 1640 (Gibco) supplemented with 20% DHS (R&D), 1% PenStrep (ThermoFisher), and 25 ng/ml M-CSF (R&D). On day 4, additional plating media was added. On day 7, macrophages were polarized to an M0 (25 ng/ml M-CSF), M1 (50 ng/ml IFN-γ (R&D) + 10 ng/ml LPS (InvivoGen)), or M2 (20 ng/ml

IL-4 (R&D)) phenotype for 24-48 hours prior to use. Phenotype was validated via flow cytometry with human anti-CD64 and anti-HLA-DR antibodies (M1 markers) and human anti-CD36 and anti-CD180 antibodies (M2 markers). U937 and THP-1 monocytes were obtained from ATCC. THP-1 macrophages were plated using PMA (Sigma), and polarized to M0, M1, and M2 phenotype as above.

Generation of murine BMDM and PBMC. All animal experiments were approved by the Institutional Animal Care and Use Committee at the University of Washington and were conducted in accordance with use and regulations. Murine bone marrow derived macrophages (BMDM) were generated as previously described [17]. Briefly, the femur and tibia from 6-8 week Balb/c mice were flushed of bone marrow and cells were cultured in the same media as human macrophages (described above) supplemented with 25 ng/ml murine M-CSF (Miltenyi). On day 4, additional media supplemented with 25 ng/ml murine M-CSF was added. On day 7, macrophage were polarized to an M0 (25 ng/ml murine M-CSF), M1 (50 ng/ml IFN-γ (R&D) + 10 ng/ml LPS (InvivoGen)) or M2 (20 ng/ml IL-4 (R&D)) phenotype 24-48 hours prior to use. PBMCs were isolated via terminal blood draw from the vena cava using Ficoll-Paque (GE) density gradient centrifugation.

Antibodies and flow cytometry. For binding studies involving antibodies, cells were blocked with FcBlock (human (Miltenyi) or murine (BioLegend)) according to manufacturer's instructions. The following dyes and antibodies were used to stain cells: Zombie Violet (1:500 in 100 ul 10^{-6} cells, BioLegend), Zombie Yellow (1:500 in 100 ul 10^{-6} cells, BioLegend), SuperBright 702 anti-human CD56 (1:100, ThermoFisher), SuperBright 600 anti-human CD19 (1:20, ThermoFisher), PE anti-human CD3 (1:100, BioLegend), FITC anti-human CD14 (1:200 BioLegend), PE-Cy7 anti-human CD14 (1:40, Fisher), APC/Cy7 anti-mouse CD45 (1:100, Miltenyi), eFluor450 anti-mouse CD3 (1:100, BioLegend), Alexa Fluor 594 anti-mouse CD4 (1:20, BioLegend), FITC anti-mouse CD8 (1:1000, BioLegend), PE anti-mouse CD11b (1:40, BioLegend), FITC anti-mouse Ly6G (1:40, BioLegend), PE anti-human CD64 (1:20, BioLegend), FITC anti-human HLA/DR (1:20, BioLegend), FITC anti-human CD36 (1:20, BioLegend), APC anti-human CD206 (1:100, BioLegend), DAPI (300 nM, XX), Phalloidin-FITC (1:100, Invitrogen). OneComp eBeads (Invitrogen) were used to prepare single-color controls for

compensation if needed. Stained samples were analyzed with a MACSQuant Analyzer 10 (Miltenyi) or Attune NxT (Invitrogen) flow cytometer.

Aptamer binding assays. For individual aptamer binding, cells (0.5 x 10^6) were incubated with 50 nM folded aptamer (in Wash Buffer (WB) supplemented with 10% FBS and 100 μg/ml tRNA) and antibody cocktail for 20-30 min at 4°C (unless otherwise indicated). Aptamers were ordered with a Cy5-label as it is a brighter fluorophore than FAM/FITC; however, fluorophore labeling has no effect on binding. All aptamer binding was compared to a nonspecific aptamer sequence control. After binding, cells were washed twice in 200 μl of WB supplemented with 1% BSA. Stained cells were fixed in 200 μl of WB with 1% BSA and 0.5% PFA before analysis via flow cytometry. For aptamer internalization assay, monocytes were incubated with the aptamer at 50 nM at 37°C for 10, 20 and 30 minutes, washed with 500 μl WB, and external receptors were cleaved with 0.25% trypsin at 37°C for 3 minutes. For macrophage binding assays, plated cells (1-2 x 10^6) were incubated with 50 nM aptamer, washed with PBS without ions, and lifted with Versene (Gibco) for 20 min at 4°C or TrypLE (Fisher) for 30 min at 37°C. Cells were processed for analysis via flow cytometry as above. GraphPad Prism 7.0 was used to calculate the total binding dissociation constant. BLI studies were conducted on a FortéBio Octet Red96 instrument, as previously described [21].

Droplet digital PCR. Plated cells (1-2 x 10^6) in a 6-well TC plate (Corning) were washed twice with WB, incubated with 50 nM (individual) or 200 nM (round binding) folded aptamer (in WB supplemented with 10% FBS and 100 μg/ml tRNA) for 30 min at 4°C, and washed five times with WB supplemented with BSA. Cells were lysed and DNA was recovered via DNeasy kit (Qiagen) according to manufacturer's instructions. DNA was quantified using a Qubit (Thermo) and serially diluted in molecular water. DNA and primers (extended aptamer and reference 12S ribosomal RNA gene) were added to Eva Green Master Mix (Biotium) and analyzed via ddPCR according to manufacturer's instructions.

Imaging. For monocyte confocal assays, coverslips were coated with 10 μg/ml poly-D-lysine at 37°C for 2 hours. Cells were bound with 50 nM aptamer and plated onto coverslips by centrifuging at 2,000 rpm for 10 minutes. Cells were fixed in 4% PFA, stained with Phalloidin-FITC (1:100)

and DAPI (300 nM), and mounted onto glass slides. For macrophage confocal assays, coverslips were coated with 45 μg /ml collagen for 1 hour at room temperature. Monocytes were plated onto coverslips and cultured into macrophages. After polarization, macrophages were bound with 100 nM aptamer, fixed, stained, and covered. Images were taken on a Leica SP8X. Humans tumors were obtained from the Washington Cancer Consortium Breast Specimen Repository and Registry in accordance with guidelines established by the University of Washington Institutional Review Board. All patient information was de-identified prior to sharing with investigators. Tumors were fixed in 4% PFA overnight and dehydrated via sucrose gradient. Tumors were frozen in OCT and sectioned in 10 μm thick sections using a cryosectioner (Leica CM1850). Sections were fixed (4% PFA, 10 min at room temperature), blocked and permeabilized (2% DKS + 2% BSA + 0.3% Triton-X in TBS, 1 hour at room temperature), and stained with primary antibody overnight at 4°C in a humidified box. Sections were washed three times in TBS-0.1% Tween (30 minutes each) followed by incubation with secondary antibody and DAPI (1 hour at room temperature). Sections were washed three times in TBS-0.1% Tween, blocked with 50 μg/ml salmon sperm (Invitrogen) for 1 hour at 4°C, and incubated with 1 μM folding aptamer (in WB supplemented with 10% FBS and 100 μg/ml tRNA) for 1 hour at 4°C. Sections were washed three times with TBS-0.1% Tween and covered with coverslip. Images were taken on a Nikon Eclipse TI. Images were analyzed on ImageJ version 2.0.0-rc-69/1.52i. A region-of-interest (ROI) was drawn around image areas with aptamer signal; the same ROI was used in A2 and SCRM images. Colocalization was analyzed using the Coloc2 plug-in. Statistical significance was determined based on the Spearman rank correlation in two independent images.

***In vivo* intraperitoneal binding.** Donors were screened for binding prior to monocyte isolation. Monocytes (1 x 10^6) were injected i.p. into NSG mice (Jackson). After 10 min, aptamer (125 nM A2 or SCRM + 625 nM unlabeled NS aptamer) were injected i.p. in WB. After 30 minutes, the mouse was sacrificed by cervical dislocation. Cells were recovered via peritoneum lavage, as described. Recovered cells were incubated with ACK Lysis Buffer (Invitrogen) for 5 min at room temperature, and were processed for analysis via flow cytometry.

Statistical analysis. Significance was determined by ANOVA (multiple groups) or a two-tailed student's t-test in Graphpad Prism 7. All flow cytometry analysis was completed using FlowJo.

2.6 Acknowledgements

This work was supported by NIH (1R01CA177272). We thank Dr. Gary Liu for his guidance on fluorescent imaging, and Ian Cardle for support on flow cytometry; Dr. Nathanial Peters and W. M. Keck Microscopy Center (S10 OD016240) for confocal microscopy support; and Kelly Williams (Environmental and Forest Services Shared Genetics Laboratory) for support on the droplet digital PCR. We are grateful to the Breast Specimen Repository, a collaboration among the Fred Hutchinson Cancer Research Center, the University of Washington Medical Center, and Harborview Medical Center, Seattle, WA and Overlake Hospital and Medical Center, Bellevue, WA, for the human breast cancer samples used in this study.

2.7 Conflict of Interest

The authors report no conflicts of interest.

2.8 Supplemental Information

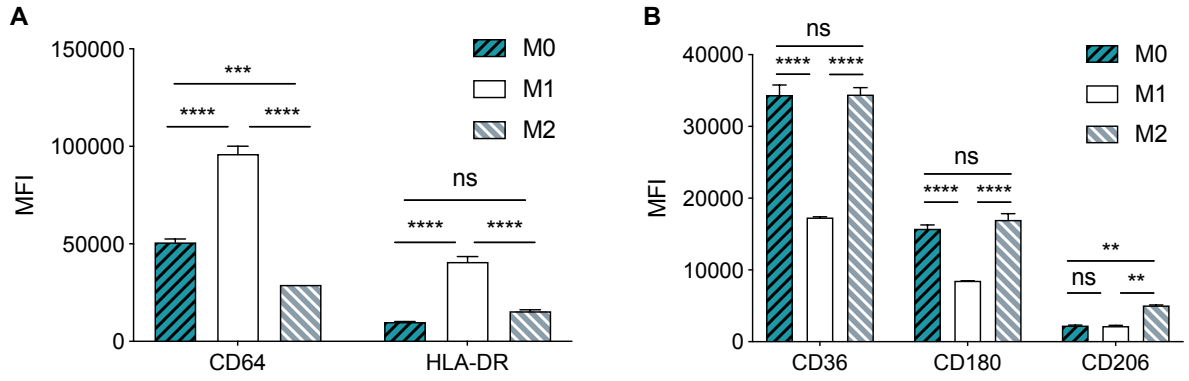

*Figure S2.1: Macrophage phenotype validation by flow cytometry. Isolated monocytes were cultured and polarized into M0-, M1-, and M2-like macrophages. Macrophage phenotype was confirmed by assessing M1 markers CD64 and HLA-DR (A) and M2 markers CD36 and CD180 (B). Significance was determined by ANOVA (CD64 M0 vs M2 ***p = 0.0001; ****p < 0.0001) (HLA-DR ****p < 0.0001) (CD36 ****p < 0.0001) (CD180 ****p < 0.0001) (CD206 M0 vs M2 **p = 0.0056; M1 vs M2 **p = 0.0048)*

	Aptamer % representation of all reads in each round					Enrichment between rounds y/x			
Rank	% R9	% R8	% R7	% R6	% R5	9/8	8/7	7/6	6/5
1	21	10	2	0	0	2	4	6	12
2	3	1	0	0	0	4	5	3	26
3	3	4	2	0	0	1	2	3	33
4	2	3	5	3	0	1	1	2	62
5	2	1	1	1	0	2	1	1	20
6	2	1	0	0	0	2	7	9	14
7	2	1	0	0	0	2	8	7	12
8	1	1	0	0	0	2	4	10	28
9	1	1	1	0	0	1	2	2	11
10	1	1	0	0	0	2	7	9	18

Motif 1
29 bp, 60/200 apt.

Motif 2
29bp, 8/200 apt.

Motif 3
22bp, 24/200 apt.

Motif 4
21bp, 4/200 apt.

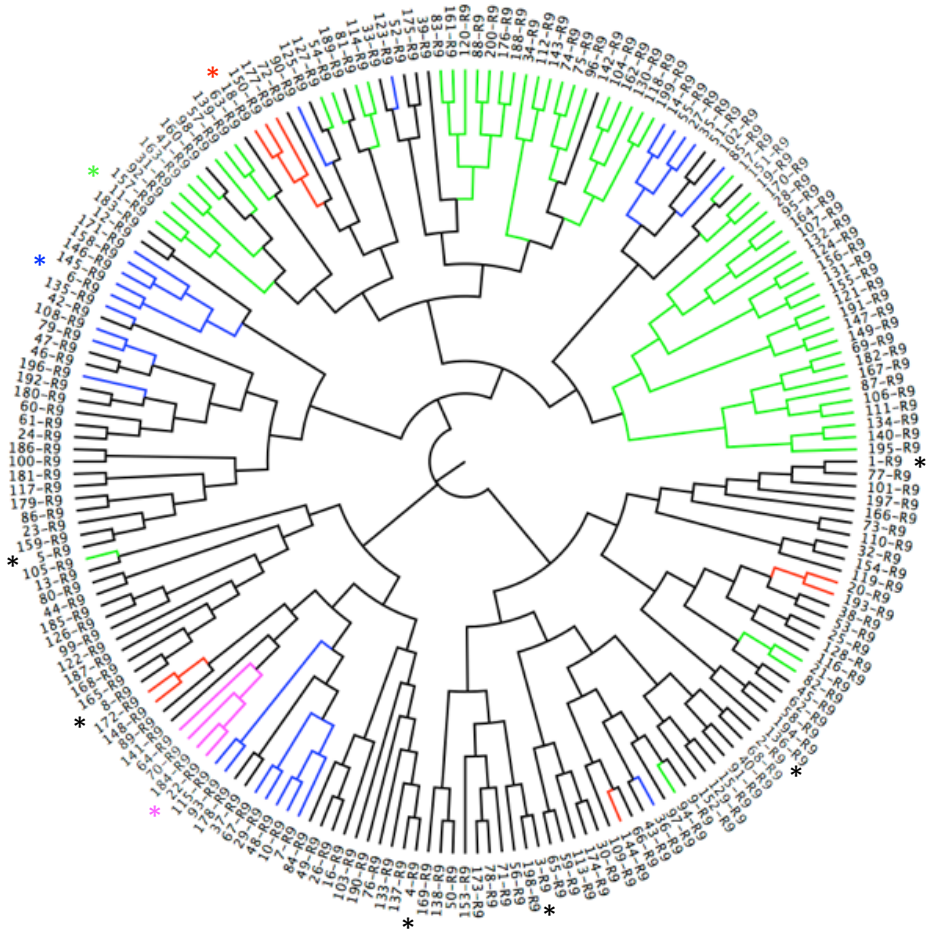

Motif	Motif Sequence from meme-suite.org

Motif 1	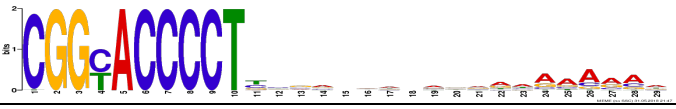
Motif 2	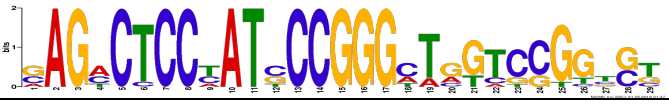
Motif 3	
Motif 4	

Figure S2.2: Aptamer sequence analysis. A) FASTAptamer was used to determine aptamer representation based on reads per million (RPM), as well as aptamer enrichment between rounds. Enrichment was calculated as (RPM of round y)/(RPM of round x). Above is an example analysis of the top 100 aptamers from round 9. Purchased aptamers are highlighted in purple. B) Motifs of the top 200 sequences (based on RPM) were tracked through rounds. The top 200 sequences from round 9 are displayed in a phylogenetic tree and the motif sequences are displayed in the table. Aptamers with conserved motifs are indicated in the tree. Purchased aptamers are denoted with an asterisk (*).

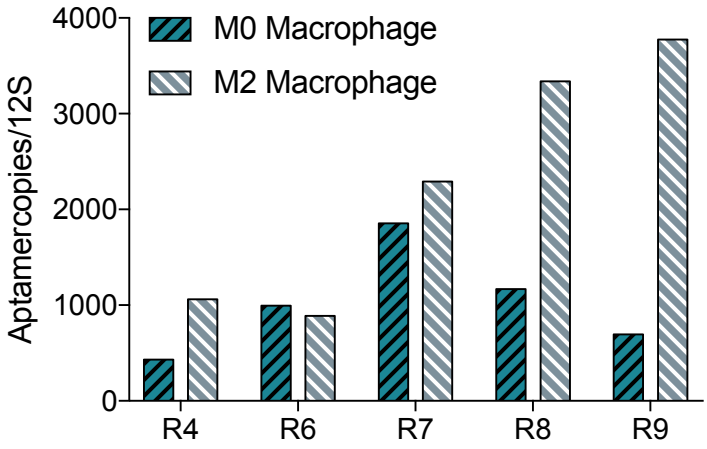

Figure S2.3: Round binding to M0- and M2-like macrophages. Resulting aptamer pools (200 nM) from each round were bound against M0- and M2-like macrophages. Aptamers and macrophage DNA were recovered and assessed by droplet digital PCR. Aptamer copies were normalized to cell number (copies of ribosomal RNA 12S gene).

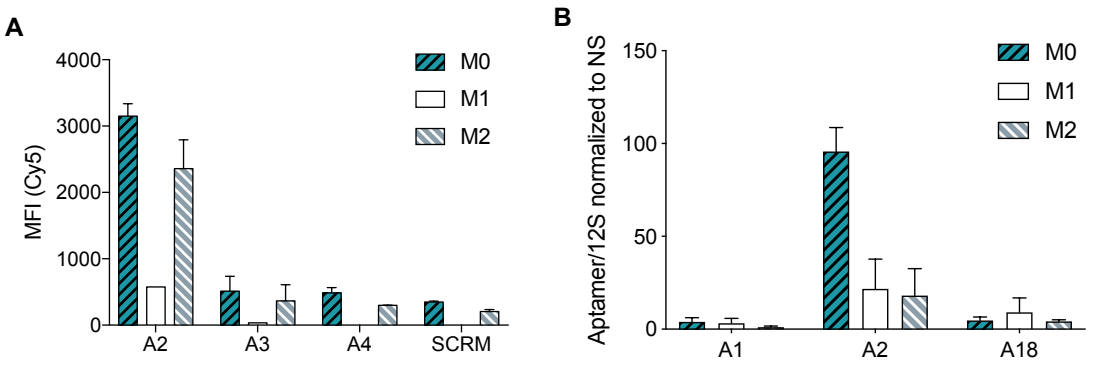

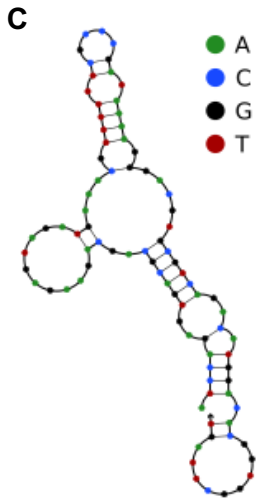

D

Table 1. DNA sequences used in this work

Oligonucleotide	*Sequence*
52-Base Pair Library Design	5'-ATCCAGAGTGACGCAGCA-52N-TGGACACGGTGGCTTAGT-3'
A2 Aptamer	GAAGAGTAGATGAAACGTTTTTTCGCCCGATAAAAGGGACGTGCGTCAGACA
SCRM Aptamer	ATGATAGTGACGTACGGACTAGGGATCACCCATATCATGTAGAGGAAGTACG
Primer	*Sequence*
Aptamer Forward Primer	5'-FAM-ATCCAGAGTGACGCAGCA-3'
Aptamer Reverse Primer	5'-biotin-ACTAAGCCACCGTGTCCA-3'
Extended Aptamer Forward Primer	5'-GCATCCAGAGTGACGCAGCA-3'
Extended Aptamer Reverse Primer	5'-GCACTAAGCCACCGTGTCCA-3'
rRNA 12S Forward Primer	5'-AAACTGCTCGCCAGAACACT-3'
rRNA 12S Reverse Primer	5'-CATGGGCTACACCTTGACCT-3'

Figure S2.4: Aptamer binding, structure and DNA sequences. A-B) Selected aptamers were bound against M0-, M1-, and M2-like macrophages and analyzed using flow cytometry (A) or ddPCR (B). C) The predicted free structure of DNA aptamer A2 at 4°C using Nupack. D) Table of the aptamer and primer sequences used in this paper.

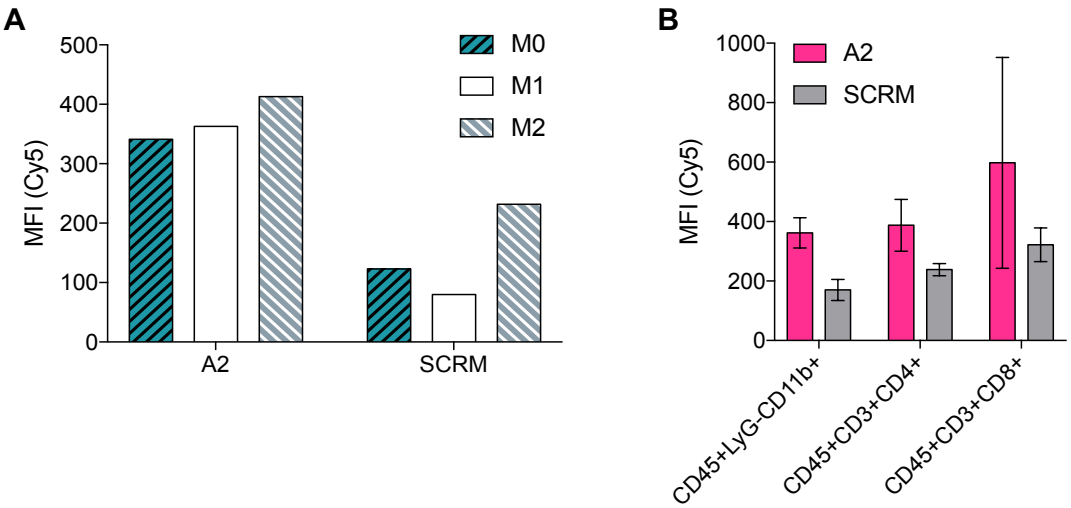

Figure S2.5: Aptamer A2 binding was assessed against murine macrophages and PBMCs. A) Murine macrophages were cultured from isolated bone marrow and polarized to M0-, M1-, and M2-like phenotypes. There was no significant difference in binding of A2 and SCRM. B) PBMCs were isolated from murine blood by Ficoll gradient and assessed for binding to monocytes ($CD45^+LyG^-CD11b^+$), $CD4^+$ T-cells ($CD45^+CD3^+CD4^+$) and $CD8^+$ T-cells ($CD45^+CD3^+CD8^+$) by flow cytometry. There was no significant difference in binding of A2 and SCRM.

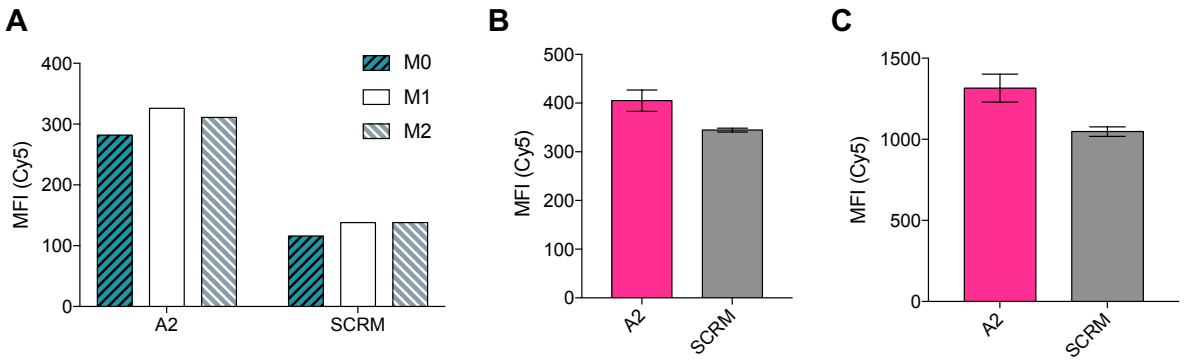

Figure S2.6: Aptamer A2 binding to THP-1 macrophages and THP-1 and U937 monocytes. A) THP-1 macrophages were polarized to M0-, M1-, and M2-like phenotypes and aptamer binding was assessed by flow cytometry. B-C) Aptamer binding to THP-1 monocytes (B) and U937 monocytes (C) was assessed by flow cytometry.

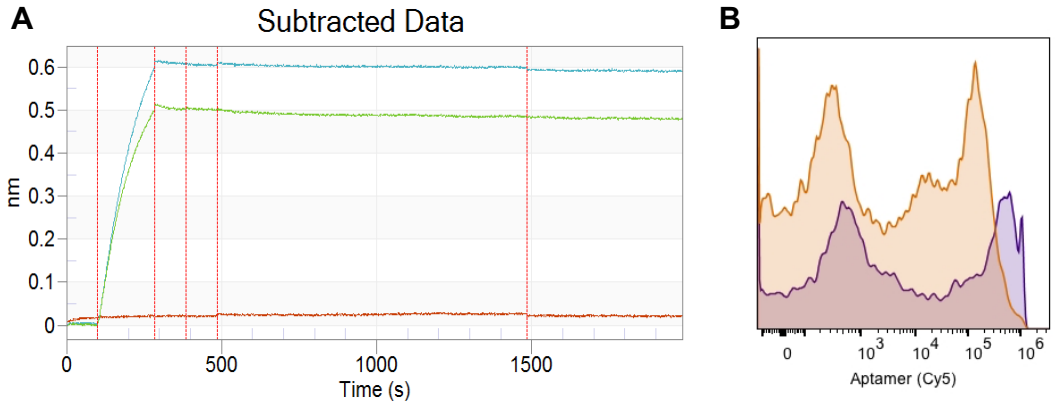

Figure S2.7: Aptamer binding to CD14 protein by surface plasma resonance. A) Aptamer A2 (green) binding to purified CD14 binding was compared to a nonspecific aptamer control (blue). Aptamer-protein association is measured by changes in optical readout. B) Jurkats were transfected to express the CD14 receptors. Aptamer (A2 purple, SCRM orange) binding to transfected cells was assessed by flow cytometry.

References

(1) Kalos, M., Levine, B. L., Porter, D. L., Katz, S., Grupp, S. A., Bagg, A., and June, C. H. (2011) T Cells with Chimeric Antigen Receptors Have Potent Antitumor Effects and Can Establish Memory in Patients with Advanced Leukemia. *Science Translational Medicine 3*.

(2) Andon, F. T., Digifico, E., Maeda, A., Erreni, M., Mantovani, A., Alonso, M. J., and Allavena, P. (2017) Targeting tumor associated macrophages: The new challenge for nanomedicine. *Semin Immunol 34*, 103-113.

(3) Tumeh, P. C., Harview, C. L., Yearley, J. H., Shintaku, I. P., Taylor, E. J., Robert, L., Chmielowski, B., Spasic, M., Henry, G., Ciobanu, V., et al. (2014) PD-1 blockade induces responses by inhibiting adaptive immune resistance. *Nature 515*, 568-71.

(4) Sharma, P., and Allison, J. P. (2015) The future of immune checkpoint therapy. *Science 348*, 56-61.

(5) McGrath, K. E., Frame, J. M., and Palis, J. (2015) Early hematopoiesis and macrophage development. *Semin Immunol 27*, 379-87.

(6) Klichinsky, M., Ruella, M., Shestova, O., Lu, X. M., Best, A., Zeeman, M., Schmierer, M., Gabrusiewicz, K., Anderson, N. R., Petty, N. E., et al. (2020) Human chimeric antigen receptor macrophages for cancer immunotherapy. *Nature Biotechnology*.

(7) Morrissey, M. A., Williamson, A. P., Steinbach, A. M., Roberts, E. W., Kern, N., Headley, M. B., and Vale, R. D. (2018) Chimeric antigen receptors that trigger phagocytosis. *Elife 7*.

(8) Ngambenjawong, C., Gustafson, H. H., and Pun, S. H. (2017) Progress in tumor-associated macrophage (TAM)-targeted therapeutics. *Adv Drug Deliv Rev 114*, 206-221.

(9) Noy, R., and Pollard, J. W. (2014) Tumor-associated macrophages: from mechanisms to therapy. *Immunity 41*, 49-61.

(10) Sylvestre, M., Crane, C. A., and Pun, S. H. (2019) Progress on Modulating Tumor-Associated Macrophages with Biomaterials. *Adv Mater*, e1902007.

(11) Bingle, L., Brown, N. J., and Lewis, C. E. (2002) The role of tumour-associated macrophages in tumour progression: implications for new anticancer therapies. *J Pathol 196*, 254-65.

(12) Dong, X., Chu, D., and Wang, Z. (2017) Leukocyte-mediated Delivery of Nanotherapeutics in Inflammatory and Tumor Sites. *Theranostics 7*, 751-763.

(13) Zeisberger, S. M., Odermatt, B., Marty, C., Zehnder-Fjallman, A. H., Ballmer-Hofer, K., and Schwendener, R. A. (2006) Clodronate-liposome-mediated depletion of tumour-associated macrophages: a new and highly effective antiangiogenic therapy approach. *Br J Cancer 95*, 272-81.

(14) Ries, C. H., Cannarile, M. A., Hoves, S., Benz, J., Wartha, K., Runza, V., Rey-Giraud, F., Pradel, L. P., Feuerhake, F., Klaman, I., et al. (2014) Targeting tumor-associated macrophages with anti-CSF-1R antibody reveals a strategy for cancer therapy. *Cancer Cell 25*, 846-59.

(15) Martinez, F. O., and Gordon, S. (2014) The M1 and M2 paradigm of macrophage activation: time for reassessment. *F1000Prime Rep 6*, 13.

(16) Mantovani, A., Sozzani, S., Locati, M., Allavena, P., and Sica, A. (2002) Macrophage polarization: tumor-associated macrophages as a paradigm for polarized M2 mononuclear phagocytes. *Trends in Immunology 23*, 549-555.

(17) Cieslewicz, M., Tang, J., Yu, J. L., Cao, H., Zavaljevski, M., Motoyama, K., Lieber, A., Raines, E. W., and Pun, S. H. (2013) Targeted delivery of proapoptotic peptides to tumor-associated macrophages improves survival. *Proc Natl Acad Sci U S A 110*, 15919-24.

(18) Keefe, A. D., Pai, S., and Ellington, A. (2010) Aptamers as therapeutics. *Nat Rev Drug Discov 9*, 537-550.

(19) Chen, L., Rashid, F., Shah, A., Awan, H. M., Wu, M., Liu, A., Wang, J., Zhu, T., Luo, Z., and Shan, G. (2015) The isolation of an RNA aptamer targeting to p53 protein with single amino acid mutation. *Proc Natl Acad Sci U S A 112*, 10002-7.

(20) Sefah, K., Shangguan, D., Xiong, X., O'Donoghue, M. B., and Tan, W. (2010) Development of DNA aptamers using Cell-SELEX. *Nat Protoc 5*, 1169-85.

(21) Kacherovsky, N., Cardle, II, Cheng, E. L., Yu, J. L., Baldwin, M. L., Salipante, S. J., Jensen, M. C., and Pun, S. H. (2019) Traceless aptamer-mediated isolation of CD8(+) T cells for chimeric antigen receptor T-cell therapy. *Nat Biomed Eng 3*, 783-795.

(22) Nikitina, E., Larionova, I., Choinzonov, E., and Kzhyshkowska, J. (2018) Monocytes and Macrophages as Viral Targets and Reservoirs. *Int J Mol Sci 19*.

(23) Alam, K. K., Chang, J. L., and Burke, D. H. (2015) FASTAptamer: A Bioinformatic Toolkit for High-throughput Sequence Analysis of Combinatorial Selections. *Mol Ther Nucleic Acids 4*, e230.

(24) Bailey, T. L., Boden, M., Buske, F. A., Frith, M., Grant, C. E., Clementi, L., Ren, J., Li, W. W., and Noble, W. S. (2009) MEME SUITE: tools for motif discovery and searching. *Nucleic Acids Res 37*, W202-8.
(25) Taylor, S. C., Laperriere, G., and Germain, H. (2017) Droplet Digital PCR versus qPCR for gene expression analysis with low abundant targets: from variable nonsense to publication quality data. *Sci Rep 7*, 2409.
(26) Sica, A., and Mantovani, A. (2012) Macrophage plasticity and polarization: in vivo veritas. *J Clin Invest 122*, 787-95.
(27) Siegel, G., Kluba, T., Hermanutz-Klein, U., Bieback, K., Northoff, H., and Schafer, R. (2013) Phenotype, donor age and gender affect function of human bone marrow-derived mesenchymal stromal cells. *BMC Med 11*, 146.
(28) Yong, K. S. M., Her, Z., and Chen, Q. (2018) Humanized Mice as Unique Tools for Human-Specific Studies. *Arch Immunol Ther Exp (Warsz) 66*, 245-266.
(29) Mallikaratchy, P. R., Ruggiero, A., Gardner, J. R., Kuryavyi, V., Maguire, W. F., Heaney, M. L., McDevitt, M. R., Patel, D. J., and Scheinberg, D. A. (2011) A multivalent DNA aptamer specific for the B-cell receptor on human lymphoma and leukemia. *Nucleic Acids Res 39*, 2458-69.
(30) Acinas, S. G., Sarma-Rupavtarm, R., Klepac-Ceraj, V., and Polz, M. F. (2005) PCR-induced sequence artifacts and bias: insights from comparison of two 16S rRNA clone libraries constructed from the same sample. *Appl Environ Microbiol 71*, 8966-9.
(31) Mantovani, A., Sica, A., Sozzani, S., Allavena, P., Vecchi, A., and Locati, M. (2004) The chemokine system in diverse forms of macrophage activation and polarization. *Trends Immunol 25*, 677-86.
(32) Wang, G., Liu, J., Chen, K., Xu, Y., Liu, B., Liao, J., Zhu, L., Hu, X., Li, J., Pu, Y., et al. (2017) Selection and characterization of DNA aptamer against glucagon receptor by cell-SELEX. *Sci Rep 7*, 7179.
(33) Sippel, T. R., Radtke, S., Olsen, T. M., Kiem, H. P., and Rongvaux, A. (2019) Human hematopoietic stem cell maintenance and myeloid cell development in next-generation humanized mouse models. *Blood Adv 3*, 268-274.
(34) Hou, J., Yang, X., Li, S., Cheng, Z., Wang, Y., Zhao, J., Zhang, C., Li, Y., Luo, M., Ren, H., et al. (2019) Accessing neuroinflammation sites: Monocyte/neutrophil-mediated drug delivery for cerebral ischemia. *Sci Adv 5*, eaau8301.
(35) Qian, B. Z., Li, J., Zhang, H., Kitamura, T., Zhang, J., Campion, L. R., Kaiser, E. A., Snyder, L. A., and Pollard, J. W. (2011) CCL2 recruits inflammatory monocytes to facilitate breast-tumour metastasis. *Nature 475*, 222-5.
(36) Olingy, C. E., Dinh, H. Q., and Hedrick, C. C. (2019) Monocyte heterogeneity and functions in cancer. *J Leukoc Biol 106*, 309-322.
(37) Hou, W., Gibbs, J. S., Lu, X., Brooke, C. B., Roy, D., Modlin, R. L., Bennink, J. R., and Yewdell, J. W. (2012) Viral infection triggers rapid differentiation of human blood monocytes into dendritic cells. *Blood 119*, 3128-31.
(38) Ayala-Nunez, N. V., Follain, G., Delalande, F., Hirschler, A., Partiot, E., Hale, G. L., Bollweg, B. C., Roels, J., Chazal, M., Bakoa, F., et al. (2019) Zika virus enhances monocyte adhesion and transmigration favoring viral dissemination to neural cells. *Nat Commun 10*, 4430.
(39) Moyes, K. W., Lieberman, N. A., Kreuser, S. A., Chinn, H., Winter, C., Deutsch, G., Hoglund, V., Watson, R., and Crane, C. A. (2017) Genetically Engineered Macrophages: A Potential Platform for Cancer Immunotherapy. *Hum Gene Ther 28*, 200-215.
(40) Muraoka, D., Seo, N., Hayashi, T., Tahara, Y., Fujii, K., Tawara, I., Miyahara, Y., Okamori, K., Yagita, H., Imoto, S., et al. (2019) Antigen delivery targeted to tumor-associated macrophages overcomes tumor immune resistance. *J Clin Invest 129*, 1278-1294.
(41) Sanchez-Torres, C., Garcia-Romo, G. S., Cornejo-Cortes, M. A., Rivas-Carvalho, A., and Sanchez-Schmitz, G. (2001) CD16+ and CD16- human blood monocyte subsets differentiate in vitro to dendritic cells with different abilities to stimulate CD4+ T cells. *Int Immunol 13*, 1571-81.
(42) Kapellos, T. S., Bonaguro, L., Gemund, I., Reusch, N., Saglam, A., Hinkley, E. R., and Schultze, J. L. (2019) Human Monocyte Subsets and Phenotypes in Major Chronic Inflammatory Diseases. *Front Immunol 10*, 2035.
(43) Ding, D., Yang, C., Lv, C., Li, J., and Tan, W. (2020) Improving Tumor Accumulation of Aptamers by Prolonged Blood Circulation. *Anal Chem 92*, 4108-4114.
(44) Shigdar, S., Macdonald, J., O'Connor, M., Wang, T., Xiang, D., Al Shamaileh, H., Qiao, L., Wei, M., Zhou, S. F., Zhu, Y., et al. (2013) Aptamers as theranostic agents: modifications, serum stability and functionalisation. *Sensors (Basel) 13*, 13624-37.

Part II

Developing immunogenic polymer-peptide conjugates

Chapter 3

Rational design of polymeric carriers for improved peptide delivery[3]

Shixian Lv, Meilyn Sylvestre, Alexander Prossnitz, Lucy Yang, and Suzie Pun

3.1 Abstract

In recent decades, peptides, have emerged as promising therapeutics for cancer applications, as peptides possess high potency, excellent selectivity, and low toxicity. Combined with an improved understanding of tumor biology and immuno-oncology, peptides have demonstrated robust anti-tumor efficacy in pre-clinical tumor models. However, the translation of peptides with intracellular targets into clinical therapies has been severely hindered by limitations in their intrinsic structure, such as low systemic stability, rapid clearance, and poor membrane permeability, that impedes intracellular delivery. In this review article, we summarize recent advances in polymer-mediated intracellular delivery of peptides for cancer therapy, including both therapeutic peptides and peptide antigens. We highlight strategies to engineer polymeric materials to increase peptide delivery efficiency, especially cytosolic delivery, which plays a crucial role to potentiate peptide-based therapies. Finally, we discuss future opportunities for peptides in cancer treatment, with an emphasis on the design of polymer nanocarriers for optimized peptide delivery.

3.2 Introduction

Successful delivery of anti-cancer agents after absorption into the bloodstream requires the following four sequential steps: (1) circulation in the blood compartment; (2) extravasation from blood vasculature and subsequent diffusion and penetration into the tumor tissue; (3) internalization by tumor cells; and (4) trafficking of free drug to target intracellular sites. The overall delivery efficiency, regarded as the percentage of free drug inside target cells, is a product of the efficiencies of these four steps. To achieve the highest overall efficiency, it is important to maximize the efficiency of each step and to ensure that none of the four efficiencies is near-zero.

[3] *Partial reprint with permission from Lv, S., Sylvestre, M., et al. Design of polymeric carriers for intracellular peptide delivery in oncology applications. Chem. Rev. (2021). Copyright 2021 American Chemical Society.*

However, each step presents its own biological barriers that effect overall delivery efficiency, such as complicated nanoparticle-biology interactions, premature drug release, “leaky” tumor blood vessels, dense tumoral extracellular matrix, high interstitial fluid pressure, heterogeneity of tumor micro-environment and tumor cells, and cell membrane barrier.[1] To overcome these barriers, it is crucial that nanoparticles are rationally designed with desirable physicochemical properties (**Figure 3.1**).

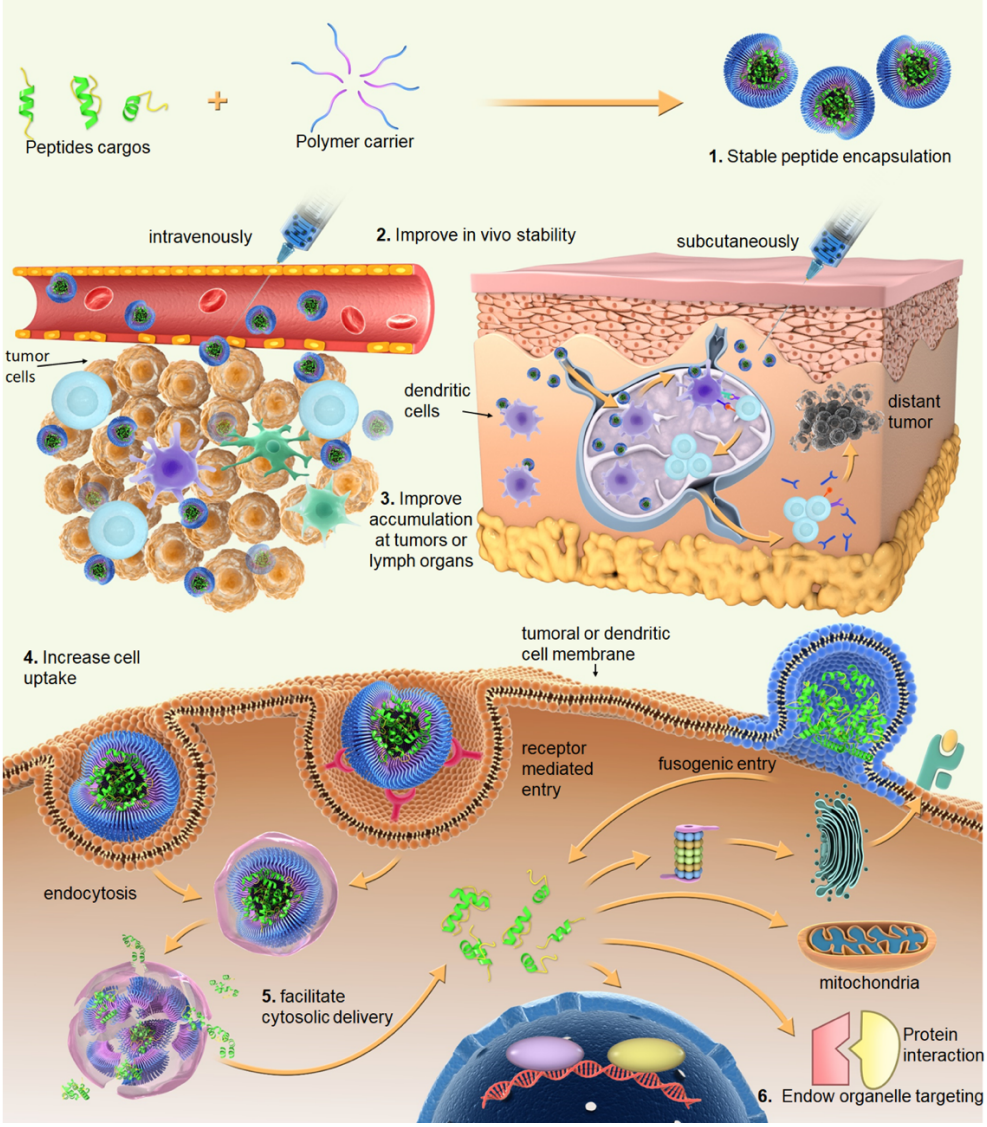

Figure 3.1: Schematic demonstration of challenges in polymer-mediated in vivo and intracellular delivery of peptide therapeutics for cancer treatment.

In addition to facing the aforementioned biological barriers, peptide therapeutics must also overcome additional challenges of poor *in vivo* stability and low cell membrane penetration. Compared to small molecule drugs, peptide therapeutics are more susceptible to proteolysis. Furthermore, small molecule drugs (*e.g.*, doxorubicin and paclitaxel) are able to cross cell membranes via passive diffusion or active transport, which is not possible for most peptide therapeutics due to their hydrophilicity and size. Additionally, peptide hydrophilicity and secondary structure (α-helix or β-sheet) can impede efficient encapsulation in nanocarriers. These intrinsic limitations of peptide therapeutics further complicate the design of polymeric nanoparticles for peptide delivery. For vaccine applications, intradermal delivery of peptide antigens also requires stable encapsulation to prevent degradation by interstitial proteases, enhance drainage to LNs, and facilitate cell uptake and presentation by APCs (Figure 4.1). In this section, we will discuss the strategies for engineering polymeric nanocarriers to overcome these limitations.

3.2.1 Increase in vivo stability

The *in vivo* stability of NPs can be improved by tuning the surface properties (such as PEGylation). When most peptide-polymer NPs enter a biological environment (*e.g.*, blood or extracellular matrix), the particle surface is rapidly coated by absorption of various biomolecules (typically proteins), leading to the formation of a 'corona'. For intravenously injected NPs, this protein corona increases clearance by the reticuloendothelial system (RES), as the binding of opsonins onto NPs can trigger recognition and clearance by the mononuclear phagocyte system (MPS). For poorly perfused tissues with low extravasation efficiency, (*e.g.*, solid tumors), a longer circulation time may be necessary to enhance NP exposure in the tumor microvasculature and to promote extravasation.[2] Therefore, rapid clearance significantly decreases overall delivery efficacy. To address this biological barrier, NP surface properties can be designed to reduce nonspecific interactions between NPs and serum proteins, increasing *in vivo* stability and prolonging circulation.

Among various approaches to reduce NP-protein interactions, the most widely used is PEGylation. Coating the NP surface with hydrophilic PEG reduces protein adsorption through hydrophilicity and steric repulsion, decreasing MPS clearance. Many PEGylated drug formulations have been

approved for clinical use or are under clinical investigation. This strategy extends to polymeric peptide and protein delivery as well. For example, Lim et al. designed a long circulating PEG-poly(L-lysine)(-grafted 2,3 dimethyl maleic anhydride)-poly(lactic acid) triblock copolymer to co-deliver pro-apoptotic peptide D-$(KLAKLAK)_2$ and chemo-drug doxorubicin (DOX) to KB tumors *in vivo*.[3]

Although PEGylation has been extensively used over the past decades, many issues have also arisen. Critically, PEGylated peptide-polymer conjugates can raise anti-PEG antibodies, which result in increased drug clearance, hypersensitivity responses, and reduced efficacy.[4] Preclinical work has also shown that peptide-polymer conjugates with immunogenic peptides act as adjuvants to induce anti-PEG antibody reactions. These issues with PEGylation motivated the investigation into alternative biocompatible polymers. Zwitterionic polymers, which contain equal cationic and anionic groups, have garnered increasing attention in the design of long-circulating NPs. With electrostatically-induced hydration and neutral charge, zwitterionic polymers exhibit outstanding resistance to nonspecific protein adsorption. Nanoparticles coated with zwitterionic polymers showed superior biocompatibility, prolonged blood circulation time, and negligible immune response.[5] Wang et al. incorporated zwitterionic properties in their dendrimer platform for controlled release of insulin in mice (**Figure 3.2**). The authors developed a Janus dendrimer system consisting of two distinct dendrons with protein binding and protein repelling properties, respectively.[6] The protein-binding dendron was tethered with a combination of charged and hydrophobic moieties, which drove self-assembly into the core of the nanocarrier. The second dendron was modified with zwitterionic molecules to form a highly hydrophilic and anti-fouling surface that prevented protein adsorption. Compared to PEGylated nanocarriers, the zwitterionic nanocarriers greatly prolonged the *in vivo* pharmacokinetic profiles.

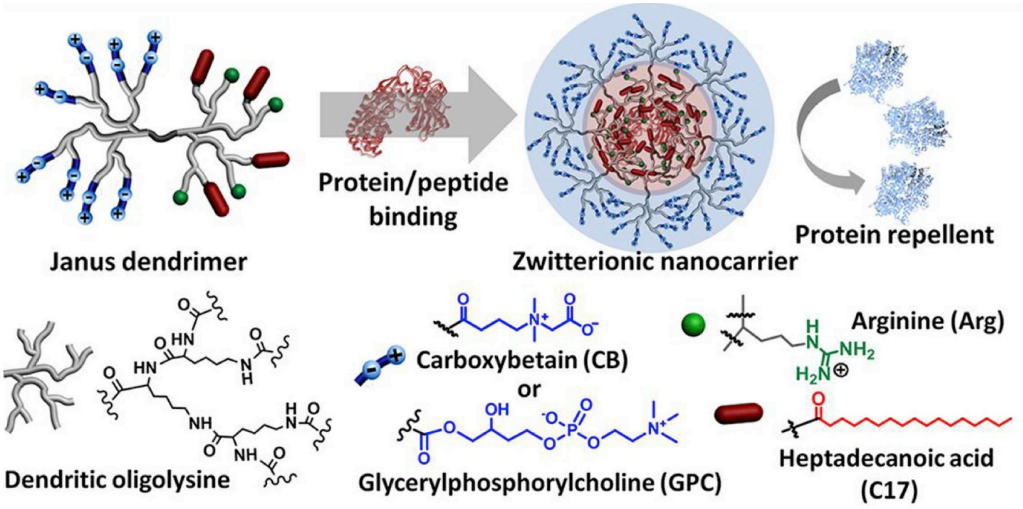

Figure 3.2. Schematic representation of the chemical structure of zwitterionic Janus dendrimer with the protein binding and antifouling features. Reprinted with permission from ref[6]. Copyright 2019 Elsevier.

Another strategy to improve the *in vivo* residence time of NPs is to modify the NP surface with 'self' markers that prevent normal cells from activating the MPS. For example, coating NPs with cell membranes in a camouflage approach endows NPs with antigenic diversity and biological benefits. Red blood cell (RBC) membranes are loaded with abundant self-markers (*e.g.*, CD47), which can help NPs escape recognition from the immune system. As such, RBC-membrane coating of NPs is a powerful strategy to extend blood circulation time and minimize immune response. Currently, only a few membrane-coated polymeric NPs have been reported for anti-cancer peptide delivery. In one study, Guo et al. developed erythrocyte-membrane coated PLGA-nanoparticles for antigenic peptide delivery.[7] A mannose-inserted membrane structure was constructed to actively target APCs in the lymphatic organ, and redox-sensitive peptide-conjugated PLGA nanoparticles were fabricated to facilitate intracellular peptide cleavage release. The nano-vaccine enhanced *in vitro* cell uptake and potentiated an antigen-depot effect *in vivo*, promoting retention in draining lymph nodes. In addition to membrane coatings, albumin and CD47 peptide can also be displayed to prolong blood circulation of NPs.

Surface charge is another important parameter that affects a nanomedicine's stealth property during circulation. Highly positively (ζ-potential $\approx +40$ mV) or negatively (ζ-potential ≈ -40 mV) charged particles are rapidly cleared from the bloodstream by the MPS and thus have very short

circulation times compared to neutral nanocarriers (ζ-potential ≈ ±10 mV). In addition, uncharged or slightly neutral particles can easily diffuse through tumors, while those with highly positive or negative charges are inevitably trapped by the electrostatic band pass formed by the dense extracellular matrix. Therefore, it is favorable to design polymeric NPs with neutral or slightly negative surface charge. While dense hydrophilic coatings and neutral surface charge provide better NP circulation and enhance NP retention in the tumor microvasculature, this surface shielding also decreases cellular uptake. Therefore, it is necessary to balance stability and uptake when designing NPs, which is discussed in the next section.

3.2.2 Improve accumulation and cell uptake

Drug activity depends on drug concentration delivered to the target site as well as duration of exposure. For peptide drugs acting on malignant cells or tumor-associated cells, drug efficacy is contingent on the circulation time (Section 4.2), the extent of extravasation at the tumor, tumor penetration and retention, and, for peptides with intracellular targets, cellular uptake and subsequent intracellular trafficking. The target site for peptide vaccines are the dendritic cells in the lymph nodes, where tumor antigen presentation and resulting anti-tumor immunity is coordinated. In addition to providing increased circulation time and stability to peptide therapeutics, polymer delivery systems can facilitate tumor or lymph node delivery and cell internalization.

3.2.2.1. Tumor accumulation and penetration

After peripheral administration, peptides and peptide-loaded polymers enter the tumor tissue from the circulation through either paracellular transport between endothelial cells or transcellular transport through endothelial cells. The tumor vasculature has been reported to be leakier than normal vasculature due to intercellular gaps between endothelial cells, incomplete basement membrane, and a paucity of smooth muscle cells.[8,9] As a result, nano-sized carriers can accumulate preferentially at solid tumors that possess leaky vasculature. This enhanced permeability and retention (EPR) principle is one of the key concepts for cancer nanotechnology; carriers with a hydrodynamic diameter larger than ~20 nm avoid rapid kidney filtration and carriers smaller than the tumor-dependent inter-endothelial spacing can extravasate into the tumor tissue.[10,11] Thus, polymeric carriers for solid tumors have generally been designed to have hydrophilic shielding

and range in size between 20-200 nm in diameter.[12] These design principles have been applied to polymeric formulations for tumor delivery of peptides in murine cancer models.[13-15] However, the broad relevance of EPR-based tumor delivery for clinical nanomedicines is the subject of significant discussion and debate.[16,17] Many nanomedicines that perform well in animal models have not translated to clinical success.[18] A broad analysis of tumor accumulation by nanoparticle formulations revealed that a median 0.7% injected dose is delivered to the solid tumor across varying materials, size, charge, and tumor models.[19] However, a recent study reveals some drawbacks to analyzing tumor delivery using the % injected dose metric and calls for more extensive meta-analyses before conclusions can be drawn.[20]

Transcytosis of delivery carriers through the tumor endothelium has recently emerged as a potential mechanism for tumor delivery that does not rely on the EPR effect. The Shen and Gu groups recently described a polymer-drug conjugate that is converted by γ-glutamyl transpeptidase, a membrane-bound enzyme expressed on endothelial cells and tumor cells near the vasculature, from a long-circulating zwitterionic form to a polycation. The cationic polymer is then internalized by caveolae-mediated endocytosis and transcytosed. Tumor accumulation and penetration is increased by the γ-glutamyl transpeptidase-responsive polymer compared to control polymers, and resulted in increased anti-tumor efficacy when used for camptothecin chemotherapy delivery. Polymer carriers that facilitate transcytosis through the tumor endothelium for peptide therapeutics is therefore an exciting future area of research.[21]

Peptide therapeutics that act directly on tumor cells without bystander effect require effective penetration through the solid tumor. Studies in mice using model particles with defined sizes revealed that systemically-delivered particles with diameters ~30-50 nm result in the highest tumor accumulation compared to bigger or smaller particles; ultra-small particles (<20 nm) are rapidly eliminated by diffusing back into the blood or removed via lymphatic vessels, while larger particles have restricted tumor penetration due to their size.[22,23] The size limitation of polymeric delivery systems relying on diffusion for tumor penetration therefore have limited loading capacity for peptide drugs and emphasizes the need for potent peptides. Alternatively, external stimuli such as light have been used to increase tumor penetration of responsive polymer systems. For example, tumor penetration and delivery of a lytic melittin peptide was enhanced by complexing the peptide

with a porphyrin derivative before functionalization with hyaluronic acid polymer. Laser irradiation increased tumor penetration and reduced tumor growth.[14] With a similar design, Jia et al. developed a nanocomplex of a cytolytic peptide, melittin, an NIR-absorbing molecule, cypate, and a tumor-targeting polymer, HA to overcome the size paradox of nanomedicines (**Figure 3.3**).[24] At pH 7.4, the complexes were negatively charged nanospheres (~50 nm), which were suitable for long-term systemic circulation. When these nanospheres actively targeted tumors, the weakly acidic tumor microenvironment triggered an *in situ* transformation of the nanospheres to net-like nanofibers. Compared with the nanospheres, the nanofibers not only exhibited an inhibitory effect on tumor cell mobility, but also significantly prolonged the tumor retention time. Moreover, the nanofibers could be photodegraded into smaller nanospheres (~25 nm) by irradiation, which enabled deep tumor penetration of the loaded melittin and effective tumor eradication.

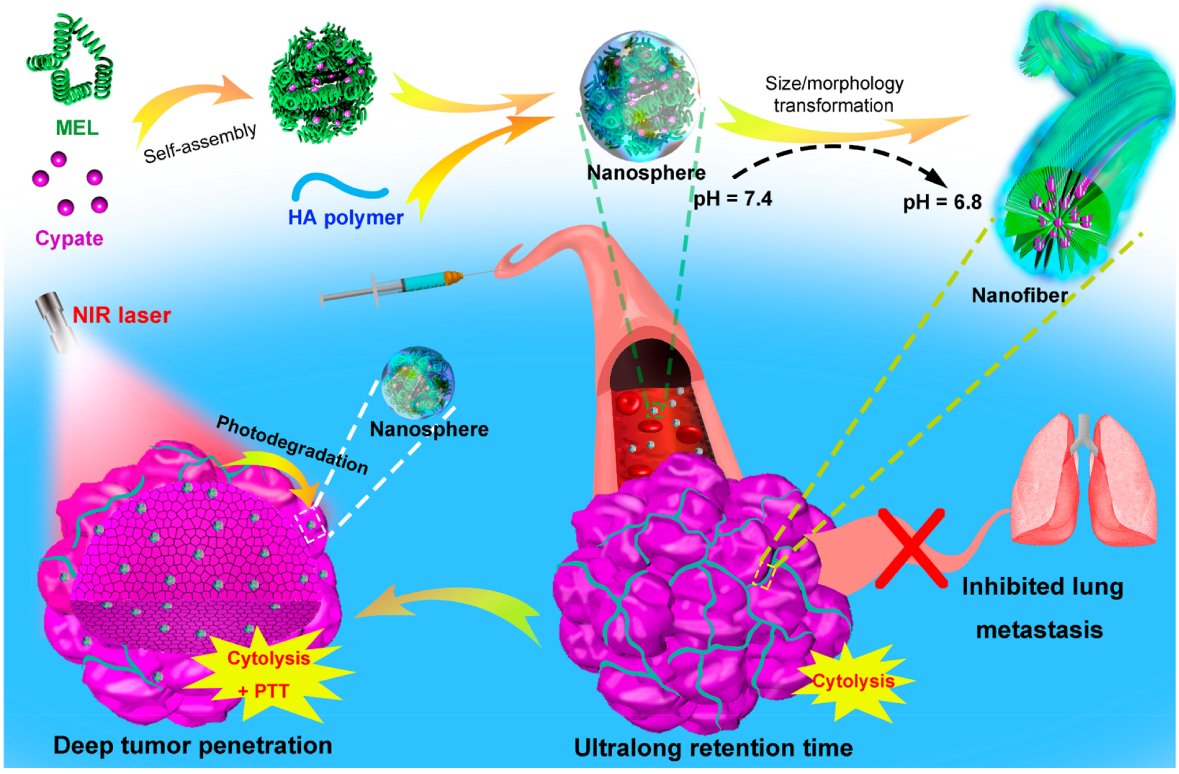

Figure 3.3: Schematic representation of the fabrication of melittin/Cypate@HA complexes and their mechanism for tumor accumulation/penetration. Reprinted with permission from ref[24]. Copyright 2019 American Chemical Society.

A recent publication from the Chan group reports that the majority of nanoparticles delivered to tumors are either in the extracellular matrix or internalized by tumor-associated macrophage near the vasculature.[25] Two major implications for peptide therapeutics from this work are: first, tumor-associated macrophages are an attractive, druggable target cell for peptide therapeutics, and second, tumor-responsive delivery systems that minimize phagocytic internalization during circulation and extravasation but can mediate cell internalization after tumor penetration are needed for tumor cell delivery.[26,27]

3.2.2.2. Cell uptake

Due to their large size that precludes diffusion through the cell membrane, peptide drugs or nano-sized carriers are typically internalized into cells through energy-mediated, vesicular transport. Endocytosis of peptides or peptide-loaded carriers is induced by interaction with the cell surface either through non-specific charge interactions or through specific ligand-receptor interactions. To increase specificity of uptake, several research groups have also reported environmentally-responsive polymer systems that induce cellular uptake only in the tumor microenvironment.

3.2.2.2.1. Charge-mediated uptake

Cationic carriers interact electrostatically with anionic cell membranes to trigger internalization. Primary and secondary amines are often used to impart charge. For example, mixed polymer micelles formed by assembly of PEG-modified PCL, PEI-modified PCL, and loaded with peptide antigens are efficiently internalized through charge interactions by DCs.[28] Polymers functionalized with guanidinium groups are also readily internalized by cells.[29,30] Polynorbornene-based backbones functionalized with diguanidines and peptide antigens are rapidly internalized by monocytes, demonstrating potential as peptide vaccine carriers. However, cationic carriers can be internalized non-specifically and therefore typically require localized administration.

3.2.2.2.2. Receptor-mediated uptake

Cell entry of drugs and drug carriers mediated by ligand-receptor interactions is called “active targeting.” Several studies using both polymeric and lipid nanoparticles reveal that active targeting of PEGylated, long-circulating particles does not affect overall particle biodistribution in rodent tumor models.[31-33] However, while overall dose to tumor is not increased, actively-targeted carriers

are internalized more by cancer cells and can therefore still be beneficial, especially for intracellular delivery of biologic drugs.[34]

Ligand classes utilized for active targeting include small molecules, peptides, aptamers, polysaccharides, and proteins such as antibodies.[35] An example of a small molecule ligand frequently used for peptide vaccine delivery is mannose, which binds to mannose receptor, CD206, a highly expressed receptor on dendritic cells and other antigen-presenting cells. Mannose functionalization of several polymeric carriers has increased peptide antigen delivery *in vivo* to dendritic cells, resulting in improved anti-tumor efficacy compared to control, untargeted polymers. [7,36-39] In one notable case, mannose-functionalized PLGA particles were loaded with cancer antigen peptides and two Toll-like receptor (TLR) agonists. Compared to non-targeted particles, mannose-functionalized particles accumulated more in lymph nodes and were more effective in increasing survival and reducing tumor growth rate (**Figure 3.4**).[40]

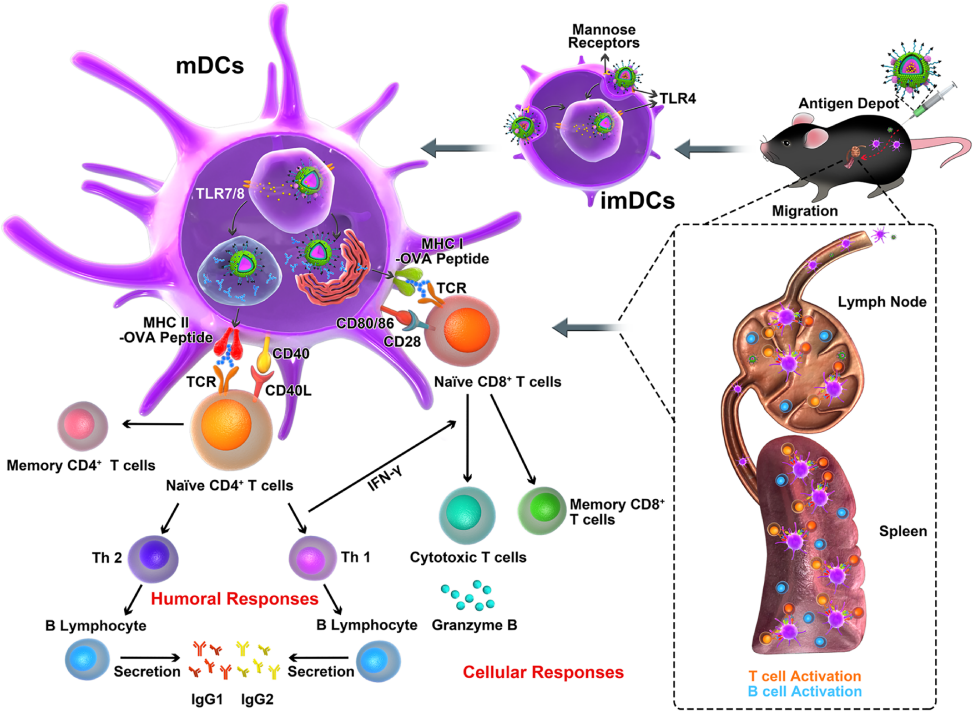

Figure 3.4: Illustration of the targeted co-delivery of an antigen and dual agonists by mannose targeting NPs. Reprinted with permission from ref[40]. Copyright 2019 American Chemical Society.

Peptides applied for targeting include cell penetrating peptides (which primarily interact with cell surfaces via charge) and receptor-binding peptides. The reader is referred to other recent excellent

reviews summarizing targeting peptides for cancer applications.[41,42] In one example, the multivalency afforded by polymer systems was used to increase the effectiveness of an IL-4-targeting peptide for delivery of a polymer-peptide conjugate for cancer cell killing.[43]

Another commonly used class of peptide ligands is polysaccharides, which bind to receptors with lectin-like domains. Hyaluronic acid, an anionic glycosaminoglycan, is used to provide both prolonged circulation to nanoparticles as well as targeting and uptake in cancer cells over-expressing CD44. β-Glucans are found in certain bacteria, as well as certain cereals and fungi, and have been used in peptide antigen delivery to both target and activate antigen presenting cells.[44]

Finally, proteins and antibodies provide high specificity for receptor targets, although production costs are usually higher than the aforementioned methods.[45,46] Cruz et al. used PLGA nanoparticles modified with various antibodies against dendritic cell receptors (CD40, DEC-205, and CD11c) and concluded that CD40 targeting mediated the highest levels of antigen delivery.[47]

3.2.2.2.3. Environment-triggered uptake

The dichotomies between desired nanoparticle inertness during circulation and interaction-mediated cell uptake upon reaching target cells can be reconciled through the design of stimuli-responsive polymers. The extracellular pH in solid tumors is often slightly acidic (pH 6.5-7) due to the production of acidic metabolites and slightly hypoxic (1-2% lower O_2) due to high oxygen demand by rapidly proliferating tumor cells.[48,49] The acidic tumor microenvironment has been used to transform soluble polymers that readily penetrate tumors into self-assembled polymeric nanoparticles that are then internalized by cancer cells. Poly(β-thioester) backbones were decorated with cytotoxic peptide KLA which were then anionized by reversible cis-aconitic anhydride (CAA) modification. In the acidic tumor environment, the CAA capping group is hydrolyzed, resulting in hydrophobic domains that drive polymer self-assembly into nanoparticles that are then internalized by malignant cells (**Figure 3.5**).[50] Chen et al. designed a surface charge-switchable system for codelivery of proapoptotic peptide KLA and p53 plasmid.[51] The charge-switchable PEG-shield (PEG-PLL(DA)) was used to coat the NPs by electrostatic interaction. At the physiological pH 7.4 in the bloodstream, PEG-PLL(DA) could extend the circulating time. After the accumulation at tumor sites, tumor-acidity-triggered charge switch led to the detachment

of PEG-PLL(DA) from the complex, resulting in efficient tumor cell entry by folate-mediated uptake and electrostatic attraction (**Figure 3.6**). Similarly, the hypoxic tumor environment can act as an environmental trigger to (1) enhance nanoparticle accumulation in the tumor *via* targeting moieties against overactivated hypoxia-related enzymes or (2) induce physical or chemical transformation for accelerated drug release.[52] Hypoxia-responsive groups (e.g. nitroimidazoles, nitrobenzyl alcohols, and azo derivatives) are reduced in hypoxic conditions, enhancing nanocarrier hydrophilicity and subsequent drug release. Yeh, et al. coupled copolymers with a hydrophobic p-nitrobenzyl derivative which was catalyzed by overexpressed enzyme nitroreductase, liberating amino groups in the polymer side chains for enhanced drug release.[53] The nanocarriers selectively released its drug cargo doxorubicin under hypoxic conditions and demonstrated robust anti-tumor efficacy *in vitro* and *in vivo*.

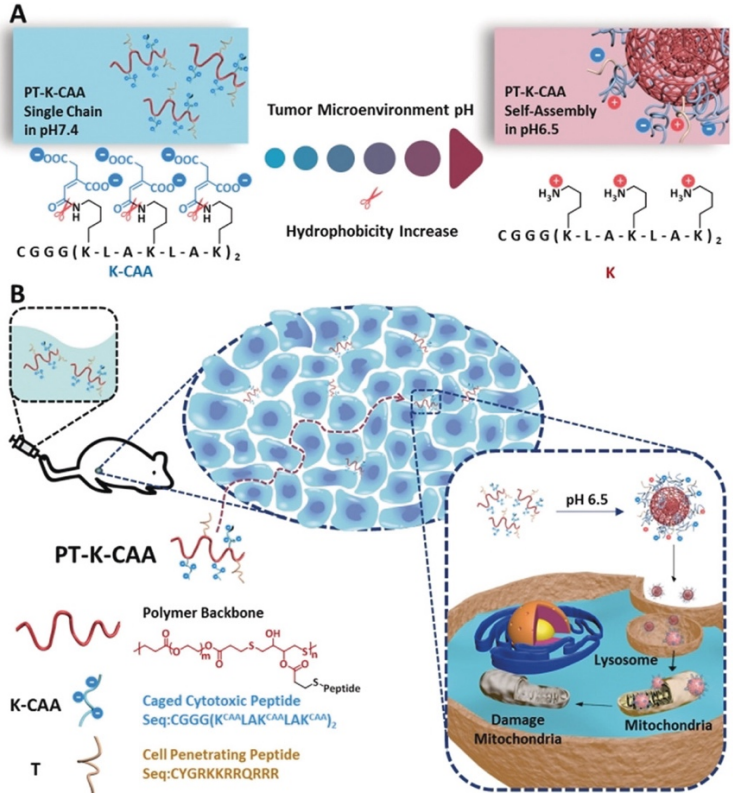

Figure 3.5: Nanoparticles hydrolyze in tumor microenvironment to increase cellular internalization. (A) Process of PT-K-CAA hydrolysis, which leads to its self-assembly. (B) Process for the penetration of PT-K-CAA in the tumor microenvironment. Reprinted with permission from ref[50]. Copyright 2019 Wiley-VCH GmbH & Co. KGaA.

Extracellular enzymes upregulated in the tumor microenvironment such as MMP-2 have also been exploited to trigger polymer switching to achieve tumor-selective accumulation and penetration, controlled drug release, and intracellular delivery. Polymers have been conjugated to MMP-sensitive PEG for prolonged blood circulation, followed by PEG de-shielding to expose peptides that then facilitate cancer cell uptake and delivery of proapoptotic peptides (Figure 4.7).[54,55] Incorporation of enzyme-cleavable linkers or sequences can also trigger site-specific drug release. MMP-2 disrupted a peptide-based hydrogel for release of anticancer peptide G3 specifically in the presence of HeLa cancer cells.[56] Kern, et al. incorporated a cathepsin-B cleavable linker to facilitate intracellular peptide release specifically in the endosome (section 4.1.2). Comprehensive reviews of protease-activated prodrugs and polymer systems can be found here.[57,58]

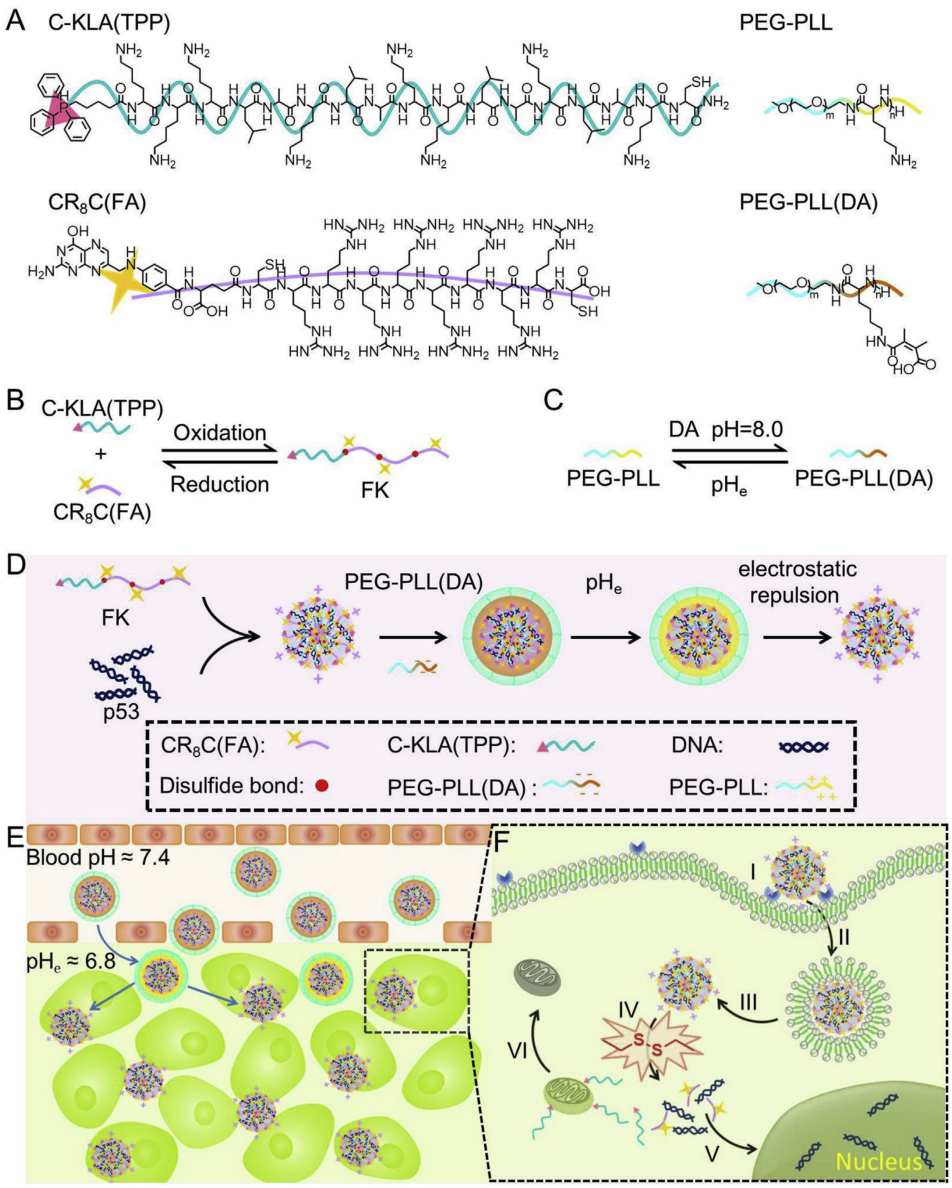

Figure 3.6 Design of a surface charge-switchable system for codelivery of proapoptotic peptide KLA and p53 plasmid: (A) Chemical structures of polymers and peptides. (B) Schematic illustration of the formation of reductive polypeptide. (C) Schematic illustration of charge-switchable PEG-PLL(DA). (D) Preparation of complex. (E) Illustration of the stealth property and accumulated in tumor. (F) Illustration of the KLA peptide and p53 complexes mediated cancer therapy. Reprinted with permission from ref[51]. Copyright 2015 Elsevier.

External stimuli can also be applied to trigger polymer conversion, achieving higher spatiotemporal control over drug release. Poly(β-thioester)s conjugated to cell penetrating and

cytotoxic peptides were modified with indocyanine green, a near-infrared dye. Tumor irradiation using a laser results in localized heating via indocyanine green, that then induce self-assembly of polymers into nanoparticles for cell internalization.[59] In another example, combination treatment of NIR irradiation for triggered release of an anti-PD-1 peptide stimulated an anti-tumor response against primary and distal tumors and significantly prolonged survival in mice.[60]

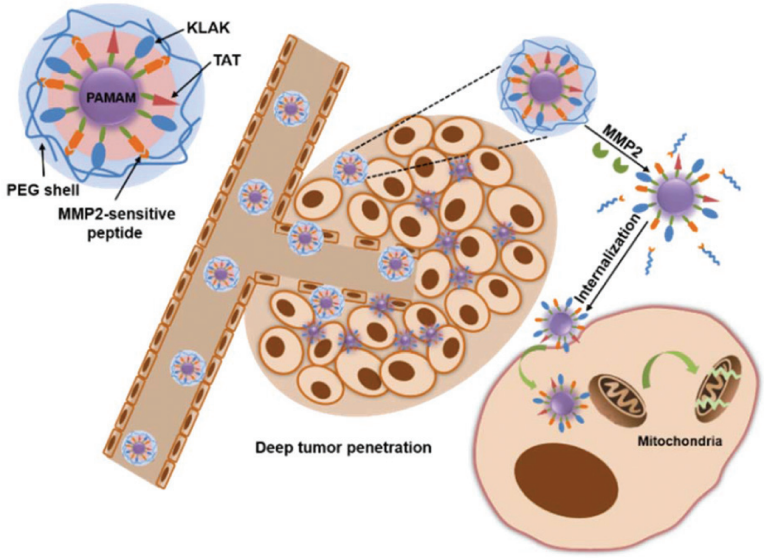

Figure 3.7: Peptide-PAMAM conjugate with MMP2-sensitive PEG and the cell-penetrating moiety TAT for efficient tumor penetration, cellular internalization and mitochondria disruption. Reprinted with permission from ref[54]. Copyright 2018 Royal Society of Chemistry.

3.2.3 Strategies to facilitate cytosolic delivery of peptides

The efficacy of biologic therapeutics with intracellular targets hinges on sufficient delivery to the desired destination. To maximize efficacy and minimize side effects, drug carriers need to successfully navigate to (1) the disease tissue, (2) relevant disease cells, and (3) appropriate intracellular targets. However, cells employ a natural defense to neutralize and eliminate foreign particles. Following endocytic uptake, cells trap foreign matter in endosomes and sort them for lysosomal degradation, rendering them inactive and barring delivery to the appropriate intracellular target.[61] Ultimately, many peptides with promising potential *in vitro* cannot be translated *in vivo* due to low bioavailability, critically hampering their therapeutic impact.[62] As such, it is vital to design delivery vehicles that can escape the endocytic pathway and deliver their cargo to the desired intracellular target.

As previously discussed, peptides suffer from poor serum stability and protease degradation. Upon cellular internalization, the proteolytic enzymes in endolysosomes also degrade peptide cargo.[62] Additionally, the endosomal membrane bars cytosolic peptide delivery, as the size and hydrophilic nature of peptide therapeutics limits their permeation and transport across lipophilic membranes. One proposed strategy to escape the endosome is to employ CPPs that penetrate the plasma membrane to deliver of a range of therapeutic cargos (*e.g.*, peptides, proteins, nucleic acids). It was later realized that the majority of CPPs were eventually targeted to the endosome or ejected from the cell.[62-64] Furthermore, CPP conjugation accelerated blood clearance due to the highly cationic charges. Thus, nanoscale biomaterials are often employed to overcome the endosomal escape challenge.

When designing polymer biomaterials for intracellular peptide delivery, inspiration can be derived from viral or bacterial pathogens that efficiently penetrate the host membrane for replication. Enveloped viruses access the cell cytosol and transfect cells by a membrane fusion mechanism, while non-enveloped viruses escape endolysosomal compartments via pore formation or membrane disruption mechanisms.[64] Similar to viruses, bacteria have evolved mechanisms to translocate from the endosome to the cytosol. Peptide endotoxins predominately form pores in the endosomal membrane, and can even do so in a pH-sensitive manner, whereby peptides adopt a random coil structure at pH 7.4 but transition to an amphipathic alpha-helical conformation that creates pores in the membrane of acidic endosomes. These mechanisms can be exploited to design smart polymeric carriers that surmount the endosomal barrier and improve intracellular delivery. Here, we will discuss polymers that employ four key strategies to facilitate endosomal escape for cytosolic cargo delivery: (1) the proton sponge effect, (2) pore formation, (3), membrane fusion, and (4) triggered response to external stimuli (**Figure 3.8**).

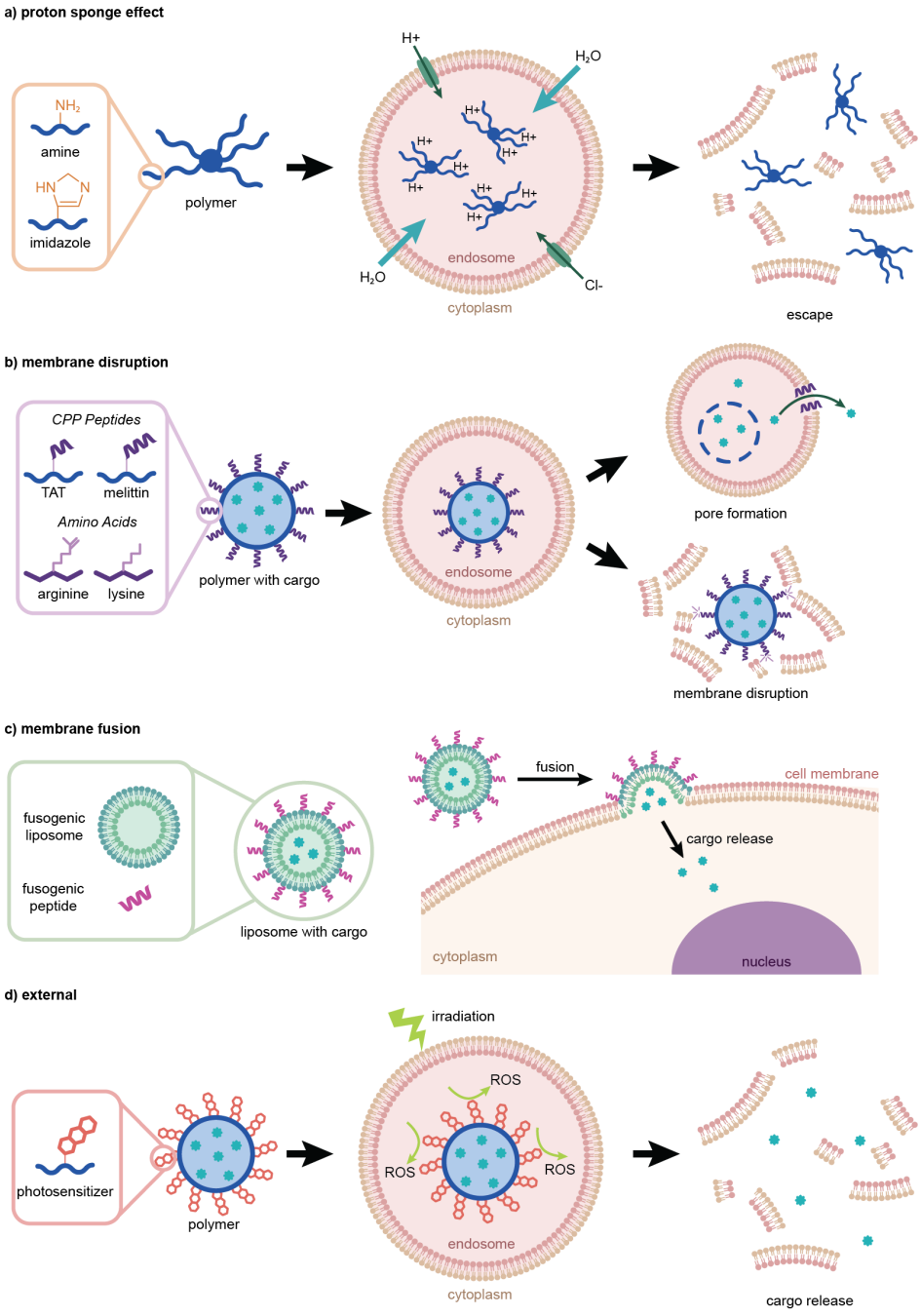

Figure 3.8. Mechanisms of endosomal escape. (A) Polymers can exploit the proton sponge effect through incorporation of chemical groups (e.g., amines, imidazoles) to trigger an influx of ions and water to burst the endosome. (B) Carriers can be equipped with peptides (e.g., CPPs) to form pores in or disrupt the endosomal membrane, facilitating cargo release into the cytosol. (C) While primarily employed by lipid-based carriers, fusion with the cell membrane can mediate cytosolic

cargo delivery while bypassing the endosome. This can be achieved with fusogenic peptides or coatings. (D) External stimuli, such as light irradiation, can trigger endosomal disruption to release cargo into the cytosol.

3.2.3.1 Proton sponge effect

The proton sponge effect hypothesizes that agents with high buffering capacity can induce endosomal rupture and subsequent release of entrapped components.[64,65] Specifically, protonation of amine groups triggers an influx of protons and chloride ions, resulting in osmotic swelling and endosomal bursting. A comparative study found that endosomal size and leakiness inversely correlates with escape capacity: small endosomes are more easily ruptured by the proton sponge effect compared with larger endosomes, and leakier endosomes are less able to be burst, as endosomal leakiness prevents sufficient osmotic pressure buildup to induce rupture.[66]

In addition to polymer composition, the architecture and rigidity of the cationic polymer chains affect the mechanism of endosomal escape.[67] Super-resolution imaging of intracellular polyplexes revealed that highly branched, rigid polymers are extremely effective in inducing osmotic swelling and endosomal escape. Similarly, length and density of surface oligoarginine modifications influenced endocytic pathway and subsequent intracellular sorting.[68] Particles modified with shorter oligoarginine chains were quickly sorted for lysosomal degradation, whereas particles with longer chains were able to reach the late endosome and cytosol. While cationic biomaterials are primarily used to facilitate endosomal escape for nucleic acids, lessons from these systems can be applied for peptide delivery.

PEI, with its high density of primary, secondary and tertiary amines, best demonstrates the proton sponge effect.[69,70] Together, the amine groups of PEI result in a high buffering capacity between pH 8-10 (maximum) and pH 4-7 (second maximum). At physiological conditions, about 50-55% of the PEI amine groups are protonated. Upon endosomal internalization of PEI complexes, additional amine groups protonate in the acidic endosomal/lysosomal environments, eventually mediating endosomal release through the proton sponge effect.

PEI has been extensively utilized in anti-cancer vaccine formulations. Li et. al. employed polymeric hybrid micelles (PHMs) to generate a robust anti-cancer immune response in mice.[28] The PHMs were composed of polycaprolactone (PCL)-PEI and PCL-polyethyleneglycol (PEG) diblocks and co-delivered peptide antigen and adjuvant (oligodeoxynucleotide CpG). Trp2 is a peptide residue of the Trp2 protein, a tumor-associated antigen. The authors sought to activate T cells to recognize and eliminate Trp2-expressing cells. Optimization of the PCL-PEI proportion in PHMs (< 10%) balanced CpG condensation, toxicity, dendritic cell (DC) uptake, and lymph node accumulation and migration. Together, this system elicited an antigen-specific cytotoxic T cell (CTL) response against Trp2 peptide, inhibiting tumor growth. Investigation of dermal irritation at the injection site revealed comparable irritation to saline injection, suggesting that the PHM is biocompatible. In another vaccine system, Rajendrakumar et al. formulated nanocomplexes containing poly(sorbitol)-*co*-PEI (PSPEI) complexed with tumor lysate protein and adjuvant poly I:C (PSPEI-PAA).[15] In a B16F10 subcutaneous model, PSPEI-PAA showed high DC uptake in lymph nodes, and increased tumor infiltration by CTLs. Ultimately, CTLs in PSPEI-PAA-treated mice demonstrated an enhanced killing effect toward tumor cells, significantly inhibiting tumor growth. These examples demonstrate the efficiency of PEI in mediating endosomal escape for subsequent MHC loading in anti-cancer vaccines.

Recently, fluoroamphiphiles have emerged as promising carriers for cytosolic cargo delivery, as they benefit from high uptake and endosomal escape, and possess excellent self-assembly properties.[71,72] Zhang et al. grafted PEI with fluoroalkanes and demonstrated efficient cytosolic delivery of proteins and peptides with varying size and charge (**Figure 3.9**).[73] Compared to materials modified with alkanes or cycloalkanes, fluorination improved protein/peptide encapsulation and cellular uptake while limiting toxicity. Generally, longer fluoroalkyl chains and higher fluorination improves gene delivery, but for protein/peptide delivery, this is not always the case, as these properties could also result in poor protein encapsulation. Thus, the authors demonstrated that the length of the fluoroalkyl chain and degree of fluorination need to be optimized prior to use.

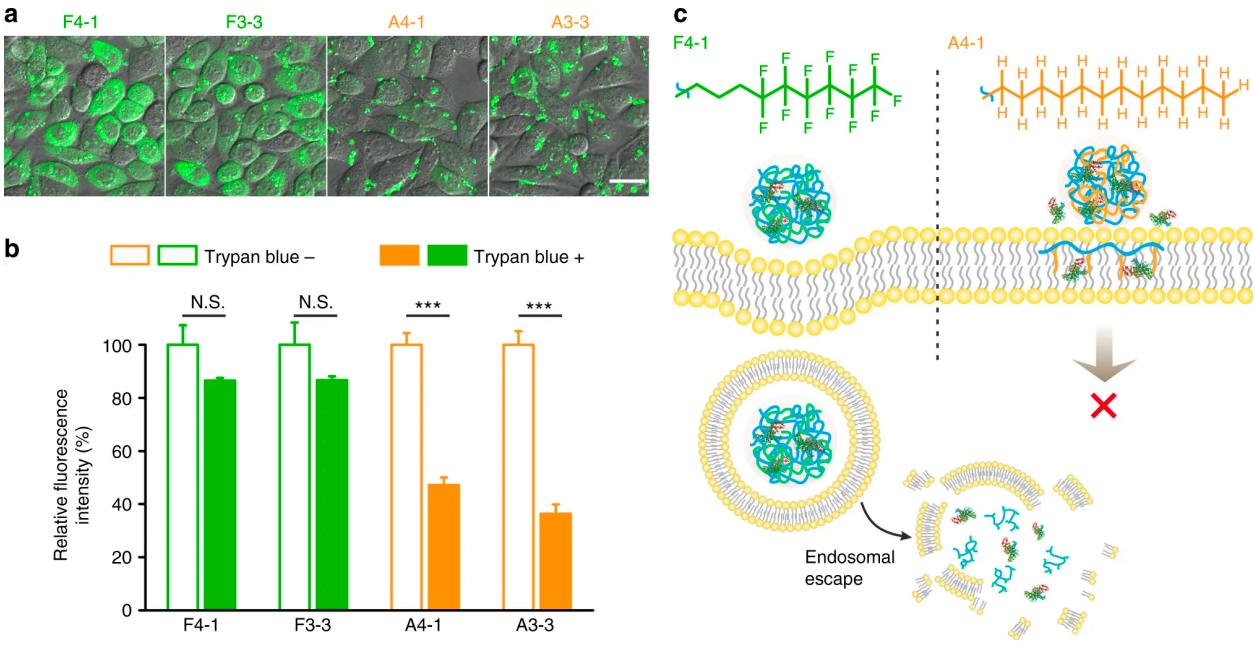

Figure 3.9: Fluorination of polymers to mediate cytosolic protein delivery. PEI was grafted with fluoroalkanes to facilitate protein/peptide encapsulation and endosomal escape. Longer fluoroalkyl chains and higher fluorination enhanced delivery. Reprinted with permission ref[73]. Copyright 2018 Royal Society of Chemistry.

PBAEs are another class of cationic polymers often utilized to facilitate cytosolic delivery *via* the proton sponge effect.[74] Due to the polyamine nature of these polymers, they lend themselves well toward endosomal buffering. Furthermore, with lower charge density, they are typically less toxic than their PEI and poly(L-lysine) counterparts. Qiao et al. utilized PBAE copolymers for targeted peptide and acid-triggered drug release to breast cancer tumors.[75] PEG-grafted PBAEs were loaded with a cyclopeptide RA-V and a NIR fluorescent probe. At acidic pH, the tertiary amines of PBAE were protonated, inducing dissociation of the polymer and release of its cargo. Confocal microscopy confirmed that following cell uptake, the micelles co-localized with lysosomes; the subsequent endosomal drop in pH released the peptide, which then accessed the cytosol, destroyed cell mitochondria, and induced cell death. When injected into MCF-7 tumor bearing mice, the micelles exhibited an effective anti-tumor ability. In a similar platform, Qiao et al. formulated PBAE micelles to co-deliver the cytotoxic peptide $(KLAKLAK)_2$ and the chemotherapeutic doxorubicin to MCF-7 tumors.[76] The enhanced cancer-killing effect of these micelles was attributed to the efficient internalization into cells, lysosomal escape (mediated by the proton

sponge effect due to incorporation of PBAE), and disruption of mitochondria in cells. This PBAE platform was also used to deliver another chemotherapeutic, docetaxel, with dual-targeted pro-apoptotic peptide $CGKRK_D(KLAKLAK)_2$.[77] The combinatorial delivery of peptide and chemotherapeutic cargos displayed a synergistic anti-tumor effect.

Poly(dimethylaminoethyl methacrylate) (PDMEAMA) is a polyolefin that contains only tertiary amines and can be easily synthesized via RDRP with varying molecular weights and architectures.[78] PDMAEMA has been applied for peptide and protein delivery.[79] Toyoda et al. used PDMAEMA-based nanogels loaded with antigen peptide hgp-$100_{25\text{-}33}$ to vaccinate mice against melanoma, resulting in reduced tumor growth compared to free peptide controls.[80]

PC7A is a similar polymer to PDMAEMA, containing tertiary amines that can buffer acidic pH to facilitate endosomal escape. PC7A has been reported to activate the stimulator of interferon genes (STING), lending itself as a potent adjuvant for cancer applications.[81] Luo et al. synthesized PC7A nano-vaccines to boost systemic anti-tumor T cell responses in mice.[81,82] These ultra-pH-sensitive micelles were loaded with ovalbumin and the resulting CTL response was evaluated. The PC7A micelles demonstrated enhanced cross-presentation over control groups, suggesting improved endosomal disruption and antigen transport from the endosome to the cytosol and ER for subsequent MHC loading. Combinatorial treatment with radiation therapy significantly enhanced therapeutic response in both primary and distal tumors.

In addition to polymers containing tertiary amines or weak acids, polymers whose side chains have buffering capacity at mildly acidic conditions can induce the proton sponge effect and subsequent endosomal escape.[83] Lim et al. employed a pH-sensitive triblock polymer co-loaded with a pro-apoptotic peptide and an anti-cancer chemotherapeutic for combination cancer therapy.[84] The polymer carrier comprised poly(ethylene glycol)-poly(L-lysine)(-grafted 2,3 dimethyl maleic anhydride)-poly(lactic acid) (PEG-PLL(-*g*-DMA)-PLA) and was complexed with the pro-apoptotic peptide D-$(KLAKLAK)_2$ via electrostatic interactions. Upon endosomal internalization and acidification, the amide bond between the DMA and PLL was cleaved, exposing the amine residues on PLL and triggering the proton sponge effect and endolysosomal destabilization. The acidic environment also prompted the release of the pro-apoptotic peptide, which subsequently

interacted with the mitochondrial membrane, inducing cell death. Incorporation of chemotherapeutic Doxorubicin enhanced nanoparticle cytotoxicity and anti-cancer efficacy. This platform successfully inhibited tumor growth in a KB tumor-bearing nude mice after two intravenous administrations.

Despite demonstrated cytosolic delivery, controversy remains regarding the proton sponge effect. A comprehensive review of the evidence supporting and denouncing the theory has been published.[85] Some works report that the osmotic pressure and membrane swelling within the endosome is insufficient to disrupt membrane integrity.[86] Additionally, not all polymers that buffer within the endosomal range can induce endosomal escape.[87] In regards to PEI, Benjaminson et al. demonstrated that PEI did not affect lysosomal pH, further discounting the proton sponge hypothesis.[88] This controversy emphasizes the need for a better understanding of cellular transport processes and how different materials can be used to manipulate these pathways.

3.2.3.2 Anionic membrane-destabilizing polymers

Certain anionic, carboxylated polymers can destabilize membrane bilayers in a pH-sensitive manner and have therefore been applied to facilitate cytosolic delivery of cargos.[89,90] When deprotonated, these polymers are hydrophilic coils, and upon protonation in acidic environments, collapse into a hydrophobic globule state. Qiu et al. synthesized nano-vaccines from PAA, an amphiphilic polyanion with pH-dependent membrane destabilizing activity, to enhance peptide-antigen presentation in DCs, ultimately prolonging survival, enhancing $CD8^+$ T cell activation, and reducing metastatic lesions in mice.[91] The conformation change of pPAA at physiological and acidic pH facilitated endosomal escape, as it switched from a hydrophilic, soluble state at pH 7.4 to a hydrophobic, membrane interactive state upon protonation of the carboxylic acid groups at acidic pH. The pPAA nanoplexes were loaded with the peptide-antigen SIINFEKL and the adjuvant α-galactosylceramide (α-GalCer) through facile electrostatic complexation in a "mix and go" approach. Nanoplexes enhanced immunogenicity and intracellular delivery, resulting in increased antigen uptake and presentation, and improved $CD8^+$ T cell activation. In a B16-OVA tumor model in mice, the nanoplexes significantly reduced tumor growth and improved overall survival.

3.2.3.3 Pore formation

Pore formation occurs when the internal membrane tension that enlarges a pore is higher than the line tension that closes the pore.[62] Molecules such as peptides can intercalate with the pore and reduce the line tension, thus creating a pore in the lipid membrane. In particular, CPPs have emerged as promising facilitators for cell entry and endosomal escape.[92] CPPs are short peptides (10-30 AA residues) that are typically cationic, containing arginine and lysine residues, or amphipathic, consisting of hydrophobic and hydrophilic residues. However, CPPs lack cell specificity, as they can translocate through the plasma membrane of many different cell types, resulting in high off-target toxicity.[93] To address this, CPPs can be anchored to targeting moieties that facilitate specific recognition of target tissues and cells. As with chemical side groups in polymers that induce the proton sponge effect, different amino acids in CPPs can bring exogenous molecules into cells and enhance their endosomal escape behavior.[94] A variety of CPPs, such as melittin and TAT, have been utilized in polymer delivery systems in order to facilitate cell entry and/or endosomal escape.

Melittin, the lytic peptide in bee venom, has been extensively used in cancer applications as a therapeutic cargo and/or CPP.[95] However, its clinical translation is impeded by its high non-specific cytotoxicity and hemolytic activity. We overcame this limitation and safely harnessed the lytic activity of this peptide by engineering triggered display of melittin using a virus-inspired polymer for endosomal release (VIPER) (**Figure 3.10**).[96] VIPER consists of a (1) cationic block, comprising PDMAEMA and poly(oligo(ethylene glycol) monomethyl ether methacrylate (POEGMA) and (2) a pH-sensitive block, comprising poly(2-diisopropylaminoethyl methacrylate) (PDIPAMA) and poly(pyridyl disulfide ethyl methacrylate) (PPDSEMA). Melittin is conjugated to the second block by disulfide exchange with PPDSEMA and DIPAMA a sharp phase transition from hydrophobic to hydrophilic at pH 6.3. Together, this platform shielded melittin at physiological pH 7.4, but upon cellular internalization and endosomal acidification, melittin was unveiled and facilitated endosomal disruption of the endolysosomal membrane. Screening a library of lytic peptides conjugated to VIPER revealed that lytic behavior alone is insufficient to facilitate gene delivery, as only certain peptides were able to promote endosomal escape.[97]

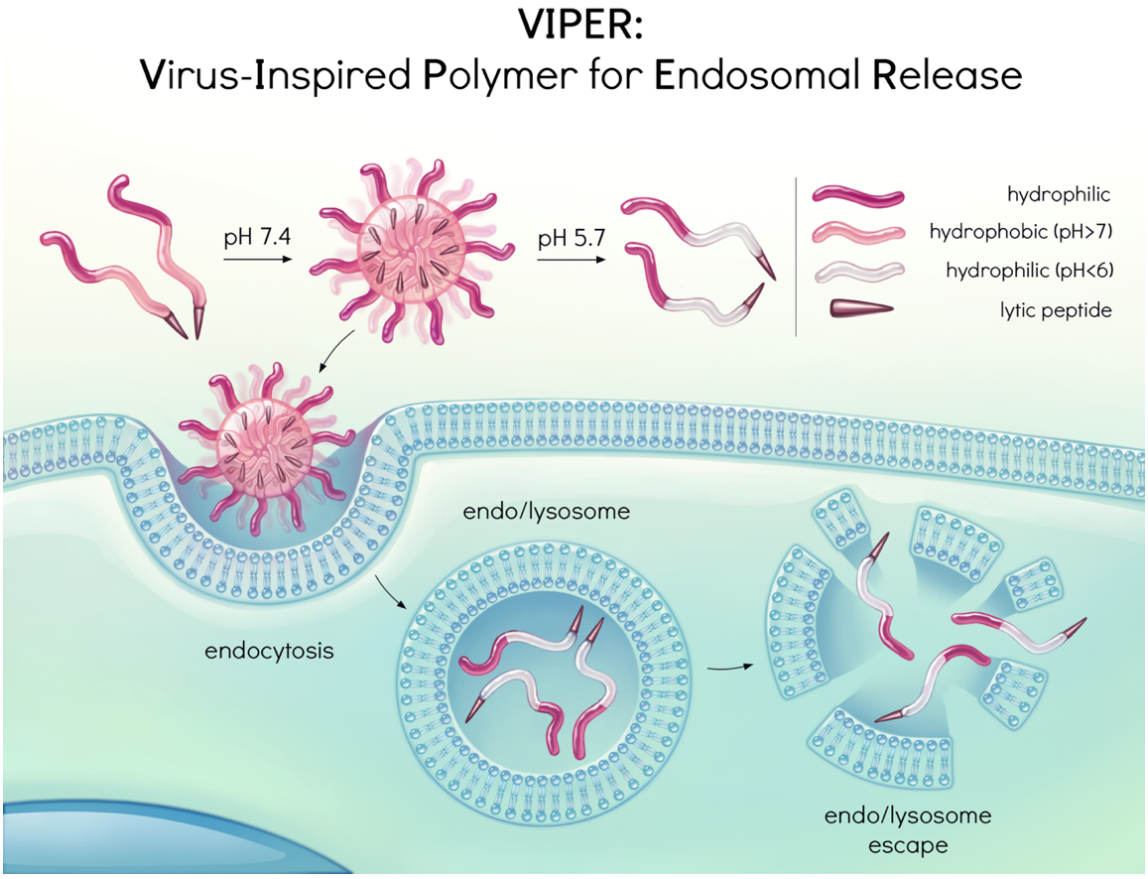

Figure 3.10: Lytic peptides to mediate endosomal escape. CPPs, such a melittin, are commonly employed to disrupt the endosomal membrane to facilitate cytosolic cargo delivery. In the VIPER platform, melittin was conjugated to a pH-triggered polymer which shielded the lytic peptide at physiological pH, but exposed it at endosomal pH.

Other CPPs have also been widely utilized to facilitate peptide delivery to cells. Backlund et al. used CPP-based polymer mimics, protein transduction domain mimics (PTDMs), to promote delivery of adjuvant CpG and peptide antigens OVA or SIINFEKL to monocytes and DCs.[29] In comparison to direct peptide-adjuvant conjugation to CPPs, the polymer-based platform facilitated higher uptake by monocytes. This platform successfully induced DC activation and MHC antigen presentation. Overall, this work demonstrated the successful application of PTDMs to stimulate a specific immune response in antigen-presenting cells.

However, it is important to recognize that endosomal lysis alone does not necessarily translate to improved cargo delivery. Lee et al. demonstrated that incorporation of cleavable linkers between the carrier and cargo was necessary to achieve sufficient cytosolic release of a protein cargo.[98] This strategy has enhanced cytosolic delivery of peptides and proteins in gene editing and vaccine applications.[99,100]

3.2.3.4 Cell membrane fusion

Direct fusion of the carrier membrane with cellular plasma membrane facilitates cytosolic delivery in a non-disruptive manner that bypasses the endosome. This can be enabled by fusogenic peptides that fuse with the cellular membrane and allow translocation of carrier contents into the cytosol. For example, hemagglutinin is a fusogenic peptide on viruses that converts from anionic, hydrophilic coil to a hydrophobic helical structure at acidic pH. This new structure enables fusion of the viral membrane with the cellular membrane. Alternatively, lipid coatings can facilitate membrane fusion, as in the case of fusogenic liposomes or extracellular membrane coatings.[101] Here, the lipid bilayers can fuse directly with the cellular plasma membrane to mediate cytosolic delivery. While the following examples may not deliver peptide cargos, lessons learned from these strategies can be broadly applied to a variety of cargos.

Fusogenic peptides can be incorporated onto the surface of nanoparticles to facilitate cytosolic delivery of encapsulated cargo. Several synthetic models derive inspiration from the SNARE protein complex, in which coiled-coil formation of complementary SNARE protein units on opposing membranes drives lipid mixing followed by pore formation and concomitant content transfer. Yang et al. developed an artificial membrane fusion system by embedding coiled-coil lipopeptides into the liposomal and cellular membranes, respectively, enabling targeted fusion.[102] Liposomes were decorated with one lipopeptide (CPK_3), and live cells were modified with the complementary peptide (CPE_3), which enabled spontaneous fusion with modified cells. This system circumvented the endosomal pathways, bypassing the hurdles of endosomal entrapment and degradation. The authors also applied this system to lipid-coated silica nanoparticles and demonstrate cytosolic delivery.[103]

In another example of membrane coatings, the Zhang group coated their nanoparticles with cancer cell membranes for cancer vaccine applications.[104] PLGA nanoparticles were coated with cancer cell membranes, forming cancer cell membrane-coated nanoparticles (CCNPs) that retained antigen functionalization (*e.g.*, glycoprotein 100). The adjuvant monophosphoryl lipid A was incorporated into the CCNPs, which facilitated robust DC maturation and subsequent T activation *in vitro*. Similarly, Yang et al. encapsulated immune-adjuvant nanoparticles with cancer cell membranes modified with mannose.[105] PLGA nanoparticles were (1) loaded with the adjuvant imiquimod, (2) coated with cancer cell membranes, whose surface proteins acted as tumor antigens, and (3) modified with mannose to facilitate targeting of antigen-presenting cells. Together, this vaccine activated DCs in a tumor-type specific manner, resulting in robust $CD8^+$ T cell generation in the spleen and strong anti-tumor efficacy in mice.

Fusogenic platforms have exhibited high efficiency in delivery of CRISPR-Cas9 proteins as well. Lee et al. screened a library of guanidium-functionalized poly(oxanorborneneimide) (PONI) homopolymers to determine optimal molecular weight for protein delivery.[106] The polymer-protein nanocomposites (PPNCs) self-assembled from oligo(glutamate)-tagged (E-tagged) proteins and PONI homopolymers, and the authors determined that the highest molecular weight PONI facilitated the highest (~90%) cytosolic and nuclear delivery efficiency. Cargo delivery occurred within ~40 seconds of PPNC incubation with cells, supporting the concept that delivery undergoes membrane fusion rather than an endocytosis-dependent pathway. Cellular treatment with inhibitors of endocytosis had negligible effect on cargo delivery; only a cholesterol-depletion agent interfered with delivery.

3.2.3.5 External stimuli

External stimuli (*e.g.*, heat, light and ultrasound) are also utilized to mediate endosomal escape for various cargos. For instance, light-activation of photosensitizers to burst endosomes through oxidation is a promising strategy to facilitate endosomal escape.[107] In this approach, the carrier delivers a photosensitizer, which generates reactive oxygen species (ROS) under light irradiation. The ROS damage the membranes of endosomes, inducing cytosolic release of therapeutics trapped in endocytic vesicles. Because they are locally activated by external applied stimuli,

photosensitizer platforms can have higher spatial precision than conventional therapies. The reader is directed to reviews of PS and polymer-platforms.[108]

Han et al. fabricated a delivery system to target cellular mitochondria for photosensitizer and peptide delivery (**Figure 3.11**).[109] This system (PPK) comprised the photosensitizer protoporphyrin IX (PpIX) and the pro-apoptotic peptide $(KLAKLAK)_2$, linked via a short PEG linker. The authors confirmed ROS generation under light irradiation, which increased cellular internalization of PPK, facilitating mitochondrial targeting and disruption. The combinatorial ROS generation and cytotoxic peptide delivery translated to robust tumor inhibition in an H22 hepatic carcinoma tumor model.

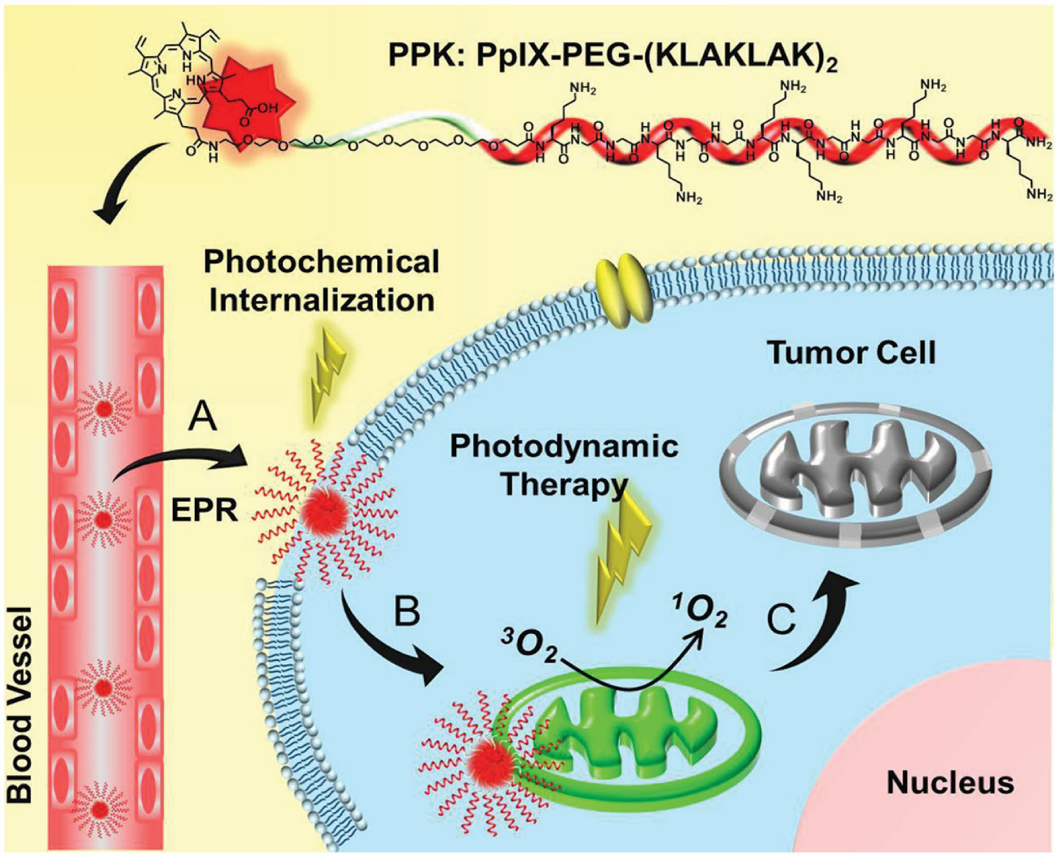

Figure 3.11: Incorporation of photosensitizers into polymer carriers can improve cellular internalization and targeting. Short-term light irradiation generated ROS to disrupt cellular membranes and facilitate uptake. Once internalized, a pro-apoptotic mitochondrial-targeted KLA peptide guided the NPs to the mitochondria, whereupon long-term irradiation generated

additional ROS to induce cell death. Reprinted with permission from ref[109]. Copyright 2020 Wiley-VCH GmbH.

In another example, Ji et al. developed biodegradable poly(ester amide) nanocarriers to co-deliver photosensitizer and antigen to DCs to potentiate an antigen-specific $CD8^+$ T cell response.[110] Arginine and phenylalanine based poly(ester amide) (Arg-Phe-PEA) nanoparticles were loaded with (1) the antigen ovalbumin (OVA), which is processed into the peptide SIINFEKL, and (2) the aluminum phthalocyanine disulfonate (AlPcS2a), which embeds in the membrane of the endocytic compartment, localizing photochemical disruption to the endocytic membrane. The amino acids arginine and phenylalanine were specifically selected to confer a cationic charge, enabling complexation with negatively charged payloads. Irradiation disrupted the endolysosomal membranes to facilitate transmigration of the nanoparticles into the cytosol, where enzymes degraded the polymer to accelerate OVA release. *In vivo*, this platform successfully immunized mice, evidenced by significantly increased SIINFEKL-specific $CD8^+$ T cell populations.

3.2.3.6 Methods to monitor intracellular peptide delivery

The primary techniques used are fluorescence-based (e.g. flow cytometry, confocal laser scanning microscopy (CLSM)), but non-fluorescence based methods (e.g. MALDI-TOF, Raman spectroscopy) and NanoSIMs have also been utilized to monitor cellular internalization and intracellular trafficking. A review of methods to monitor cytosolic delivery are presented here.[111]

Fluorescence is a particularly powerful tool to visualize endolysosomal release of polymer nanoparticles via (1) CLSM, (2) flow cytometry, or (3) fluorescence activated cell sorting. In general, CLSM is the most widely used technique as it is simple, easy to analyze, and adaptable. In CLSM, the carrier, cargo, or organelle can be fluorescently labeled. For the former two, diffuse fluorescence throughout the cells confirms cytosolic release. Endolysosomal vesicles can also be labeled *via* pH-sensitive probes (e.g. LysoTracker, SNARF-1) to monitor carrier-endosome colocalization and endosomal acidification kinetics. Additionally, linker cleavage or drug release from polymer conjugates can be monitored via Forster resonance energy transfer (FRET). However, these probes are all pH-sensitive and require optimization. In a recent report, the Duvall group published a label-free method to quantify endosomal disruption via redistribution of a

fluorescent fusion Galectin (Gal) 8.[112] Gal8 is constitutively expressed throughout the cell cytoplasm, but redistributes and binds to the inner face of endosomal membranes, presenting as fluorescent punctate. This high-throughput platform enables rapid screening of materials' endolytic activity.

Cellular uptake can also be quantified by flow cytometry if the carrier is fluorescently-labeled. Preliminary work investigating pulse width analysis can semi-quantitate endolysosomal escape, as there may be some correlation between pulse width and trafficking pathway.[113] The combination of fluorescence-activated cell sorting (FACS) and fluorescence correlation spectroscopy (FCS) enables quantification of intracellular uptake and internalization pathway (e.g. cytosolic delivery or degradation).[114] In this method, cells were incubated with fluorescently-labeled peptides, sorted for viability, lysed, and the cytosolic fraction was isolated. FCS was then used to quantify the amount of fluorescently-labeled peptide (whole and degraded) in these lysates.

Non-fluorescent techniques have also been used to characterize peptide uptake. Biotinylated peptides were captured from cell lysates and analyzed via matrix-assisted laser desorption/ionization time-of-flight mass spectrometry (MALDI-TOF MS).[115] Isotopic labeling enabled further distinction from endogenous peptides and subsequent quantification of the amount of intact internalized peptide. A review of strategies to quantify and analyze peptide internalization efficiency and pathways via MALDI-TOF MS can be found here.[116]

3.2.3.7 Challenges in cytosolic delivery

While significant advances in the development of new bioactive therapeutics has been made, achieving sufficient cytosolic delivery remains a critical hurdle in attaining therapeutic efficacy. As discussed, nanoparticle localization to tumor cells is the first major challenge in peptide delivery. However, once nanoparticles are uptaken by target cells, the therapeutic still needs to reach the appropriate intracellular target. In order to achieve this, the nanoparticles and its active therapeutic cargo must escape entrapment and destruction in the endo-lysosome. While strategies discussed in this section accomplish varying success in overcoming this hurdle, either by destabilizing the endosome membrane or fusing with the cellular membrane, there still remains much to be learned regarding endosomal uptake, escape, and induced immune response.

In many cases, incorporation of elements to facilitate targeting and cargo delivery triggers adverse immune events, rendering the therapeutic toxic or imposing strict therapeutic indexes. For example, PEI is highly efficient at mediating endolysosomal escape, but can be extremely toxic at high doses.[117] Toxicity is strongly correlated with degree of branching and molecular weight. Oftentimes, carriers need to compromise on efficacy in order to minimize toxicity. Thus, maintaining this delicate balance between efficacy and toxicity is key design challenge. Yet this is only the first of many obstacles in engineering non-toxic therapeutics. The mechanism and timing of endosomal escape also effects toxicity, as exhibited by the degree of inflammasome activation and subsequent inflammation. Baljon et al. demonstrated that carriers that mediated early endosomal escape with minimal lysosomal rupture were associated with higher cargo delivery and less inflammasome-mediate inflammation.[118] On the other hand, carriers that did not escape the early endosome, trafficked to the lysosome, and induced lysosomal rupture, were more likely to be associated with inflammasome activation. In vaccine applications, endosomal maturation inversely correlates with the degree of MHC cross-presentation, again emphasizing how the timing of escape can enhance therapeutic efficacy.[119] As such, it is critical to design carriers with controlled timing of endosomal escape in order to maximize efficacy and minimize toxicity.

Yet, while strategies to facilitate endosomal escape, and perhaps even engineer the timing of this escape, enhance therapeutic efficacy, the effects of endosomal disruption or fusion mechanism on innate cell signaling are still not fully understood.[120] During viral and bacterial infections, cells have developed mechanisms to raise danger signals in response to unplanned membrane perturbations. While the immune response enables the body to mount a defense against the pathogens, it could also result in loss of therapeutic tolerance. This is best demonstrated by PEG, a “stealth” polymer that was once heralded as the panacea to facilitating biocompatibility, but is now implicated in severe adverse allergic reactions. To design truly biocompatible delivery systems, additional research is needed to understand how carrier composition and timing of endosomal escape relate with toxicity and immune activation.

Even if these factors are carefully incorporated into nanoparticles, it does not guarantee therapeutic delivery and efficacy, as endosomal escape does not entirely prevent peptide degradation.

Cytosolic peptidases like tripeptidyl peptidase II (TPPII), leucine aminopeptidase (LAP), and thimet oligopeptidase (TOP) can degrade peptides with varying specificities.[121] TPPII removes N-terminal tripeptides and LAP removes hydrophobic amino acids from the N-terminus. These proteases can significantly attenuate peptide activity. To address this, peptide modification such as D-amino acid substitution or cyclization can reduce susceptibility to proteolytic activity.[122,123] However, all modified peptides must be screened for stability and activity. Furthermore, peptide intermediates may also be more or less toxic, and thus must be monitored as well.[124]

Overall, it is critical to understand how endosomal escape impacts immune cells in order to maintain therapeutic efficacy and tolerance. And while peptides permit extensive modification to help overcome proteolytic degradation, this also complicates manufacturing and requires extensive re-testing of safety and activity. Moving forward, currently identified peptides can be specifically engineered to address these challenges, or future peptide discovery can be deliberate in considering these factors.

3.3 Conclusions and Perspectives

As a promising class of therapeutics, peptides have received increasing attention in the war against cancer. In this review article, we summarize the potential of peptide therapeutics for cancer treatment and the limitations of peptide drugs. We also highlight how to improve the delivery of peptide therapeutics by rational design of polymer carriers.

Peptide anti-tumor agents possess several advantages when compared to the other anti-cancer candidates such as chemo-drugs and antibodies. First, peptides are easy to synthesize by well-established methods and are amenable for further modification, allowing cost-effective scale-up production. In addition, a library of 21 natural amino acids and numerous non-natural amino acids can be utilized for peptide synthesis, providing a great chemical diversity of peptides, which in turn endow the peptides' versatile functions. Peptides may not only display a broad spectrum of anti-tumor activity by membrane-lysis, regardless of development of drug resistance, but can also be designed to target almost any proteins and protein-protein interactions with high specificity. Various peptides have been developed to target signal transduction pathways, tumor suppressor proteins, as well as transcription factors, which induce selective tumor cell death without damaging

healthy cells. Peptides can also be utilized as antigens to trigger an anti-tumor immune response. As a result, peptide can serve as an ideal arsenal to treat cancer with high selectivity and low toxicity. Although there are advantages for peptide-based cancer therapy, peptides do have significant limitations derived from their intrinsic structure. A key issue for the peptide drugs is their high susceptibility to proteolysis. Other shortages, such as fast blood clearance and low tissue and cell penetration, severely hamper the efficacy of peptides for *in vivo* applications. Currently, there are only a few peptides used clinically for cancer therapy.

Further development of nanotechnology provides the potential to overcome the limitations of peptides. Polymers can encapsulate peptides with different physicochemical properties to form stable formulations and can endow controlled peptide release. Rational design of functional polymer carries can also improve the *in vivo* stability of peptide cargos, increase accumulation at target tissues (*e.g.*, tumors and lymph nodes), and facilitate cell uptake, which significantly enhance overall efficacy of peptide therapeutics. In addition, through incorporation of various functionalities, polymers can enable endosomal escape and cytosolic delivery of peptide cargos, which is vital for peptides with intracellular molecular targets.

Despite these advances in the delivery of peptide therapeutics by polymer carriers, there remain challenges in the pathway toward clinical application of peptide-based nanomedicines for cancer treatment. First, to maximize efficacy, efficient delivery is required, not only to the target cells, but also to the intracellular location of the drug target. To date, a major limitation for the clinical translation of anti-tumor nanomedicines remains low delivery efficiency of drug carriers to tumor regions. Unlike small molecule drugs which can diffuse into target cells after release from delivery vehicles accumulated at the tumor site, peptides with intracellular targets generally require assisted delivery from the carrier. The larger size of the polymeric peptide carrier therefore suffers from restricted diffusion and penetration in tumor tissue. Strategies to increase peptide delivery throughout solid tumors are therefore needed. A deeper understanding of the tumor microenvironment and NP-tumor interactions are necessary to guide the design of polymer carriers for improved tumor accumulation and penetration. Alternatively, peptide engineering approaches that increase the cell permeability of peptides released at the tumor site could also improve peptide efficacy. Delivery of peptide cargos (either therapeutic or antigen peptides) with the ability to

stimulate immune cells may provide another solution to treat tumors without necessitating deep tumor penetration. Second, the safety of peptide-polymer conjugates remains understudied. As potentially immunogenic motifs, peptides can elicit immune responses either directly against its own sequence or act as an adjuvant to induce an immune response against its carrier. As more polymeric peptide delivery vehicles advance toward clinical testing, the field will benefit from additional safety and immunogenicity studies using these formulations. Finally, polymer carriers need to balance functionality and complexity, as these can affect production reproducibility and scale-up ability, which are critical factors for clinical application. In addition to the engineering of polymeric vehicles for improved peptide delivery, the administration route and site need to be considered. Based on the cellular targets of peptide cargos and the properties of polymeric carriers, suitable administration route (such as intravenous, intradermal, and intramuscular injections) should be carefully chosen for optimized outcomes.

In conclusion, while the potential for peptide delivery with polymeric nanocarriers for cancer treatment is tremendous, further scientific research about tumor biology and NP-tumor interactions is necessary to design the next generation of peptide-polymer conjugates, which can enhance the applicability of peptide anti-tumor therapeutics for clinical translation.

References

1 Sun, Q., Zhou, Z., Qiu, N. & Shen, Y. Rational Design of Cancer Nanomedicine: Nanoproperty Integration and Synchronization. *Adv Mater* **29**, doi:10.1002/adma.201606628 (2017).

2 Shi, J., Kantoff, P. W., Wooster, R. & Farokhzad, O. C. Cancer nanomedicine: progress, challenges and opportunities. *Nat Rev Cancer* **17**, 20-37, doi:10.1038/nrc.2016.108 (2017).

3 Haggag, Y. A., Matchett, K. B., Falconer, R. A., Isreb, M., Jones, J., Faheem, A., McCarron, P. & El-Tanani, M. Novel Ran-RCC1 Inhibitory Peptide-Loaded Nanoparticles Have Anti-Cancer Efficacy In Vitro and In Vivo. *Cancers* **11**, doi:10.3390/Cancers11020222 (2019).

4 Zhang, P., Sun, F., Liu, S. J. & Jiang, S. Y. Anti-PEG antibodies in the clinic: Current issues and beyond PEGylation. *J Control Release* **244**, 184-193, doi:10.1016/j.jconrel.2016.06.040 (2016).

5 Peng, S., Ouyang, B., Men, Y., Du, Y., Cao, Y., Xie, R., Pang, Z., Shen, S. & Yang, W. Biodegradable zwitterionic polymer membrane coating endowing nanoparticles with ultra-long circulation and enhanced tumor photothermal therapy. *Biomaterials* **231**, 119680, doi:10.1016/j.biomaterials.2019.119680 (2020).

6 Wang, L. L., Shi, C. Y., Wang, X., Guo, D. D., Duncan, T. M. & Luo, J. T. Zwitterionic Janus Dendrimer with distinct functional disparity for enhanced protein delivery. *Biomaterials* **215**, doi:10.1016/j.biomaterials.2019.119233 (2019).

7 Guo, Y. Y., Wang, D., Song, Q. L., Wu, T. T., Zhuang, X. T., Bao, Y. L., Kong, M., Qj, Y., Tan, S. W. & Zhang, Z. P. Erythrocyte Membrane-Enveloped Polymeric Nanoparticles as Nanovaccine for Induction of Antitumor Immunity against Melanoma. *Acs Nano* **9**, 6918-6933, doi:10.1021/acsnano.5b01042 (2015).

8 Hashizume, H., Baluk, P., Morikawa, S., McLean, J. W., Thurston, G., Roberge, S., Jain, R. K. & McDonald, D. M. Openings between defective endothelial cells explain tumor vessel leakiness. *Am J Pathol* **156**, 1363-1380, doi:Doi 10.1016/S0002-9440(10)65006-7 (2000).

9 Maeda, H. Tumor-Selective Delivery of Macromolecular Drugs via the EPR Effect: Background and Future Prospects. *Bioconjugate Chem* **21**, 797-802, doi:10.1021/bc100070g (2010).
10 Yamaoka, T., Tabata, Y. & Ikada, Y. Distribution and Tissue Uptake of Poly(Ethylene Glycol) with Different Molecular-Weights after Intravenous Administration to Mice. *J Pharm Sci-Us* **83**, 601-606, doi:DOI 10.1002/jps.2600830432 (1994).
11 Kang, H., Rho, S., Stiles, W. R., Hu, S., Baek, Y., Hwang, D. W., Kashiwagi, S., Kim, M. S. & Choi, H. S. Size-Dependent EPR Effect of Polymeric Nanoparticles on Tumor Targeting. *Adv Healthc Mater* **9**, doi:10.1002/Adhm.201901223 (2020).
12 Davis, M. E., Chen, Z. & Shin, D. M. Nanoparticle therapeutics: an emerging treatment modality for cancer. *Nat Rev Drug Discov* **7**, 771-782, doi:10.1038/nrd2614 (2008).
13 Chen, S., Fan, J. X., Liu, X. H., Zhang, M. K., Liu, F., Zeng, X., Yan, G. P. & Zhang, X. Z. A self-delivery system based on an amphiphilic proapoptotic peptide for tumor targeting therapy. *J Mater Chem B* **7**, 778-785, doi:10.1039/c8tb02945h (2019).
14 Jia, H. R., Zhu, Y. X., Xu, K. F. & Wu, F. G. Turning Toxicants into Safe Therapeutic Drugs: Cytolytic Peptide-Photosensitizer Assemblies for Optimized In Vivo Delivery of Melittin. *Adv Healthc Mater* **7**, doi:10.1002/Adhm.201800380 (2018).
15 Rajendrakumar, S. K., Mohapatra, A., Singh, B., Revuri, V., Lee, Y. K., Kim, C. S., Cho, C. S. & Park, I. K. Self-Assembled, Adjuvant/Antigen-Based Nanovaccine Mediates Anti-Tumor Immune Response against Melanoma Tumor. *Polymers-Basel* **10**, doi:10.3390/Polym10101063 (2018).
16 Danhier, F. To exploit the tumor microenvironment: Since the EPR effect fails in the clinic, what is the future of nanomedicine? *J Control Release* **244**, 108-121, doi:10.1016/j.jconrel.2016.11.015 (2016).
17 Wilhelm, S., Tavares, A. J., Dai, Q., Ohta, S., Audet, J., Dvorak, H. F. & Chan, W. C. W. Analysis of nanoparticle delivery to tumours. *Nature Reviews Materials* **1**, doi:10.1038/natrevmats.2016.14 (2016).
18 Stirland, D. L., Nichols, J. W., Miura, S. & Bae, Y. H. Mind the gap: A survey of how cancer drug carriers are susceptible to the gap between research and practice. *J Control Release* **172**, 1045-1064, doi:10.1016/j.jconrel.2013.09.026 (2013).
19 Wilhelm, S., Tavares, A. J., Dai, Q., Ohta, S., Audet, J., Dvorak, H. F. & Chan, W. C. Analysis of nanoparticle delivery to tumours. *Nature reviews materials* **1**, 1-12 (2016).
20 Price, L. S., Stern, S. T., Deal, A. M., Kabanov, A. V. & Zamboni, W. C. A reanalysis of nanoparticle tumor delivery using classical pharmacokinetic metrics. *Science Advances* **6**, eaay9249 (2020).
21 Zhou, Q., Shao, S. Q., Wang, J. Q., Xu, C. H., Xiang, J. J., Piao, Y., Zhou, Z. X., Yu, Q. S., Tang, J. B., Liu, X. R., Gan, Z. H., Mo, R., Gu, Z. & Shen, Y. Q. Enzyme-activatable polymer-drug conjugate augments tumour penetration and treatment efficacy. *Nat Nanotechnol* **14**, 799-+, doi:10.1038/s41565-019-0485-z (2019).
22 Tang, L., Yang, X. J., Yin, Q., Cai, K. M., Wang, H., Chaudhury, I., Yao, C., Zhou, Q., Kwon, M., Hartman, J. A., Dobrucki, I. T., Dobrucki, L. W., Borst, L. B., Lezmig, S., Helferich, W. G., Ferguson, A. L., Fan, T. M. & Cheng, J. J. Investigating the optimal size of anticancer nanomedicine. *P Natl Acad Sci USA* **111**, 15344-15349, doi:10.1073/pnas.1411499111 (2014).
23 Sykes, E. A., Chen, J., Zheng, G. & Chan, W. C. W. Investigating the Impact of Nanoparticle Size on Active and Passive Tumor Targeting Efficiency. *Acs Nano* **8**, 5696-5706, doi:10.1021/nn500299p (2014).
24 Jia, H. R., Zhu, Y. X., Liu, X. Y., Pan, G. Y., Gao, G., Sun, W., Zhang, X. D., Jiang, Y. W. & Wu, F. G. Construction of Dually Responsive Nanotransformers with Nanosphere-Nanofiber-Nanosphere Transition for Overcoming the Size Paradox of Anticancer Nanodrugs. *Acs Nano* **13**, 11781-11792, doi:10.1021/acsnano.9b05749 (2019).
25 Dai, Q., Wilhelm, S., Ding, D., Syed, A. M., Sindhwani, S., Zhang, Y. W., Chen, Y. Y., MacMillan, P. & Chan, W. C. W. Quantifying the Ligand-Coated Nanoparticle Delivery to Cancer Cells in Solid Tumors. *Acs Nano* **12**, 8423-8435, doi:10.1021/acsnano.8b03900 (2018).
26 Cieslewicz, M., Tang, J. J., Yu, J. L., Cao, H., Zavaljevski, M., Motoyama, K., Lieber, A., Raines, E. W. & Pun, S. H. Targeted delivery of proapoptotic peptides to tumor-associated macrophages improves survival. *P Natl Acad Sci USA* **110**, 15919-15924, doi:10.1073/pnas.1312197110 (2013).
27 Ngambenjawong, C., Gustafson, H. H. & Pun, S. H. Progress in tumor-associated macrophage (TAM)-targeted therapeutics. *Adv Drug Deliver Rev* **114**, 206-221, doi:10.1016/j.addr.2017.04.010 (2017).
28 Li, H. M., Li, Y. P., Wang, X., Hou, Y. Y., Hong, X. Y., Gong, T., Zhang, Z. R. & Sun, X. Rational design of Polymeric Hybrid Micelles to Overcome Lymphatic and Intracellular Delivery Barriers in Cancer Immunotherapy. *Theranostics* **7**, 4383-4398, doi:10.7150/thno.20745 (2017).

29 Backlund, C. M., Parhamifar, L., Minter, L., Tew, G. N. & Andresen, T. L. Protein Transduction Domain Mimics Facilitate Rapid Antigen Delivery into Monocytes. *Mol Pharmaceut* **16**, 2462-2469, doi:10.1021/acs.molpharmaceut.9b00070 (2019).
30 Chang, H., Lv, J., Gao, X., Wang, X., Wang, H., Chen, H., He, X., Li, L. & Cheng, Y. Rational Design of a Polymer with Robust Efficacy for Intracellular Protein and Peptide Delivery. *Nano Lett* **17**, 1678-1684, doi:10.1021/acs.nanolett.6b04955 (2017).
31 Bartlett, D. W., Su, H., Hildebrandt, I. J., Weber, W. A. & Davis, M. E. Impact of tumor-specific targeting on the biodistribution and efficacy of siRNA nanoparticles measured by multimodality in vivo imaging. *P Natl Acad Sci USA* **104**, 15549-15554, doi:DOI 10.1073/pnas.0707461104 (2007).
32 Hussain, S., Pluckthun, A., Allen, T. M. & Zangemeister-Wittke, U. Antitumor activity of an epithelial cell adhesion molecule-targeted nanovesicular drug delivery system. *Mol Cancer Ther* **6**, 3019-3027, doi:10.1158/1535-7163.MCT-07-0615 (2007).
33 Kirpotin, D. B., Drummond, D. C., Shao, Y., Shalaby, M. R., Hong, K., Nielsen, U. B., Marks, J. D., Benz, C. C. & Park, J. W. Antibody targeting of long-circulating lipidic nanoparticles does not increase tumor localization but does increase internalization in animal models. *Cancer Res* **66**, 6732-6740, doi:10.1158/0008-5472.CAN-05-4199 (2006).
34 Bartlett, D. W. & Davis, M. E. Impact of tumor-specific targeting and dosing schedule on tumor growth inhibition after intravenous administration of siRNA-containing nanoparticles. *Biotechnol Bioeng* **99**, 975-985, doi:10.1002/bit.21668 (2008).
35 Zhou, Z. J., Yan, Y., Wang, L., Zhang, Q. & Cheng, Y. Y. Melanin-like nanoparticles decorated with an autophagy-inducing peptide for efficient targeted photothermal therapy. *Biomaterials* **203**, 63-72, doi:10.1016/j.biomaterials.2019.02.023 (2019).
36 Conniot, J., Scomparin, A., Peres, C., Yeini, E., Pozzi, S., Matos, A. I., Kleiner, R., Moura, L. I. F., Zupancic, E., Viana, A. S., Doron, H., Gois, P. M. P., Erez, N., Jung, S., Satchi-Fainaro, R. & Florindo, H. F. Immunization with mannosylated nanovaccines and inhibition of the immune-suppressing microenvironment sensitizes melanoma to immune checkpoint modulators. *Nat Nanotechnol* **14**, 891-+, doi:10.1038/s41565-019-0512-0 (2019).
37 Kakwere, H., Ingham, E. S., Allen, R., Mahakian, L. M., Tam, S. M., Zhang, H., Silvestrini, M. T., Lewis, J. S. & Ferrara, K. W. Toward Personalized Peptide-Based Cancer Nanovaccines: A Facile and Versatile Synthetic Approach. *Bioconjugate Chem* **28**, 2756-2771, doi:10.1021/acs.bioconjchem.7b00502 (2017).
38 Silva, J. M., Zupancic, E., Vandermeulen, G., Oliveira, V. G., Salgado, A., Videira, M., Gaspar, M., Graca, L., Preat, V. & Florindo, H. F. In vivo delivery of peptides and Toll-like receptor ligands by mannose-functionalized polymeric nanoparticles induces prophylactic and therapeutic anti-tumor immune responses in a melanoma model. *J Control Release* **198**, 91-103, doi:10.1016/j.jconrel.2014.11.033 (2015).
39 Zou, C. M., Jiang, G. Y., Gao, X. Q., Zhang, W., Deng, H., Zhang, C., Ding, J. H., Wei, R., Wang, X. Q., Xi, L. & Tan, S. W. Targeted co-delivery of Trp-2 polypeptide and monophosphoryl lipid A by pH-sensitive poly (beta-amino ester) nano-vaccines for melanoma. *Nanomed-Nanotechnol* **22**, doi:10.1016/j.nano.2019.102092 (2019).
40 Zhang, L. H., Wu, S. J., Qin, Y., Fan, F., Zhang, Z. M., Huang, C. L., Ji, W. H., Lu, L., Wang, C., Sung, H. F., Leng, X. G., Kong, D. L. & Zhu, D. W. Targeted Codelivery of an Antigen and Dual Agonists by Hybrid Nanoparticles for Enhanced Cancer Immunotherapy. *Nano Lett* **19**, 4237-4249, doi:10.1021/acs.nanolett.9b00030 (2019).
41 Spicer, C. D., Jumeaux, C., Gupta, B. & Stevens, M. M. Peptide and protein nanoparticle conjugates: versatile platforms for biomedical applications. *Chem Soc Rev* **47**, 3574-3620, doi:10.1039/c7cs00877e (2018).
42 Zhang, C., Wu, W., Li, R. Q., Qiu, W. X., Zhuang, Z. N., Cheng, S. X. & Zhang, X. Z. Peptide-Based Multifunctional Nanomaterials for Tumor Imaging and Therapy. *Adv Funct Mater* **28**, doi:10.1002/Adfm.201804492 (2018).
43 Sarangthem, V., Kim, Y., Singh, T. D., Seo, B. Y., Cheon, S. H., Lee, Y. J., Lee, B. H. & Park, R. W. Multivalent Targeting Based Delivery of Therapeutic Peptide using AP1-ELP Carrier for Effective Cancer Therapy. *Theranostics* **6**, 2235-2249, doi:10.7150/thno.16425 (2016).
44 Wang, H. X., Yang, B., Wang, Y. L., Liu, F., Fernandez-Tejada, A. & Dong, S. W. beta-Glucan as an immune activator and a carrier in the construction of a synthetic MUC1 vaccine. *Chem Commun* **55**, 253-256, doi:10.1039/c8cc07691j (2019).
45 Chang, H. C., Zou, Z. Z., Wang, Q. H., Li, J., Jin, H., Yin, Q. X. & Xing, D. Targeting and Specific Activation of Antigen-Presenting Cells by Endogenous Antigen-Loaded Nanoparticles Elicits Tumor-Specific Immunity. *Adv Sci*, doi:10.1002/Advs.201900069 (2019).

46 Kim, S. Y., Phuengkham, H., Noh, Y. W., Lee, H. G., Um, S. H. & Lim, Y. T. Immune Complexes Mimicking Synthetic Vaccine Nanoparticles for Enhanced Migration and Cross-Presentation of Dendritic Cells. *Adv Funct Mater* **26**, 8072-8082, doi:10.1002/adfm.201603651 (2016).
47 Cruz, L. J., Rosalia, R. A., Kleinovink, J. W., Rueda, F., Lowik, C. W. G. M. & Ossendorp, F. Targeting nanoparticles to CD40, DEC-205 or CD11c molecules on dendritic cells for efficient CD8(+) T cell response: A comparative study. *J Control Release* **192**, 209-218, doi:10.1016/j.jconrel.2014.07.040 (2014).
48 Neri, D. & Supuran, C. T. Interfering with pH regulation in tumours as a therapeutic strategy. *Nat Rev Drug Discov* **10**, 767-777, doi:10.1038/nrd3554 (2011).
49 Muz, B., de la Puente, P., Azab, F. & Azab, A. K. The role of hypoxia in cancer progression, angiogenesis, metastasis, and resistance to therapy. *Hypoxia* **3**, 83-92, doi:10.2147/Hp.S93413 (2015).
50 Cong, Y., Ji, L., Gao, Y. J., Liu, F. H., Cheng, D. B., Hu, Z. Y., Qiao, Z. Y. & Wang, H. Microenvironment-Induced In Situ Self-Assembly of Polymer-Peptide Conjugates That Attack Solid Tumors Deeply. *Angew Chem Int Edit* **58**, 4632-4637, doi:10.1002/anie.201900135 (2019).
51 Chen, S., Rong, L., Lei, Q., Cao, P. X., Qin, S. Y., Zheng, D. W., Jia, H. Z., Zhu, J. Y., Cheng, S. X., Zhuo, R. X. & Zhang, X. Z. A surface charge-switchable and folate modified system for co-delivery of proapoptosis peptide and p53 plasmid in cancer therapy. *Biomaterials* **77**, 149-163, doi:10.1016/j.biomaterials.2015.11.013 (2016).
52 Li, Y. C., Jeon, J. & Park, J. H. Hypoxia-responsive nanoparticles for tumor-targeted drug delivery. *Cancer Lett* **490**, 31-43, doi:10.1016/j.canlet.2020.05.032 (2020).
53 Zhang, P., Yang, H. L., Shen, W., Liu, W. G., Chen, L. & Xiao, C. S. Hypoxia-Responsive Polypeptide Nanoparticles Loaded with Doxorubicin for Breast Cancer Therapy. *Acs Biomater Sci Eng* **6**, 2167-2174, doi:10.1021/acsbiomaterials.0c00125 (2020).
54 Liu, F. H., Hou, C. Y., Zhang, D., Zhao, W. J., Cong, Y., Duan, Z. Y., Qiao, Z. Y. & Wang, H. Enzyme-sensitive cytotoxic peptide-dendrimer conjugates enhance cell apoptosis and deep tumor penetration. *Biomater Sci-Uk* **6**, 604-613, doi:10.1039/c7bm01182b (2018).
55 Qiao, Z. Y., Zhao, W. J., Gao, Y. J., Cong, Y., Zhao, L. N., Hu, Z. Y. & Wang, H. Reconfigurable Peptide Nanotherapeutics at Tumor Microenvironmental pH. *Acs Appl Mater Inter* **9**, 30426-30436, doi:10.1021/acsami.7b09033 (2017).
56 Chen, C. X., Zhang, Y., Hou, Z., Cui, X. J., Zhao, Y. R. & Xu, H. Rational Design of Short Peptide-Based Hydrogels with MMP-2 Responsiveness for Controlled Anticancer Peptide Delivery. *Biomacromolecules* **18**, 3563-3571, doi:10.1021/acs.biomac.7b00911 (2017).
57 Yao, Q., Kou, L. F., Tu, Y. & Zhu, L. MMP-Responsive 'Smart' Drug Delivery and Tumor Targeting. *Trends Pharmacol Sci* **39**, 766-781, doi:10.1016/j.tips.2018.06.003 (2018).
58 Hu, Q. Y., Katti, P. S. & Gu, Z. Enzyme-responsive nanomaterials for controlled drug delivery. *Nanoscale* **6**, 12273-12286, doi:10.1039/c4nr04249b (2014).
59 Liu, F. H., Cong, Y., Qi, G. B., Ji, L., Qiao, Z. Y. & Wang, H. Near-Infrared Laser-Driven in Situ Self-Assembly as a General Strategy for Deep Tumor Therapy. *Nano Lett* **18**, 6577-6584, doi:10.1021/acs.nanolett.8b03174 (2018).
60 Luo, L. H., Yang, J., Zhu, C. Q., Jiang, M. S., Guo, X. M., Li, W., Yin, X. Y., Yin, H., Qin, B., Yuan, X. L., Li, Q. P., Du, Y. Z. & You, J. Sustained release of anti-PD-1 peptide for perdurable immunotherapy together with photothermal ablation against primary and distant tumors. *J Control Release* **278**, 87-99, doi:10.1016/j.jconrel.2018.04.002 (2018).
61 Shete, H. K., Prabhu, R. H. & Patravale, V. B. Endosomal Escape: A Bottleneck in Intracellular Delivery. *J Nanosci Nanotechno* **14**, 460-474, doi:10.1166/jnn.2014.9082 (2014).
62 Varkouhi, A. K., Scholte, M., Storm, G. & Haisma, H. J. Endosomal escape pathways for delivery of biologicals. *J Control Release* **151**, 220-228, doi:10.1016/j.jconrel.2010.11.004 (2011).
63 Steinauer, A., LaRochelle, J. R., Knox, S. L., Wissner, R. F., Berry, S. & Schepartz, A. HOPS-dependent endosomal fusion required for efficient cytosolic delivery of therapeutic peptides and small proteins. *P Natl Acad Sci USA* **116**, 512-521, doi:10.1073/pnas.1812044116 (2019).
64 Duchardt, F., Fotin-Mleczek, M., Schwarz, H., Fischer, R. & Brock, R. A comprehensive model for the cellular uptake of cationic cell-penetrating peptides. *Traffic* **8**, 848-866, doi:10.1111/j.1600-0854.2007.00572.x (2007).
65 Bus, T., Traeger, A. & Schubert, U. S. The great escape: how cationic polyplexes overcome the endosomal barrier. *J Mater Chem B* **6**, doi:10.1039/c8tb00967h (2018).

66 Vermeulen, L. M. P., Brans, T., Samal, S. K., Dubruel, P., Demeester, J., De Smedt, S. C., Remaut, K. & Braeckmans, K. Endosomal Size and Membrane Leakiness Influence Proton Sponge-Based Rupture of Endosomal Vesicles. *Acs Nano* **12**, 2332-2345, doi:10.1021/acsnano.7b07583 (2018).
67 Wojnilowicz, M., Glab, A., Bertucci, A., Caruso, F. & Cavalieri, F. Super-resolution Imaging of Proton Sponge-Triggered Rupture of Endosomes and Cytosolic Release of Small Interfering RNA. *Acs Nano* **13**, 187-202, doi:10.1021/acsnano.8b05151 (2019).
68 Zhou, J. L. & Chau, Y. Different oligoarginine modifications alter endocytic pathways and subcellular trafficking of polymeric nanoparticles. *Biomater Sci-Uk* **4**, 1462-1472, doi:10.1039/c6bm00371k (2016).
69 Akinc, A., Thomas, M., Klibanov, A. M. & Langer, R. Exploring polyethylenimine-mediated DNA transfection and the proton sponge hypothesis. *J Gene Med* **7**, 657-663, doi:Doi 10.1002/Jgm.696 (2005).
70 Sonawane, N. D., Szoka, F. C. & Verkman, A. S. Chloride accumulation and swelling in endosomes enhances DNA transfer by polyamine-DNA polyplexes. *J Biol Chem* **278**, 44826-44831, doi:10.1074/jbc.M308643200 (2003).
71 Wang, H., Wang, Y. T., Wang, Y., Hu, J. J., Li, T. F., Liu, H. M., Zhang, Q. & Cheng, Y. Y. Self-Assembled Fluorodendrimers Combine the Features of Lipid and Polymeric Vectors in Gene Delivery. *Angew Chem Int Edit* **54**, 11647-11651, doi:10.1002/anie.201501461 (2015).
72 Liu, H. M., Wang, Y., Wang, M. M., Xiao, J. R. & Cheng, Y. Y. Fluorinated poly(propylenimine) dendrimers as gene vectors. *Biomaterials* **35**, 5407-5413, doi:10.1016/j.biomaterials.2014.03.040 (2014).
73 Zhang, Z. J., Shen, W. W., Ling, J., Yan, Y., Hu, J. J. & Cheng, Y. Y. The fluorination effect of fluoroamphiphiles in cytosolic protein delivery. *Nat Commun* **9**, doi:10.1038/S41467-018-03779-8 (2018).
74 Shenoy, D., Little, S., Langer, R. & Amiji, M. Poly(ethylene oxide)-modified poly(beta-amino ester) nanoparticles as a pH-sensitive system for tumor-targeted delivery of hydrophobic drugs. 1. In vitro evaluations. *Mol Pharmaceut* **2**, 357-366, doi:10.1021/mp0500420 (2005).
75 Qiao, Z. Y., Zhang, D., Hou, C. Y., Zhao, S. M., Liu, Y., Gao, Y. J., Tan, N. H. & Wang, H. A pH-responsive natural cyclopeptide RA-V drug formulation for improved breast cancer therapy. *J Mater Chem B* **3**, 4514-4523, doi:10.1039/c5tb00445d (2015).
76 Qiao, Z. Y., Hou, C. Y., Zhang, D., Liu, Y., Lin, Y. X., An, H. W., Li, X. J. & Wang, H. Self-assembly of cytotoxic peptide conjugated poly(beta-amino ester)s for synergistic cancer chemotherapy. *J Mater Chem B* **3**, 2943-2953, doi:10.1039/c4tb02144d (2015).
77 Mozhi, A., Ahmad, I., Okeke, C. I., Li, C. & Liang, X. J. pH-sensitive polymeric micelles for the Co-delivery of proapoptotic peptide and anticancer drug for synergistic cancer therapy. *Rsc Adv* **7**, 12886-12896, doi:10.1039/c6ra27054a (2017).
78 Agarwal, S., Zhang, Y., Maji, S. & Greiner, A. PDMAEMA based gene delivery materials. *Mater Today* **15**, 388-393, doi:Doi 10.1016/S1369-7021(12)70165-7 (2012).
79 Kern, H. B., Srinivasan, S., Convertine, A. J., Hockenbery, D., Press, O. W. & Stayton, P. S. Enzyme-Cleavable Polymeric Micelles for the Intracellular Delivery of Proapoptotic Peptides. *Mol Pharmaceut* **14**, 1450-1459, doi:10.1021/acs.molpharmaceut.6b01178 (2017).
80 Toyoda, M., Hama, S., Ikeda, Y., Nagasaki, Y. & Kogure, K. Anti-cancer vaccination by transdermal delivery of antigen peptide-loaded nanogels via iontophoresis. *Int J Pharmaceut* **483**, 110-114, doi:10.1016/j.ijpharm.2015.02.024 (2015).
81 Luo, M., Wang, H., Wang, Z. H., Cai, H. C., Lu, Z. G., Li, Y., Du, M. J., Huang, G., Wang, C. S., Chen, X., Porembka, M. R., Lea, J., Frankel, A. E., Fu, Y. X., Chen, Z. J. J. & Gao, J. M. A STING-activating nanovaccine for cancer immunotherapy. *Nat Nanotechnol* **12**, 648-+, doi:10.1038/Nnano.2017.52 (2017).
82 Luo, M., Liu, Z. D., Zhang, X. Y., Han, C. H., Samandi, L. Z., Dong, C. B., Sumer, B. D., Lea, J., Fu, Y. X. & Gao, J. M. Synergistic STING activation by PC7A nanovaccine and ionizing radiation improves cancer immunotherapy. *J Control Release* **300**, 154-160, doi:10.1016/j.jconrel.2019.02.036 (2019).
83 Pack, D. W., Putnam, D. & Langer, R. Design of imidazole-containing endosomolytic biopolymers for gene delivery. *Biotechnol Bioeng* **67**, 217-223, doi:Doi 10.1002/(Sici)1097-0290(20000120)67:2<217::Aid-Bit11>3.0.Co;2-Q (2000).
84 Lim, C., Won, W. R., Moon, J., Sim, T., Shin, Y., Kim, J. C., Lee, E. S., Youn, Y. S. & Oh, K. T. Co-delivery of D-(KLAKLAK)(2) peptide and doxorubicin using a pH-sensitive nanocarrier for synergistic anticancer treatment. *J Mater Chem B* **7**, 4299-4308, doi:10.1039/c9tb00741e (2019).
85 Vermeulen, L. M. P., De Smedt, S. C., Remaut, K. & Braeckmans, K. The proton sponge hypothesis: Fable or fact? *Eur J Pharm Biopharm* **129**, 184-190, doi:10.1016/j.ejpb.2018.05.034 (2018).
86 Won, Y. Y., Sharma, R. & Konieczny, S. F. Missing pieces in understanding the intracellular trafficking of polycation/DNA complexes. *J Control Release* **139**, 88-93, doi:10.1016/j.jconrel.2009.06.031 (2009).

87 Funhoff, A. M., van Nostrum, C. F., Koning, G. A., Schuurmans-Nieuwenbroek, N. M. E., Crommelin, D. J. A. & Hennink, W. E. Endosomal escape of polymeric gene delivery complexes is not always enhanced by polymers buffering at low pH. *Biomacromolecules* **5**, 32-39, doi:10.1021/bm034041+ (2004).
88 Benjaminsen, R. V., Mattebjerg, M. A., Henriksen, J. R., Moghimi, S. M. & Andresen, T. L. The possible "proton sponge " effect of polyethylenimine (PEI) does not include change in lysosomal pH. *Molecular therapy : the journal of the American Society of Gene Therapy* **21**, 149-157, doi:10.1038/mt.2012.185 (2013).
89 Yessine, M. A., Lafleur, M., Meier, C., Petereit, H. U. & Leroux, J. C. Characterization of the membrane-destabilizing properties of different pH-sensitive methacrylic acid copolymers. *Bba-Biomembranes* **1613**, 28-38, doi:10.1016/S0005-2736(03)00137-8 (2003).
90 Murthy, N., Robichaud, J. R., Tirrell, D. A., Stayton, P. S. & Hoffman, A. S. The design and synthesis of polymers for eukaryotic membrane disruption. *J Control Release* **61**, 137-143, doi:Doi 10.1016/S0168-3659(99)00114-5 (1999).
91 Qiu, F., Becker, K. W., Knight, F. C., Baljon, J. J., Sevimli, S., Shae, D., Gilchuk, P., Joyce, S. & Wilson, J. T. Poly(propylacrylic acid)-peptide nanoplexes as a platform for enhancing the immunogenicity of neoantigen cancer vaccines. *Biomaterials* **182**, 82-91, doi:10.1016/j.biomaterials.2018.07.052 (2018).
92 Radis-Baptista, G., Campelo, I. S., Morlighem, J. E. R. L., Melo, L. M. & Freitas, V. J. F. Cell-penetrating peptides (CPPs): From delivery of nucleic acids and antigens to transduction of engineered nucleases for application in transgenesis. *J Biotechnol* **252**, 15-26, doi:10.1016/j.jbiotec.2017.05.002 (2017).
93 Cerrato, C. P., Kunnapuu, K. & Langel, U. Cell-penetrating peptides with intracellular organelle targeting. *Expert Opin Drug Del* **14**, 245-255, doi:10.1080/17425247.2016.1213237 (2017).
94 Martens, T. F., Remaut, K., Demeester, J., De Smedt, S. C. & Braeckmans, K. Intracellular delivery of nanomaterials: How to catch endosomal escape in the act. *Nano Today* **9**, 344-364, doi:10.1016/j.nantod.2014.04.011 (2014).
95 Rady, I., Siddiqui, I. A., Rady, M. & Mukhtar, H. Melittin, a major peptide component of bee venom, and its conjugates in cancer therapy. *Cancer Lett* **402**, 16-31, doi:10.1016/j.canlet.2017.05.010 (2017).
96 Cheng, Y. L., Yumul, R. C. & Pun, S. H. Virus-Inspired Polymer for Efficient In Vitro and In Vivo Gene Delivery. *Angew Chem Int Edit* **55**, 12013-12017, doi:10.1002/anie.201605958 (2016).
97 Peeler, D. J., Thai, S. N., Cheng, Y. L., Horner, P. J., Sellers, D. L. & Pun, S. H. pH-sensitive polymer micelles provide selective and potentiated lytic capacity to venom peptides for effective intracellular delivery. *Biomaterials* **192**, 235-244, doi:10.1016/j.biomaterials.2018.11.004 (2019).
98 Lee, Y. J., Johnson, G., Peltier, G. C. & Pellois, J. P. A HA2-Fusion tag limits the endosomal release of its protein cargo despite causing endosomal lysis. *Bba-Gen Subjects* **1810**, 752-758, doi:10.1016/j.bbagen.2011.05.013 (2011).
99 Wang, M., Zuris, J. A., Meng, F. T., Rees, H., Sun, S., Deng, P., Han, Y., Gao, X., Pouli, D., Wu, Q., Georgakoudi, I., Liu, D. R. & Xu, Q. B. Efficient delivery of genome-editing proteins using bioreducible lipid nanoparticles. *P Natl Acad Sci USA* **113**, 2868-2873, doi:10.1073/pnas.1520244113 (2016).
100 Wang, K. W., Yang, Y., Xue, W. & Liu, Z. H. Cell Penetrating Peptide-Based Redox-Sensitive Vaccine Delivery System for Subcutaneous Vaccination. *Mol Pharmaceut* **15**, 975-984, doi:10.1021/acs.molpharmaceut.7b00905 (2018).
101 Kube, S., Hersch, N., Naumovska, E., Gensch, T., Hendriks, J., Franzen, A., Landyogt, L., Siebrasse, J. P., Kubitscheck, U., Hoffmann, B., Merkel, R. & Csiszar, A. Fusogenic Liposomes as Nanocarriers for the Delivery of Intracellular Proteins. *Langmuir* **33**, 1051-1059, doi:10.1021/acs.langmuir.6b04304 (2017).
102 Yang, J., Bahreman, A., Daudey, G., Bussmann, J., Olsthoorn, R. C. L. & Kros, A. Drug Delivery via Cell Membrane Fusion Using Lipopeptide Modified Liposomes. *Acs Central Sci* **2**, 621-630, doi:10.1021/acscentsci.6b00172 (2016).
103 Yang, J., Tu, J., Lamers, G. E. M., Olsthoorn, R. C. L. & Kros, A. Membrane Fusion Mediated Intracellular Delivery of Lipid Bilayer Coated Mesoporous Silica Nanoparticles. *Adv Healthc Mater* **6**, doi:10.1002/Adhm.201700759 (2017).
104 Fang, R. H., Hu, C. M. J., Luk, B. T., Gao, W. W., Copp, J. A., Tai, Y. Y., O'Connor, D. E. & Zhang, L. F. Cancer Cell Membrane-Coated Nanoparticles for Anticancer Vaccination and Drug Delivery. *Nano Lett* **14**, 2181-2188, doi:10.1021/nl500618u (2014).
105 Yang, R., Xu, J., Xu, L. G., Sun, X. Q., Chen, Q., Zhao, Y. H., Peng, R. & Liu, Z. Cancer Cell Membrane-Coated Adjuvant Nanoparticles with Mannose Modification for Effective Anticancer Vaccination. *Acs Nano* **12**, 5121-5129, doi:10.1021/acsnano.7b09041 (2018).

106 Lee, Y., Luther, D. C., Goswami, R., Jeon, T., Clark, V., Elia, J., Gopalakrishnan, S. & Rotello, V. M. Direct Cytosolic Delivery of Proteins Through Co-Engineering of Proteins and Polymeric Delivery Vehicles. *J Am Chem Soc*, doi:10.1021/jacs.9b12759 (2020).
107 Selbo, P. K., Weyergang, A., Hogset, A., Norum, O. J., Berstad, M. B., Vikdal, M. & Berg, K. Photochemical internalization provides time- and space-controlled endolysosomal escape of therapeutic molecules. *J Control Release* **148**, 2-12, doi:10.1016/j.jconrel.2010.06.008 (2010).
108 Demazeau, M., Gibot, L., Mingotaud, A. F., Vicendo, P., Roux, C. & Lonetti, B. Rational design of block copolymer self-assemblies in photodynamic therapy. *Beilstein J Nanotech* **11**, 180-212, doi:10.3762/bjnano.11.15 (2020).
109 Han, K., Lei, Q., Wang, S. B., Hu, J. J., Qiu, W. X., Zhu, J. Y., Yin, W. N., Luo, X. & Zhang, X. Z. Dual-Stage-Light-Guided Tumor Inhibition by Mitochondria-Targeted Photodynamic Therapy. *Adv Funct Mater* **25**, 2961-2971, doi:10.1002/adfm.201500590 (2015).
110 Liu, G. H., Hu, J. M., Zhang, G. Y. & Liu, S. Y. Rationally Engineering Phototherapy Modules of Eosin-Conjugated Responsive Polymeric Nanocarriers via Intracellular Endocytic pH Gradients. *Bioconjugate Chem* **26**, 1328-1338, doi:10.1021/bc500548r (2015).
111 Battistella, C. & Klok, H. A. Controlling and Monitoring Intracellular Delivery of Anticancer Polymer Nanomedicines. *Macromol Biosci* **17**, doi:10.1002/Mabi.201700022 (2017).
112 Kilchrist, K. V., Dimobi, S. C., Jackson, M. A., Evans, B. C., Werfel, T. A., Dailing, E. A., Bedingfield, S. K., Kelly, I. B. & Duvall, C. L. Gal8 Visualization of Endosome Disruption Predicts Carrier-Mediated Biologic Drug Intracellular Bioavailability. *Acs Nano* **13**, 1136-1152, doi:10.1021/acsnano.8b05482 (2019).
113 Wensley, H. J., Johnston, D. A., Smith, W. S., Holmes, S. E., Flavell, S. U. & Flavell, D. J. A Flow Cytometric Method to Quantify the Endosomal Escape of a Protein Toxin to the Cytosol of Target Cells. *Pharm Res-Dordr* **37**, doi:10.1007/s11095-019-2725-1 (2020).
114 Rezgui, R., Blumer, K., Yeoh-Tan, G., Trexler, A. J. & Magzoub, M. Precise quantification of cellular uptake of cell-penetrating peptides using fluorescence-activated cell sorting and fluorescence correlation spectroscopy. *Bba-Biomembranes* **1858**, 1499-1506, doi:10.1016/j.bbamem.2016.03.023 (2016).
115 Burlina, F., Sagan, S., Bolbach, G. & Chassaing, G. Quantification of the cellular uptake of cell-penetrating peptides by MALDI-TOF mass spectrometry. *Angew Chem Int Edit* **44**, 4244-4247, doi:10.1002/anie.200500477 (2005).
116 Aubry, S., Aussedat, B., Delaroche, D., Jiao, C. Y., Bolbach, G., Lavielle, S., Chassaing, G., Sagan, S. & Burlina, F. MALDI-TOF mass spectrometry: A powerful tool to study the internalization of cell-penetrating peptides. *Bba-Biomembranes* **1798**, 2182-2189, doi:10.1016/j.bbamem.2009.11.011 (2010).
117 Moghimi, S. M., Symonds, P., Murray, J. C., Hunter, A. C., Debska, G. & Szewczyk, A. A two-stage poly(ethylenimine)-mediated cytotoxicity: Implications for gene transfer/therapy. *Molecular Therapy* **11**, 990-995, doi:10.1016/j.ymthe.2005.02.010 (2005).
118 Baljon, J. J., Dandy, A., Wang-Bishop, L., Wehbe, M., Jacobson, M. E. & Wilson, J. T. The efficiency of cytosolic drug delivery using pH-responsive endosomolytic polymers does not correlate with activation of the NLRP3 inflammasome (vol 7, pg 1888, 2019). *Biomater Sci-Uk* **7**, 2200-2200, doi:10.1039/c9bm90022e (2019).
119 Weimershaus, M., Mauvais, F. X., Saveanu, L., Adiko, C., Babdor, J., Abramova, A., Montealegre, S., Lawand, M., Evnouchidou, I., Huber, K. J., Chadt, A., Zwick, M., Vargas, P., Dussiot, M., Lennon-Dumenil, A. M., Brocker, T., Al-Hasani, H. & van Endert, P. Innate Immune Signals Induce Anterograde Endosome Transport Promoting MHC Class I Cross-Presentation. *Cell Rep* **24**, 3568-3581, doi:10.1016/j.celrep.2018.08.041 (2018).
120 Staring, J., Raaben, M. & Brummelkamp, T. R. Viral escape from endosomes and host detection at a glance. *J Cell Sci* **131**, doi:10.1242/jcs.216259 (2018).
121 Reits, E., Griekspoor, A., Neijssen, J., Groothuis, T., Jalink, K., van Veelen, P., Janssen, H., Calafat, J., Drijfhout, J. W. & Neefjes, J. Peptide diffusion, protection, and degradation in nuclear and cytoplasmic compartments before antigen presentation by MHC class I. *Immunity* **18**, 97-108, doi:Doi 10.1016/S1074-7613(02)00511-3 (2003).
122 Gentilucci, L., De Marco, R. & Cerisoli, L. Chemical Modifications Designed to Improve Peptide Stability: Incorporation of Non-Natural Amino Acids, Pseudo-Peptide Bonds, and Cyclization. *Curr Pharm Design* **16**, 3185-3203, doi:Doi 10.2174/138161210793292555 (2010).
123 Ngambenjawong, C., Gustafson, H. H., Pineda, J. M., Kacherovsky, N. A., Cieslewicz, M. & Pun, S. H. Serum Stability and Affinity Optimization of an M2 Macrophage-Targeting Peptide (M2pep). *Theranostics* **6**, 1403-1414, doi:10.7150/thno.15394 (2016).

124 Starr, C. G. & Wimley, W. C. Antimicrobial peptides are degraded by the cytosolic proteases of human erythrocytes. *Bba-Biomembranes* **1859**, 2319-2326, doi:10.1016/j.bbamem.2017.09.008 (2017).

Chapter 4

Replacement of L-amino acid peptides with D-amino acid peptides mitigates anti-PEG antibody generation against polymer-peptide conjugates in mice[4]

*Meilyn Sylvestre, *Shixian Lv, Lucy F. Yang, Nicholas Luera, David J. Peeler, Bing-Mae Chen, Steve R. Roffler, and Suzie H. Pun
*equally contributing authors

4.1 Abstract

The generation of anti-PEG antibodies in response to PEGylated proteins, peptides, and carriers significantly limits their clinical applicability. IgM antibodies mediate the clearance of these therapeutics upon repeat injection, resulting in toxicity and hindered therapeutic efficacy. We observed this phenomenon in our polymer platform, virus-inspired polymer for endosomal release (VIPER), which employs pH-sensitive triggered display of a lytic peptide, melittin, to facilitate endosomal escape. While the polymer-peptide conjugate was well tolerated after a single injection, we observed unexpected mortality upon repeat injection. Thus, the goal of this work was to enhance the safety and tolerability of VIPER for frequent dosing. Based on previous reports on anti-PEG antibodies and the adjuvant activity of melittin, we characterized the antibody response to polymer, peptide, and polymer-peptide conjugates after repeat-dosing and measured high IgM titers that bound PEG. By substituting the L-amino acid peptide for its D-amino acid enantiomer, we significantly attenuated the anti-PEG antibody generation and toxicity, permitting repeat-injections. We attempted to rescue mice from L-melittin induced toxicity by prophylactic injection of platelet activating factor (PAF) antagonist CV-6209, but observed minimal effect, suggesting that PAF is not the primary mediator of the observed hypersensitivity response. Overall, we demonstrated that the D-amino acid polymer-peptide conjugates, unlike L-amino acid polymer-peptide conjugates, exhibit good tolerability *in vivo*, even upon repeat administration, and do not elicit the generation of anti-PEG antibodies.

---

[4] *Reprinted with permission from Sylvestre, M., Lv, S., et al. Replacement of L-amino acid peptides with D-amino acid peptides mitigates anti-PEG antibody generation against polymer-peptide conjugates in mice. J Control. Rel., **331**, 142-153 (2021). Copyright 2021 Elsevier B.V.*

4.2 Introduction

PEGylated proteins and peptides are clinically-successful delivery formulations and among the highest revenue therapeutics on the market.[1] However, anti-PEG antibodies, which can result in increased drug clearance, hypersensitivity responses, and reduced efficacy, remain a significant clinical hurdle.[2,3] Recent studies have reported toxicity following repeat-administration of PEG-containing therapeutics, which has been linked with accelerated blood clearance (ABC) mediated by an anti-PEG antibody response, resulting in rapid clearance of PEGylated carriers, complement activation, and anaphylactic reaction.[4-8] For example, a significant fraction of patients receiving PEGylated urate oxidase (38%) developed anti-PEG antibodies after injection, significantly hindering therapeutic efficacy.[9] Furthermore, the presence of anti-PEG antibodies has been closely associated with rapid clearance of PEG-asparaginase (ASP), rendering the therapy ineffective.[6] In fact, pre-existing anti-PEG antibodies have been identified as a risk factor to predict patient reactions to PEG-ASP, emphasizing the clinical importance of anti-PEG antibodies.[10] Seminal work by Richter and Akerblom first revealed that anti-PEG antibodies are generated after injection of animals with PEG-conjugated proteins, but not with free PEG.[11] These studies and others reveal that the conjugated biologics act as adjuvants in inducing anti-PEG antibodies; indeed, the extent and presence of anti-PEG antibodies generally correlates with the immunogenicity of conjugated protein.[12-14] These findings from the history of PEGylated proteins reveal important immunogenicity considerations for the growing suite of polymer-protein and polymer-peptide conjugates that are in preclinical development for biologics delivery.[15,16] While other anti-polymer antibodies have been identified (e.g., against silicone breast implants), anti-PEG antibodies are the best studied and this work may be generalized for other polymer-conjugates.[17]

We incorporated PEG into our polymer platform, virus-inspired polymer for endosomal release (VIPER), which facilitates pH-triggered, intracellular delivery of therapeutic cargos.[18,19] Briefly, VIPER comprises a hydrophilic and hydrophobic block that self-assemble into micelles. The lytic peptide melittin is conjugated to the hydrophobic block, which undergoes a sharp phase transition at acidic pH for triggered display and endosomal rupture. Thus, melittin is shielded at physiological pH 7.4 but is exposed at endosomal pH 5.7, rupturing the endosome for cargo delivery to the cell cytosol. In contrast to previous iterations of VIPER, this work utilized a PEG

hydrophilic block instead of pOEGMA. We observed that this formulation was well tolerated following a single intravenous (i.v.) injection, but triggered unexpected mortality upon repeat-dosing of melittin-containing micelles. The goal of this work was to improve the safety and tolerability of VIPER for frequent i.v. dosing. While this work specifically focused on VIPER, a peptide-conjugate wielding the immunogenic peptide melittin, these findings can be broadly applied to other polymer-peptide conjugates with biologically-active peptides.

Because mortality was only observed upon repeat-dosing, we posited that toxicity was associated with an adaptive immune response rather than the inherent lytic activity of melittin. Specifically, we hypothesized that melittin acted as an adjuvant to induce an antibody response against the polymer carrier, resulting in anti-PEG antibody generation and toxicity A growing body of literature utilizes the adjuvant activity of melittin in vaccines to markedly enhance antibody titers.[20,21] Yet, this immunogenic activity of melittin can be reduced by replacing L-amino acids with D-amino acids, resulting in lower antibody generation.[22-24] Broadly, D-amino acid substitutions can reduce peptide:MHC affinity and subsequent presentation efficiency to T and B cells, reducing immunogenicity *in vivo* and attenuating IgG and IgM antibody response.[24,25] Applying these findings to our polymer-peptide platform, we hypothesized that utilizing D-melittin instead of L-melittin would diminish anti-PEG antibody generation, reducing immunogenicity and permitting repeat-dosing.

In this work, we compared the *in vitro* activity and *in vivo* safety of L- and D-melittin VIPER micelles. First, we validated comparable peptide and micelle activity *in vitro* by cytotoxicity and hemolysis assays, and confirmed endosomal rupture. Next, we compared the maximum tolerated dose (MTD) of L-melittin VIPER-micelles (LMM) and D-melittin VIPER-micelles (DMM). Using an immunodeficient nonobese diabetic-severe combined immunodeficiency (nod-*scid*) mouse model, we confirmed that LMM-toxicity was associated with an immune response. We then investigated antibody generation against peptide, micelles, and polymer upon repeat-injection of LMM or DMM *via* enzyme linked immunosorbent assay (ELISA). Finally, we evaluated the efficacy of a platelet-activating factor (PAF) antagonist to rescue mice from toxicity. Ultimately, we demonstrated that while LMM and DMM behaved similarly *in vitro*, DMM promoted an enhanced safety profile *in vivo*. Mice treated with DMM exhibited a higher MTD and tolerated

four injections, whereas mice receiving LMM only tolerated two injections. This can be attributed to the generation of anti-PEG antibodies: LMM induced a robust IgG and IgM antibody response against PEG, whereas DMM did not. Overall, we showed that polymer-peptide conjugates with D-amino acid peptides mitigate the production of anti-carrier antibodies and are safe for frequent dosing. This work has major implications for protein- and peptide-PEG conjugates, as we demonstrate that reducing the immunogenicity of the biologic can reduce generation of anti-polymer antibodies.

4.3 Results

4.3.1 Synthesis of melittin micelles

The polymer was synthesized as by reversible addition-fragmentation chain-transfer (RAFT) polymerization of 2-diisopropylaminoethyl methacrylate (DIPAMA) and pyridyl disulfide ethyl methacrylate (PDSEMA) using PEGylated macro chain transfer agents (CTAs) (**Figure 4.1A**). In contrast to previous iterations of VIPER, we used a PEG block instead of pOEGMA, as PEG confers increased solubility and is commercially available. The pH-sensitive block comprised DIPAMA, which transitions sharply from hydrophobic to hydrophilic at acidic pH, copolymerized with PDSEMA, which enables conjugation with thiolated peptides. The block copolymers self-assemble into micelles at physiological pH 7.4, but disassemble into polymer chains below endosomal pH 6.3. Thus, peptides conjugated to DIPAMA are shielded at pH 7.4, but are exposed upon cellular internalization into endosomes.

The molar ratio of ethylene glycol, DIPAMA, and PDSEMA was found to be 113:40:2 by ^{1}H NMR (**Supplemental Figure 4.1**). Therefore, the polymer was determined to be PEG_{113}-*b*-p($DIPAMA_{40}$-*co*-$PDSEMA_{2}$). This polymer structure without conjugated peptide is referred to as control polymer (CP). L or D-melittin was incorporated by disulfide exchange at a polymer:peptide feeding ratio of 1:1.5, yielding L-melittin or D-melittin micelles (LMM or DMM, respectively) with a final peptide loading content of 16.2 wt%. UV absorbance at 353 nm was used to monitor conjugation kinetics, which showed that the conjugation reaction occurred rapidly in the mixture solvent of methanol and water (V:V 5:1) (**Supplemental Figure 4.2**). We confirmed that polymer and polymer-peptide conjugates self-assembled into micelles at pH 7.4 with hydrodynamic diameters of 34.6 ± 9.9, 32.9 ± 12.5, and 32.2 ± 11.0 nm for CP, LMM, and DMM, respectively

(**Figure 4.1B**) (**Table 4.1**). Critical micellar concentration (CMC) of the micelles was assessed using the Nile red method (ex/em 557/625 nm), and was determined to be 0.017, 0.027, and 0.030 mg/mL for CP, LMM, and DMM, respectively (**Table 4.1**) (**Supplemental Figure 4.3**). Micelles were tested for pH-sensitivity in buffers with various pH, and the pH transition point was determined to be pH 6.3, which is consistent with that of p(DIPAMA) (**Figure 4.1C, D**). Lastly, micelles demonstrated long term stability for 48 hours in the presence of serum (10% FBS) at 37 ºC (**Supplemental Figure 4.3**). Overall, these data show that the synthesized micelles have comparable physical properties independent of peptide conjugation, similar to findings in our previous work.[19]

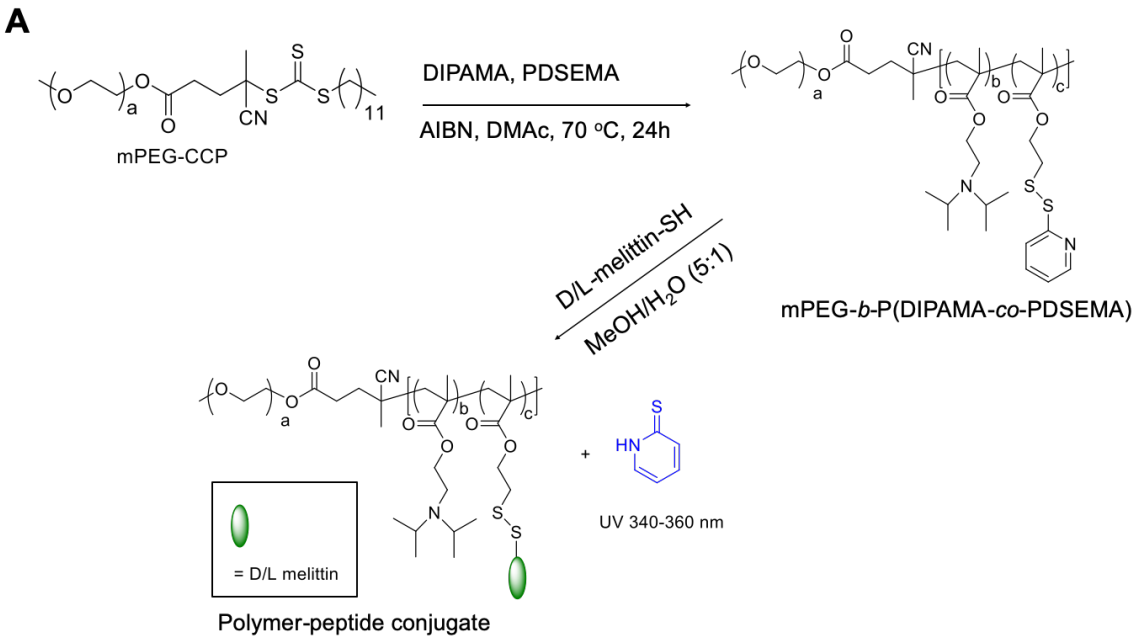
A
mPEG-CCP
DIPAMA, PDSEMA
AIBN, DMAc, 70 °C, 24h
mPEG-b-P(DIPAMA-co-PDSEMA)
D/L-melittin-SH
MeOH/H2O (5:1)
UV 340-360 nm
= D/L melittin
Polymer-peptide conjugate

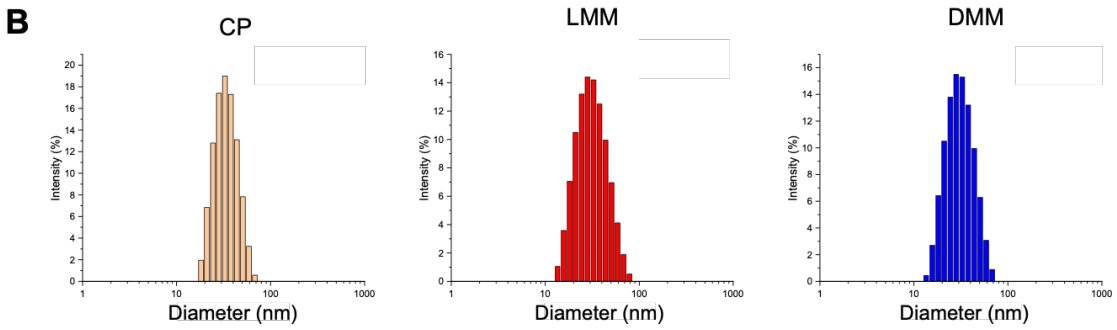
B
CP
LMM
DMM
Intensity (%)
Diameter (nm)

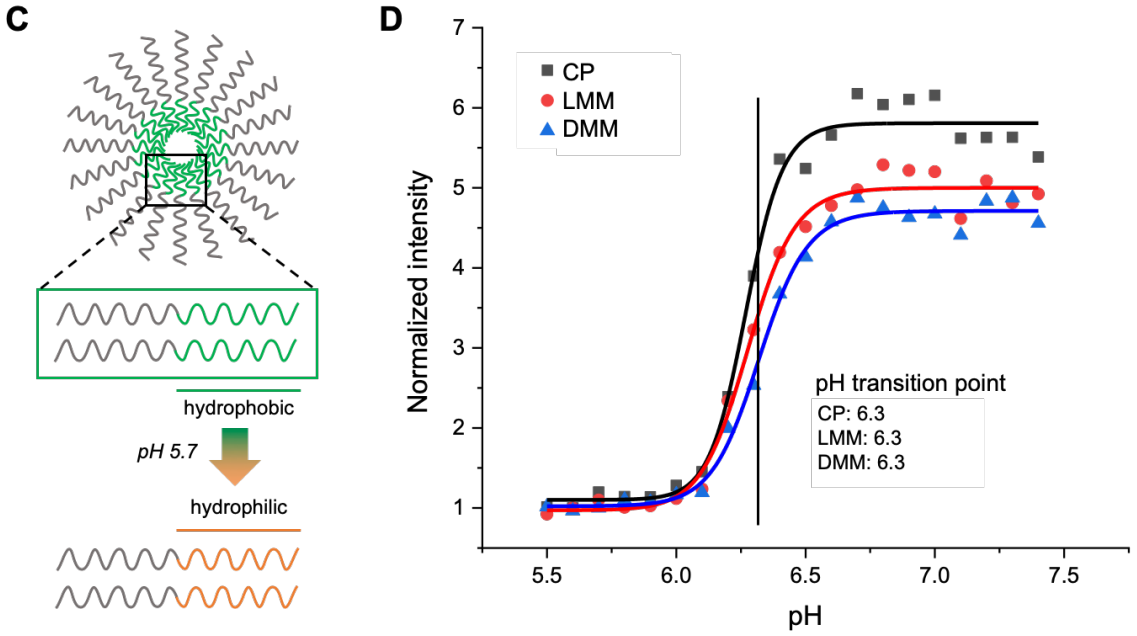
C
hydrophobic
pH 5.7
hydrophilic
D
CP
LMM
DMM
Normalized intensity
pH
pH transition point
CP: 6.3
LMM: 6.3
DMM: 6.3

Figure 4.1: Polymer synthesis of micelles. A) Micelles were synthesized by RAFT polymerization of PEG, DIPAMA, and PDSEMA. L- or D-melittin was conjugated onto the polymer via disulfide exchange, yielding L-melittin micelles (LMM) or D-melittin micelles (DMM). Micelles without peptide are denoted as control polymer (CP). B) The hydrodynamic diameter of micelles were assessed by dynamic light scattering (DLS) and was determined to be 34.6 ± 9.9, 32.9 ± 12.5, and 32.2 ± 11.0 nm for CP, LMM, and DMM, respectively. C) A schematic demonstrating the phase transition of DIPAMA, which switches from hydrophobic to hydrophilic at acidic pH. This enables pH-triggered display of melittin for endosomal escape. D) The transition point of micelles was determined to be pH 6.3 for CP, LMM, and DMM.

	Diameter (nm)	**CMC (mg/mL)**
CP	34.6 ± 9.9	0.017
LMM	32.9 ± 12.5	0.027
DMM	32.2 ± 11.0	0.030

Table 4.1: Characterization of micelles. The hydrodynamic diameter of micelles was determined by DLS. The critical micelle concentration was determined by Nile Red.

4.3.2 In vitro activity of L- and D-melittin peptides and micelles is comparable

Because melittin is a lytic peptide, we validated *in vitro* activity of melittin and micelles by measuring cytotoxicity and blood hemolytic activity. To determine cytotoxicity, we incubated RAW 264.7 cells with peptide and micelles for 24h and measured viability by an MTS/PMS assay. Both L- and D-melittin peptides and micelles demonstrated comparable toxicity, as indicated by similar half maximal inhibitory concentrations (IC_{50}) (**Figure 4.2A-B**) (**Table 4.2**). To assess hemolytic activity, we incubated human red blood cells (RBCs) with peptides and micelles at pH 6.4 and 7.4 and evaluated lysis (**Table 4.2**).[26] We expected peptides to have similar hemolytic activity regardless of pH, whereas we expected micelles to only be lytic at acidic pH (**Figure 4.2C-F**). While peptides demonstrated slightly higher hemolytic activity at neutral pH 7.4 compared to acidic pH 6.4, this slight difference could be attributed to peptide aggregation, which is influenced by salt concentration and pH of the buffer.[27] We observed ~100% lysis by LMM and DMM at pH 6.4, and no lysis at pH 7.4, confirming that VIPER successfully shields melittin at physiological

pH and only triggers display of melittin at acidic pH. Both LMM and DMM exhibited comparable hemolytic concentrations for 50% RBC lysis (HC_{50}) (**Figure 4.2E-F**). Lastly, we assessed the ability of LMM and DMM to escape the endosome in a Gal8-GFP-RAW 264.7 reporter cell line (**Figure 4.2G**).[28] Gal8-GFP is constitutively expressed throughout the cell cytoplasm. Upon endosomal disruption, Gal8-GFP redistributes and binds to the inner face of endosomal membranes; disrupted endosomes are expressed as green punctate in cells. Micelles (12.5 μM peptide) were incubated with cells for 16-18 h at 37 ºC, fixed, and stained for nuclei. Cells were imaged on a confocal microscope. Both LMM and DMM induced GFP^+ punctate, confirming that both formulations disrupt the endosome. Micelles without melittin (CP) had no lytic or cytotoxic activity (**Supplemental Figure 4.4**).

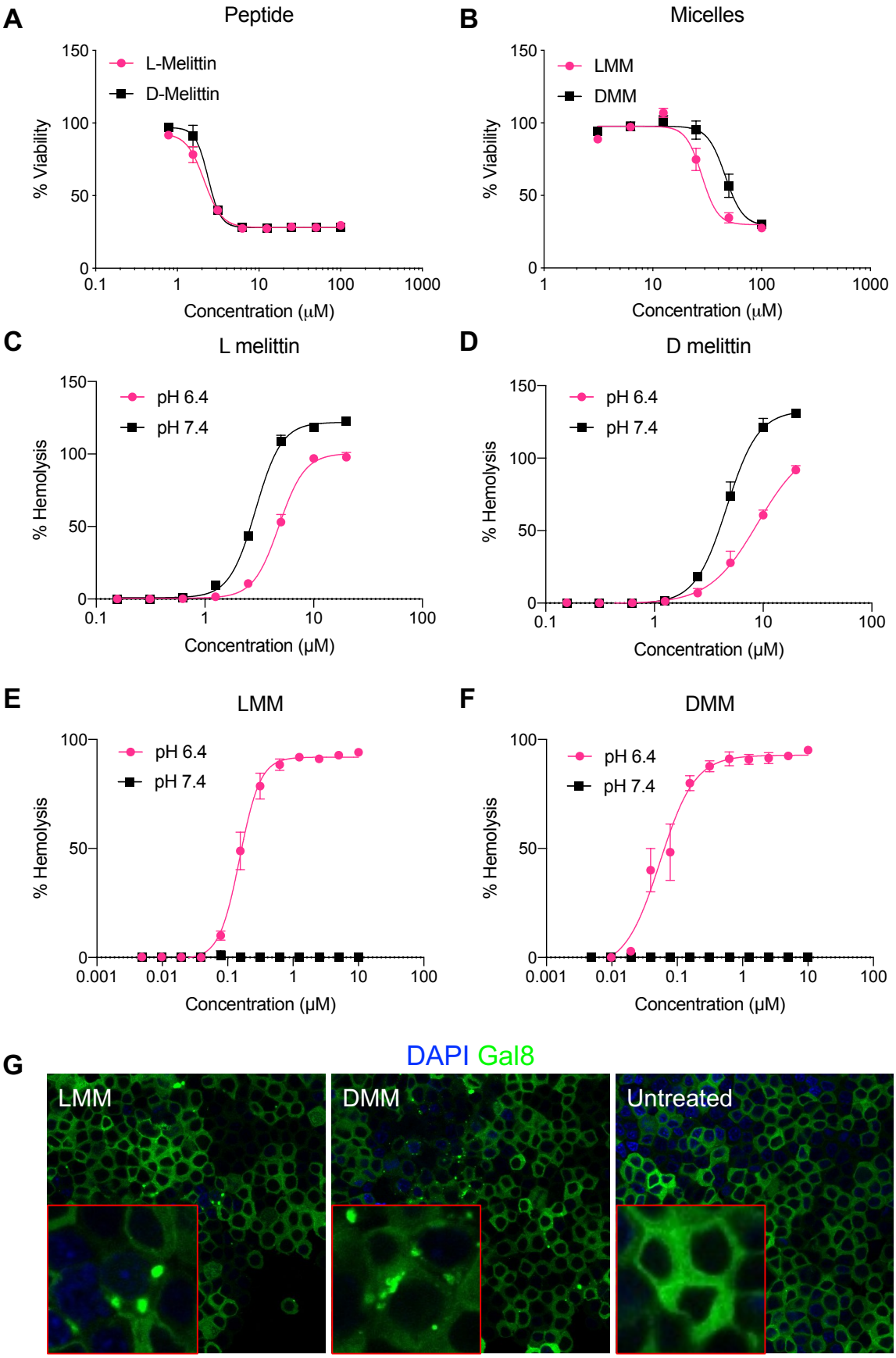
A
Peptide
L-Melittin
D-Melittin
% Viability
Concentration (μM)
B
Micelles
LMM
DMM
% Viability
Concentration (μM)
C
L melittin
pH 6.4
pH 7.4
% Hemolysis
Concentration (μM)
D
D melittin
pH 6.4
pH 7.4
% Hemolysis
Concentration (μM)
E
LMM
pH 6.4
pH 7.4
% Hemolysis
Concentration (μM)
F
DMM
pH 6.4
pH 7.4
% Hemolysis
Concentration (μM)
G
DAPI Gal8
LMM
DMM
Untreated

Figure 4.2: In vitro activity of L- and D-melittin peptides and micelles. A-B) L- and D-melittin peptide (A) and micelles (B) were incubated with RAW 264.7 cells for 24 h and viability was assessed. C-F) Hemolytic activity of peptide (C-D) and micelles (E-F) was evaluated against RBCs at pH 6.4 and 7.4. G) Endosomal disruption by LMM and DMM was evaluated in Gal8-GFP-RAW 264.7 cells. Endosomal disruption is expressed as GFP^+ (green) punctae as Gal8-GFP binds to the inner face of endosomal membranes. Image insets (outlined in red) are single-cell magnification images.

	Viability	**Hemolysis HC_{50} (μM)**	
	IC_{50} (μM)	*pH 6.4*	*pH 7.4*
	Peptide		
L-melittin	2.13 ± 0.1	4.80 ± 0.1	2.92 ± 0.5
D-melittin	2.38 ± 0.1	8.89 ± 0.7	4.63 ± 0.1
	Micelles		
LMM	28.23 ± 2.7	0.15 ± 0.004	N/A
DMM	46.42 ± 2.0	0.05 ± 0.004	N/A

Table 4.2: Cytotoxic and hemolytic activity of melittin. The half maximal inhibitory concentration (IC_{50}) of L- and D-melittin peptide and micelles was determined against RAW 264.7 cells after 24 h incubation. The hemolytic concentration that lysed 50% of red blood cells (RBCs) (HC_{50}) was determined against human RBCs after 1h incubation.

4.3.3 Incorporation of D-melittin increases maximum tolerated dose (MTD)

Due to similar *in vitro* behavior, we expected LMM and DMM to exhibit similar *in vivo* activity. We did not measure safety of peptide alone, as this has been reported previously.[24,29] We determined the MTD by injecting micelles i.v. at 10, 20, 30, or 40 mg melittin/kg into normal mice and recording survival and weight for 14 days. The MTD of DMM was twice that of LMM; mice tolerated DMM at a dose up to 20 mg/kg, whereas LMM was tolerated only up to 10 mg/kg. Several mice (2/4) survived DMM injection at 30 mg/kg, whereas no mice (0/4) tolerated LMM at the same dose. Most mice (3/4) survived LMM injection at 20 mg/kg, but all mice (4/4) survived DMM at the same dose (**Figure 4.3A-B**). Cohorts receiving 20 mg/kg of LMM or 30 mg/kg of

DMM exhibited weight loss in the days immediately following injection, but weight rapidly recovered within 4 days (**Figure 4.3C-D**). No mice survived injection of 40 mg/kg of either LMM or DMM. Together, these results indicate there is some acute toxicity for both peptide-micelle analogues at high concentrations, likely due to the lytic activity of melittin, but DMM are better tolerated overall. Based on survival and weight loss, we determined the MTD of LMM and DMM as approximately 10 and 20 mg/kg, respectively (**Table 4.3**).

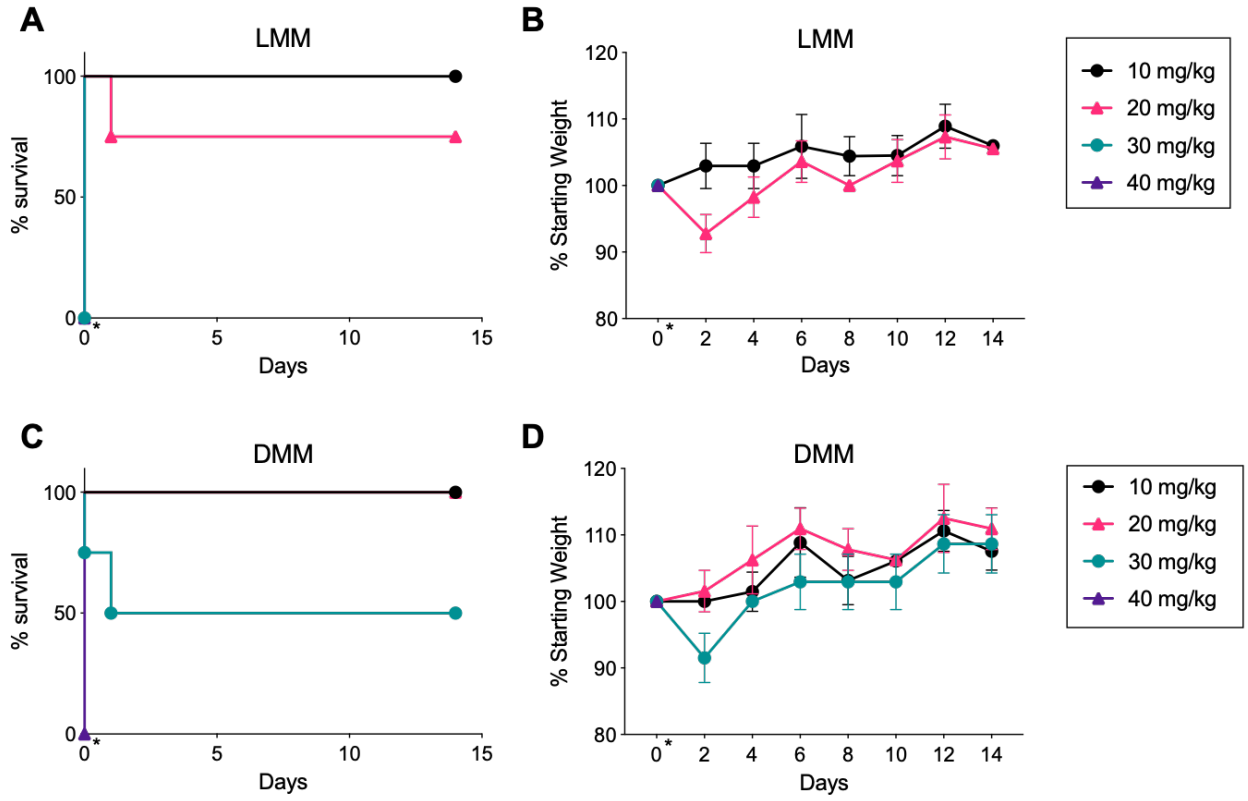

Figure 4.3: MTD determination of LMM and DMM. A-B) Survival and weight of normal mice injected with LMM at 10, 20, 30, or 40 mg/kg. The day of injection (day 0) is indicated with an asterisk (*). Weight was measured for 14 days following injection. C-D) Survival and weight of mice injected with DMM at 10, 20, 30, or 40 mg/kg. (n = 4 mice/group)

Death of mice		
Dose	*LMM*	*DMM*
10 mg/kg	0/4	0/4
20 mg/kg	1/4	0/4

30 mg/kg	4/4	2/4
40 mg/kg	4/4	4/4

Table 4.3: Death of mice after LMM or DMM injection. Based on survival and weight loss, the MTD of LMM and DMM was determined as approximately 10 and 20 mg/kg, respectively. (n = 4 mice/group)

4.3.4 Incorporation of D-melittin enables safe, repeated dosing of micelles

Next, we investigated the safety of repeat injections of melittin micelles in normal mice. Mice were injected IV with LMM or DMM at 5 mg melittin/kg every 4th day for a total of 4 injections. This dose was chosen as it is below the MTD of both peptide-micelles, enabling us to evaluate the safety of micelles without attributing death to acute toxicity. While the cumulative dosage is the MTD of LMM, we hypothesized that the micelles would demonstrate less toxicity than a single bolus when accounting for clearance and recovery time between injections. While all mice tolerated the first two injections well, as indicated by maintenance of weight, none of the mice (0/6) in the LMM cohort survived the 3rd injection (**Figure 4.4A-B**). Some mice (2/6) died within the first 2 hours following injection; the remaining mice (4/6) died within the next 24 hours. Mice exhibited signs of anaphylaxis, such as lethargy, loss of activity, and depressed breathing. All mice (6/6) in the DMM cohort survived and tolerated the remaining 3rd and 4th injections well. Mice injected with DMM exhibited no adverse effects, even at 21 days past the 4th injection. We hypothesized that the 3rd injection of LMM triggered the observed toxicity and mortality, as no weight loss or abnormal behavior was observed in mice following the 2nd injection.

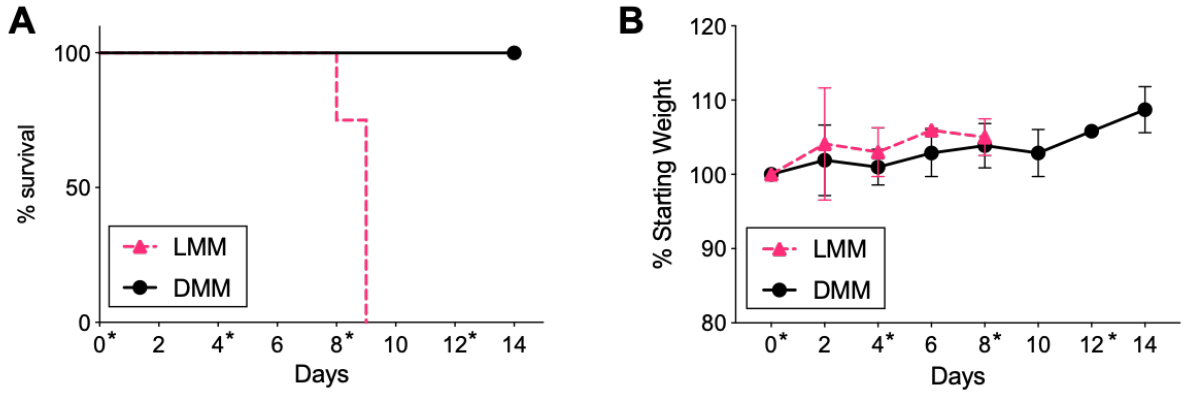

Figure 4.4: Survival and weight of mice receiving repeat injections of LMM and DMM. A) Mice were injected with LMM or DMM at 5 mg/kg every 4 days, for a total of 4 injections. All mice(6/6) receiving LMM died after the 3rd injection; all mice (6/6) receiving DMM tolerated all 4 injections well. Days of injection (0, 4, 8, 12) are indicated with an asterisk (*). B) Mice weight was recorded following injection with LMM or DMM. (n = 6 mice/group)

4.3.5 The adaptive immune response is attenuated in DMM-treated mice

Because mice receiving LMM died following the 3rd injection, but exhibited no adverse effects between injections, we hypothesized that an adaptive immune response was triggered upon receiving the 3rd treatment. This immune response was activated specifically by LMM, since we did not observe any deaths with repeat injections of DMM. To confirm that the immune system played a role in the death of mice upon repeat-injection, we injected normal and immune-deficient nod-*scid* gamma (NSG) mice with LMM at 2, 4, 6, and 8 mg/kg every 4th day. Both mice are on a Balb/c background, accounting for differences that could be attributed to mouse strain.[23] We investigated a wider range of concentrations to better understand the influence of individual injection dose on toxicity upon repeat injection. Normal mice injected at doses above 5 mg/kg exhibited weight loss after the second injection, while no weight loss was observed in mice receiving doses below 5 mg/kg (**Figure 4.5A**). Due to this extreme weight loss, mice at 6 and 8 mg/kg did not receive the 3rd and 4th injections. NSG mice did not exhibit weight loss, regardless of dose, and tolerated repeat injections at 6 and 8 mg/kg (**Figure 4.5B**).

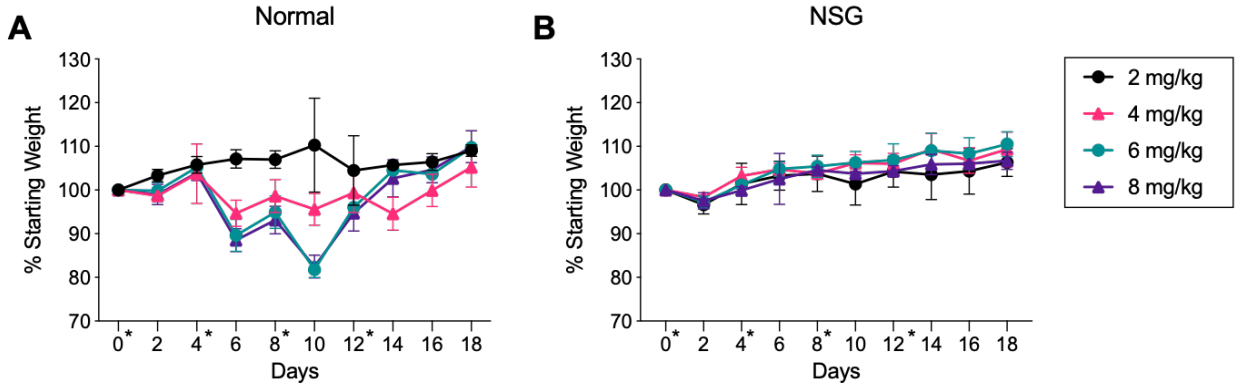

Figure 4.5: LMM injections in normal and NSG mice. Normal (A) or NSG (B) mice were injected i.v. with LMM at 2, 4, 6, and 8 mg/kg. Normal mice were not administered the 3rd or 4th injection at 6 or 8 mg/kg due to weight loss. Days of injection (0, 4, 8, 12) are indicated with an asterisk (*). (n = 4 mice/group)

Because normal mice experienced weight loss but NSG mice were unaffected, this study supported our hypothesis that an inflammatory adaptive immune response was responsible for adverse effects of LMM dosing. Therefore, we next investigated antibody generation following repeat injection of micelles. Because prior results indicated that mice tolerated the first two injections well, we investigated antibody titers immediately after the 3rd injection. Mice were injected IV with LMM or DMM micelles at 5 mg/kg every 4th day. Immediately following the 3rd injection, mice were sacrificed and serum was assessed for IgG and IgM antibodies against micelles, polymer, and peptide via ELISA. IgG and IgM antibodies were evaluated because of their role in binding to PEGylated conjugates and mediating type II hypersensitivity reactions. LMM-treated mice generated significant IgG and IgM antibody titers against LMM, CP, and 10k PEG (**Figure 4.6A-F**). In contrast, antibodies from DMM-treated mice were often below the limit of detection. Antibodies in LMM or DMM-treated mice primarily bound to polymer, with very little binding to peptide, confirming that LMM induced anti-PEG antibodies (**Figure 4.6G-H**). Control mice that did not receive peptide-micelles generated negligible levels of IgG or IgM antibodies (**Supplemental Figure 4.5**).

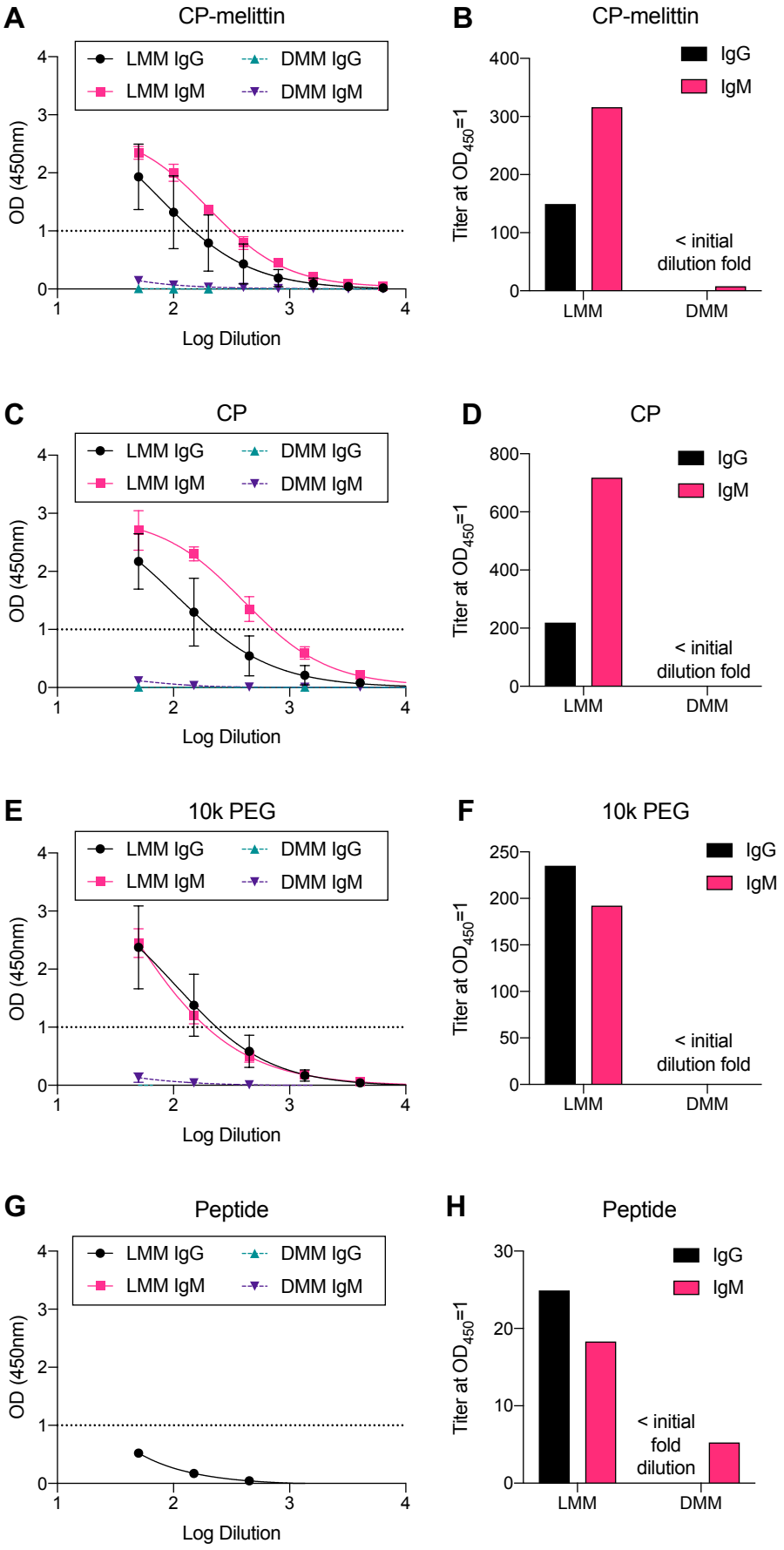
A
CP-melittin
LMM IgG
LMM IgM
DMM IgG
DMM IgM
OD (450nm)
Log Dilution
B
CP-melittin
IgG
IgM
Titer at OD450=1
< initial dilution fold
LMM
DMM
C
CP
D
CP
E
10k PEG
F
10k PEG
G
Peptide
H
Peptide
< initial fold dilution

Figure 4.6: IgG and IgM antibodies against micelles, polymer, and peptide. Mice were injected i.v. with LMM or DMM (5 mg/kg). Immediately after the 3rd injection, mice were sacrificed and serum was analyzed for IgG and IgM antibodies against micelles (A,B), CP (C,D), 10k PEG (E,F), or peptide (G,H).

We also investigated liver toxicity following repeat injection of micelles via hematoxylin and eosin (H&E) staining and liver enzyme (alanine transaminase (ALT), aspartate transaminase (AST)) activity in serum. Mice were injected with either PBS, LMM, or DMM at 5 mg/kg on days 0 and 4. Mice were sacrificed 6 hours after receiving the 2nd injection to avoid the mortality observed after the 3rd injection with LMM. Liver H&E was completed and no abnormalities in the liver were observed in any of the mice (**Figure 4.7A-C**). This suggests that hepatotoxicity is not a factor in the observed deaths. ALT and AST levels were within the normal range for all groups as well, further supporting this conclusion[30,31] (**Figure 4.7D-E**).

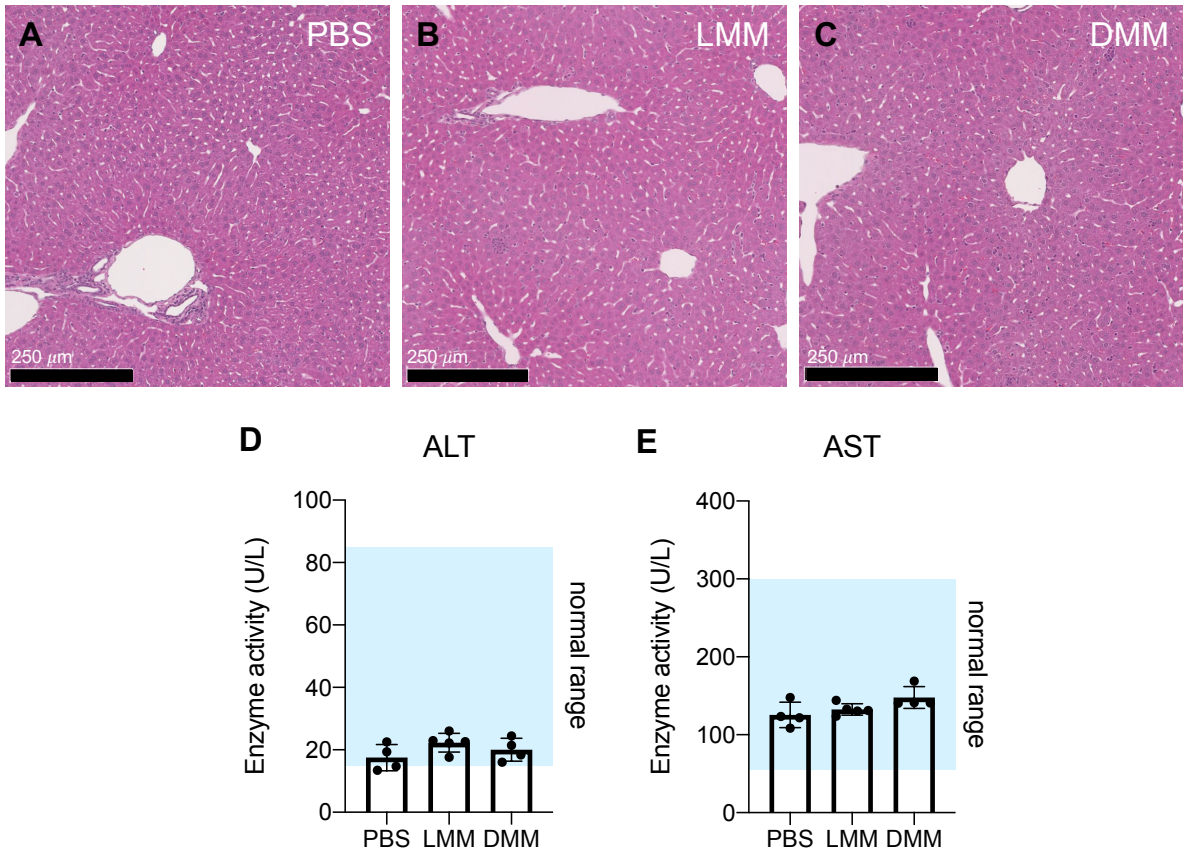

Figure 4.7: *Liver toxicity after micelle injection was evaluated by H&E and ALT/AST activity. Mice were injected IV with PBS, LMM, or DMM (5 mg/kg) on days 0 and 4. Six hours after the 2nd injection, mice were sacrificed and livers and serum were collected for H&E staining (A-C) or liver enzyme (ALT, AST) analysis (D, E). H&E images are at 10X magnification (n = 3 mice/group). (For ALT/AST analysis, n = 4-5 mice/group)*

4.3.6 PAF receptor antagonist extends survival but does not rescue mice

Based on micelle toxicity and immune response, we hypothesized that the platelet activating factor (PAF) receptor could be associated with both acute and adaptive toxicity. PAF is a phospholipid signaling molecule that plays a central role in normal and pathological responses, particularly inflammation, allergy, and shock.[32,33] Its receptor, PAFR, is expressed on the surface of many cells, including platelets, macrophages, and neutrophils. PAF has been implicated in the immune response against lipid nanoparticles, in which mice exhibited signs of acute toxicity and shock-like symptoms (*e.g.,* edema, hypovolemia). Prophylactic blockade of the PAFR can rescue mice and completely prevent immune-mediated toxicity against lipid nanoparticles.[34-36]

We observed shock-like symptoms in mice following injection of a high single dose or repeat-dosing of micelles that we linked to an immune response. Thus, we next attempted to rescue mice with an intraperitoneal (i.p.) injection of PAFR antagonist CV-6209 prior to micelle injection, as reported.[34,35] We sought to rescue normal Balb/c mice from LMM-associated toxicity prior to either a single injection at 30 mg/kg or a 3rd injection at 5 mg/kg. The dose of 30 mg/kg was selected because it is above the MTD of both LMM and DMM. Furthermore, some mice (3/4) survived treatment with LMM at 20 mg/kg, but none (0/4) survived treatment at 30 mg/kg. Thus, this selected dose would ensure that rescue could be attributed to pre-treatment with the PAF antagonist. We also investigated the effect of prophylactic treatment prior to the 3rd injection because of the toxicity at this dosing regimen; neither the first or second injections were toxic at the selected dose. CV-6209 was unable to rescue mice from acute toxicity at 30 mg/kg; all mice (4/4) died within 1 hour of LMM injection. However, CV-6209 did exhibit some prophylactic effect on mice receiving repeat-injections. Mice who did not receive CV-6209 died within 30-60 minutes of injection. Mice receiving CV-6209 exhibited some signs of toxicity but remained alert, active, and responsive. Yet, all treated mice died within 24 hours. Overall, CV-6209 was unable

to rescue mice from acute toxicity, but did extend survival by several hours in mice receiving repeat-injections.

4.4 Discussion and Conclusion

Here, we report the replacement of L-amino acid peptides with D-amino acid peptides in polymer-peptide conjugates to attenuate anti-polymer antibody generation. Specifically, we replaced L-melittin for D-melittin in our VIPER platform, which enhanced safety *in vivo* by increasing the MTD and reducing anti-PEG antibody generation, ultimately enabling frequent repeat-dosing. While these findings are specific to VIPER, they can be applied to other peptide-polymer systems.

We first validated that both L- and D- peptide and micelles possess similar physical properties (e.g., diameter, pH transition, and CMC) and biologic behavior *in vitro*, as demonstrated by comparable cytotoxicity, hemolysis, and endosomal disruption. These findings are consistent with those by Boeckle, et. al., who showed that PEI conjugates with D-melittin exhibited similar lytic activity to conjugates with L-melittin, but offered the advantage of being non-immunogenic.[37] Differences between the peptide analogues were primarily observed *in vivo,* as the MTD of DMM (20 mg/kg) was twice that of LMM (10 mg/kg). Significantly, DMM enabled frequent, repeat-dosing, whereas LMM resulted in premature mortality. We first confirmed that toxicity was immune-related by administering LMM to both normal and immunodeficient NSG mice and evaluating weight loss. NSG mice lack mature T and B cells, whereas normal mice have complete immune functionality. While normal mice rapidly lost weight following two repeat-injections, NSG mice maintained weight and tolerated all four injections. Thus, we posited that LMM induced anti-PEG antibodies in normal mice, which mediated toxicity and death upon repeat-injection. While anti-PEG antibodies can be generated in both a T cell dependent (TD) and independent (TI) mechanism, it is likely that the immune response raised by VIPER is TD. A report by Mima, et. al. demonstrated that the immunogenic conjugate PEG-OVA induced anti-PEG antibodies, whereas free PEG did not. This immune response was determined to be TD, as antibodies were generated in normal mice but not in T cell deficient mice.[12] These results are parallel to our findings, as our peptide-polymer platform raised anti-PEG antibodies, but polymer micelles without peptide did not. In contrast, antibodies generated in a TI manner trigger antibody formation

regardless of cargo, as Ichihara, et. al. showed that empty PEGylated liposomes elicited anti-PEG IgM in normal and T cell deficient mice.[38]

We next evaluated the antibody response to micelles upon repeat injection. In PEGylated platforms, IgM is the primary antibody generated and is responsible for the rapid clearance of PEGylated liposomes, protein-, and peptide-conjugates.[12,39,40] ELISA analysis of generated antibodies exhibited the specificity of anti-PEG IgM antibodies for the terminal methoxy or the backbone of the polymer.[41,42] In this work, we observed that LMM-treated mice generated robust IgG and IgM antibody response against micelles and polymer, while DMM-treated mice generated a negligible antibody response. Antibodies from LMM-treated mice bound both LMM and CP (no melittin) micelles, suggesting that the polymer, rather than the peptide, is the antigen target. We confirmed this by assessing antibody binding against 10k PEG, which validated that antibodies bound the polymer. These anti-PEG antibodies demonstrated higher binding to polymer micelles than to 10k PEG, which has also been observed with other clones of anti-PEG antibodies (data not shown). This phenomenon could perhaps be explained by micelle structure, which could increase avidity and facilitate a higher observed binding affinity. Lastly, antibodies showed negligible binding to peptide without polymer. These results support our hypothesis that induced toxicity is due to a hypersensitivity response against LMM, in which L-melittin acts as an adjuvant to elicit antibodies against the PEG in the polymer backbone. The first two injections prime the immune system to generate antibodies against the carriers, and the third injection triggers the generation of IgG and IgM antibodies against the PEG backbone.[43] In contrast, DMM did not generate an antibody-based immune response and was well tolerated in four repeat-injections. These results are supported by the literature, as the adjuvant activity of L-melittin and the reduced immunogenicity of D-melittin have been reported. [5,20,24] Neither formulation elicited liver toxicity, as evaluated by H&E liver staining and ALT/AST enzyme activity in serum.

Lastly, we investigated the role of PAF in toxicity following acute and repeat-dosing of LMM, as PAFR has been implicated in lipid nanoparticle-associated toxicity.[34-36] Thus, we investigated the effect of prophylactic treatment with PAF antagonist CV-6209 prior to LMM injection of either a single injection (30 mg/kg) or repeat-injection (3rd treatment). While CV-6209 was unable to entirely rescue mice, it extended survival in mice receiving a repeat-injection, suggesting that the

PAFR is associated with LMM-toxicity. The inability to completely prevent mortality could be attributed to insufficient dose, requirement of a longer time period between CV-6209 and micelle injection, or involvement of other immune cascades that we have not yet identified.

Overall, we demonstrated that exchanging a natural peptide for its D-amino acid enantiomer mitigates the generation of anti-polymer antibodies, enabling safe, repeat-dosing of polymer-peptide conjugates. This phenomenon can be explained by the enhanced resistance to proteolytic degradation of D-peptides, preventing processing by antigen presenting cells and subsequent recognition and antibody generation by T and B cells.[24] Another report suggests that the lack of immunogenicity of D-amino acid analogues is due to enzymatic resistance, prolonging retention and circulation *in vivo*.[44] This delayed degradation could result in toxicity if the melittin is unable to be cleared from the body. However, we did not observe adverse effects at 7 or 14 days after repeat- or MTD injections, respectively.

Our work has additional implications for anti-cancer therapeutics. While VIPER employs melittin to facilitate endosomal escape, this lytic peptide has been used extensively in traditional medicines and cancer applications.[45-48] Melittin disrupts cell membranes to induce immunogenic cell death by releasing intracellular contents (e.g., tumor associated antigens) and stimulating T cell and natural killer cell immunity.[49-51] However, free peptide induces extensive non-specific hemolysis and severe off-target toxicity, and suffers from poor pharmacokinetics, requiring an appropriate drug delivery vehicle to realize its therapeutic potential.[52,53] Our findings can be applied to these carrier formulations, as we have demonstrated a strategy to enhance the safety of melittin, significantly attenuating the generation of anti-PEG antibodies and enabling safe, repeated dosing.

In conclusion, our findings add to the repertoire of strategies to enhance the safety of PEG-containing therapeutics. There is an increasing need to address this issue as the occurrence of anti-PEG in the healthy population has rapidly grown from ~0.2% to ~72% in the past four decades.[6,54,55] While Yang, et. al. found that the majority of people have low levels of anti-PEG antibodies, this study underscored the importance of pre-screening patients prior to administration of PEG-therapeutics. Another strategy to enhance the safety of PEG-conjugates is to suppress anti-PEG antibody generation, as we have shown here with D-amino acid peptide substitution. Approaching the problem from another side, Sherman, et. al. characterized the immunogenicity of

different PEG polymers and demonstrated that methoxy PEG was more immunogenic than hydroxy PEG, as methoxy PEG elicited higher antibody titers.[56] This strategy was effective in protein-polymer conjugates with interferon, uricase, and albumin. For cases in which pre-existing anti-PEG antibodies are already present, McSweeney, et. al. demonstrated that saturating anti-PEG antibody binding with infusion of 40 kDa restored PEGylated liposome circulation time.[57] Yet, despite these advances in characterizing the immunogenicity of PEGylated conjugates, there remains a need to better understand how the composition of PEGylated conjugates affects the generation and specificity of anti-PEG antibodies. Further discernment of the relationship between PEG architecture and immunogenicity is critical in order to create the next generation of biocompatible PEG-conjugates.

4.5 Experimental Procedures

Materials. PEG macro CTA was ordered from Sigma. PDSEMA was synthesized as described previously.[58] L- and D-melittin (GIGAVLKVLTTGLPALISWIKRKRQQC) peptides were synthesized through solid phase peptide synthesis on a microwave peptide synthesizer (Liberty Blue CEM) using L- or D-amino acids, respectively. Peptides were cleaved from resin in a trifluoroacetic acid (TFA) cocktail with 5% dimethoxybenzene 2.5% triisopropylsilane and 2.5% ethanedithiol, and 2.5% deionized water. Crude peptide was precipitated twice in cold diethyl ether and purified by reverse-phase HPLC using 0.1% TFA water and acetonitrile. Peptide molecular mass was determined by MALDI-TOF (University of Washington Department of Medicinal Chemistry Mass Spectrometry Center) in a CHCA:DHB 2:1 matrix. All other chemicals were purchased from Sigma and used as received.

Polymer synthesis. Block copolymer PEG_{113}-*b*-p($DIPAMA_{40}$-*co*-$PDSEMA_2$) was prepared with RAFT polymerization. In brief, PEG macro CTA (1000 mg, 0.182 mmol), DIPAMA (1850 mg, 7.58 mmol), PDSEMA (190 mg, 0.89 mmol) and azobisisobutyronitrile (AIBN) (3 mg, 0.018 mmol) were dissolved in 15 mL dimethylacetamide (DMAc), purged in argon, and immersed in an oil bath at 70°C.[18] After 24h, the polymerization was quenched with liquid nitrogen and the polymer was purified by dialysis against methanol for 2 days (yield: 80%). Synthesized peptides were conjugated to the PDSEMA monomer via disulfide exchange reaction in a mixture of methanol and water (5:1) at a polymer:peptide molar ratio of 1:1.5. After 8 h, the polymer-peptide

conjugates were purified by dialysis against DI water for 2 days. To prepare the micelles, the polymers or polymer-peptide conjugates were first dissolved in acidic phosphate buffer (pH 4.0), and the pH was adjusted to pH 7-8. All micelles were sterile filtered using a 0.22 mm pore filter.

Polymer characterization. Polymer was characterized by ^{1}H NMR on a Bruker AV 300 in deuterated chloroform ($CDCl_3$). Peptide conjugation with PDSEMA was monitored by UV at 353 nm for the release of 2-thiopyridine. Micelle size was assessed by dynamic light scattering (DLS) at 0.5 mg/mL in PBS 7.4. Critical micellar concentration (CMC) of the micelles was determined using a Nile red method (ex/em 557/625 nm) with 0.5 μg/mL of dye. The CMC was determined as the inflection point on the emission curve.

Cell culture. RAW 264.7 macrophages were obtained from ATCC and cultured in RPMI 1640 (Gibco) supplemented with 10% FBS (Gibco). For toxicity assays, macrophages were seeded at 15k cells/well in a 96-well plate. Cells were cultured with peptide or micelles for 24 hours and viability was determined by MTS/PMS (Promega) by plate reader. The Gal8-RAW 264.7 cell line was generated through similar means as described.[28] Briefly, RAW cells were co-transfected with plasmids containing a transposable Gal8-GFP construct and PiggyBac transposon (gift of Prof. Jordan Green) using Lipofectamine 2000 (3:1 molar ratio transposon:transposase plasmid). Cells were sorted for the top 5% brightest GFP^{+} singlet cell events using a FACS Aria sorter (BD), expanded, and sorted three more times to yield a population of Gal8-GFP^{high} cells.

Hemolysis assays. Hemolysis assays were conducted as described.[26] Human blood was obtained in accordance with guidelines established by the University of Washington Institutional Review Board. Briefly, human blood was washed in 150 mM NaCl and washed twice. Blood was transferred to PBS pH 7.4, washed, and resuspended in PBS at each pH to be tested (pH 6.4, 7.4). Blood was diluted 1:50 and 190 μl of diluted blood was plated in a V-bottom 96 well plate. Samples were incubated with peptide in appropriate pH at 37°C for 1h. Supernatant was transferred to a clear, flat bottom 96-well plate and absorbance (541 nm) was detected on a plate reader. Triton X-100 20% (w/v) was used as a positive control, and PBS at appropriate pH was used as a negative control.

Imaging. N01 coverslips were coated with bovine collagen I (Thermo) (45 μg/mL) for 1h at room temperature. Gal8-RAW 264.7 cells were plated (300-400k) onto coverslips overnight, and were incubated with peptide or micelles for 16-18h in complete media. Cells were fixed in 4% PFA and stained with DAPI (1:1000). Slides were imaged on a confocal microscope with a 63X oil immersion objective (Leica SP8X). For H&E imaging, livers were submitted to the UW Histology & Imaging Core for tissue processing and staining.

Animal studies. All animal studies were approved by the Institutional Animal Care and Use Committee at the University of Washington and were conducted in accordance use and regulations. Female Balb/c mice (6-8 weeks) were ordered from Charles River Laboratories. Particles were injected i.v. (intravenous) via tail vein injections at indicated doses. Mice were injected every 4th day. Mice were humanely euthanized when euthanasia criteria were met (e.g., hunched, squinting, low to no activity, depressed respiration). Terminal blood draws were collected from the vena cava after drug overdose or CO_2 euthanization. Serum was collected in serum separator tubes (BD) by allowing blood to coagulate for 30 minutes at room temperature, followed by centrifugation at 1000 xg for 10 minutes at 4 °C. Serum was stored at -80°C. For PAF rescue studies, mice were injected with PAF antagonist CV-6209 (Cayman) by intraperitoneal (i.p.) injection (50 μg per mouse) 5 minutes prior to micelle injection, as described.[34]

Enzyme linked immunosorbent assays (ELISA). Assays were performed as previously reported.[55,59] Briefly, micelles (1 μg/mL) were coated onto flat-bottom MaxiSorp 96-well plates overnight at 4 °C. Wells were washed with PBS and blocked with 5% skim milk (Difco) in PBS for 1h at room temperature. Wells were washed with PBS and incubated with serum (diluted in 2% skim milk) for 1h at room temperature on a shaker. Wells were washed twice with PBS and incubated with anti-mouse IgG-HRP or IgM-HRP secondary antibody (Jackson Laboratories) for 45 minutes at room temperature on a shaker. Wells were washed three times with PBS for 1 minute on a shaker, and incubated with TMB (Thermo) for 3-5 minutes. 2N H_2SO_4 was added to stop the reaction and absorbance (450 nm) was read on a plate reader. For peptide ELISAs, thiol-containing peptide (50 μg/mL) was immobilized onto maleimide coated plates (ThermoFisher) for 2h. Unreacted maleimides were blocked with free cysteine (10 mg/mL) for 1h, prior to continuing with the above ELISA protocol. Prism 8.0 was used to fit data and interpolate titer at OD_{450}=1

using a sigmoidal, 4PL, X is log(concentration) model. Serum ALT/AST levels were determined by a kit (Sigma), following manufacturer instructions.

4.6 Acknowledgements

This work was supported by NIH (1R01CA17727, R01NS064404, and U54CA199090). We thank Nathanial Peters and W. M. Keck Microscopy Center (S10 OD016240) for confocal microscopy support. We thank Kim Woodrow (UW Bioengineering) for use of her plate reader. We thank Prof. Andre Lieber (UW Medical Genetics) for his help reviewing the liver H&E images.

4.7 Competing Interests

S.H.P. has submitted a patent with the U.S. Patent and Trademark Office (WO2018027164A1) related to VIPER. S.H.P., S.L., and M.S. have filed a provisional patent on the DMM technology. The other authors have no competing interests.

4.8 Supplemental Information

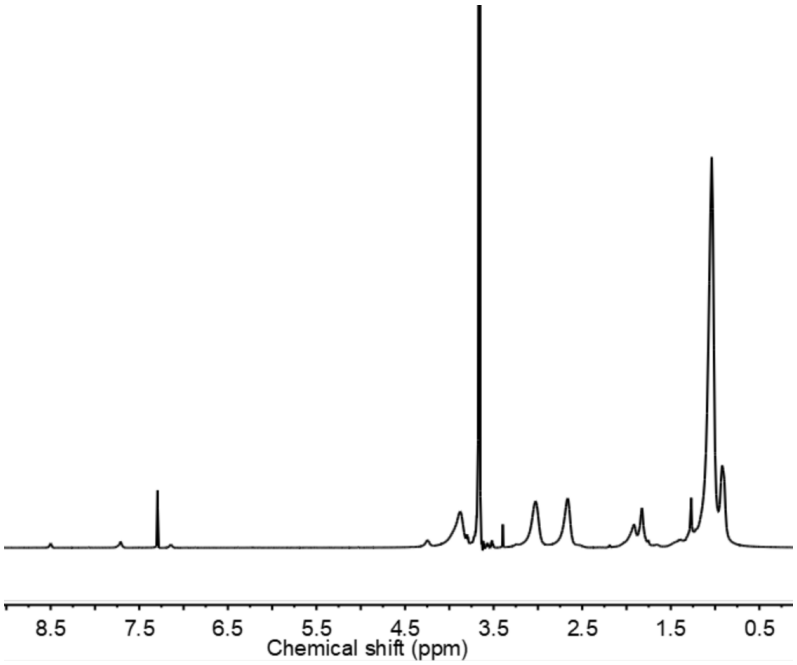

Supplemental Figure 41: ^{1}H NMR spectrum of PEG_{113}-b-p($DIPAMA_{40}$-co-$PDSEMA_{2}$) in CDCl3.

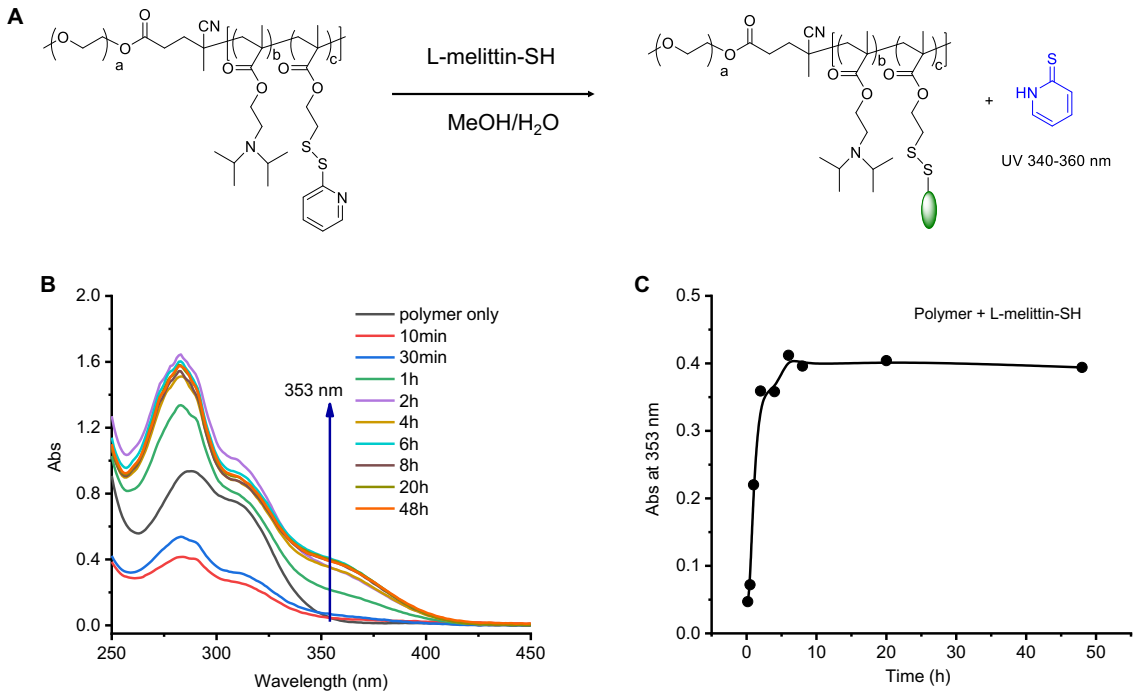

Entry	Peptide	Polymer/peptide feeding ratio	Obtained Polymer/peptide ratio[a]	Peptide loading efficacy (%)[a]	Peptide loading content (%)[a]
1	L-melittin	1:1.5	1:1	67%	16.2%
2	D-melittin	1:1.5	1:1	67%	16.2%

Supplemental Figure 4.2: A) Polymer was functionalized with peptide by disulfide exchange. B) Reaction kinetics were monitored by UV spectroscopy for the release of 2-thiopyridine. C) After 20 hours, the absorption was saturated and the polymer was purified to remove side products and unreacted peptide.

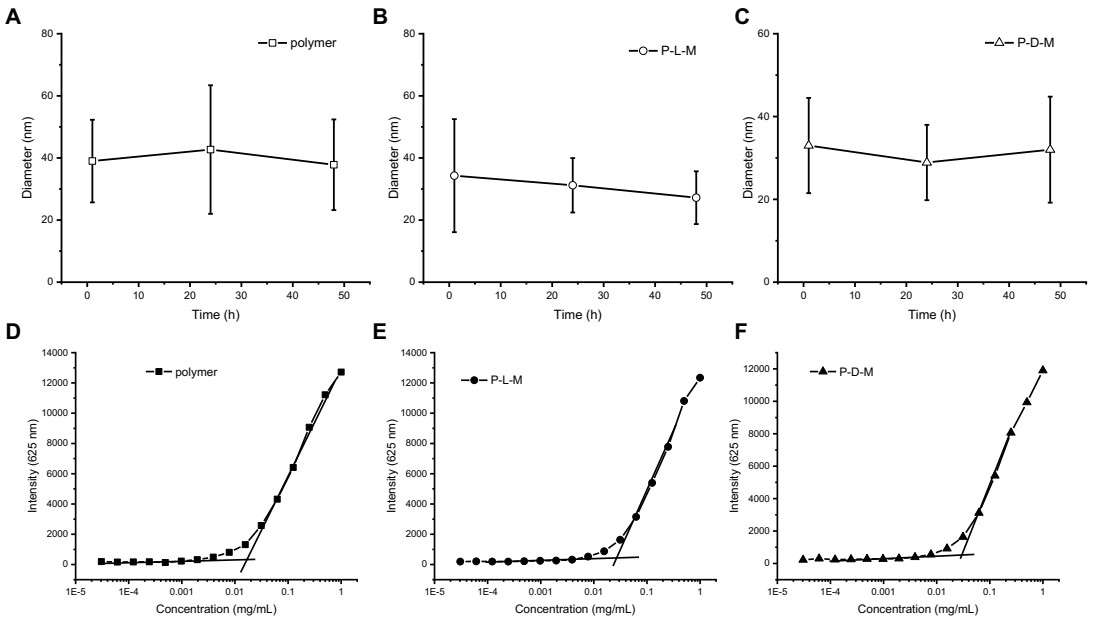

Entry	Micelles	CMC (mg/mL)
1	CP	0.017
2	LMM	0.027
3	DMM	0.030

Supplemental Figure 4.3: Stability (A-C) and CMC (D-F) of CP (A, D), L-melittin (B, E), and D-melittin (C, F) micelles in 10% FBS at 37 ºC over 48 hours.

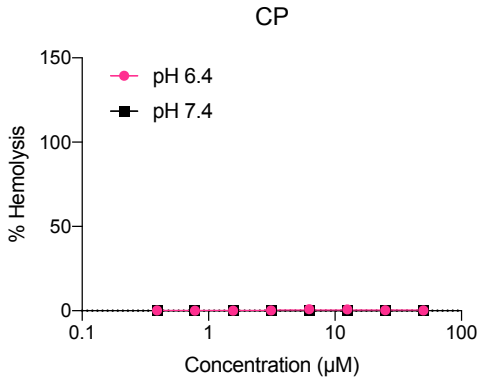

Supplemental Figure 4.4: Hemolytic activity of CP against RBCs at pH 6.4 and 7.4.

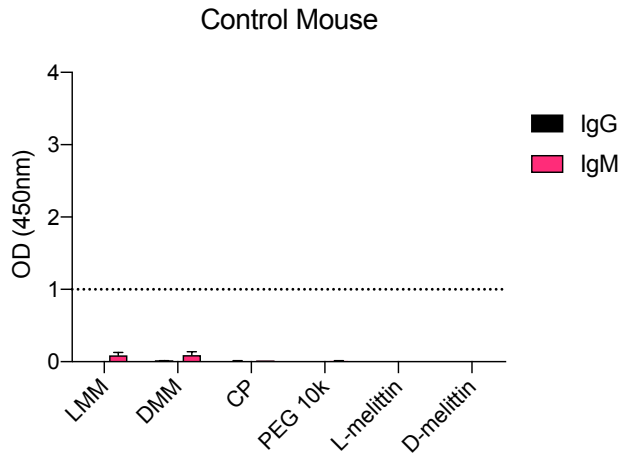

Supplemental Figure 4.5: Antibody generation in serum from untreated mice.

References

1 Kang, J. S., Deluca, P. P. & Lee, K. C. Emerging PEGylated drugs. *Expert Opin Emerg Drugs* **14**, 363-380, doi:10.1517/14728210902907847 (2009).

2 Zhang, P., Sun, F., Liu, S. & Jiang, S. Anti-PEG antibodies in the clinic: Current issues and beyond PEGylation. *J Control Release* **244**, 184-193, doi:10.1016/j.jconrel.2016.06.040 (2016).

3 Yang, Q. & Lai, S. K. Anti-PEG immunity: emergence, characteristics, and unaddressed questions. *Wiley Interdiscip Rev Nanomed Nanobiotechnol* **7**, 655-677, doi:10.1002/wnan.1339 (2015).

4 Hsieh, Y. C., Wang, H. E., Lin, W. W., Roffler, S. R., Cheng, T. C., Su, Y. C., Li, J. J., Chen, C. C., Huang, C. H., Chen, B. M., Wang, J. Y., Cheng, T. L. & Chen, F. M. Pre-existing anti-polyethylene glycol antibody reduces the therapeutic efficacy and pharmacokinetics of PEGylated liposomes. *Theranostics* **8**, 3164-3175, doi:10.7150/thno.22164 (2018).

5 Ishida, T. & Kiwada, H. Accelerated blood clearance (ABC) phenomenon upon repeated injection of PEGylated liposomes. *Int J Pharm* **354**, 56-62, doi:10.1016/j.ijpharm.2007.11.005 (2008).

6 Armstrong, J. K., Hempel, G., Koling, S., Chan, L. S., Fisher, T., Meiselman, H. J. & Garratty, G. Antibody against poly(ethylene glycol) adversely affects PEG-asparaginase therapy in acute lymphoblastic leukemia patients. *Cancer* **110**, 103-111, doi:10.1002/cncr.22739 (2007).

7 Abu Lila, A. S., Kiwada, H. & Ishida, T. The accelerated blood clearance (ABC) phenomenon: clinical challenge and approaches to manage. *J Control Release* **172**, 38-47, doi:10.1016/j.jconrel.2013.07.026 (2013).

8 Elsadek, N. E., Hondo, E., Shimizu, T., Takata, H., Abu Lila, A. S., Emam, S. E., Ando, H., Ishima, Y. & Ishida, T. Impact of Pre-Existing or Induced Anti-PEG IgM on the Pharmacokinetics of Peginterferon Alfa-2a (Pegasys) in Mice. *Mol Pharm* **17**, 2964-2970, doi:10.1021/acs.molpharmaceut.0c00366 (2020).

9 Ganson, N. J., Kelly, S. J., Scarlett, E., Sundy, J. S. & Hershfield, M. S. Control of hyperuricemia in subjects with refractory gout, and induction of antibody against poly(ethylene glycol) (PEG), in a phase I trial of subcutaneous PEGylated urate oxidase. *Arthritis Res Ther* **8**, R12, doi:10.1186/ar1861 (2006).

10 Liu, Y., Smith, C. A., Panetta, J. C., Yang, W., Thompson, L. E., Counts, J. P., Molinelli, A. R., Pei, D., Kornegay, N. M., Crews, K. R., Swanson, H., Cheng, C., Karol, S. E., Evans, W. E., Inaba, H., Pui, C. H., Jeha, S. & Relling, M. V. Antibodies Predict Pegaspargase Allergic Reactions and Failure of Rechallenge. *J Clin Oncol* **37**, 2051-2061, doi:10.1200/JCO.18.02439 (2019).

11 Richter, A. W. & Akerblom, E. Antibodies against polyethylene glycol produced in animals by immunization with monomethoxy polyethylene glycol modified proteins. *Int Arch Allergy Appl Immunol* **70**, 124-131, doi:10.1159/000233309 (1983).

12 Mima, Y., Hashimoto, Y., Shimizu, T., Kiwada, H. & Ishida, T. Anti-PEG IgM Is a Major Contributor to the Accelerated Blood Clearance of Polyethylene Glycol-Conjugated Protein. *Mol Pharm* **12**, 2429-2435, doi:10.1021/acs.molpharmaceut.5b00144 (2015).

13 Shiraishi, K. & Yokoyama, M. Toxicity and immunogenicity concerns related to PEGylated-micelle carrier systems: a review. *Sci Technol Adv Mater* **20**, 324-336, doi:10.1080/14686996.2019.1590126 (2019).

14 Webster, R., Elliott, V., Park, B. K., Walker, D., Hankin, M. & Taupin, P. in *PEGylated Protein Drugs: Basic Science and Clinical Applications* Ch. Milestones in Drug Therapy, 127-146 (Birkhäuser Basel, 2009).
15 Pelegri-O'Day, E. M., Lin, E. W. & Maynard, H. D. Therapeutic protein-polymer conjugates: advancing beyond PEGylation. *J Am Chem Soc* **136**, 14323-14332, doi:10.1021/ja504390x (2014).
16 Ekladious, I., Colson, Y. L. & Grinstaff, M. W. Polymer-drug conjugate therapeutics: advances, insights and prospects. *Nat Rev Drug Discov* **18**, 273-294, doi:10.1038/s41573-018-0005-0 (2019).
17 Tenenbaum, S. A., Rice, J. C., Espinoza, L. R., Cuéllar, M. L., Plymale, D. R., Sander, D. M., Williamson, L. L., Haislip, A. M., Cluck, O. S., Tesser, J. R. P., Nogy, L., Stribrny, K. M., Bevan, J. Á. & Garry, R. F. Use of antipolymer antibody assay in recipients of silicone breast implants. *The Lancet* **349**, 449-454, doi:10.1016/s0140-6736(96)07131-0 (1997).
18 Cheng, Y., Yumul, R. C. & Pun, S. H. Virus-Inspired Polymer for Efficient In Vitro and In Vivo Gene Delivery. *Angew Chem Int Ed Engl* **55**, 12013-12017, doi:10.1002/anie.201605958 (2016).
19 Peeler, D. J., Thai, S. N., Cheng, Y., Horner, P. J., Sellers, D. L. & Pun, S. H. pH-sensitive polymer micelles provide selective and potentiated lytic capacity to venom peptides for effective intracellular delivery. *Biomaterials* **192**, 235-244, doi:10.1016/j.biomaterials.2018.11.004 (2019).
20 Kind, L. S., Ramaika, C. & Allaway, E. Antigenic, adjuvant and permeability enhancing properties of melittin in mice. *Allergy* **36**, 155-160, doi:10.1111/j.1398-9995.1981.tb01830.x (1981).
21 Bramwell, V. W., Somavarapu, S., Outschoorn, I. & Alpar, H. O. Adjuvant action of melittin following intranasal immunisation with tetanus and diphtheria toxoids. *J Drug Target* **11**, 525-530, doi:10.1080/10611860410001670080 (2003).
22 Paull, B., Yunginger, J. & Gleich, G. Melittin: An allergen of honeybee venom. *Journal of Allergy and Clinical Immunology* **59**, 334-338, doi:10.1016/0091-6749(77)90056-2 (1977).
23 King, T., Kochoumian, L. & Joslyn, A. Melittin-specific monoclonal and polyclonal IgE and IgG1 antibodies from mice. *J Immunol* **133**, 2688-2673 (1984).
24 King, T. P., Wade, D., Coscia, M. R., Mitchell, S., Kochoumian, L. & Merrifield, B. Structure-immunogenicity relationship of melittin, its transposed analogues, and D-melittin. *J Immunol* **153**, 1124-1131 (1994).
25 Nakagawa, Y., Kikuchi, H. & Takahashi, H. Molecular analysis of TCR and peptide/MHC interaction using P18-I10-derived peptides with a single D-amino acid substitution. *Biophys J* **92**, 2570-2582, doi:10.1529/biophysj.106.095208 (2007).
26 Evans, B. C., Nelson, C. E., Yu, S. S., Beavers, K. R., Kim, A. J., Li, H., Nelson, H. M., Giorgio, T. D. & Duvall, C. L. Ex vivo red blood cell hemolysis assay for the evaluation of pH-responsive endosomolytic agents for cytosolic delivery of biomacromolecular drugs. *J Vis Exp*, e50166, doi:10.3791/50166 (2013).
27 Bello, J., Bello, H. R. & Granados, E. Conformation and aggregation of melittin: dependence on pH and concentration. *Biochemistry* **21**, 461-465, doi:10.1021/bi00532a007 (1982).
28 Kilchrist, K. V., Dimobi, S. C., Jackson, M. A., Evans, B. C., Werfel, T. A., Dailing, E. A., Bedingfield, S. K., Kelly, I. B. & Duvall, C. L. Gal8 Visualization of Endosome Disruption Predicts Carrier-Mediated Biologic Drug Intracellular Bioavailability. *ACS Nano* **13**, 1136-1152, doi:10.1021/acsnano.8b05482 (2019).
29 LeBeau, A. M., Brennen, W. N., Aggarwal, S. & Denmeade, S. R. Targeting the cancer stroma with a fibroblast activation protein-activated promelittin protoxin. *Mol Cancer Ther* **8**, 1378-1386, doi:10.1158/1535-7163.MCT-08-1170 (2009).
30 Huang, W.-C., Shen, J.-J., Liou, C.-J., Kuo, M.-L., Chang, Y.-P., Yang, R.-C. & Li, M.-L. Enhancing Th1 Cell Activities in Mice by Short-term Oral Administration of Gynostemma pentaphyllum Extracts. *BioFormosa* **42**, 9-16 (2007).
31 *Clinical Pathology Data for BALB/C Mouse Colonies in North America*, <https://www.criver.com/products-services/find-model/balbc-mouse?region=3611>
32 Gill, P., Jindal, N. L., Jagdis, A. & Vadas, P. Platelets in the immune response: Revisiting platelet-activating factor in anaphylaxis. *J Allergy Clin Immunol* **135**, 1424-1432, doi:10.1016/j.jaci.2015.04.019 (2015).
33 Upton, J. & Vadas, P. Potential Therapeutic Strategies for Severe Anaphylaxis Targeting Platelet-Activating Factor and PAF Acetylhydrolase. *Current Treatment Options in Allergy* **1**, 232-246, doi:10.1007/s40521-014-0020-2 (2014).
34 Judge, A., McClintock, K., Phelps, J. R. & Maclachlan, I. Hypersensitivity and loss of disease site targeting caused by antibody responses to PEGylated liposomes. *Mol Ther* **13**, 328-337, doi:10.1016/j.ymthe.2005.09.014 (2006).

35 Jackson, M. A., Patel, S. S., Yu, F., Cottam, M. A., Glass, E. B., Dollinger, B. R., Hoogenboezem, E. N., Patil, P., Liu, D. D., Kelly, I. B., Bedingfield, S. K., King, A. R., Miles, R. E., Hasty, A. M., Giorgio, T. D. & Duvall, C. L. Kupffer Cell Release of Platelet Activating Factor Drives Dose Limiting Toxicities of Nucleic Acid Nanocarriers., doi:10.1101/2020.02.11.944504 (2020).
36 Rabinovici, R., AS, R., Yue, T. & Feuerstein, G. Biological responses to liposome-encapsulated hemoglobin (LEH) are improved by a PAF antagonist. *Circ Shock* **31**, 431-445 (1990).
37 Boeckle, S., Wagner, E. & Ogris, M. C- versus N-terminally linked melittin-polyethylenimine conjugates: the site of linkage strongly influences activity of DNA polyplexes. *J Gene Med* **7**, 1335-1347, doi:10.1002/jgm.783 (2005).
38 Ichihara, M., Shimizu, T., Imoto, A., Hashiguchi, Y., Uehara, Y., Ishida, T. & Kiwada, H. Anti-PEG IgM Response against PEGylated Liposomes in Mice and Rats. *Pharmaceutics* **3**, 1-11, doi:10.3390/pharmaceutics3010001 (2010).
39 Wang, X., Ishida, T. & Kiwada, H. Anti-PEG IgM elicited by injection of liposomes is involved in the enhanced blood clearance of a subsequent dose of PEGylated liposomes. *J Control Release* **119**, 236-244, doi:10.1016/j.jconrel.2007.02.010 (2007).
40 Shiraishi, K., Kawano, K., Maitani, Y., Aoshi, T., Ishii, K. J., Sanada, Y., Mochizuki, S., Sakurai, K. & Yokoyama, M. Exploring the relationship between anti-PEG IgM behaviors and PEGylated nanoparticles and its significance for accelerated blood clearance. *J Control Release* **234**, 59-67, doi:10.1016/j.jconrel.2016.05.010 (2016).
41 Neun, B. W., Barenholz, Y., Szebeni, J. & Dobrovolskaia, M. A. Understanding the Role of Anti-PEG Antibodies in the Complement Activation by Doxil in Vitro. *Molecules* **23**, doi:10.3390/molecules23071700 (2018).
42 Saifer, M. G., Williams, L. D., Sobczyk, M. A., Michaels, S. J. & Sherman, M. R. Selectivity of binding of PEGs and PEG-like oligomers to anti-PEG antibodies induced by methoxyPEG-proteins. *Mol Immunol* **57**, 236-246, doi:10.1016/j.molimm.2013.07.014 (2014).
43 Zolnik, B. S., Gonzalez-Fernandez, A., Sadrieh, N. & Dobrovolskaia, M. A. Nanoparticles and the immune system. *Endocrinology* **151**, 458-465, doi:10.1210/en.2009-1082 (2010).
44 Sela, M. & Zisman, E. Different roles of D-amino acids in immune phenomena. *FASEB J* **11**, 449-456, doi:10.1096/fasebj.11.6.9194525 (1997).
45 Terwilliger, T. C. & Eisenberg, D. The structure of melittin. *The Journal of Biological Chemistry* **257**, 6016-6022 (1982).
46 Soman, N. R., Baldwin, S. L., Hu, G., Marsh, J. N., Lanza, G. M., Heuser, J. E., Arbeit, J. M., Wickline, S. A. & Schlesinger, P. H. Molecularly targeted nanocarriers deliver the cytolytic peptide melittin specifically to tumor cells in mice, reducing tumor growth. *J Clin Invest* **119**, 2830-2842, doi:10.1172/JCI38842 (2009).
47 Yu, X., Dai, Y., Zhao, Y., Qi, S., Liu, L., Lu, L., Luo, Q. & Zhang, Z. Melittin-lipid nanoparticles target to lymph nodes and elicit a systemic anti-tumor immune response. *Nat Commun* **11**, 1110, doi:10.1038/s41467-020-14906-9 (2020).
48 Orsolic, N. Bee venom in cancer therapy. *Cancer Metastasis Rev* **31**, 173-194, doi:10.1007/s10555-011-9339-3 (2012).
49 Orsolic, N., Terzic, S., Sver, L. & Basic, I. Honey-bee products in prevention and/or therapy of murine transplantable tumours. *Journal of the Science of Food and Agriculture* **85**, 363-370, doi:10.1002/jsfa.2041 (2005).
50 Yu, X., Chen, L., Liu, J., Dai, B., Xu, G., Shen, G., Luo, Q. & Zhang, Z. Immune modulation of liver sinusoidal endothelial cells by melittin nanoparticles suppresses liver metastasis. *Nat Commun* **10**, 574, doi:10.1038/s41467-019-08538-x (2019).
51 Liu, M., Wang, H., Liu, L., Wang, B. & Sun, G. Melittin-MIL-2 fusion protein as a candidate for cancer immunotherapy. *J Transl Med* **14**, 155, doi:10.1186/s12967-016-0910-0 (2016).
52 Rady, I., Siddiqui, I. A., Rady, M. & Mukhtar, H. Melittin, a major peptide component of bee venom, and its conjugates in cancer therapy. *Cancer Lett* **402**, 16-31, doi:10.1016/j.canlet.2017.05.010 (2017).
53 Pan, H., Soman, N. R., Schlesinger, P. H., Lanza, G. M. & Wickline, S. A. Cytolytic peptide nanoparticles ('NanoBees') for cancer therapy. *Wiley Interdiscip Rev Nanomed Nanobiotechnol* **3**, 318-327, doi:10.1002/wnan.126 (2011).
54 Yang, Q., Jacobs, T. M., McCallen, J. D., Moore, D. T., Huckaby, J. T., Edelstein, J. N. & Lai, S. K. Analysis of Pre-existing IgG and IgM Antibodies against Polyethylene Glycol (PEG) in the General Population. *Anal Chem* **88**, 11804-11812, doi:10.1021/acs.analchem.6b03437 (2016).

55 Chen, B. M., Su, Y. C., Chang, C. J., Burnouf, P. A., Chuang, K. H., Chen, C. H., Cheng, T. L., Chen, Y. T., Wu, J. Y. & Roffler, S. R. Measurement of Pre-Existing IgG and IgM Antibodies against Polyethylene Glycol in Healthy Individuals. *Anal Chem* **88**, 10661-10666, doi:10.1021/acs.analchem.6b03109 (2016).

56 Sherman, M. R., Williams, L. D., Sobczyk, M. A., Michaels, S. J. & Saifer, M. G. Role of the methoxy group in immune responses to mPEG-protein conjugates. *Bioconjug Chem* **23**, 485-499, doi:10.1021/bc200551b (2012).

57 McSweeney, M. D., Price, L. S. L., Wessler, T., Ciociola, E. C., Herity, L. B., Piscitelli, J. A., DeWalle, A. C., Harris, T. N., Chan, A. K. P., Saw, R. S., Hu, P., Jennette, J. C., Forest, M. G., Cao, Y., Montgomery, S. A., Zamboni, W. C. & Lai, S. K. Overcoming anti-PEG antibody mediated accelerated blood clearance of PEGylated liposomes by pre-infusion with high molecular weight free PEG. *J Control Release* **311-312**, 138-146, doi:10.1016/j.jconrel.2019.08.017 (2019).

58 Wilson, J. T., Keller, S., Manganiello, M. J., Cheng, C., Lee, C. C., Opara, C., Convertine, A. & Stayton, P. S. pH-Responsive nanoparticle vaccines for dual-delivery of antigens and immunostimulatory oligonucleotides. *ACS Nano* **7**, 3912-3925, doi:10.1021/nn305466z (2013).

59 Su, Y. C., Chen, B. M., Chuang, K. H., Cheng, T. L. & Roffler, S. R. Sensitive quantification of PEGylated compounds by second-generation anti-poly(ethylene glycol) monoclonal antibodies. *Bioconjug Chem* **21**, 1264-1270, doi:10.1021/bc100067t (2010).

Chapter 5

Development of D-melittin polymeric nanoparticles for anti-cancer treatment

*Shixian Lv, *Meilyn Sylvestre, Kefan Song, and Suzie H. Pun
*equally contributing authors

5.1 Abstract

Melittin, the primary peptide component of bee venom, is a potent cytolytic anti-cancer peptide with established anti-tumor activity. However, its application is hampered by its strong, nonspecific hemolytic activity and intrinsic instability. To address these shortcomings, delivery systems are used to facilitate the safe delivery of melittin, reducing nonspecific hemolysis and improving stability. Yet, a recent study revealed that even when fully encapsulated in delivery vehicles, melittin is still immunogenic and can act as an adjuvant to elicit a fatal antibody immune response against the delivery carrier, further hindering the systemic administration of melittin formulations. We discovered that substitution of L-amino acids with D-amino acids mitigates this problem: D-melittin nanoformulations induce significantly decreased immune response, resulting in excellent safety without compromising cytolytic potential. We now report the first application of D-melittin and its micellar formulations for cancer treatment. D-melittin was delivered by a pH-sensitive polymer carrier that (*i*) forms micellar nanoparticles at normal physiological conditions, encapsulating melittin, and (*ii*) dissociates at endosomal pH, restoring melittin activity. D-melittin micelles (DMM) exhibits significant cytotoxicity and induces hemolysis in a pH-dependent manner. In addition, DMM induce immunogenic cell death, revealing its potential for cancer immunotherapy. Indeed, *in vivo* studies demonstrated the superior safety profile of DMM over free peptide and improved efficacy at prohibiting tumor growth. Overall, we present the first application of micellar D-melittin for cancer therapy. These findings establish a new strategy for safe, systemic delivery of melittin, unlocking a potential pathway toward clinical translation for cytotoxic peptides as anti-cancer agents. which can revolutionize *in vivo* delivery of therapeutic peptides and peptide antigens.

5.2 Introduction

Anti-cancer peptides (ACPs) have emerged as a promising class of cancer therapeutics due to their ease of synthesis, high potency, and cell selectivity [1, 2]. ACPs exert anti-tumor activity through various and distinctive mechanisms, such as specifically targeting tumor suppressive signaling pathways or inducing cell death through membranolytic activity [3-6]. Compared to conventional chemotherapeutics, ACPs possess better selectivity and lower off-target toxicity to normal cells. Importantly, cancer cells have a low risk of developing drug resistance against ACPs because they effect critical cell pathways that cells cannot bypass [7]. This highlights another major advantage of ACPs, as drug resistance is increasingly responsible for the failure of chemotherapy [1, 8]. Given the attractive properties of ACPs, there has been increasing interest in the development of ACP delivery systems [2, 9, 10].

Melittin, the active 26-amino acid peptide component of honeybee venom, is a potent and natural ACP with established anti-tumor efficacy against a broad spectrum of cancers, including prostate, breast, and liver cancer[11, 12]. Its cationic charge and amphipathic properties enable melittin to interact with and disrupt biological membranes[13, 14]. In addition to being membranolytic, melittin can also modulate multiple cell signaling pathways, such as inhibiting angiogenesis, inducing cell cycle arrest, and preventing metastasis [15]. Despite melittin's great potential for cancer treatment, melittin also suffers from significant drawbacks that limit its clinical application, including nonspecific hemolysis, rapid clearance and degradation, and poor tumor accumulation [15]. To address these issues, melittin has been incorporated into drug delivery systems such as polymer-peptide conjugates or nanoparticle (NP) with the goal of decreasing nonspecific hemolysis to enhance safety *in vivo* and to increase bioavailability in tumors [16-19].

While some drug delivery platforms have facilitated safe melittin delivery, these systems can also introduce new challenges, as demonstrated by the generation of an adaptive immune response to the delivery carrier. Similar to the generation of anti-PEG antibodies against PEGylated platforms, systemic administration of conjugates with bioactive drugs can trigger a host immune response, eliciting antibodies against the carrier and resulting in accelerated blood clearance and hypersensitivity reactions [20, 21]. This adverse immune response is attributed to the bioactive drug, which acts as an adjuvant to activate the immune system against the carrier. Studies have

shown that the generated immune response correlates with the immunogenicity of the loaded cargos [22]. In contrast to most small molecule chemotherapeutics, melittin is an immunogenic host defense peptide that can therefore elicit a severe immune response [15, 16, 23]. Indeed, we recently demonstrated that repeat systemic administration of our PEGylated melittin micelles was fatal in mice and that death could be attributed to the robust generation of anti-PEG antibodies [24]. By substituting the L-amino acids with D-amino acids, we attenuated the immune response, ultimately enhancing the therapeutic index of our delivery platform without compromising bioactivity of the peptide. Based on these findings, we hypothesized that D-melittin could serve as a safer alternative to L-melittin for systemic cancer delivery applications.

Herein, we report the application of D-melittin micelle (DMM) nanoformulations for treatment of solid tumors. We employed a polymer platform, virus inspired polymer for endosomal release (VIPER), to facilitate intracellular melittin delivery [25]. D-melittin was conjugated to an ultra pH-sensitive polymer that shields melittin at physiological pH and rapidly unsheathes melittin at endosomal pH. Thus, the polymer-peptide conjugate self-assembles into micellar nanoparticles at physiological pH and dissociates after entry into the cells (**Fig. 5.1**). After characterizing the polymer-peptide conjugate, we examined its activity *in vitro* and *in vivo.* First, the cytotoxic activity of free peptide and polymer-peptide conjugates was investigated against different tumor cells. The ability of these formulations to induce immunogenic cell death, as characterized by calreticulin (CRT) surface expression, ATP secretion, and HMGB1 release, was also evaluated. Next, the safety profiles of D-melittin peptide and micelles were established in normal mice, as determined by the maximum tolerated dose (MTD). Finally, the *in vivo* anti-tumor efficacy was evaluated in CT26 (colon cancer) and 4T1 (breast cancer) tumor-bearing mice. To the best of our knowledge, this is the first application of D-melittin for cancer therapy, which can help unveil the promising potential of melittin for *in vivo* therapeutic use.

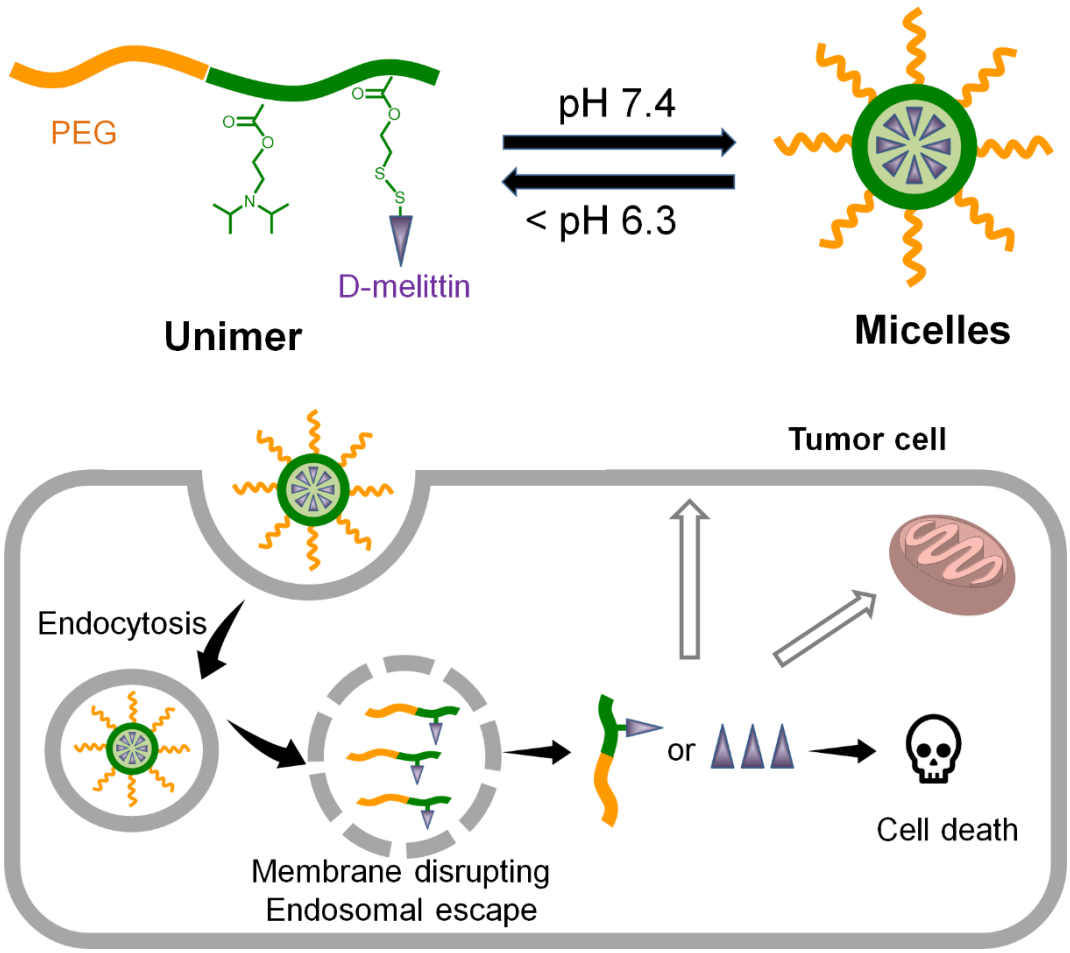

Figure 5.1: *Design of D-melittin conjugate for systemic delivery of melittin for cancer therapy.*

5.3. Results

5.3.1 Polymer synthesis of melittin micelles

The PEG-VIPER polymer was synthesized by reversible addition-fragmentation chain-transfer (RAFT) polymerization of DIPAMA and PDSEMA with PEGylated macro chain transfer agents (PEG-CTAs), as previously described [24, 25]. The DIPAMA block confers pH-sensitivity, as DIPAMA sharply transitions from hydrophobic at neutral pH to hydrophilic at acidic pH, and PDSEMA enables conjugation with thiol-containing peptides (**Fig. 5.2A**). These polymers self-assemble into micelles at neutral pH (7.4) with a diameter of 32.6 ± 13 nm (**Fig. 5.2B**), yielding D-melittin micelles (DMM). The obtained micelles had a critical micelle concentration (CMC) of 0.03 mg/mL in PBS (7.4) and were stable in PBS containing 10% FBS for over two days, indicating good colloidal stability (**Fig. 5.2C**). Additionally, we demonstrate that these micelles disassemble

into polymer chains at acidic pH 6.4 (**Fig. 5.2D**), exposing conjugated peptides upon cellular internalization in endosomes.

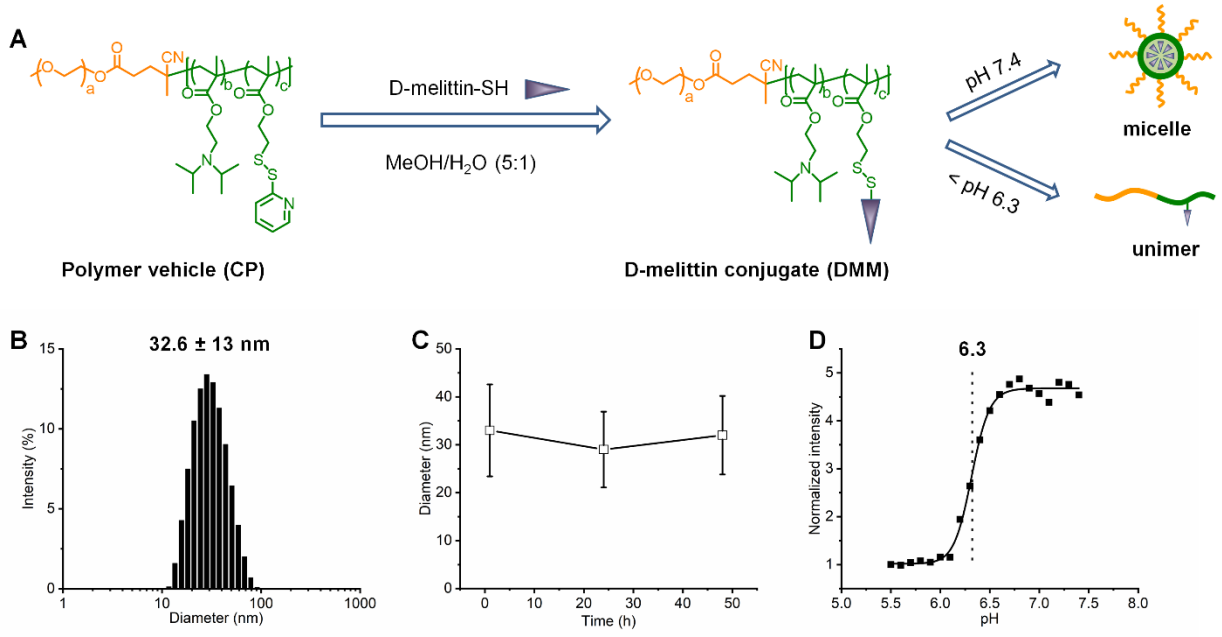

Figure 5.2: *Synthesis and characterization of D-melittin conjugate. A) Synthesis route for D-melittin conjugate and its self-assembly behavior under different pH conditions. B) Size distribution of D-melittin micelles (DMM) in PBS. C) Size stability of DMM in PBS containing 10% FBS. D) pH-transition study of DMM.*

5.3.2 Lytic activity in vitro

The lytic activity of D-melittin peptides and micelles was evaluated *in vitro via* cell toxicity and hemolysis assays, and visualization of endosomal escape. Peptide and micelles were potent against both human (A549, MDA-MB-435) and murine tumor cells (3T3, CT26) (**Fig. 5.2A-D, Table 1**), as indicated by similar half maximal inhibitory concentrations (IC_{50}) across cell lines. Micelles without peptide (CP) had no cytotoxic activity (**Fig. S5.1**). Both peptide and micelles demonstrate robust toxicity in wild type (WT) and doxorubicin-resistant (DOX-R) MDA-MB-435 cells (**Fig. 5.2C-D**, with confirmation of doxorubicin-resistance is reported in **Fig. S5.2**). While the IC_{50} of free peptide is comparable in WT and DOX-R lines (3.53 ± 0.2 and 3.44 ± 0.3 μM, respectively), the IC_{50} of DMM is 10-fold lower in DOX-R cells compared to WT cells (30.09 ± 3.9 and 2.98 ± 0.7 μM in WT and DOX-R, respectively). Notably, DMM is 10-fold more cytotoxic compared to free peptide in DOX-R cells. Next, hemolytic activity was evaluated against human red blood cells

(RBCs) at pH 5.4, 6.4, and 7.4 (**Fig. 5.3E-F, Table 2**), a range that covers endosomal pH, micelle transition point, and physiological pH, respectively. The peptide was lytic at all pH values and exhibited increasing activity at higher pH, as indicated by decreasing concentration for 50% RBC hemolysis (HC_{50}) with increasing pH. In contrast, the HC_{50} of DMM was 10-40 fold lower than free peptide at acidic conditions, yet exhibited no lytic activity at pH 7.4, confirming both the potent lytic activity of DMM at endosomal pH (5.4 - 6.4) and its safe encapsulation of D-melittin at physiological pH (7.4). Lastly, endosomal disruption was evaluated in the Gal8-GFP-RAW 264.7 reporter cell line (**Fig. 5.2H**) [26]. Cells constitutively express Gal8-GFP throughout their cytoplasm, but upon endosomal disruption, redistribute and bind to the inner face of endosomes. Thus, disrupted endosomes can be visualized as green punctae. Cells were additionally stained with propidium iodine (PI) to assess viability of cells and the percent of live cells (PI^-) expressing punctae was quantified. While D-melittin did not disrupt endosomes (0.03%), DMM induced GFP^+ punctate in nearly 10% of live cells. Although micelles without melittin (CP) were also capable of disrupting endosomes to some extent (0.17%), CP had no cytotoxic or hemolytic activity (**Fig. S5.1**). Overall, both D-melittin and DMM were shown to be cytotoxic and hemolytic, but DMM has no hemolytic activity at pH 7.4. Furthermore, DMM was capable of disrupting cell endosomes whereas free peptide was not.

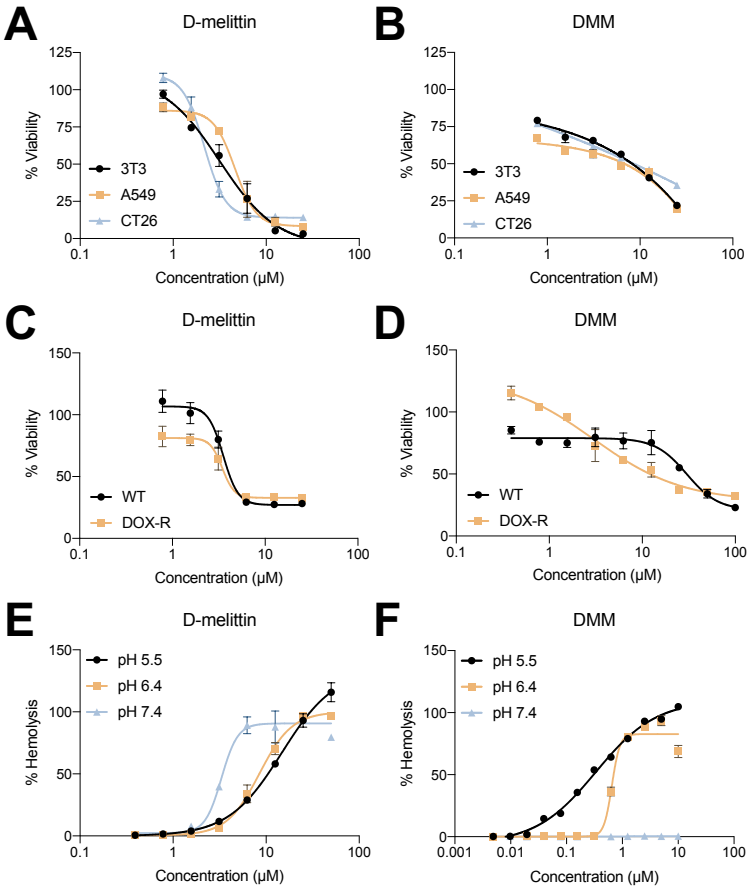
A
D-melittin
% Viability
3T3
A549
CT26
Concentration (μM)
B
DMM
C
WT
DOX-R
D
E
pH 5.5
pH 6.4
pH 7.4
% Hemolysis
F

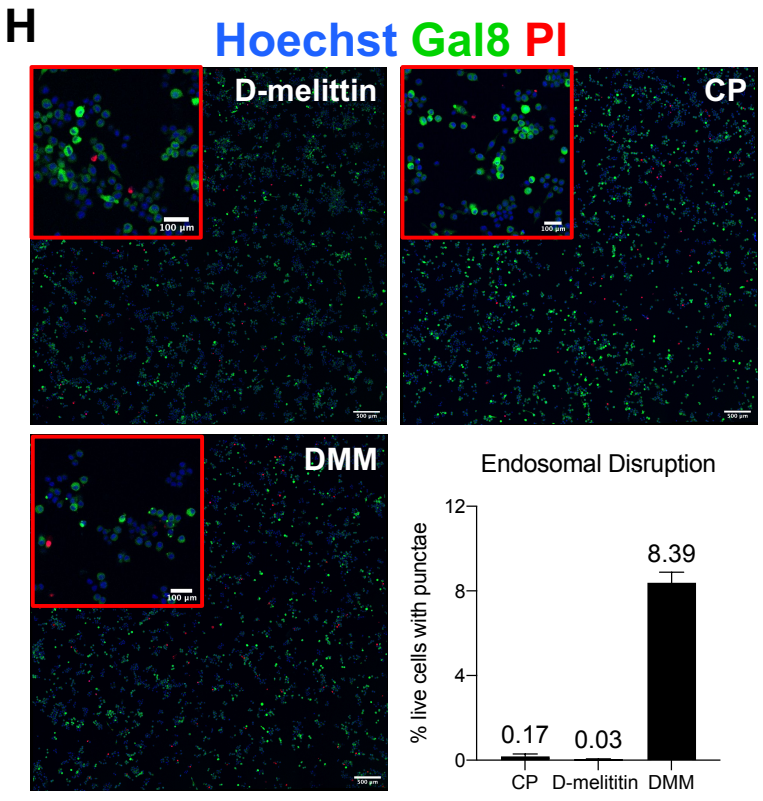
H
Hoechst Gal8 PI
D-melittin
CP
DMM
100 μm
Endosomal Disruption
% live cells with punctae
8.39
0.17
0.03
CP
D-melititin
DMM

Figure 5.3*: Peptide and micelle activity in vitro. A-B) D-melittin peptide (A) and micelles (B) were incubated with human and murine tumor cells (3T3, A549, and CT26) for 24 hours, and viability was assessed via MTS assay. C-D) D-melittin peptide (C) and micelles (D) were incubated with both wild type (WT) and doxorubicin-resistant (DOX-R) MDA-MB-435 cells for 24 hours, and viability was assess via MTS assay. E-F) Hemolytic activity of peptide (E) and (F) micelles was determined against red blood cells (RBCs) at pH 5.4, 6.4, and 7.4. H) Endosomal escape of micelles was demonstrated in Gal8-GFP-RAW 264.7 macrophages (500 μm scale). Endosomal disruption is observed as green punctae, as Gal8-GFP$^+$ binds to the inner membrane of endosomes. Image insets (red) are magnification of cells (100 μm scale).*

Viability IC_{50} (μM)		
Cell line	D-melittin	DMM
3T3	3.2	8.5
A549	4.5	6.9
CT26	2.2	11.6
MDA-MB-435 WT	3.5	30.1
MDA-MB-435 DOX-R	3.4	3.0

Table 5.1: *Toxicity of D-melittin peptide and micelles against a range of human and murine tumor cell lines. For DMM, the concentration is expressed as containing a peptide equivalent to free peptide.*

Hemolysis HC_{50} (μM)			
Entry	pH 5.4	pH 6.4	pH 7.4
D-melittin	14.8	8.5	3.3
DMM	0.33	0.65	N/A

Table 5.2: *Hemolytic activity of D-melittin peptide and micelles at pH 5.4, 6.4, and 7.4. For DMM, the concentration is expressed as containing a peptide equivalent to free peptide.*

5.3.3 Characterization of immunogenic cell death (ICD)

Based on prior reports of melittin-induced NLRP3 inflammasome activation, we next investigated if D-melittin peptide and micelles could induce immunogenic cell death (ICD), as evaluated by the three major hallmarks of ICD: surface expression of calreticulin (CRT) and extracellular release of high mobility group protein B1 (HMGB1) and ATP (**Fig. 3A**) [23, 29, 30]. These events occur during (CRT, ATP release) and after (HMGB1) cellular apoptosis, and thus were evaluated at 24 and 48 hours post-incubation[31]. To assess translocation of CRT from the nucleus to the cell surface, CT26 cells were incubated with peptide or micelles for 24 hours and stained with an anti-CRT antibody (**Fig. 3B**). In contrast to micelles without peptide (CP), both peptide (****$p < 0.0001$) and micelles (****$p < 0.0001$) induced significantly higher CRT surface-expression. Extracellular HMGB1 was assessed in cell supernatant via ELISA after 48 hour incubation with peptide or micelles at IC_{50} concentrations (**Fig. 3C**). Both D-melittin (**$p = 0.0031$) and DMM (****$p < 0.0001$) induced a significantly higher increase in HMGB1 release over CP-treated cells, and DMM induced significantly higher release compared to D-melittin (****$p < 0.0001$). Similarly, a robust increase in extracellular ATP (24 hour incubation) was observed in DMM-treated cells, while ATP release in D-melittin and CP-treated cells was negligible (**Fig. 3D**). Together, these results suggest that DMM is capable of inducing ICD in cancer cells.

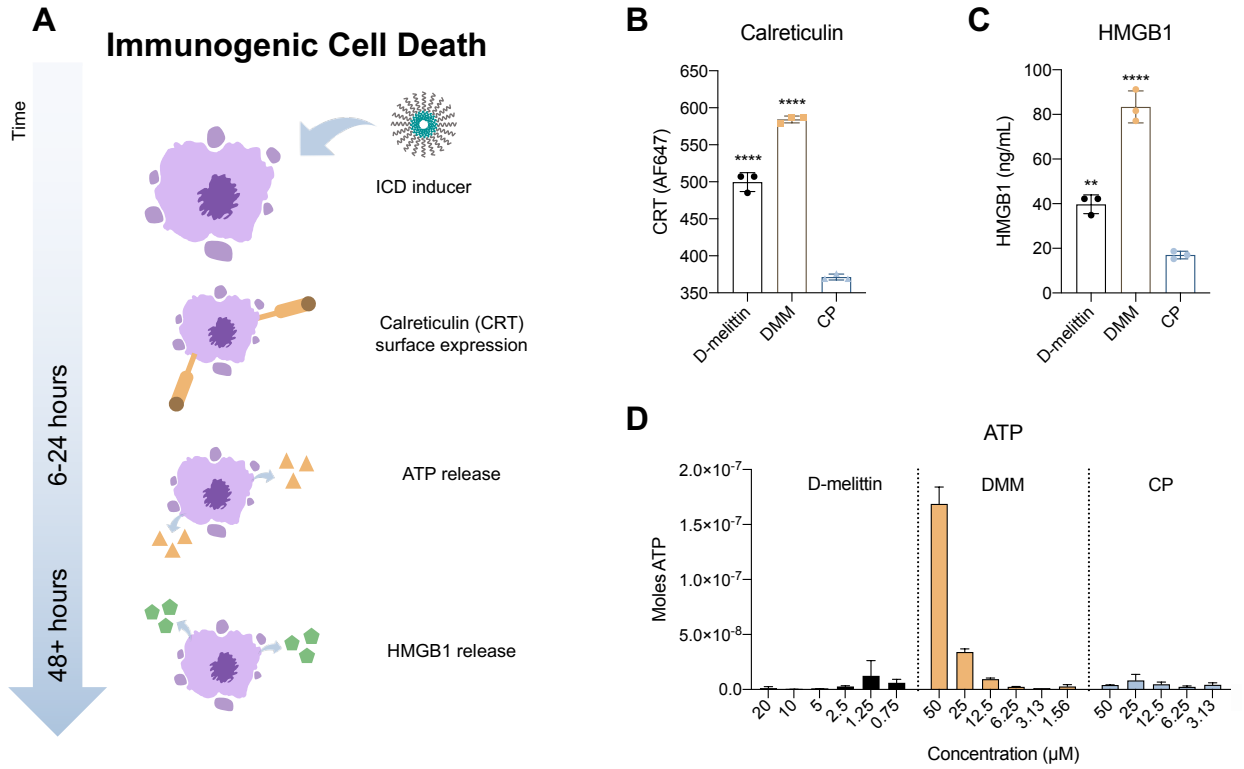

Figure 5.4: *Evaluation of immunogenic cell death in CT26 cancer cells. A) A schematic of the primary hallmarks of ICD: calreticulin (CRT) surface expression and ATP and HMGB1 release. Translocation of CRT to the cell surface and ATP release occur in pre-apoptotic and dying cells, and occur over a time course of hours. HMGB1 release occurs in dying and dead cells and occurs over a time course of days. B) Cells were incubated with peptide or micelles for 24 hours and surface expression of CRT was measured via flow cytometry. C) Extracellular HMGB1 concentration was measured in cell supernatant via ELISA after 48 hour incubation with peptide or micelles. D) Extracellular ATP was measured in cell supernatant via luciferin reaction.*

5.3.4 Safety of free peptide and micelles in vivo

We next evaluated the maximum tolerated dose (MTD) of free peptide and micelles *in vivo* to determine appropriate doses for anti-cancer treatment (**Table 5.3**). MTD was determined by injecting mice intravenously (IV) with peptide or micelles and monitoring weight loss, survival, and overall disposition; mice were euthanized when euthanasia criteria (i.e. difficulty breathing) were met. The MTD of micelles in normal mice was previously determined to be 20 mg peptide/kg (an equivalent of 125 mg micelles/kg) [24]. Due to the highly lytic nature of free peptide, the range

of tested doses was 10-fold lower; normal mice were injected with D-melittin at 2, 4, 6, and 8 mg/kg. While all mice survived an injection of peptide at 4 mg/kg, this dose was poorly tolerated (lethargy, poor grooming), and the MTD was determined to be 2 mg/kg, which is 10-fold lower than that of micelle-encapsulated peptide.

D-melittin free peptide		DMM	
Dose	Deaths	Dose	Deaths
2 mg/kg	0/4	10 mg/kg	0/4
4 mg/kg	0/4	20 mg/kg	0/4
6 mg/kg	4/4	30 mg/kg	2/4
8 mg/kg	4/4	40 mg/kg	4/4
MTD	2 mg/kg	MTD	20 mg/kg

Table 5.3: *MTD of D-melittin and D-melittin micelles. Normal mice were injected with a range of concentrations and sacrificed when euthanasia criteria were met. While mice survived following peptide injection at 4 mg/kg, this dose was poorly tolerated. The MTD of free peptide and micelles was determined to be 2 mg/kg and 20 mg peptide/kg, respectively. For DMM, the dose is expressed in regards to peptide amount in the formulation. (n = 4 mice/group)*

5.3.5 Safety of particles upon repeat injection

Although we have previously established that the incorporation of D-amino acids abrogated the generation of anti-PEG antibodies and extended survival, we additionally sought to confirm safety of these particles for repeat injection via hematoxylin and eosin (H&E) staining and analysis of serum ALT/AST enzymes[24]. Mice were injected every 4th day with (*i*) PBS, (*ii*) CP, (*iii*) D-melittin 2 mg/kg, or (*iv*) DMM 5 mg peptide/kg for a total of 3 injections. Twenty-four hours following the final injection, blood was drawn and major organs (heart, lung, liver, kidney, spleen) were harvested and submitted for H&E processing (**Fig. 5.5**). Slides were evaluated by a blinded veterinary pathologist and changes were graded on a 1 (minimal) to 4 (severe) scale (**Table S5.1**). Overall, no clinically significant treatment-related changes were noted. This was supported by activity of ALT/AST enzymes in the serum, which was all within normal range (**Fig. 5.6**).

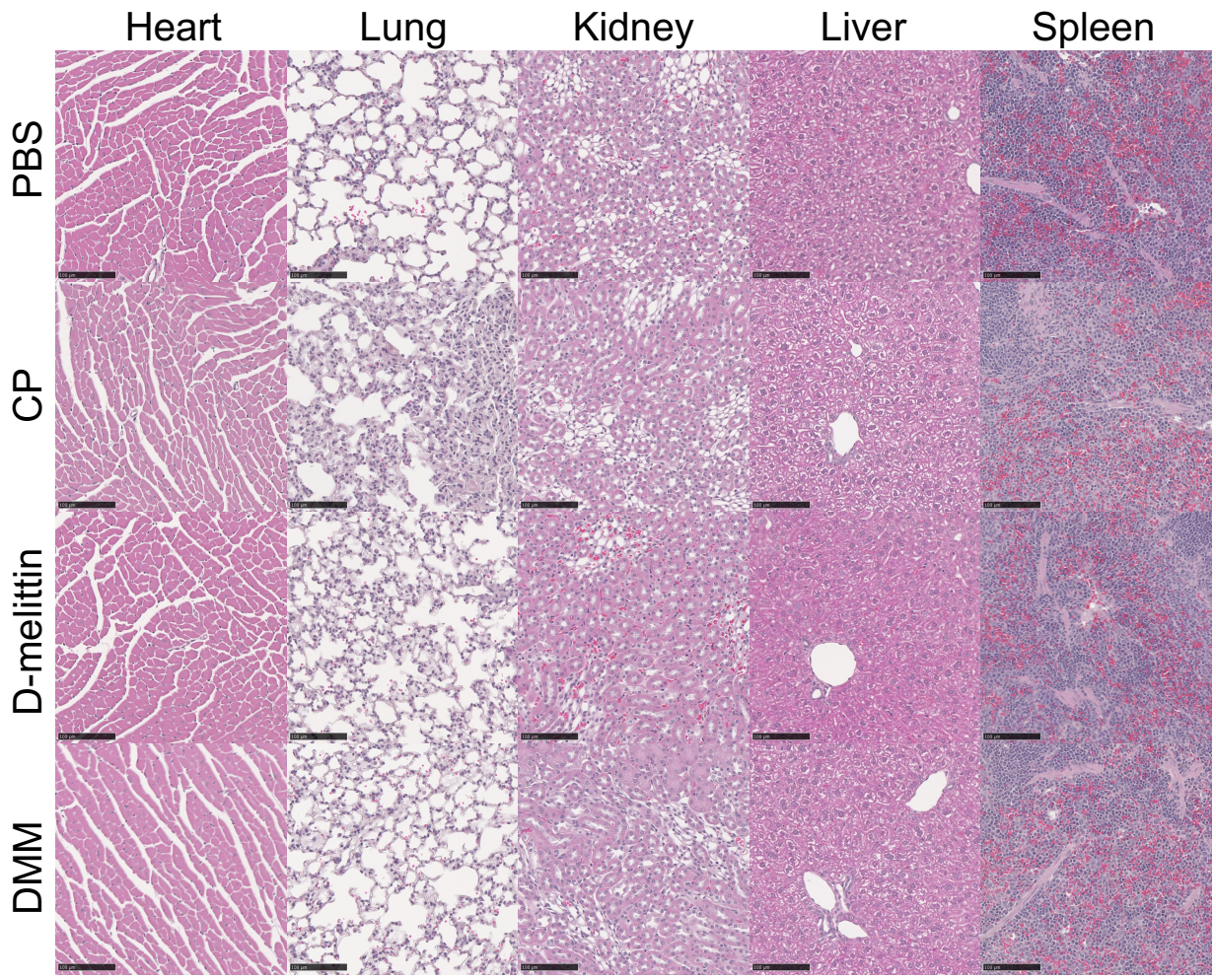

Figure 5.5: *H&E staining of major organs after repeat injection of peptide and particles. Mice were injected IV with (i) PBS, (ii) CP, (iii) D-melittin 2 mg/kg or (iv) DMM 5 mg peptide/kg every 4th day for a total of 3 injections. Twenty-four hours after the 3rd injection, organs were harvested and processed for H&E staining, and evaluated by a blinded third-party. Overall, there were no identified treatment-related changes. The black scale bar represents 100 μm. (n = 2 mice/group)*

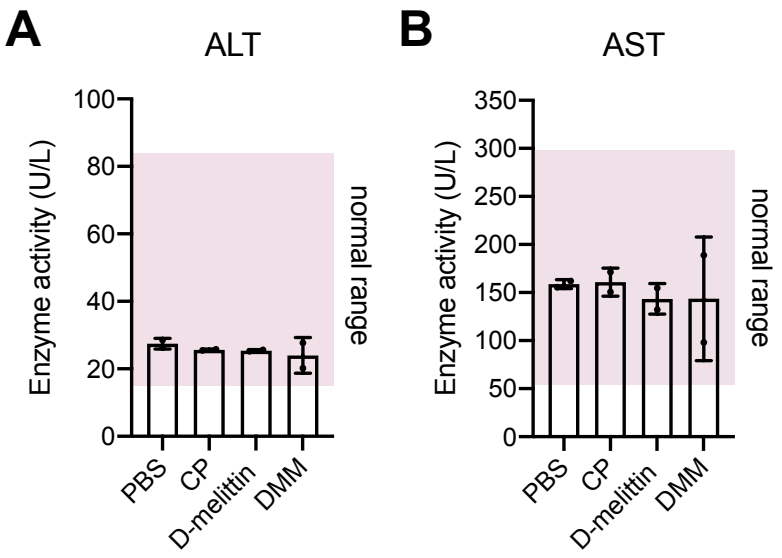

Figure 5.6: *Serum ALT/AST activity. The activity of ALT (A) and AST (B) enzymes in the serum was evaluated via ELISA. All values were within normal range. (n = 2 mice/group)*

5.3.6 Anti-tumor efficacy of D-melittin peptide and micelles in vivo

After determining safe, injectable doses of free peptide and micelles, we next compared anti-tumor efficacy of each in a CT26 colon cancer model. Eight days after subcutaneous tumor inoculation (1M cells) in the right inguinal flank, mice were injected IV every 4th day with (*i*) PBS, (*ii*) D-melittin 2 mg/kg, or (*iii*) DMM 5 mg peptide/kg for a total of 3 treatments (**Fig. 5.7A**). We have previously observed that polymer without melittin (CP) has no anti-tumor efficacy (**Fig. S5.3**) *in vivo*, so we did not include CP-treatment in this study. While D-melittin-treated mice had smaller tumors than PBS-treated mice *(***p = 0.0009*), there was no difference in survival between the groups (*p = 0.2265*) (**Fig. 5.7B-C**). In contrast, DMM-treated mice had significantly smaller tumors than both PBS *(****p < 0.0001*) and peptide- (*****p < 0.0001*) treated mice, as well as extended survival (***p = 0.045*). D-melittin was dosed at its MTD, which was largely ineffective at inhibiting tumor growth. On the other hand, polymer encapsulation of D-melittin permitted higher peptide dosing (5 mg peptide/kg), which was sufficient to slow tumor growth and thus enhance anti-tumor efficacy. Together, this data demonstrates the poor anti-cancer efficacy (tumor reduction, survival) of free peptide and the potential of DMM for cancer treatment.

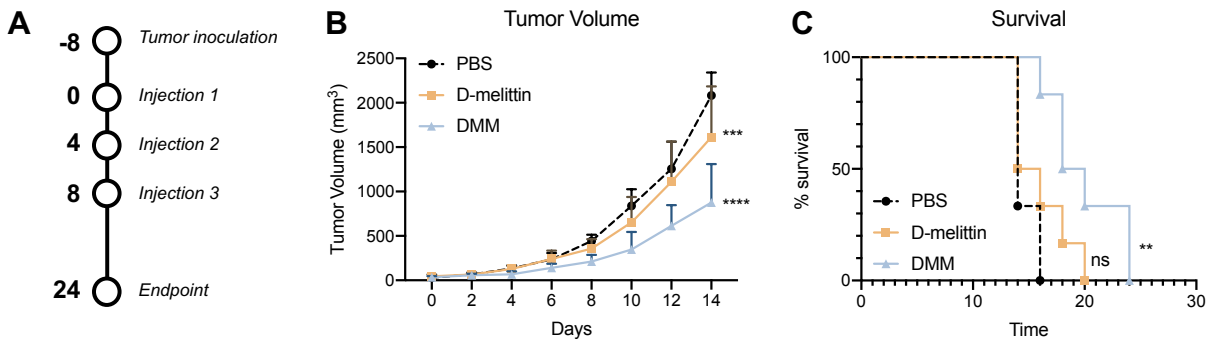

Figure 5.7: *Evaluation of anti-tumor effects of free peptide and micelles in a CT26 tumor model. A) Mice were inoculated subcutaneously with CT26 tumor cells (1M). Eight days later, mice were injected IV with (i) PBS, (ii) D-melittin 2 mg/kg, or (iii) DMM 5 mg peptide/kg every 4th day for a total of 3 injections. B) Tumor volume was measured every 2nd day. Significance is denoted in comparison to PBS-treated mice, calculated with a two-way ANOVA. D-melittin-treated mice had significantly smaller (***p = 0.0009) tumors than PBS mice, and DMM-treated mice had significantly smaller tumors than PBS-treated (****p < 0.0001) and D-melittin-treated (****p < 0.0001) mice. C) Survival of mice after treatment. Mice were sacrificed when euthanasia criteria were met (e.g., tumor volume > 10% of body weight). Significance is denoted in comparison to PBS-treated mice and was calculated with a Gehan-Breslow-Wilcoxon test. There was no significance (ns) in survival between PBS- and D-melittin treated groups, whereas DMM mice survived significantly longer PBS- (**p = 0.0029) and D-melittin (*p = 0.045) treated mice. (n = 6 mice/group)*

5.3.7 Anti-tumor efficacy of combinatorial DMM&ICB treatment

We next investigated anti-tumor efficacy of DMM in combination with immune checkpoint blockade (ICB) therapy, anti-CTLA-4 and anti-PD-1 antibodies, in murine breast (4T1) and colon (CT26) cancer models. In this work (section 5.3.3), we demonstrated that DMM induced ICD *in vitro*, which provided a beneficial anti-tumor effect. 4T1 and CT26 tumor models were used because they have high immune infiltration compared to other syngeneic murine models and have moderate to low mutational burden, and thus respond to ICB therapy to different extents [32]. ICB therapy has marked response in CT26 tumors, whereas 4T1 tumors are more resistant to treatment [33]. These two tumor models enabled us to differentiate synergistic efficacy of our treatment from

tumor-specific responses. Overall, we hypothesized that DMM could induce ICD of tumor cells which could subsequently activate tumor infiltrating leukocytes (TIL) and synergize with ICB to disrupt negative immune regulatory checkpoints, ultimately resulting in robust immune activation and tumor growth inhibition.

Eight days after inoculation, tumor-bearing mice were treated with (*i*) PBS, (*ii*) ICB 100 μg/mouse, (*iii*) DMM 5 mg peptide/kg or (*iv*) DMM 5 mg peptide/kg + ICB 100 μg/mouse (**Fig. 5.8A**). Micelles were injected every 4th day IV and ICB treatment was administered intraperitoneally (IP) on days following DMM treatment. In a 4T1 tumor model, ICB and DMM alone had no efficacy in slowing tumor growth, while combinatorial treatment of DMM+ICB significantly reduced tumor growth compared to PBS *(****$p < 0.0001$*), ICB (****$p < 0.0001$), and DMM (****$p < 0.0001$) (**Fig. 5.8B**).

In CT26 tumor-bearing mice, DMM showed mild efficacy in reducing tumor growth (****$p < 0.0001$) compared to PBS, while ICB and DMM+ICB were robustly able to halt tumor growth and in some mice, completely eliminate tumors (**Fig. 5.8C**). Mice in the ICB and DMM+ICB cohorts had significantly smaller tumors than PBS- (****$p < 0.0001$) and DMM- (****$p < 0.0001$) treated mice. However, there was no difference in tumor growth between ICB and DMM+ICB treated mice ($p = 0.9619$). Statistical significance was evaluated at 14 days following treatment; shortly after this timepoint, mice in PBS and DMM groups were euthanized due to increasing tumor burden and statistical tests could not be performed. In the ICB and DMM&ICB cohorts, 3 and 2 mice, respectively, were cured entirely of tumors. To investigate if treatment resulted in anti-tumor immune memory, mice were re-challenged with CT26 cells (1M) under the opposing inguinal nipple. None of these mice grew additional tumors, suggesting that ICB treatment, alone or in combination with DMM, can induce anti-tumor memory.

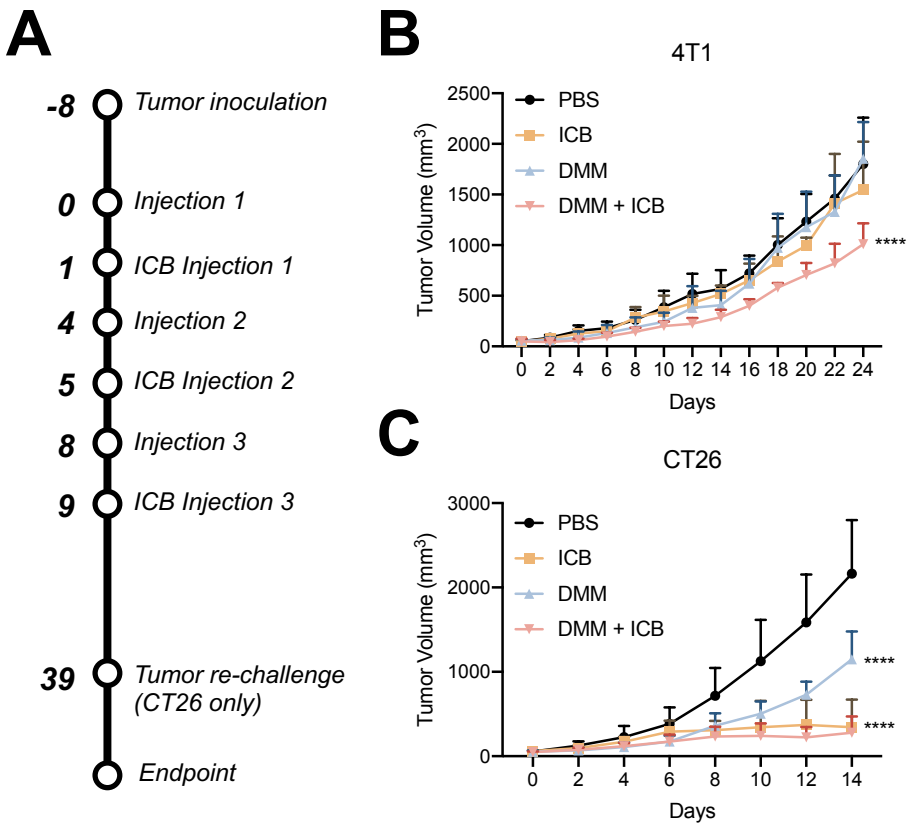

Figure 5.8: *Tumor reduction with combinatorial ICB in 4T1 and CT26 tumors. A) Time line of tumor inoculation and treatment. B) 4T1 tumor growth in mice treated with (i) PBS, (ii) ICB, (iii) DMM, or (iv) DMM+ICB. Combinatorial treatment of DMM+ICB significantly reduced tumor growth compared to PBS (****$p < 0.0001$), ICB (****$p < 0.0001$), and DMM (****$p < 0.0001$). Significance was calculated via two-way ANOVA and is denoted in regards to PBS. C) CT26 tumor growth in mice treated with (i) PBS, (ii) ICB, (iii) DMM, or (iv) DMM+ICB for the first 14 days after treatment. Mice receiving ICB and DMM+ICB treatment had significantly smaller tumors than mice treated with PBS- (****$p < 0.0001$) or DMM- (****$p < 0.0001$). There was no significance (ns) between ICB and DMM+ICB mice. Significance was calculated via two-way ANOVA and is denoted in regards to PBS. (n = 6 mice/group)*

5.4 Discussion and Conclusion

Here, we report the first development of D-melittin nanoformulations for anti-tumor applications. We previously reported that replacement of L-amino acids with D-amino acids in polymer-peptide delivery systems abrogates the generation of anti-polymer antibodies with minimal effect on

activity of the polymer-peptide platform [24]. This work opened up the possibility of evaluation D-melittin as an anti-cancer agent in a polymer-drug conjugate formulation that minimizes non-specific cytolysis without immunogenicity resulting from repeated dosing. Here, we show that D-melittin micelles (DMM) exert broad anti-tumor activity against various types of tumor cells, even cells that have developed resistance against traditional chemotherapeutics. In normal mice, DMM was safe for repeat systemic administration and could be administered at 10-fold higher dose compared to free peptide. Furthermore, DMM synergized with immune checkpoint blockade (ICB) and significantly inhibited tumor growth in tumor-bearing mice. These findings have broad applicability for all polymer-peptide conjugates, as it demonstrates that D-amino acid peptides can enhance platform safety while retaining tumoricidal activity *in vivo*.

We have pursued the use of D-melittin due to enhanced safety *in vivo*, despite exhibiting slightly reduced lytic capacity compared to L-melittin *in vitro* [24]. Conjugation of peptide to the polymer endows the peptide with acute pH-responsive behavior while also enhancing the lytic activity of the peptide at acidic conditions. Furthermore, D-amino acids can potentially enhance endosomal escape, as D-peptides persist longer than L-peptides within the cell [34]. Najjar, et al. demonstrated the enhanced endosomolytic behavior with D- and L- analogs of dimeric fluorescent (df) TAT, a cell penetrating peptide, and showed that the heightened protease stability of D-dfTAT prolonged intracellular retention and accumulation within late endosomes, ultimately resulting in more severe endosomal leakage and disruption of transcriptional programming[34]. Furthermore, the authors discuss how endocytosis and endosomal escape were impacted in opposite ways by peptide chirality: D-dfTAT was less prone to cellular internalization than L-dfTAT but exhibited increased endosomal escape. This reduced propensity of D-peptides for uptake can likely be attributed to reduced capacity to trigger endocytosis rather than a difference in binding to heparan sulfates [35]. However, our drug delivery system bypasses this entirely, as the polymer is in micellar form during cellular internalization and transitions to a linear form in the endosome, unsheathing the peptide and capitalizing on the amplified endosomolytic activity of D-peptides.

Furthermore, incorporation of D-melittin enabled application of our platform for systemic injections. Although the potential of melittin as a cancer therapeutic has been established, its severe nonspecific lytic activity poses significant challenges for clinical translation. Our work here adds

to the repertoire of strategies to systemically deliver melittin and other lytic peptides for cancer treatment [15, 36]. This vastly expands the scope of use of lytic ACPs, which are often constrained to intra-tumoral delivery to avoid related toxicity from systemic delivery [16, 37]. This could be particularly impactful to treatment of metastatic cancers, which are disseminated in distant locations from the primary tumor and do not benefit from enhanced permeation and retention (EPR) within large tumors [38]. Due to the controversial relevance of the EPR effect in humans and high variability of its effect between patients and cancer types, safe systemic delivery of lytic peptides is also valuable for treatment of primary tumors [39].

We next characterized if D-melittin induced immunogenic cell death (ICD), a form of inflammatory cell death that releases danger associated molecular patterns (DAMPs) which can elicit an anti-cancer immune response[40]. We expected melittin peptide and micelles to induce ICD, as L-melittin has been reported to induce NLRP3 inflammasome activation and production of IL-1β [23]. While melittin bypasses pyroptosis, we hypothesized that melittin could induce other forms of ICD. In this report, we verified that D-melittin and DMM induced surface expression of calreticulin (CRT) and extracellular release of ATP and HMGB1. Apoptotic cells traffic CRT from the endoplasmic reticulum to the cell surface, where the exposed CRT serves as an “eat me” signal to antigen presenting cells (APCs), which can induce subsequent tumor antigen presentation and tumor-specific responses [41]. This step usually precedes morphological signs of apoptosis and occurs in the early stages of ICD [31, 40]. Dying cells also release ATP, which serves as a “find me” signal to APCs and triggers NLRP3-inflamamsome-based cytokine secretion. Similarly, HMGB1 release acts as an attractant for various immune cells and can induce dendritic cell maturation and stimulate the production of pro-inflammatory cytokines from innate immune cells. HMGB1 is released by cells during the later stages of ICD [31, 40]. Here, we observed increased CRT expression, ATP secretion, and HMGB1 in melittin-treated groups. In fact, DMM induced significantly higher markers of ICD compared to free peptide; this effect is not attributed to the polymer, as CP did not induce hardly any indication of these events. Rather, ICD is likely initiated by cytosolic delivery of melittin. These results synergize with our aforementioned conclusions that polymer-conjugation enhanced the lytic activity of the peptide, and that the use of D-amino acids contributes to its robust capacity for intracellular delivery. While the extent of ICD was rather modest, we nonetheless concluded that DMM can induce ICD in cancer cells. This

modest efficacy could potentially be linked with the timing of endosomal disruption. Rupture of early endosomes facilitates improved cytosolic delivery and minimal NLRP3 inflammasome activation, whereas rupture of late endosomes/lysosomes resulted in reduced cytosolic delivery and strong NLRP3 inflammasome activation [42]. As the VIPER platform was initially designed to optimize endosomal escape for nucleic acid delivery, the modified DMM platform may have highest activity in early endosomes, minimizing inflammasome activity. Polymer incorporation of specific amino acids (e.g. pre-defined ratio of histidine:tryptophan) has been reported to increase the degree of lysosome rupture and thus the degree of inflammasome activation [43]. Such design considerations can be applied to our delivery platform to promote both cytosolic delivery and inflammasome activation for ICD. We could also employ a different pH-sensitive monomer that has a pH-transition point a lower pH and thus is activated in late endosomes, promoting inflammasome activation [44]. However, the exact correlation between the timing and minimal stimuli requirements for inflammasome activation is unclear, so the modified platform would require optimization.

Melittin-induced death is classically characterized by cell membrane disruption and pore formation, resulting in osmotic cell lysis and death [15]. However, the mechanism of death has also been connected with disruption of the mitochondrial membrane potential, similar to the KLA peptide, and with the toxic intracellular accumulation of Ca^{2+}, either via calmodulin inhibition or L-type Ca^{2+} activation [45]. The exact mechanism by which melittin mediates the increase of intracellular calcium concentrations has yet to be confirmed.

After characterizing our platform *in vitro,* we measured the safety of free peptide and micelles *in vivo* after single and repeat (total of 3, every 4^{th} day) injections. The MTD of D-melittin was determined to be 2 mg/kg, which is 10-fold lower than the MTD of DMM (20 mg peptide/kg), further emphasizing how polymer encapsulation remarkably expanded the therapeutic index of D-melittin. Polymer conjugation increased the maximum injectable dose by 10-fold (the top of the therapeutic window), while only affecting the efficacious drug concentration by 1.5- to 5-fold (the bottom of the therapeutic window), as shown for the cancer cell lines tested in **Table 5.1**. Another aspect of *in vivo* toxicity to consider is the high polymer concentration (125 mg/kg) of DMM employed to deliver therapeutic doses of melittin (20 mg peptide/kg). We have not assessed the

MTD of polymer alone (CP) in mice, as cytotoxicity and hemolysis studies demonstrated its safety in biological settings at concentrations up to 100 μM (1.6 mg/mL). It is likely that the MTD of DMM is limited by the toxicity of the peptide and not by the polymer, but we have yet to investigate this.

Upon characterizing activity *in vitro* and safety *in vivo*, we compared activity of D-melittin and DMM in CT26 tumor-bearing mice and demonstrated that free peptide had poor anti-tumor efficacy. Although the MTD of DMM is 10-fold higher, we selected a lower dose 5 mg/kg due to increased efficacy of the particles compared to free peptide. While D-melittin had modest reduction of tumor growth, DMM significantly reduced tumor growth and extended survival compared to PBS- and D-melittin-treated mice. It is likely that the dose-limiting toxicity of free-peptide prevented sufficient amounts of peptide from reaching tumor cells. Furthermore, peptides suffer from poor pharmacokinetics *in vivo*; while D-amino acids can prolong circulation by reducing degradation by proteases, the small size (~2 kD) of the peptide means it is readily filtered by the kidney[46]. On the other hand, polymer encapsulation enhances the dose that can safely be administered while also increasing the molecular weight to avoid renal filtration [47]. This is well demonstrated in this study, as we can safely deliver a sufficiently high dose of D-melittin to inhibit tumor growth in mice. Application of neutral PEGylated micelles for tumor targeting is widely reported, as the PEG coating enhances biodistribution and the neutral charge reduces macrophage uptake and increases tumor accumulation [48]. While the exact uptake mechanism of the PEGylated micelles by tumor cells is not elucidated here, we can make inferences about cell-particle interactions based on prior reports. PEG is historically employed to prolong *in vivo* circulation by shielding particles from the reticuloendothelial system, facilitating tumor accumulation and uptake [49]. Still, not all PEG-coatings are equivalent, and factors such as chain length and density differentially influence cellular uptake. In micelles with mixed PEG chain lengths, a higher proportion of short chains increased protein adsorption and nanoparticle coalescence, prompting cellular uptake [50]. In another study, similar neutral, PEG-micelles were internalized by cells within 2 hours, and these particles were transported through cell monolayers [51]. Further investigation revealed that these interactions occurred through various uptake mechanisms, including clathrin-, energy-, and cholesterol-mediated endocytosis.

Lastly, we investigated if DMM synergized with ICB treatment in 4T1 and CT26 tumor-bearing mice. These tumors have varying mutational burden, which means that they respond to ICB therapy to differing degrees[32, 33]. While the robust efficacy of ICB in CT26 tumors could perhaps dampen some enthusiasm for the DMM platform, we argue that DMM holds greatest potential in tumor models that are resistant to ICB treatment or traditional chemotherapy treatments. Perhaps melittin is more cytotoxic against cells that are transformed or mutated; this could be an interesting avenue for additional investigation as it has not yet been reported. We also characterized tumor-infiltrating leukocyte (TIL) populations after treatment with 3 doses of peptide and conjugates, but did not detect substantial differences in TILs between groups under the current dosing conditions (**Fig. S5.4**). Perhaps iteration on the particle design to enhance inflammasome activation, as well as optimization of dosing conditions, could significantly modulate TIL populations.

Additional future work on this project includes incorporation of targeting ligands into the hydrophilic block of the polymer to further promote specific targeting and uptake. While the nanoparticle's physical particles largely drive its accumulation in tumors, conjugation with targeting ligands can promote interactions with and uptake by tumor cells and enhance cell killing. We will also evaluate antitumor efficacy at higher DMM peptide concentrations, closer to its MTD (20 mg peptide/kg).

In summary, we report the first application of D-melittin for cancer therapy, emphasizing the promising potential of D-amino acids for *in vivo* therapeutic use. Melittin has drawn extensive attention as a potent natural ACP with broad anti-tumor activity, but its nonspecific hemolytic activity severely limited its *in vivo* applications. And though various delivery systems curb melittin's nonspecific toxicity, the peptide's potent immunogenicity facilitates the generation of a robust immune response against the carrier, further hampering its *in vivo* applications. Our lab addressed this hurdle by (1) employing VIPER, a pH-sensitive platform to facilitate controlled intracellular peptide delivery, and (2) replacing L-amino acids with D-amino acids, which transforms our technology into a safe delivery platform. Ultimately, we have designed a system that dually overcomes the challenge of peptide toxicity and immunogenicity, allowing us to recognize the full potential of melittin for cancer treatment.

In the context of ACPs, D-amino acid peptides are a largely unexplored territory[52]. There is an overall dearth of research on D-amino acids for cancer therapy, although the benefit of D-amino acids to markedly improve peptide stability and protease resistance *in vivo* has already been established[53]. Our findings first demonstrate that D-amino acids significantly enhance safety of peptide-polymer conjugates *in vivo* without compromising anti-cancer efficacy, which will benefit further development of D-amino acid peptides for cancer treatment.

5.5 Materials and methods

Materials, polymer synthesis, and characterization. Poly(ethylene glycol) methyl ether (4-cyano-4-pentanoate dodecyl trithiocarbonate) (PEG-CTA), 2-diisopropylaminoethyl methacrylate (DIPAMA), and pyridyl disulfide ethyl methacrylate (PDSEMA) were purchased from Sigma (Saint Louis, MO, USA). Fetal bovine serum (FBS) was purchased from R&D Systems (Minneapolis, MN, USA). Anti-mouse CTLA-4 (clone 9H10) and PD-1 (clone 29F.1A12) antibodies were purchased from Bio X cell. All other chemicals were purchased from Sigma and used as received.

Synthesis and characterization. Polymers and peptides were synthesized and characterized as previously described [24]. Briefly, D-melittin (GIGAVLKVLTTGLPALISWIKRKRQQC) peptides were synthesized on a microwave peptide synthesizer (Liberty Blue CEM) via solid phase peptide synthesis using L- or D-amino acids, respectively, and purified via reverse-phase HPLC in 0.1% TFA water and acetonitrile. Peptide molecular mass was determined by MALDI-TOF. To synthesize the polymer, PEG-CTA was polymerized with DIPAMA, PDSEMA, and azobisisobutyronitrile (AIBN) in dimethylacetamide (DMAc), and immersed in an oil bath at 70 °C. After 24 hours, the polymerization was quenched with liquid nitrogen and the resultant polymer (PEG_{113}-*b*-p($DIPAMA_{40}$-*co*-$PDSEMA_2$) was purified *via* dialysis against methanol and DI water. D-melittin was conjugated to PDSEMA *via* disulfide exchange reaction in methanol and water (5:1) and purified by dialysis against DI water. The micelles were prepared in acidic phosphate buffer (pH 4.0) and the pH was adjusted to pH 7-8, and sterile filtered using a 0.22 mm pore filter. Polymers were characterized by ^1H NMR in deuterated chloroform. Peptide conjugation to PDSEMA was monitored *via* UV (353 nm) for the release of 2-thiopyridine. Micelle

size was assessed by dynamic light scattering (0.5 mg/mL) and critical micellar concentration (CMC) was determined *via* Nile red method (ex/em 557/625 nm) with 0.5 mg/mL dye. The transition point of the micelles was determined using a Nile red method as previously described.

Cell culture. RAW 264.7 macrophages, CT26, and 4T1 cells were cultured in RPMI 1640 (Gibco) supplemented with 10% FBS (Gibco). For toxicity studies, cells were seeded at 15-20k cells/well in a 96 well plate. Cells were cultured with peptide or micelles for 24 hours and viability was determined by MTS/PMS (Promega) by plate reader. The Gal8-RAW 264.7 cell line was generated as previously described [26, 27]. Briefly, RAW cells were transfected with plasmids containing a transposable Gal8-GFP construct and PiggyBac transposon (generous gift of Prof. Jordan Green) using Lipofectamine 2000. Cells were sorted for the top 5% brightest GFP^+ singlet cell events, expanded, and sorted three more time to yield a population of Gal8-GFP^{high} cells.

Hemolysis assay. Hemolysis assays were conducted as described [28]. Human blood was obtained in accordance with University of Washington Institutional Review Board (IRB) guidelines. Briefly, blood was washed twice in 150 mM NaCl and resuspended in phosphate buffered saline (PBS) at each pH value to be tested (pH 5.4, 6.4, 7.4). Blood was diluted 1:50 and plated in a V-bottom 96-well plate. Samples were incubated with peptide in appropriate pH buffer at 37 °C for 1 hour. Supernatant was collected and absorbance (541 nm) was detected on a plate reader. Triton X-100 20% (w/v) and PBS at appropriate pH were used as positive and negative controls, respectively.

Imaging. Confocal imaging of endosomal escape was conducted as previously described. Briefly, Gal8-RAW 264.7 macrophages were plated (15k) in a Greinier HalfArea 96 well plate and incubated with peptide (1 μM) or micelles (6.25 μM) for 16-18 hours. Cells were imaged in Fluorobright media supplemented with 25 mM HEPES, 10% FBS, Hoechst 33342 (2000X), and PI (1000X). Wells were imaged in a 4x4 region of interest with a 20X objective (Leica SP8X).

Immunogenic cell death (ICD) characterization. ICD was characterized by surface calreticulin expression and ATP and HMGB1 secretion in cell supernatant. *Calreticulin staining.* CT26 cells were incubated with peptide (2 μM) or micelles (10 μM) for 24 hours, lifted with Accutase, and

stained with anti-calreticulin primary antibody (1:20, Abcam) followed by an anti-mouse secondary antibody (1:750), and analyzed on an Attune NxT (Invitrogen) flow cytometer. *ATP release.* CT26 cells were incubated with peptide or micelles at indicated concentrations for 24 hours and supernatant was collected and assessed for ATP concentration via the ENLITEN ATP Assay (Promega) according to manufacturer instructions. *HMGB1 release.* CT26 cells were incubated with peptide (2 μM) or micelles (10 μM) for 48 hours and supernatant was collected. Insoluble lipids were removed via centrifugation. HMGB1 concentration was assessed via ELISA (Chondrex) according to manufacturer instructions.

Animal studies. All animal studies were approved by the Institutional Animal Care and Use Committee (IACUC) at the University of Washington and were conducted in accordance with use and regulations. Female Balb/c mice (6-8 weeks) were ordered from Charles River Laboratories. Tumors (1M 4T1 or CT26 cells in 100 μl serum free RPMI) were inoculated subcutaneously under the 4th nipple (hind inguinal tumors). Treatment began on day 8 after inoculation. Mice were injected intravenously (IV) via tail vein at 5 mg peptide/kg every 4th day. Immune checkpoint blockade (ICB) antibodies (anti-PD-1 and anti-CTLA-4) were administered by intraperitoneal (IP) injection at 100 μg/mouse, on indicated days. Mice were humanely euthanized when euthanasia criteria was met (e.g. hunched, depressed respiration); tumors exceeded 10% of body weight; or tumor ulcers had discharge. For AST/ALT enzyme evaluation, serum was collected in serum separator tubes (BD), allowed to coagulate for 30 min at room temperature, and centrifuged at 1000 xg for 10 min at 4 °C. AST and ALT enzyme activity was evaluated with a kit (Sigma) following manufacturer instructions.

For tumor dissociation studies to assess TIL populations, tumor-bearing mice (100 mm^3) were injected with (*i*) PBS, (*ii*) CP, (*iii*) D-melittin 2 mg/kg, or (*iv*) DMM 5 mg peptide/kg IV. Twenty four hours later, mice were sacrificed, perfused with PBS, and tumors resected. Tumors were chopped into small pieces in serum free RPMI supplemented with DNAse I (125 U/mL) and Collagenase IV (20 U/mL) in a gentleMACS dissociator. The tumor cell suspension was filtered over a 70 μm cell strainer and prepared for flow staining. Cells were stained for viability with Zombie Violet and stained in three plates for T cells (CD45-APC/Cy7, CD4-AlexaFluor647, CD4-

PE, CD8-FITC), macrophages (CD45-APC/Cy7, CD11b-FITC, CD80-PE, CD206-BV604), and dendritic cells (CD45-APC/Cy7, CD11c-FITC, CD80-PE, MHCII-PE/Cy5).

Maximal tolerated dose (MTD) studies. Peptide or micelles were injected IV at indicated doses and mice were observed for two weeks following injection. Mice were humanely euthanized if they exhibited signs of acute distress (i.e. inability to walk, moribund) or weight loss exceeding 20% of starting body weight.

Histochemical analysis. For H&E imaging, mice were injected with peptide or micelles at indicated doses, every 4th day for a total of 3 injections. Twenty-four hours after the fourth injection, mice were sacrificed and perfused with PBS. Tissues were collection and fixed in 4% PFA for 48 hours at 4 °C, transferred to PBS, and submitted to the UW Histology and Imaging Core for tissue processing, staining, and scoring by a blinded third-party.

5.6 Acknowledgements

This work was supported by NIH (R01CA17727, R01CA257563, and U54CA199090). We thank Nathanial Peters and W. M. Keck Microscopy Center (S10 OD016240) for confocal microscopy support. We thank Kim Woodrow (University of Washington) for use of her plate reader. We thank Nora Disis (University of Washington) for her generous donation of CT26 cells and Jordan Green (Johns Hopkins University) for kindly providing the Gal8-GFP and PiggyBac transposon plasmids.

5.7 Competing Interests

S.H.P. has submitted a patent with the U.S. Patent and Trademark Office (WO2018027164A1) related to VIPER. S.H.P., S.L., and M.S. have filed a provisional patent on the DMM technology.

5.8 Supplemental Information

H&E Scoring								
	PBS		CP		D-melittin		DMM	
Heart	N	N	N	-	-	-	N	N
mononuclear infiltrate, epicardium, RV	-	-	-	1	1	1	-	-
Lung	-	-	-	N	N	-	-	-
hemorrhage, intra-alveolar, acute	1	1	1	-	-	-	-	-
lymphoid infiltrate, PV/PB	-	1	-	1	-	-	1	-
hemorrhage, perivascular, acute	-	-	-	-	-	1	-	1
mixed inflammatory cell infiltrate, PB	-	-	-	-	-	-	-	1
mixed inflammatory cell infiltrate, alveolar	-	-	-	-	-	-	1	-
Kidney	-	N	N	N	N	N	N	N
lymphoid infiltrate, pelvis	1	-	-	-	-	-	-	-
Liver	-	-	N	-	N	N	N	-
lymphoid infiltrate, perivascular	1	-	-	1	-	-	-	1
hepatocellular necrosis	-	1	-	-	-	-	-	-
Spleen	N	N	N	N	N	N	N	N

Table S5.1: H&E scoring of tissues. Pathological changes in the tissues were scored on a scale of 1 (minimal) to 4 (severe). RV = right ventricle; PV = perivascular; PB = peribronchiolar; N = no significant findings; 1 = minimal severity; 2 = mild severity; 3 = moderate severity; 4 = severe change; - = change not present. (n = 2 mice/group)

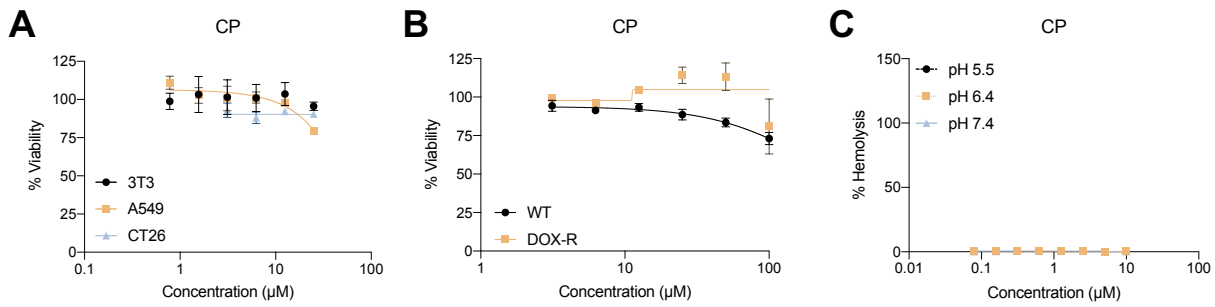

Fig. S5.1: Cytotoxicity of CP in (A) various cell lines, (B) wildtype and doxorubicin-resistant MDA-MB-435 cells, and (C) hemolytic activity of CP against human red blood cells at various pH.

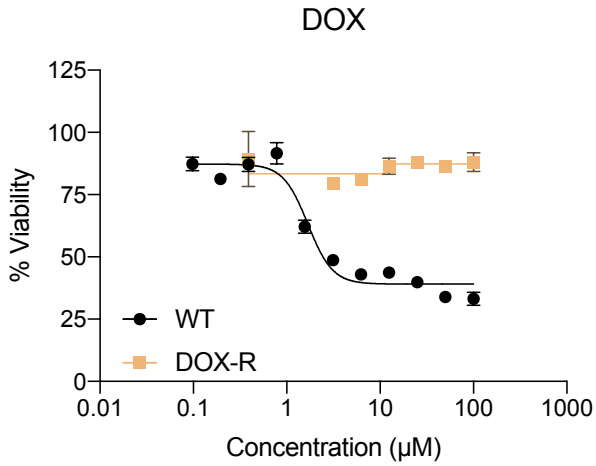

Fig. S5.2: Verification of DOX-resistant MDA-MB-435 cell line.

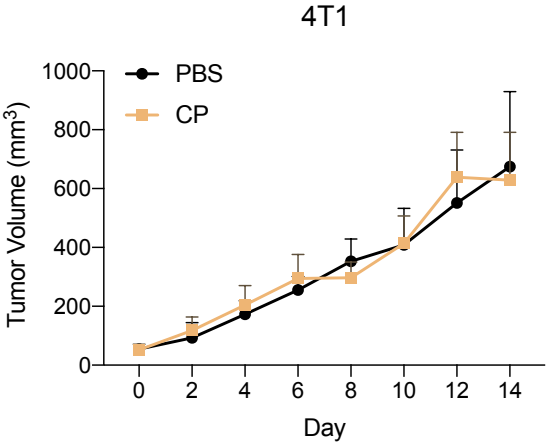

Fig. S5.3. Comparison of anti-tumor activity of PBS and CP in 4T1 tumor-bearing mice.

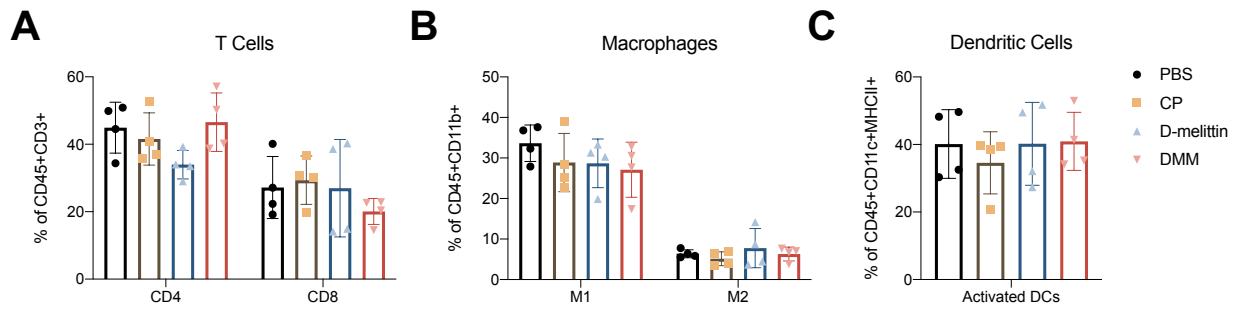

Fig. S5.4: Analysis of tumor infiltrating leukocytes after treatment. Mice were treated with (*i*) PBS, (*ii*) CP, (*iii*) D-melittin 2 mg/kg, or (*iv*) DMM 5 mg peptide/kg IV every 4th day for a total of 3 injections. Twenty-four hours after the final injection, tumors were dissociated and stained for T cell (CD4 [$CD45^+CD3^+CD4^+$] or CD8 [$CD45^+CD3^+CD8^+$]), macrophage (M1 [$CD45^+CD11b^+CD206^+$] or M2 [$CD45^+CD11b^+CD80^+$], and dendritic cell (activated [$CD45^+CD11c^+MHCII^+CD80^+$] populations.

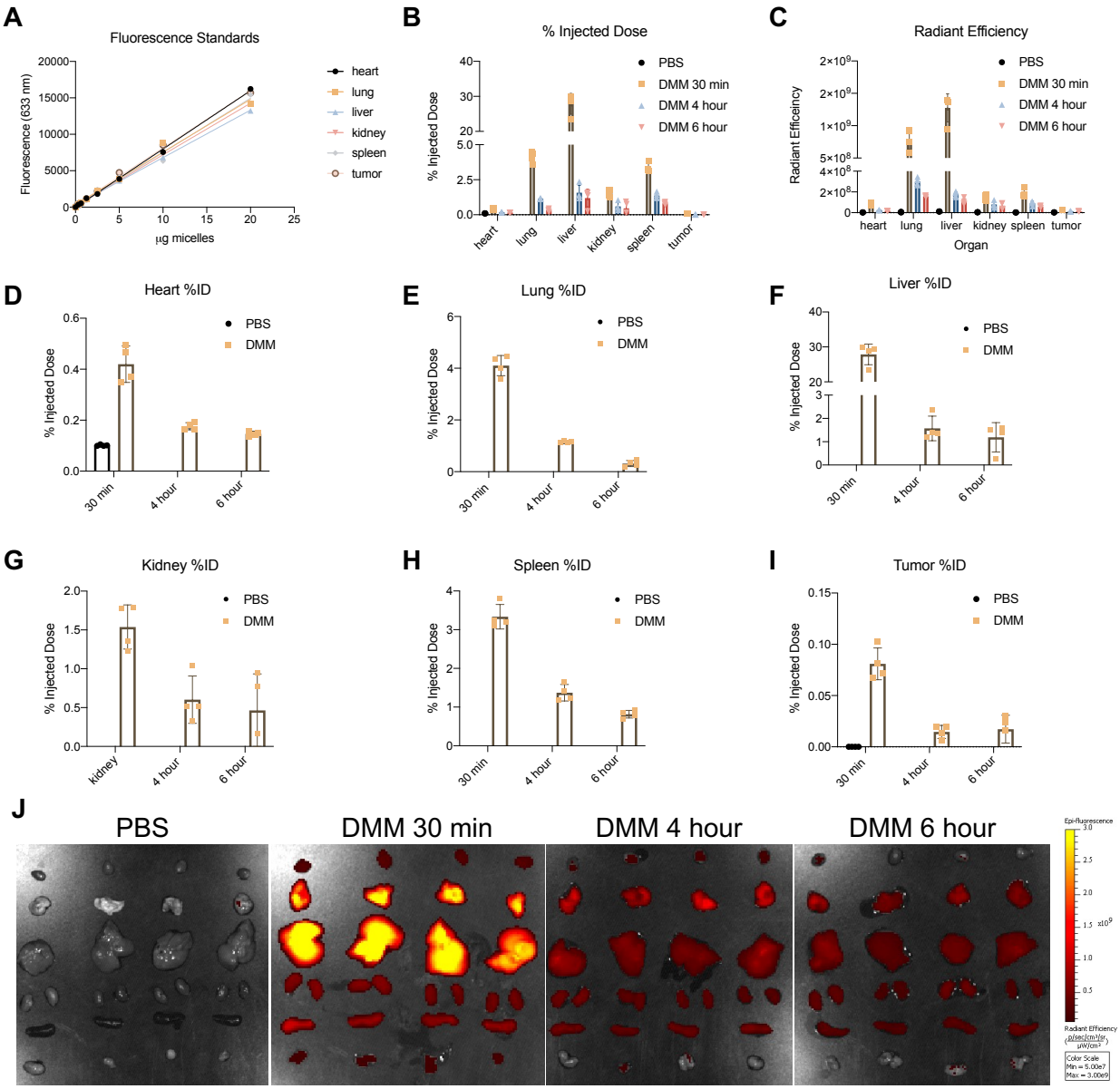

Fig. S5.5. Biodistribution of Cy5-labeled DMM (2 mg melittin/kg) in tumor-bearing mice at 30 min, 4 hour, or 6 hour post-injection. A) Fluorescence of micelles doped into organs of non-injected mice. Standard curves of were generated for each organ. B) Distribution of micelles throughout the major organs. C) Quantification of radiant efficiency, as determined by Xenogen fluorescence imaging, per organ. D-I) Quantification of the µg of micelles per µg of tissue in the heart (D), lungs (E), liver (F), kidney (G), spleen (H), and tumor (I). J) Xenogen images of micelle accumulation in organs and tumor. Organs are arranged top to bottom as heart, lungs, liver, kidney, spleen, and tumor.

References

[1] Kurrikoff K, Aphkhazava D, Langel U. The future of peptides in cancer treatment. Curr Opin Pharmacol. 2019;47:27-32.

[2] Aaghaz S, Gohel V, Kamal A. Peptides as Potential Anticancer Agents. Curr Top Med Chem. 2019;19:1491-511.

[3] Fosgerau K, Hoffmann T. Peptide therapeutics: current status and future directions. Drug Discov Today. 2015;20:122-8.

[4] Ren LF, Lv J, Wang H, Cheng YY. A Coordinative Dendrimer Achieves Excellent Efficiency in Cytosolic Protein and Peptide Delivery. Angew Chem Int Edit. 2020.

[5] Qiao ZY, Lai WJ, Lin YX, Li D, Nan XH, Wang Y, et al. Polymer-KLAK Peptide Conjugates Induce Cancer Cell Death through Synergistic Effects of Mitochondria Damage and Autophagy Blockage. Bioconjugate Chem. 2017;28:1709-21.

[6] Gianneschi NC, Sun H, Cao W, Zang N, Clemons T, Scheutz G, et al. Proapoptotic Peptide Brush Polymer Nanoparticles via Photoinitiated Polymerization-Induced Self-Assembly. Angew Chem Int Ed Engl. 2020.

[7] Felicio MR, Silva ON, Goncalves S, Santos NC, Franco OL. Peptides with Dual Antimicrobial and Anticancer Activities. Front Chem. 2017;5.

[8] Srairi-Abid N, Othman H, Aissaoui D, BenAissa R. Anti-tumoral effect of scorpion peptides: Emerging new cellular targets and signaling pathways. Cell Calcium. 2019;80:160-74.

[9] Araste F, Abnous K, Hashemi M, Taghdisi SM, Ramezani M, Alibolandi M. Peptide-based targeted therapeutics: Focus on cancer treatment. J Control Release. 2018;292:141-62.

[10] Lv S, Sylvestre M, Prossnitz AN, Yang LF, Pun SH. Design of Polymeric Carriers for Intracellular Peptide Delivery in Oncology Applications. Chemical reviews. 2021.

[11] Liu CC, Hao DJ, Zhang Q, An J, Zhao JJ, Chen B, et al. Application of bee venom and its main constituent melittin for cancer treatment. Cancer Chemoth Pharm. 2016;78:1113-30.

[12] Duffy C, Sorolla A, Wang E, Golden E, Woodward E, Davern K, et al. Honeybee venom and melittin suppress growth factor receptor activation in HER2-enriched and triple-negative breast cancer. Npj Precis Oncol. 2020;4.

[13] Memariani H, Memariani M, Moravvej H, Shahidi-Dadras M. Melittin: a venom-derived peptide with promising anti-viral properties. Eur J Clin Microbiol. 2020;39:5-17.

[14] Peeler DJ, Yen A, Luera N, Stayton PS, Pun SH. Lytic Polyplex Vaccines Enhance Antigen-Specific Cytotoxic T Cell Response through Induction of Local Cell Death. Advanced Therapeutics.

[15] Rady I, Siddiqui IA, Rady M, Mukhtar H. Melittin, a major peptide component of bee venom, and its conjugates in cancer therapy. Cancer Lett. 2017;402:16-31.

[16] Yu X, Dai YF, Zhao YF, Qi SH, Liu L, Lu LS, et al. Melittin-lipid nanoparticles target to lymph nodes and elicit a systemic anti-tumor immune response. Nat Commun. 2020;11.

[17] Liu HJ, Hu Y, Sun YJ, Wan C, Zhang ZJ, Dai XM, et al. Co-delivery of Bee Venom Melittin and a Photosensitizer with an Organic-Inorganic Hybrid Nanocarrier for Photodynamic Therapy and Immunotherapy. Acs Nano. 2019;13:12638-52.

[18] Cao J, Zhang Y, Shan YK, Wang JG, Liu F, Liu HR, et al. A pH-dependent Antibacterial Peptide Release Nano-system Blocks Tumor Growth in vivo without Toxicity. Scientific Reports. 2017;7.

[19] Cheng B, Xu PS. Redox-Sensitive Nanocomplex for Targeted Delivery of Melittin. Toxins. 2020;12.

[20] Mima Y, Hashimoto Y, Shimizu T, Kiwada H, Ishida T. Anti-PEG IgM Is a Major Contributor to the Accelerated Blood Clearance of Polyethylene Glycol-Conjugated Protein. Mol Pharmaceut. 2015;12:2429-35.

[21] Ishida T, Kiwada H. Accelerated blood clearance (ABC) phenomenon upon repeated injection of PEGylated liposomes. Int J Pharm. 2008;354:56-62.

[22] Shiraishi K, Yokoyama M. Toxicity and immunogenicity concerns related to PEGylated-micelle carrier systems: a review. Sci Technol Adv Mat. 2019;20:324-36.

[23] Martin-Sanchez F, Martinez-Garcia JJ, Munoz-Garcia M, Martinez-Villanueva M, Noguera-Velasco JA, Andreu D, et al. Lytic cell death induced by melittin bypasses pyroptosis but induces NLRP3 inflammasome activation and IL-1 beta release. Cell Death Dis. 2017;8.
[24] Sylvestre M, Lv SX, Yang LF, Luera N, Peeler DJ, Chen BM, et al. Replacement of L-amino acid peptides with D-amino acid peptides mitigates anti-PEG antibody generation against polymer-peptide conjugates in mice. J Control Release. 2021;331:142-53.
[25] Cheng YL, Yumul RC, Pun SH. Virus-Inspired Polymer for Efficient In Vitro and In Vivo Gene Delivery. Angew Chem Int Edit. 2016;55:12013-7.
[26] Kilchrist KV, Dimobi SC, Jackson MA, Evans BC, Werfel TA, Dailing EA, et al. Gal8 Visualization of Endosome Disruption Predicts Carrier-Mediated Biologic Drug Intracellular Bioavailability. Acs Nano. 2019;13:1136-52.
[27] Rui Y, Wilson DR, Choi J, Varanasi M, Sanders K, Karlsson J, et al. Carboxylated branched poly(beta-amino ester) nanoparticles enable robust cytosolic protein delivery and CRISPR-Cas9 gene editing. Sci Adv. 2019;5.
[28] Evans BC, Nelson CE, Yu SS, Beavers KR, Kim AJ, Li HM, et al. Ex Vivo Red Blood Cell Hemolysis Assay for the Evaluation of pH-responsive Endosomolytic Agents for Cytosolic Delivery of Biomacromolecular Drugs. Jove-J Vis Exp. 2013.
[29] Ma S, Song WT, Xu YD, Si XH, Lv SX, Zhang Y, et al. Rationally Designed Polymer Conjugate for Tumor-Specific Amplification of Oxidative Stress and Boosting Antitumor Immunity. Nano Lett. 2020;20:2514-21.
[30] Fucikova J, Kepp O, Kasikova L, Petroni G, Yamazaki T, Liu P, et al. Detection of immunogenic cell death and its relevance for cancer therapy. Cell Death Dis. 2020;11.
[31] Menger L, Vacchelli E, Adjemian S, Martins I, Ma YT, Shen SS, et al. Cardiac Glycosides Exert Anticancer Effects by Inducing Immunogenic Cell Death. Sci Transl Med. 2012;4.
[32] Zhong WY, Myers JS, Wang F, Wang K, Lucas J, Rosfjord E, et al. Comparison of the molecular and cellular phenotypes of common mouse syngeneic models with human tumors. Bmc Genomics. 2020;21.
[33] Kim K, Skora AD, Li ZB, Liu Q, Tam AJ, Blosser RL, et al. Eradication of metastatic mouse cancers resistant to immune checkpoint blockade by suppression of myeloid-derived cells. P Natl Acad Sci USA. 2014;111:11774-9.
[34] Najjar K, Erazo-Oliveras A, Brock DJ, Wang TY, Pellois JP. An L- to D-Amino Acid Conversion in an Endosomolytic Analog of the Cell- penetrating Peptide TAT Influences Proteolytic Stability, Endocytic Uptake, and Endosomal Escape. J Biol Chem. 2017;292:847-61.
[35] Verdurmen WPR, Bovee-Geurts PH, Wadhwani P, Ulrich AS, Hallbrink M, van Kuppevelt TH, et al. Preferential Uptake of L- versus D-Amino Acid Cell-Penetrating Peptides in a Cell Type-Dependent Manner. Chem Biol. 2011;18:1000-10.
[36] Soman NR, Baldwin SL, Hu G, Marsh JN, Lanza GM, Heuser JE, et al. Molecularly targeted nanocarriers deliver the cytolytic peptide melittin specifically to tumor cells in mice, reducing tumor growth. J Clin Invest. 2009;119:2830-42.
[37] Russell PJ, Hewish D, Carter T, Sterling-Levis K, Ow K, Hattarki M, et al. Cytotoxic properties of immunoconjugates containing melittin-like peptide 101 against prostate cancer: in vitro and in vivo studies. Cancer Immunol Immun. 2004;53:411-21.
[38] Schroeder A, Heller DA, Winslow MM, Dahlman JE, Pratt GW, Langer R, et al. Treating metastatic cancer with nanotechnology. Nat Rev Cancer. 2012;12:39-50.
[39] Bjornmalm M, Thurecht KJ, Michael M, Scott AM, Caruso F. Bridging Bio-Nano Science and Cancer Nanomedicine. Acs Nano. 2017;11:9594-613.
[40] Krysko DV, Garg AD, Kaczmarek A, Krysko O, Agostinis P, Vandenabeele P. Immunogenic cell death and DAMPs in cancer therapy. Nat Rev Cancer. 2012;12:860-75.
[41] Zhou JY, Wang GY, Chen YZ, Wang HX, Hua YQ, Cai ZD. Immunogenic cell death in cancer therapy: Present and emerging inducers. J Cell Mol Med. 2019;23:4854-65.

[42] Baljon JJ, Dandy A, Wang-Bishop L, Wehbe M, Jacobson ME, Wilson JT. The efficiency of cytosolic drug delivery using pH-responsive endosomolytic polymers does not correlate with activation of the NLRP3 inflammasome (vol 7, pg 1888, 2019). Biomater Sci-Uk. 2019;7:2200-.
[43] Manna S, Howitz WJ, Oldenhuis NJ, Eldredge AC, Shen JJ, Nihesh FN, et al. Immunomodulation of the NLRP3 Inflammasome through Structure-Based Activator Design and Functional Regulation via Lysosomal Rupture. Acs Central Sci. 2018;4:982-95.
[44] Feng Q, Wilhelm J, Gao JM. Transistor-like Ultra-pH-Sensitive Polymeric Nanoparticles. Accounts Chem Res. 2019;52:1485-95.
[45] Ceremuga M, Stela M, Janik E, Gorniak L, Synowiec E, Sliwinski T, et al. Melittin-A Natural Peptide from Bee Venom Which Induces Apoptosis in Human Leukaemia Cells. Biomolecules. 2020;10.
[46] Torchilin VP, Lukyanov AN. Peptide and protein drug delivery to and into tumors: challenges and solutions. Drug Discov Today. 2003;8:259-66.
[47] Alexis F, Pridgen E, Molnar LK, Farokhzad OC. Factors affecting the clearance and biodistribution of polymeric nanoparticles. Mol Pharmaceut. 2008;5:505-15.
[48] Xiao K, Li YP, Luo JT, Lee JS, Xiao WW, Gonik AM, et al. The effect of surface charge on in vivo biodistribution of PEG-oligocholic acid based micellar nanoparticles. Biomaterials. 2011;32:3435-46.
[49] Suk JS, Xu QG, Kim N, Hanes J, Ensign LM. PEGylation as a strategy for improving nanoparticle-based drug and gene delivery. Adv Drug Deliver Rev. 2016;99:28-51.
[50] Gao HJ, Liu JJ, Yang CH, Cheng TJ, Chu LP, Xu HY, et al. The impact of PEGylation patterns on the in vivo biodistribution of mixed shell micelles. Int J Nanomed. 2013;8:4229-46.
[51] Hu X, Yang FF, Liu CY, Ehrhardt C, Liao YH. In vitro uptake and transport studies of PEG-PLGA polymeric micelles in respiratory epithelial cells. Eur J Pharm Biopharm. 2017;114:29-37.
[52] Orafaie A, Sadeghian H, Bahrami AR, Rafatpanah H, Matin MM. Design, synthesis and evaluation of PD-L1 peptide antagonists as new anticancer agents for immunotherapy. Bioorgan Med Chem. 2021;30.
[53] Hong SY, Oh JE, Lee KH. Effect of D-amino acid substitution on the stability, the secondary structure, and the activity of membrane-active peptide. Biochem Pharmacol. 1999;58:1775-80.

Chapter 6

Development of Candidalysin polymer-peptide conjugates

*Meilyn Sylvestre, *Shixian Lv, and Suzie H. Pun
*equally contributing authors

6.1 Abstract

Candidalysin, a peptide toxin from *C. albicans*, is a potent cytolytic peptide associated with NLRP3 inflammasome activation and inflammation. We hypothesized that this inflammatory attribute could be harnessed by targeted delivery to solid tumors for local immune cell activation. We employed our polymer platform, virus inspired polymer for endosomal release (VIPER), a self-assembling pH-responsive polymer that facilitates intracellular peptide delivery, to administer Candidalysin to tumors. Although we observed that peptide and micelles were cytotoxic against a range of cancer lines and extremely hemolytic, neither Candidalysin peptide nor micelles inhibited tumor growth *in vivo*, even via direct intratumoral injection of peptide. Lack of efficacy could be attributed to a failure to induce appropriate inflammatory pathways; reduced cellular interactions from peptide in the micellar form; or over-stimulation of inflammation in the tumor environment, resulting in immune suppression. Overall, these findings add to the arsenal of peptides that VIPER can deliver, and emphasize the versatility of the VIPER delivery system.

6.2 Introduction

Overcoming immune evasion and activating the immune system has been a key thrust of cancer immunotherapies. The prevailing strategy is to reinvigorate cytotoxic effectors within the tumor microenvironment in order to induce systemic immune mechanisms for effective antitumor responses.[1] This can be achieved through programmed cell death pathways such as pyroptosis, a lytic, inflammatory cell death that features cell membrane rupture and release of cytosolic contents and proinflammatory factors.[2,3] When employed as a cancer therapy, pyroptosis inducers can effect robust activation of antigen presenting cells, immune infiltration, and tumor clearance, which has been demonstrated in several different tumor models.[4-6]

Here, we used the cytolytic peptide toxin Candidalysin, derived from the fungal pathogen *Candida albicans*, to induce inflammatory cell death in cancer cells.[7] Candidalysin triggers NLRP3-inflammasome and caspase-1 activation, stimulating immune activation, cell recruitment, and cell death in mononuclear cells and phagocytes.[8,9] We hypothesized that Candidalysin both induces tumor cells to release neoantigens and intracellular contents, and triggers activation of tumor-associated macrophages (TAMs) to boost local inflammation. TAMs represent a high proportion of tumor infiltrating cells (up to 50% solid mass) and are highly phagocytic, so are highly likely to uptake Candidalysin micelles.[10] Furthermore, the benefit of TAM-targeted therapies has been extensively reported, owing to their prevalence, spatial location throughout the tumor, and contribution to local immunosuppression.[11,12]

To deliver Candidalysin, we employed our peptide-polymer conjugate platform, virus inspired polymer for endosomal release (VIPER), to mediate intracellular delivery.[13] Peptides suffer from rapid clearance and insufficient transmembrane delivery, leading to severe endolysosomal entrapment and insufficient drug concentrations.[14-16] Polymer conjugation extends systemic circulation and confers increased resistance against enzymatic degradation. Furthermore, polymer conjugation can reduce nonspecific peptide interactions with cells, which is particularly crucial for intravenous (IV) injection of lytic peptides.[17] We previously applied VIPER to deliver peptides to cells and demonstrated the *in vivo* safety and efficacy of this platform.[18] Specifically, we employed VIPER to deliver melittin, the lytic, immunogenic peptide component of bee venom, to tumors. At physiological pH, VIPER protects its peptide cargo; following cellular internalization into acidic endosomes, VIPER dissociates and reveals melittin, which possess membranolytic activity sufficient to escape endosomes. Polymer conjugation enhanced peptide potency while also increasing the maximum tolerated dose of systemically-administered melittin, confirming the improved safety of this platform over free peptide. Additionally, this platform synergized with immune checkpoint blockade therapy to induce robust tumor inhibition in two tumor models, revealing that polymer conjugation does not compromise peptide activity. Based on these finding, we hypothesized that we could use VIPER to facilitate delivery of another immunogenic peptide, Candidalysin, for anticancer therapy.

Herein, we report the development and application of Candidalysin peptide-polymer conjugates for treatment of solid tumors. Based on the membranolytic properties of Candidalysin, we substituted Candidalysin for melittin, yielding CP-Candidalysin micelles. After synthesizing and characterizing the conjugate, we examined its activity *in vitro*. First, we assessed peptide cytotoxic and cytolytic behavior, and confirmed its ability to induce release of inflammatory cytokines *in vitro*. Next, we assessed the cytotoxicity, hemolytic activity, and capacity to disrupt endosomes of micellar formulations. Finally, we compared antitumor efficacy in CT26 tumor-bearing mice. Ultimately, Candidalysin, either as free peptide or micellar formulation, was unable to reduce tumor progression, even when administered directly into the tumor. This lack of efficacy demonstrates that inflammation and cytolysis alone is unable to activate and induce antitumor responses, and highlights the complicated interactions between tumor cells and the immune system.

6.3 Results

6.3.1 Design of polymer-peptide conjugates

VIPER is comprised of a hydrophilic block for solubility, and a pH-sensitive block for triggered display of Candidalysin. The pH sensitive block, poly(2-diisopropylaminoethyl methacrylate)-*co*-poly(pyridyl disulfide ethyl methacrylate) (p(DIPAMA-PDSEMA)), includes p(DIPAMA), which undergoes a sharp phase transition from hydrophobic to hydrophilic at pH 6.3, and PDSEMA, which enables functionalization with thiolated peptides. Monomers self-assemble into micelles that protect their peptide cargos at physiological pH 7.4, but expose peptide at acidic endosomal pH. Micelles were synthesized as a diblock copolymer by reversible addition-fragmentation chain-transfer (RAFT) polymerization of DIPAMA and PSDSEMA using PEGylated macro chain transfer agents (CTAs), as previously described (**Figure 6.1A**).[13,18] Polymer without conjugated peptide is referred to as control polymer (CP). Polymer-peptide conjugates self-assembled into micelles at pH 7.4 with hydrodynamic diameters of ~ 30.2 and 40.2 nm for CP and CP-Candidalysin micelles, respectively (**Figure 6.1B-C**). The pH transition point of micelles was determined to be around pH 6.2-6.4, which is consistent with that of DIPAMA (**Figure 6.1C**).

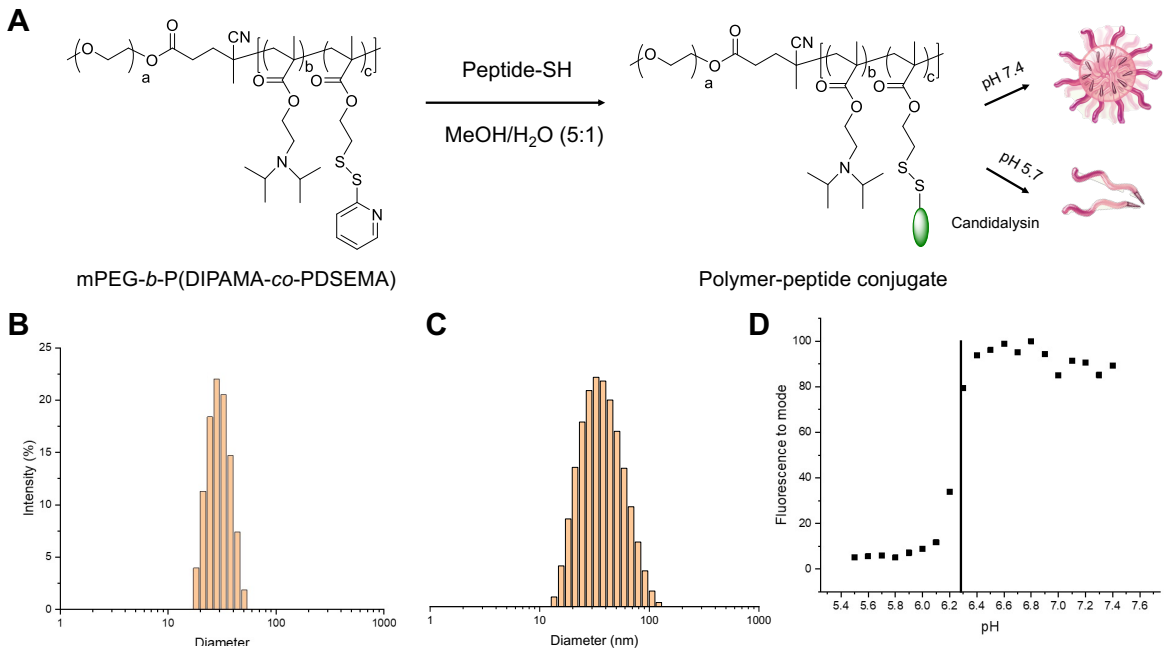

Figure 6.1*: Synthesis of Candidalysin micelles. A) Polymer was synthesized by RAFT polymerization of DIPAMA and PDSEMA using PEGylated CTAs. Micelles self-assemble at neutral and disassemble into polymer chains at acidic pH. B-C) The hydrodynamic diameter of CP (B) and CP-Candidalysin (C) micelles was determined to be 30.2 and 40.2 nm, respectively. C) The pH transition point of micelles is between pH 6.2-6.4.*

6.3.2 Peptide activity in vitro

Peptide activity *in vitro* was evaluated via cytotoxicity, membrane permeabilization, and cytokine release assays. Candidalysin was toxic against murine macrophages (RAW 264.7), colon carcinoma (CT26), and triple negative breast cancer (4T1) cells, as evidenced by low micromolar half maximal inhibitory concentrations (IC_{50}) across cell lines (**Figure 6.1A**, **Table 6.1**). To evaluate Candidalysin's ability to permeabilize cell membranes, we incubated peptide with RAW 264.7 macrophages for 10 or 30 minutes and measured membrane permeabilization via propidium iodide (PI) incorporation (**Figure 6.2B**). Approximately half of live cells rapidly incorporated PI, suggesting that Candidalysin is able to form pores in cell membranes. Finally, we assessed the ability of Candidalysin to induce IL-1β release in murine bone marrow derived macrophages (mBMDM) by incubating cells with peptide for 5 hours and quantifying IL-1β levels in the

supernatant via ELISA (**Figure 6.2C**). IL-1β release is a hallmark of NLRP3 activation. Release of IL-1β was concentration-dependent, suggesting that Candidalysin induced inflammation.

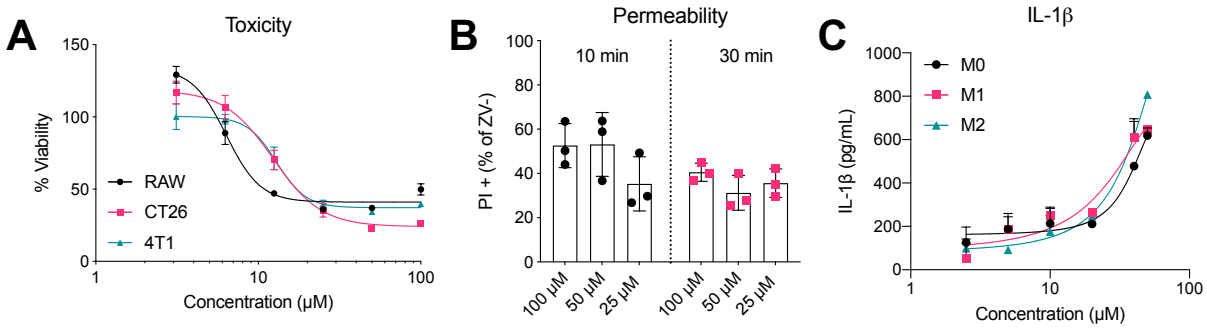

***Figure 6.2**: In vitro activity of peptide. A) Candidalysin was incubated with RAW, CT26, or 4T1 cells for 24 h and viability was assessed by MTS/PMS. B) Pore formation in cellular membranes was quantified by PI incorporation into cell membranes. RAW macrophages were incubated with peptide at indicated concentrations for 10 or 30 minutes and the % of PI+ cells was measured via flow cytometry. C) Murine bone marrow derived macrophages were incubated with peptide and IL-1β concentration in the supernatant was measured via ELISA.*

Viability IC_{50} (μM)	
Cell line	Candidalysin
RAW 264.7	6.35
CT26	12.32
4T1	12.95

***Table 6.1.** Toxicity of Candidalysin against murine macrophages and cancer cells.*

6.3.3 Micelle activity in vitro

We next investigated the cytotoxicity of Candidalysin micelles against human (A549, lung epithelial carcinoma; HEPG2 liver carcinoma) and murine (3T3, fibroblast) cells and compared activity to free peptide (**Figure 6.3A-B, Table 6.2**). While free peptide was more toxic than micelles against A549 and HEPG2 cells, the opposite trend emerges in MDA-MD-435 (human melanoma) cells: in MDA-MB-435 cells, the polymeric version is more potent than free peptide.

Overall, both peptide and micelles had low micromolar IC_{50} values. Additionally, both peptide and micelles demonstrate robust toxicity in wild type (WT) and doxorubicin-resistant (DOX-R) MDA-MB-435 cells (**Figure 6.3C-D**, with confirmation of doxorubicin-resistance reported in **Figure S6.2B**), with higher activity in drug-resistant cells. Notably, the micelles are 8-fold more cytotoxic compared to free peptide in DOX-R cells. This implies its clinical potential against tumors that develop resistance against standard chemotherapeutics.

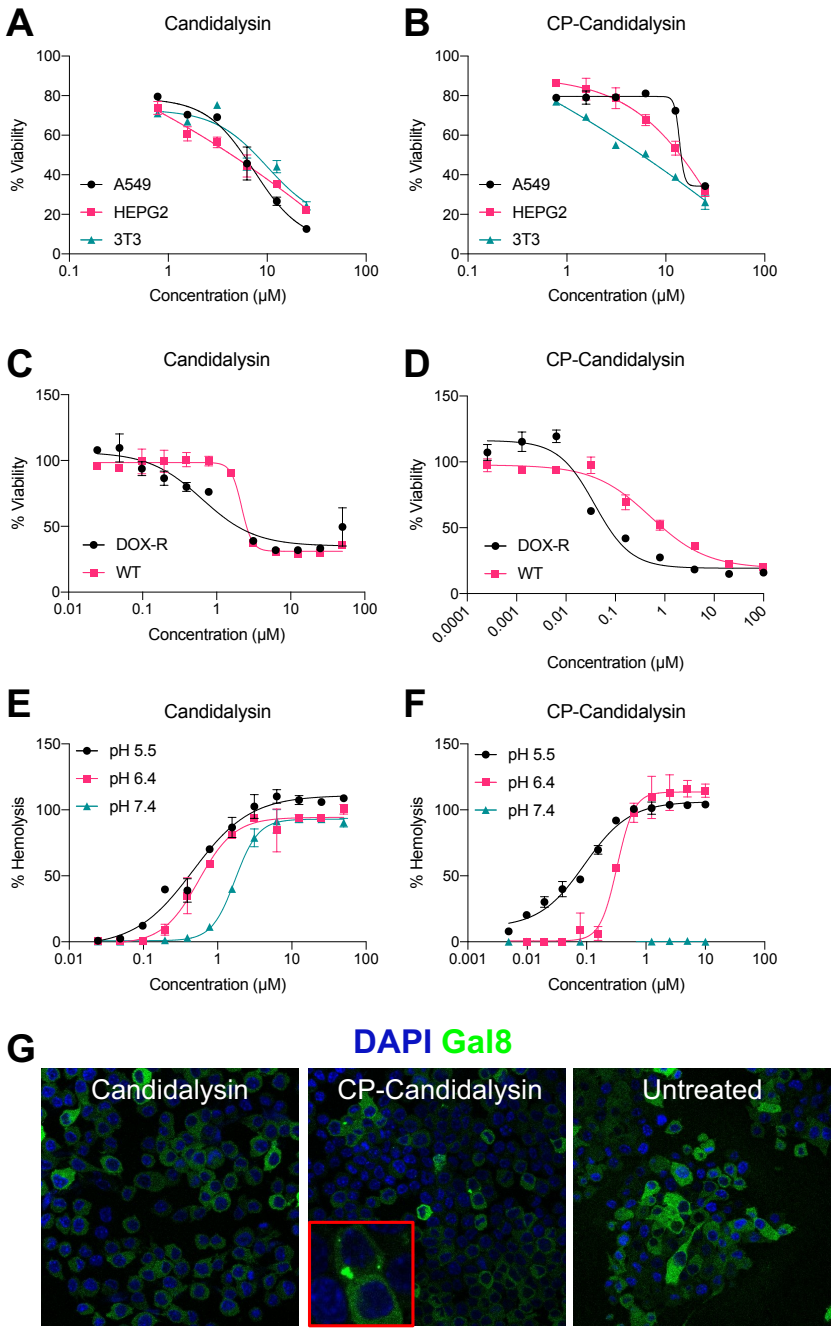

***Figure 6.3**: Toxicity of Candidalysin micelles and peptide. A-B) Toxicity of Candidalysin (A) and CP-Candidalysin micelles (B) against A549, HEPG2, and 3T3 cells. C-D) Toxicity of Candidalysin (C) and (D)CP-Candidalysin against wild type (WT) and doxorubicin-resistant (DOX-R) MDA-MB-435 cells. E-F) Hemolysis of free peptide (A) and micelles (B) against human red blood cells at pH 5.4, 6.4, and 7.4. G) Endosomal disruption in a Gal8-GFP-RAW264.7 reporter cell line. Events of endosomal disruption are expressed as GFP^+ punctae.*

Viability IC_{50} (μM)			
Cell line	Candidalysin	CP-Candidalysin	Ratio of IC_{50} of peptide:conjugate
A549	5.78	14.40	0.40
HEPG2	4.41	13.93	0.32
3T3	7.65	5.69	1.34
MDA-MB-435 WT	2.17	0.51	4.25
MDA-MB-435 DOX-R	0.64	0.04	16.0

***Table 6.2:** Cytotoxicity of peptide and micelles in murine and human tumor cell lines. For CP-Candidalysin, concentration is expressed as containing a peptide equivalent to free peptide.*

Hemolysis HC_{50} (μM)			
Entry	pH 5.4	pH 6.4	pH 7.4
Candidalysin	0.46	0.55	1.72
CP-Candidalysin	0.09	0.33	N/A

***Table 6.3**: Hemolytic activity of red blood cells at pH 5.4, 6.4, and 7.4. For CP-Candidalysin, concentration is expressed as containing a peptide equivalent to free peptide.*

We next investigated the lytic activity of peptide and micelles by assessing hemolysis of human red blood cells (RBCs) and visualizing endosomal escape. Peptide and micelles were incubated with RBCs at pH 5.4, 6.4, and 7.4, a range that covers endosomal pH, micelle transition point, and

physiological pH. Candidalysin was lytic at all pH values and exhibited higher activity with increasing acidity, indicated by decreasing concentration for 50% RBC hemolysis (HC_{50}) with decreasing pH (**Figure 6.3E**). In contrast, CP-Candidalysin micelles had robust activity at endosomal pH 5.4 and 6.4, but no activity at physiological pH 7.4, indicating that the micelles safely encapsulated peptide in a pH-dependent manner (**Figure 6.3F**). Furthermore, the HC_{50} of micelles was ~5-fold lower than free peptide at pH 5.4, and ~1.5-fold lower at pH 6.4 (**Table 6.3**), demonstrating the increased potency of conjugates at lower peptide concentrations. Micelles without peptide (CP) had no hemolytic activity (**Figure S6.2C**). Finally, the ability of peptide and micelles to disrupt endosomes was evaluated in a Gal8-GFP-RAW264.7 reporter cell line (**Figure 6.3G**). Gal8-GFP is constitutively expressed throughout the cell, but upon endosomal disruption, redistributes and binds to the inner face of the endosome. Thus, events of endosomal disruption are expressed a GFP^+ punctae. Here, only micelles were capable of disrupting endosomes and inducing GFP^+ punctae. Overall, both peptide and micelles were quite lytic, but micelles protected RBCs from hemolysis at physiological pH and only micelles were capable of disrupting endosomes.

6.3.4 Tumor reduction with CP-Candidalysin micelles

Based on observed cytotoxicity and reports of Candidalysin as a driver of immune inflammation and cell recruitment, we next investigated the application of Candidalysin for tumor reduction. Mice were inoculated with CT26 cells (1M) and injected every 4^{th} day with (*i*) PBS, (*ii*) Candidalysin 5 mg/kg, or (*iii*) CP-Candidalysin 5 mg peptide/kg for a total of 3 injections (**Figure 6.5A-B**). We observed no tumor reduction compared to PBS with either free peptide or CP-Candidalysin. Therefore, we decided to remove potential delivery limitations by direct intratumoral injection. We injected peptide and micelles intratumorally at 8 mg peptide/kg every 4^{th} day, for a total of 3 injections (**Figure 6.5C**). A higher dose was used for IT injections because dose was not limited by systemic toxicity. Direct injection of peptide or micelles did not result in tumor reduction either, suggesting that delivery barriers are not responsible for lack of observed efficacy. Overall, neither free peptide nor CP-Candidalysin reduced tumor growth, regardless of injection route.

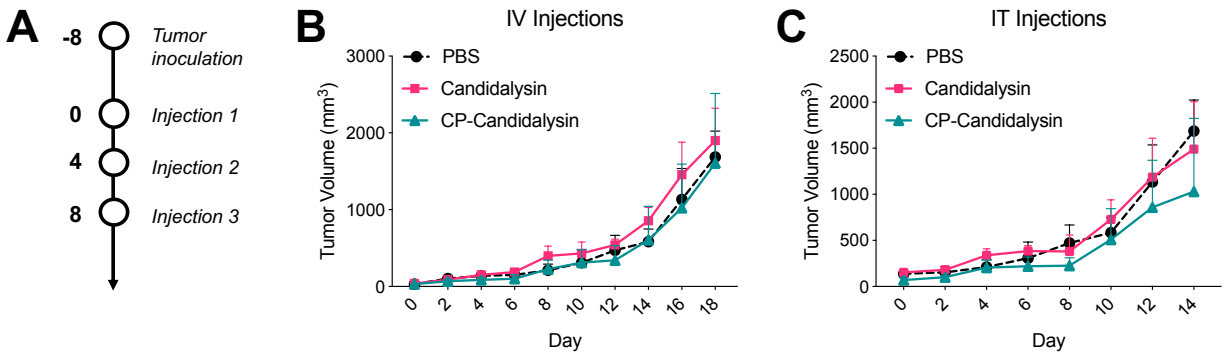

***Figure 6.5**: In vivo activity of Candidalysin. A) Mice were inoculated with CT26 flank tumors (1M cells) and injected every 4th day for a total of 3 injections. B-C) Mice were treated with (i) PBS, (ii) Candidalysin, or (iii) CP-Candidalysin, injected either IV (B) or intratumorally (C) at 5 or 8 mg peptide/kg, respectively.*

6.4 Discussion

In this work, we evaluated VIPER-mediated delivery of fungal peptide Candidalysin as a potential anti-cancer treatment. We have previously reported the use of VIPER to deliver D-melittin for cancer treatment, and thus sought to investigate if VIPER could facilitate delivery of other immunogenic peptides. We formulated self-assembling polymer-Candidalysin conjugates as polymeric micelles, using Candidalysin as both an endosomal escape and inflammatory agent. Candidalysin micelles exert broad anti-tumor activity against various murine and human cells, and exhibit increased efficacy against cells that have developed resistant to traditional chemotherapies. The IC_{50} of CP-Candidalysin micelles in doxorubicin-resistant (DOX-R) cells was 12-fold lower than in wild type (WT) cells. Additionally, polymer conjugation enhanced potency of the peptide, as demonstrated by an 16-fold lower IC_{50} of micelles compared to free peptide in MDA-MB-435 DOX-R cells. This result is interesting, as most polymer-drug conjugates are less potent than free peptide *in vitro* because of delayed release kinetics. Yet, despite this encouraging anti-tumor activity *in vitro*, neither free peptide nor Candidalysin micelles reduced tumor growth *in vivo*, even when directly injected into tumors. We initially investigated efficacy after IV injection; observing no difference compared to PBS treatment, we investigated if lack of efficacy was attributed to poor tumor delivery and injected peptide and micelles intratumorally at a higher peptide concentration. Even with direct peptide delivery to tumors, we did not observe significant differences compared to PBS treated group. Of note, we did not quantify serum IL-1β levels, so we have not confirmed

the induction of inflammation *in vivo*. However, based on *in vitro* characterization and prior reports, Candidalysin likely induces cell lysis and inflammation *in vivo*.[7]

This lack of efficacy suggests that inflammation alone is insufficient to trigger a potent anti-tumor response. In the canonical pathway, inflammasome activation if the basis for caspase-1-dependent pyroptosis.[4] Pattern recognition receptors activate NLRP3, an inflammasome complex, which interacts with downstream proteins to initiate pyroptosis and provoke maturation of inflammatory cytokines such as IL-1β. While the non-canonical pathway initially activates other caspases, NLRP3/caspase-1 activation is still a key feature. And while *C. albicans* induces pyroptotic cell death, the peptide derivative does not. [8] Candidalysin-induced macrophage lysis is independent of pyroptosis and inflammasome activation, and has not been connected with other regulated cell death pathways such as apoptosis or necroptosis. It is implied that the main cause of cell damage stems from direct interaction of Candidalysin with host cell membranes, as Candidalysin induces cell death in cells lacking key components of the NLRP3 inflammasome. While Candidalysin can activate the NLRP3 inflammasome and is cytolytic, these two observations occur independently, and Candidalysin induced cell death is pyroptosis-independent. Despite this distinction, the peptide still activates danger signaling in epithelial cells and can drive immune cell recruitment, activation, and proliferation.[9] However, the inability of Candidalysin to induce pyroptosis could be a key factor in its lack of efficacy *in vivo*.

Furthermore, since the peptide's main cytotoxic effects stem from its membranolytic interactions, polymer encapsulation may have further dampened its inflammatory effects. Although this variance was not observed *in vivo*, as intratumoral injection of free peptide did not have an effect in reducing tumor volume, we did observe reduction in markers of immunogenic cell death (ICD) with micelles *in vitro*. During ICD, cells release danger associated molecular patterns which can elicit an immune response.[19] The three main hallmarks of ICD are surface expression of calreticulin (CRT) and extracellular release of ATP and HMGB1. Calreticulin expression serves as an "eat me" signal to antigen presenting cells, while ATP and HMGB1 serve as a "find me" signal and can trigger cell maturation and stimulate pro-inflammatory cytokine production. When we treated tumor cells with Candidalysin or CP-Candidalysin, we observed a marked reduction of CRT expression between free peptide and micellar formulations (**Figure S6.3A**). Additionally,

there was little difference in ATP concentrations between formulations (**Figure S6.3B**). These findings support the conclusion that Candidalysin does not induce ICD and that the micellar formulations are less immunogenic due to reduced membrane interactions.

The role of inflammation in tumor progression could also explain the lack of observed anti-tumor efficacy. We demonstrated that Candidalysin is capable of inducing IL-1β mediated inflammation *in vitro* and hypothesized that its activity would translate *in vivo* and activate bystander cells. However, this inflammation may have driven cancer progression instead of halting it. In some cases, the increased release of tumor neo-antigens and inflammatory cytokines can result in immunosuppression and/or creation of a tumor microenvironment (TME) unfavorable for immune cell signaling.[20,21] Although antitumor efficacy with immunogenic therapies has previously been demonstrated in the CT26 tumor model, Candidalysin could activate inflammatory pathways not activated by other therapeutics.[22] Additionally, signaling triggered by inflammatory cytokines can actually increase tumor cell proliferation rates, particularly under suboptimal *in vivo* conditions such as hypoxia or lack of nutrients.[23,24] Pathogenic infections have also been linked to cancer induction and progression, as the pathogens can induce environments of chronic inflammation and produce carcinogenic metabolites.[25] *C. albicans* and Candidalysin have been implicated in oncogenic disease for their ability to activate epithelial MAPK and ERK signaling pathways, associated with growth, proliferation, and angiogenesis, and to enhance production of carcinogenic molecules such as nitrosamines and acetaldehyde.[26] However, clinical evidence linking *C. albicans* with cancer is limited and the association remains ambiguous.

Based on these results, we will not pursue additional efforts into characterizing the anti-tumor efficacy of Candidalysin. Overall, we report here the development of Candidalysin micelles, emphasizing the versatility of the VIPER platform for intracellular peptide delivery. Prior work from our group demonstrates the adaptability of VIPER with various other lytic peptides, and this work adds to the arsenal of peptides that VIPER can deliver.[17]

6.5 Experimental Procedures

Peptide synthesis. Candidalysin (SIIGIIMGILGNIPQVIQIIMSIVKAFKGNKRKKKKKKC) was synthesized using a solid phase peptide synthesizer (Liberty Blue CEM) on a rink amide resin.

Peptides were cleaved from the resin in a trifluoroacetic acid (TFA) cocktail with 5% dimethoxybenzene 2.5% triisopropylsilane and 2.5% ethanedithiol; water was included at 2.5% for peptides containing arginine. Peptides were precipitated in cold diethyl ether, and crude peptides were purified by reverse-phase high performance liquid chromatography (HPLC). Peptide molecular weight was confirmed using Matrix-Assisted Laser Desorption/Ionization-Time of Flight Mass spectrometry (MALDI-TOF) in a CHCA:DHB 2:1 matrix.

Polymer synthesis and micelle formation. Block copolymer p(PEG_{113})-*b*-p($DIPAMA_{40}$-*co*-$PDSEMA_2$) was prepared with RAFT polymerization. In brief, PEG macro CTA (1000 mg, 0.182 mmol), DIPAMA (1850 mg, 7.58 mmol), PDSEMA (190 mg, 0.89 mmol) and azobisisobutyronitrile (AIBN) (3 mg, 0.018 mmol) were dissolved in 15 ml dimethylacetamide (DMAc), purged in argon, and immersed in an oil bath at 70°C.[13] After 24h, the polymerization was quenched with liquid nitrogen and the polymer was purified by dialysis against methanol for 2 days (yield: 80%). Synthesized peptides were conjugated to the PDSEMA monomer via disulfide exchange reaction in a mixture of methanol and water (5:1) at a polymer:peptide feeding ratio of 5:1. After 8h, the polymer-peptide conjugates were purified by dialysis against DI water for 2 days. To prepare the micelles, the polymers or polymer-peptide conjugates were first dissolved in acidic phosphate buffer (pH 4.0), and the pH was adjusted to pH 7-8. Micelles were sterile filtered using a 0.22 μm pore filter.

Polymer characterization. Polymer was characterized by ^{1}H NMR on a Bruker AV 300 in deuterated chloroform ($CDCl_3$). Peptide conjugation with PDSEMA was monitored by UV at 353 nm for the release of 2-thiopyridine. Micelle size was assessed by dynamic light scattering (DLS) at 0.5 mg/ml in PBS 7.4.

Cell culture. RAW 264.7, CT26, 4T1, A459, HEPG2, and NIH 3T3 cells were obtained from ATCC and cultured in RPMI supplemented with 10% FBS and 1% Pen-Strep. Murine bone marrow derived macrophages (BMDMs) were isolated from the femurs of 6-8 week old Balb/c mice. Bone marrow was cultured in RPMI supplemented with 20% DHS, 1% Pen-Strep, and 25 ng/ml of murine M-CSF. On day 4, media was supplemented with an additional 25 ng/ml of murine M-CSF. On day 7, media was replaced and cells were polarized to an M0-like (25 ng/ml M-CSF),

M1-like (50 ng/ml IFN-γ + 10 ng/ml LPS), or M2-like (20 ng/ml IL-4) phenotype. For viability assays, cells were plated in a 96 well plate (15k/well) overnight. Cells were incubated with peptide or micelles for 24 and 48 hours and viability was assessed using MTS/PMS (Promega) and absorbance was detected on a spectrometer.

The Gal8-RAW 264.7 cell line was generated through similar means as described.[27] Briefly, RAW cells were co-transfected with plasmids containing a transposable Gal8-GFP construct and PiggyBac transposon (gift of Prof. Jordan Green) using Lipofectamine 2000 (3:1 molar ratio transposon:transposase plasmid). Cells were sorted for the top 5% brightest GFP^+ singlet cell events using a FACS Aria sorter (BD), expanded, and sorted three more times to yield a population of Gal8-GFP^{high} cells.

Hemolysis and IL-1β assays. Hemolysis assays were conducted as described.[28] Human blood was obtained in accordance with guidelines established by the University of Washington Institutional Review Board. Briefly, human blood was washed in 150 mM NaCl and washed 2X. Blood was transferred to PBS pH 7.4 and washed, and resuspended in PBS at each pH to be tested (pH 5.4, 6.4, 7.4). Blood was diluted 1:50 and 190 μl of diluted blood was plated in a V-bottom 96 well plate. Samples were incubated with peptide in appropriate pH at 37°C for 1h and centrifuged. Supernatant was transferred to a clear, flat bottom 96-well plate and absorbance (541 nm) was detected on a plate reader. Triton X-100 1% (w/v) was used as a positive control, and PBS at appropriate pH was used as a negative control. IL-1β was detected using the Mouse IL-1β ELISA MAX kit (BioLegend) per manufacturer instructions.

Cell permeability. Cell permeability was determined by flow cytometry. RAW 264.7 macrophages were lifted, stained with Zombie Violet (BioLegend), and incubated with peptide for 10 or 30 minutes at 4°C. Cells were washed, stained with propidium iodide (PI), and fluorescence was evaluated on a flow cytometer (Attune NxT, Invitrogen).

Animal studies. All animal studies were approved by the Institutional Animal Care and Use Committee at the University of Washington and were conducted in accordance use and regulations. Female Balb/c mice (6-8 weeks) were ordered from Charles River Laboratories. For both 4T1 and

CT26 tumor models, cells (1M) were injected subcutaneously in the right inguinal flank of 6-8 week old female balb/c mice (Charles River Laboratories) and tumors were measured by calipers. When tumors reached ~100 mm^3, mice were injected IV (tail vein) with 200 µl of treatment or intratumorally (IT) with 20-50 µl at the stated dose every 4^{th} day. Mice were humanely euthanized when euthanasia criteria were met (e.g., hunched, squinting, low to no activity, poor grooming).

Imaging. N01 coverslips were coated with bovine collagen I (Thermo) (45 µg/mL) for 1h at room temperature. Gal8-RAW 264.7 cells were plated (300-400k) onto coverslips overnight, and were incubated with peptide or micelles for 16-18h in complete media. Cells were fixed in 4% PFA and stained with DAPI (1:1000). Slides were imaged on a confocal microscope with a 63X oil immersion objective (Leica SP8X).

Statistical analysis. Flow data was analyzed using FlowJo. Statistical analysis was calculated using a two-way ANOVA in Graphpad Prism 8.0.

6.6 Acknowledgements

This work was supported by NIH (1R01CA177272). We thank Nathanial Peters and W. M. Keck Microscopy Center (S10 OD016240) for confocal microscopy support. We thank Kim Woodrow for use of her plate reader and Jordan Green (Johns Hopkins University) for kindly providing the Gal8-GFP and PiggyBac transposon plasmids.

6.7 Competing interests

S.H.P. has submitted a patent with the U.S. Patent and Trademark Office (WO2018027164A1) related to VIPER.

6.8 Supplemental Information

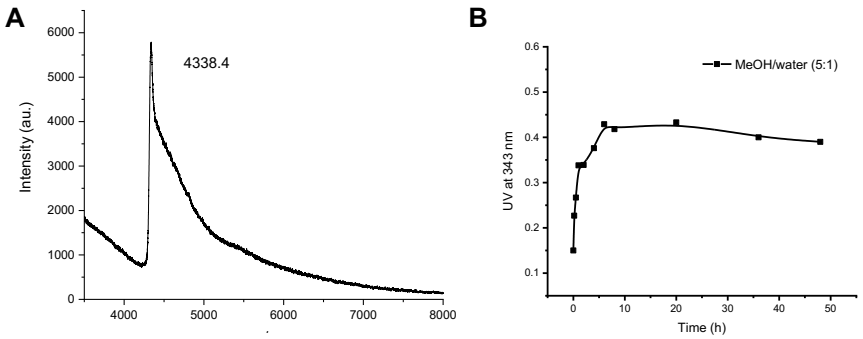

Figure S6.1: Peptide synthesis and conjugation to polymer. A) MALDI-TOF confirming synthesis of Candidalysin peptide. B) Peptide was conjugated to polymer and kinetics were monitored via UV-vis.

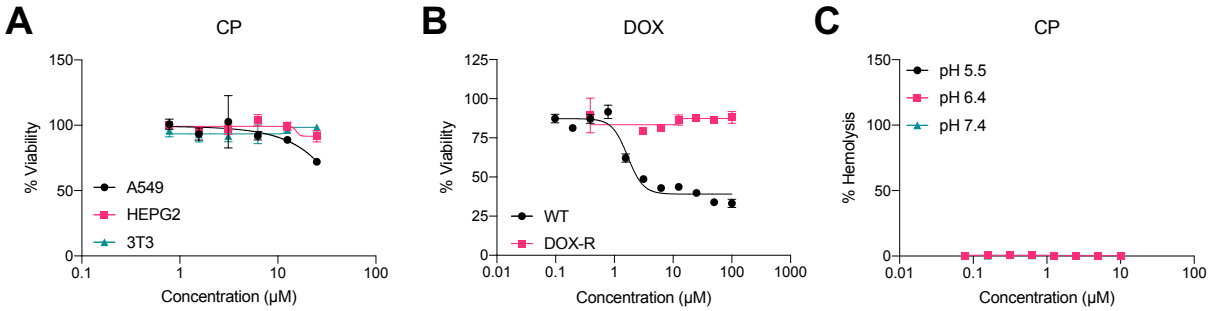

Figure S6.2: Activity of CP and confirmation of doxorubicin resistance. A) Toxicity of CP against A549, HEPG2, and 3T3 cells. B) Confirmation of doxorubicin resistance in MDA-MB-435 cells. C) Hemolytic activity of CP at pH 5.4, 6.4, and 7.4.

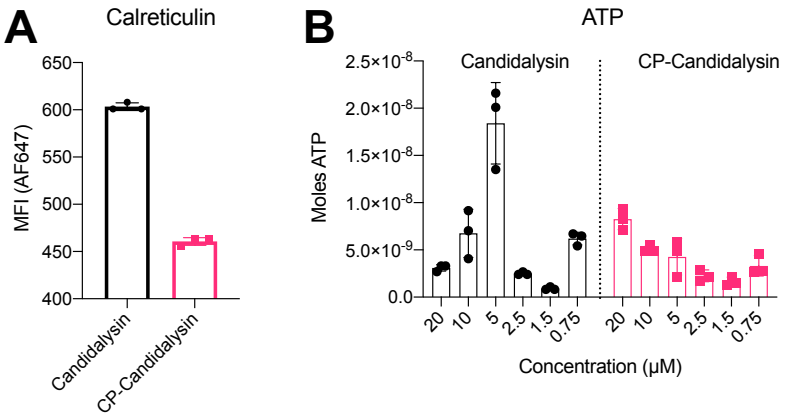

Figure S6.3: Immunogenic cell death of Candidalysin peptide and micelles. A) Calreticulin expression after incubating CT26 cells with Candidalysin and CP-Candidalysin micelles. Surface expression was evaluated with an anti-Candidalysin antibody and quantified by flow cytometry. B) ATP release after incubating CT26 cells with peptide or micelles. Extracellular ATP was quantified by luminescence.

References

1 Hiam-Galvez, K. J., Allen, B. M. & Spitzer, M. H. Systemic immunity in cancer. *Nat Rev Cancer* **21**, 345-359, doi:10.1038/s41568-021-00347-z (2021).

2 Xia, X. *et al.* The role of pyroptosis in cancer: pro-cancer or pro-"host"? *Cell Death Dis* **10**, 650, doi:10.1038/s41419-019-1883-8 (2019).

3 Wang, Y. Y., Liu, X. L. & Zhao, R. Induction of Pyroptosis and Its Implications in Cancer Management. *Front Oncol* **9**, 971, doi:10.3389/fonc.2019.00971 (2019).

4 Wang, L., Qin, X., Liang, J. & Ge, P. Induction of Pyroptosis: A Promising Strategy for Cancer Treatment. *Front Oncol* **11**, 635774, doi:10.3389/fonc.2021.635774 (2021).

5 Hage, C. *et al.* Sorafenib Induces Pyroptosis in Macrophages and Triggers Natural Killer Cell-Mediated Cytotoxicity Against Hepatocellular Carcinoma. *Hepatology* **70**, 1280-1297, doi:10.1002/hep.30666 (2019).

6 Wang, F. *et al.* Simvastatin Suppresses Proliferation and Migration in Non-small Cell Lung Cancer via Pyroptosis. *Int J Biol Sci* **14**, 406-417, doi:10.7150/ijbs.23542 (2018).

7 Naglik, J. R., Gaffen, S. L. & Hube, B. Candidalysin: discovery and function in Candida albicans infections. *Curr Opin Microbiol* **52**, 100-109, doi:10.1016/j.mib.2019.06.002 (2019).

8 Kasper, L. *et al.* The fungal peptide toxin Candidalysin activates the NLRP3 inflammasome and causes cytolysis in mononuclear phagocytes. *Nat Commun* **9**, 4260, doi:10.1038/s41467-018-06607-1 (2018).

9 Swidergall, M. *et al.* Candidalysin Is Required for Neutrophil Recruitment and Virulence During Systemic Candida albicans Infection. *J Infect Dis* **220**, 1477-1488, doi:10.1093/infdis/jiz322 (2019).

10 Vinogradov, S., Warren, G. & Wei, X. Macrophages associated with tumors as potential targets and therapeutic intermediates. *Nanomedicine (Lond)* **9**, 695-707, doi:10.2217/nnm.14.13 (2014).

11 Sylvestre, M., Crane, C. A. & Pun, S. H. Progress on Modulating Tumor-Associated Macrophages with Biomaterials. *Adv Mater*, e1902007, doi:10.1002/adma.201902007 (2019).

12 Cieslewicz, M. *et al.* Targeted delivery of proapoptotic peptides to tumor-associated macrophages improves survival. *Proc Natl Acad Sci U S A* **110**, 15919-15924, doi:10.1073/pnas.1312197110 (2013).

13 Cheng, Y., Yumul, R. C. & Pun, S. H. Virus-Inspired Polymer for Efficient In Vitro and In Vivo Gene Delivery. *Angew Chem Int Ed Engl* **55**, 12013-12017, doi:10.1002/anie.201605958 (2016).

14 Liu, X., Wu, F., Ji, Y. & Yin, L. Recent Advances in Anti-cancer Protein/Peptide Delivery. *Bioconjug Chem* **30**, 305-324, doi:10.1021/acs.bioconjchem.8b00750 (2019).

15 Torchilin, V. P. & Lukyanov, A. N. Peptide and protein drug delivery to and into tumors: challenges and solutions. *Drug Discovery Today* **8**, 259-266, doi:10.1016/s1359-6446(03)02623-0 (2003).

16 Lv, S., Sylvestre, M., Prossnitz, A. N., Yang, L. F. & Pun, S. H. Design of Polymeric Carriers for Intracellular Peptide Delivery in Oncology Applications. *Chem Rev*, doi:10.1021/acs.chemrev.0c00963 (2021).

17 Peeler, D. J. *et al.* pH-sensitive polymer micelles provide selective and potentiated lytic capacity to venom peptides for effective intracellular delivery. *Biomaterials* **192**, 235-244, doi:10.1016/j.biomaterials.2018.11.004 (2019).

18 Sylvestre, M. *et al.* Replacement of L-amino acid peptides with D-amino acid peptides mitigates anti-PEG antibody generation against polymer-peptide conjugates in mice. *J Control Release* **331**, 142-153, doi:10.1016/j.jconrel.2021.01.015 (2021).

19 Fucikova, J. *et al.* Detection of immunogenic cell death and its relevance for cancer therapy. *Cell Death Dis* **11**, 1013, doi:10.1038/s41419-020-03221-2 (2020).

20 Hou, J., Greten, T. F. & Xia, Q. Immunosuppressive cell death in cancer. *Nat Rev Immunol* **17**, 401, doi:10.1038/nri.2017.46 (2017).

21 Galluzzi, L., Buque, A., Kepp, O., Zitvogel, L. & Kroemer, G. Immunogenic cell death in cancer and infectious disease. *Nat Rev Immunol* **17**, 97-111, doi:10.1038/nri.2016.107 (2017).

22 Lin, A. G. *et al.* Non-thermal plasma induces immunogenic cell death in vivo in murine CT26 colorectal tumors. *Oncoimmunology* **7**, e1484978, doi:10.1080/2162402X.2018.1484978 (2018).
23 Grivennikov, S. *et al.* IL-6 and Stat3 are required for survival of intestinal epithelial cells and development of colitis-associated cancer. *Cancer Cell* **15**, 103-113, doi:10.1016/j.ccr.2009.01.001 (2009).
24 Greten, F. R. & Grivennikov, S. I. Inflammation and Cancer: Triggers, Mechanisms, and Consequences. *Immunity* **51**, 27-41, doi:10.1016/j.immuni.2019.06.025 (2019).
25 Parsonnet, J. Bacterial infection as a cause of cancer. *Environ Health Perspect* **103 Suppl 8**, 263-268, doi:10.1289/ehp.95103s8263 (1995).
26 Ho, J. *et al.* Candida albicans and candidalysin in inflammatory disorders and cancer. *Immunology* **162**, 11-16, doi:10.1111/imm.13255 (2021).
27 Kilchrist, K. V. *et al.* Gal8 Visualization of Endosome Disruption Predicts Carrier-Mediated Biologic Drug Intracellular Bioavailability. *ACS Nano* **13**, 1136-1152, doi:10.1021/acsnano.8b05482 (2019).
28 Evans, B. C. *et al.* Ex vivo red blood cell hemolysis assay for the evaluation of pH-responsive endosomolytic agents for cytosolic delivery of biomacromolecular drugs. *J Vis Exp*, e50166, doi:10.3791/50166 (2013).

Chapter 7

Polymer-mediated delivery of peptide R3 for cancer immunotherapy

*Shixian Lv, *Meilyn Sylvestre, James Vince, Seth Masters, and Suzie H. Pun
*equally contributing authors

7.1 Abstract

Triggering immunogenic cell death (ICD) in tumors is an emerging strategy in cancer immunotherapy. Cells undergoing ICD can alter their microenvironment, stimulating an inflammatory immune response that can control tumor growth and induce immune memory. Here, we sought to trigger necroptosis, a form of ICD, by delivering peptide R3 to the cytosol of tumor cells. Because R3 requires cytoplasmic delivery for activity, we utilized a pH-sensitie polymer, VIPER, that facilitates cell entry and endosomal escape. R3 is derived from protein RIPK3, a component of the necrosome that potentiates necroptosis and cell death. We employed the platform virus inspired polymer for endosomal release (VIPER) to facilitate intracellular peptide delivery of R3 to the cell cytosol. VIPER incorporates D-melittin, the enantiomer of L-melittin, which enables selective disruption of endosomal membranes and also permits safe, systemic delivery of the VIPER platform by attenuating the generation of anti-VIPER antibodies. While D-melittin micelles demonstrate anti-tumor activity by themselves, co-delivery of R3 enhances cytotoxicity, hemolytic activity, and endosomal escape. Furthermore, we demonstrate some anti-tumor activity *in vivo*, but this activity was inconsistent between studies. We discuss potential reasons for these differing results and suggest future directions for this project.

7.2 Introduction

Inducing immunogenic cell death (ICD) in the tumor microenvironment (TME) is an emerging strategy to stimulate the dysfunctional immune system.[1] As opposed to apoptosis, an immunologically silent form of programmed cell death, ICD leads to the prolonged exposure of danger associated molecular patterns (DAMPs) to the immune system, which can drive antigen specific immune responses.[2,3] Cells undergoing ICD are altered themselves (surface exposure of

calreticulin (CRT) to encourage phagocytosis) and also alter their microenvironment (secretion of ATP and cell death-associated release of HMGB1 to recruit immune cells).[2] In cancer, this translates to tumor-specific immune responses that can control tumor growth and protect against subsequent tumor challenges of the same type.[4] The most effective ICD inducers operate as vaccines, training the immune system in an antigen-dependent manner and inducing immune memory. Strategies that maximize the immunogenicity of dying tumors cells could synergize with other immunotherapies (e.g. immune checkpoint blockade) to support immune activation and tumor clearance.

Necroptosis, another form of programmed cell death, is caspase-independent and leads to cell swelling, membrane rupture, and release of cellular contents.[5,6] Necroptosis can be triggered by members of the tumor necrosis factor (TNF) family, toll-like receptors (TLRs), or oligonucleotide sensors. Receptor-interacting protein kinases (RIPK) 1 and 3 form the necrosome, which recruits and phosphorylates mixed lineage kinase like protein (MLKL). MLKL permeabilizes the cell membrane, leading to the release of intracellular contents. CRT exposure coupled with DAMP release recruits and activates innate immune pattern recognition receptors. Thus, necroptosis functions as a form of cell death that results in both the clearance of compromised cells while simultaneously releasing inflammatory payloads to recruit and activate immune cells.[7] Furthermore, RIPK3 has also been associated with death-independent activities, such as production of inflammatory cytokines that cross-prime T cells for vaccination responses. In cancer applications, Snyder et. al. demonstrated that ectopic introduction of necroptotic cells into the TME potentiated systemic tumor control.[8] These effects were potentiated by signaling activities downstream of RIPK1/RIPK3 necrosome formation, specifically via the RIPK3–NF-κB axis.

To trigger necroptosis in tumors, we incorporated R3 into our intracellular delivery platform VIPER ("virus inspired polymer for endosomal release"), which facilitates pH-responsive intracellular peptide delivery by employing a lytic peptide, melittin, to lyse endosomes. At physiological pH 7.4, polymers self-assemble into micelles; at endosomal pH 6.4, micelles disassemble into polymer chains. Mixed VIPER micelles incorporate polymer-peptide chains carrying melittin and R3 (**Figure 7.1A**). Melittin enables endosomal release of R3 into the cell cytosol, which initiates necroptosis that triggers immune activation (**Figure 7.1B**). In this work,

all instances of melittin refer to D-melittin, as we recently reported that incorporation of D-melittin, rather than L-melittin, is critical for safe, repeat systemic injection of VIPER.[9] D-melittin attenuates the generation of anti-carrier antibodies, enhancing the therapeutic index of our delivery platform without compromising peptide activity.

Here, we developed polymer-peptide micelles, VIPER-D-R3, that deliver R3 to tumor cells, with the goal of inducing necroptosis to trigger immune activation in cancer. After characterizing the polymer-peptide conjugate, we examined its activity *in vitro* and *in vivo*. We characterized micelle cytotoxicity, hemolytic activity, and ability to facilitate endosomal disruption. We next evaluated the extent of ICD by characterizing CRT translocation to the surface and ATP and HMGB1 release. Finally, we investigated anti-tumor efficacy of our platform in tumor-bearing mice. Ultimately, VIPER-D-R3 had variable efficacy *in vivo*, and we discuss some potential causes for this as well as alternative strategies moving forward.

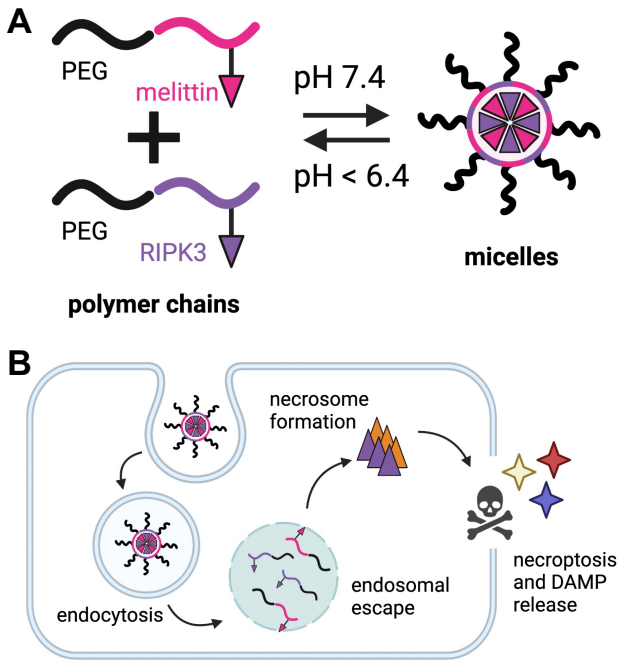

Figure 7.1: *Design of polymer-peptide conjugates bearing melittin and R3. A) Polymers self-assemble into micelles at pH 7.4, and disassemble into polymer chains at acidic pH. B) Following cellular internalization and endosomal acidification, melittin is exposed and mediates endosomal*

escape of R3. R3 then initiates formation of the necrosome and downstream signaling that potentiates necroptosis and ICD.

7.3 Results

7.3.1 Polymer synthesis and characterization

We employed our polymer platform VIPER for intracellular delivery of peptide R3, derived from protein RIPK3, to the cell cytosol. VIPER comprises two blocks: a PEG-based hydrophilic block for solubility, and a pH-sensitive block for triggered display of conjugated peptides. The pH-sensitive block, comprised of the tertiary amine-based monomer DIPAMA, undergoes a sharp phase transition from hydrophobic to hydrophilic at pH 6, and is co-polymerized with PDSEMA, which enables conjugation of thiolated peptides (**Figure 7.2A**). For R3 delivery, we synthesized VIPER conjugated to D-melittin, a membrane-lytic peptide that facilitates endosomal release, and VIPER conjugated to R3. Polymers were synthesized by reversible addition-fragmentation chain-transfer (RAFT) polymerization of 2-diisopropylaminoethyl methacrylate (DIPAMA) and pyridyl disulfide ethyl methacrylate (PSDSEMA) using PEGylated macro chain transfer agents (CTAs), as previously described.[9,10] Polymer chains self-assemble into micelles at physiological pH 7.4, protecting their peptide cargo, but expose peptide at acidic endosomal pH 6.4, facilitating endosomal release and intracellular peptide delivery. Mixed micelles were formed by combining polymer chains with D-melittin (CP-melittin) and R3 (CP-R3) at defined ratios, yielding VIPER-D-R3. Polymers without peptide are referred to as control polymer (CP). CP-melittin and CP-R3 micelles had diameters of 33.4 and 31.6 nm, respectively (**Figure 7.2B-C**); mixed VIPER-D-R3 micelles had a diameter of ~31.1 nm, regardless of the ratio of CP-R3:CP-melittin (**Figure 7.2D**). The pH transition point of all micelles was determined to be pH 6.3; at this pH, micelles disassemble into polymer chains (**Figure 7.2E-G**).

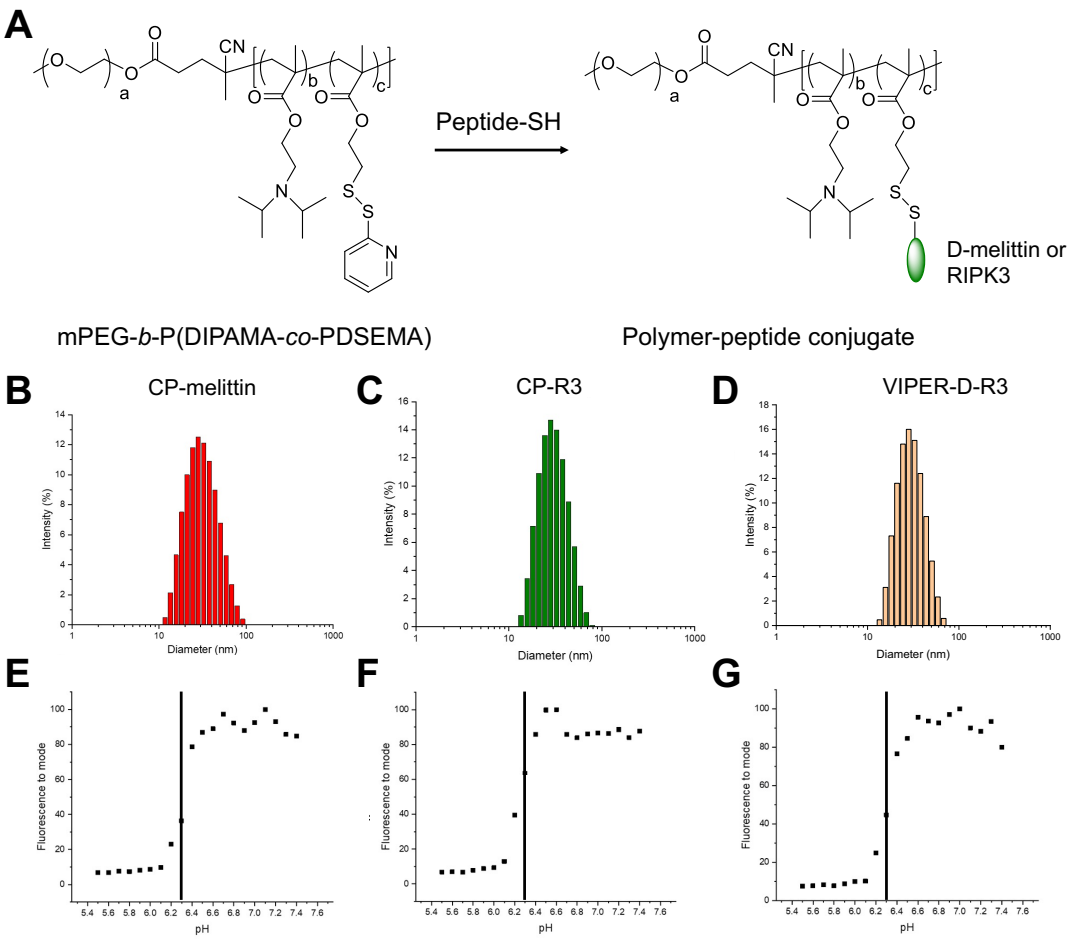

***Figure 7.2**: Characterization of micelles. A) Synthesis route for VIPER-D-R3. The PDSEMA enables conjugate with thiolated peptides. B-D) Size distribution of CP-melittin (B), CP-R3 (C), and VIPER-D-R3 (D) micelles in PBS. E-G) The pH transition point of CP-melittin (E), CP-R3 (F), and VIPER-D-R3 (G) was determined to be 6.4.*

7.3.2 Toxicity in vitro

We evaluated toxicity of peptide R3 and a control peptide derivative, cR3. A scrambled sequence retained some activity, likely due to the hydrophobicity of the sequence (data not shown). Therefore, we mutated hydrophobic amino acids within the sequence (namely leucine (L), valine (V), and isoleucine (I)) to serine (S), which is neutral and uncharged (**Figure 7.3A**). While R3 had modest toxicity against 4T1 (breast cancer), CT26 (colon carcinoma) and RAW macrophages, cR3 had minimal cytotoxicity (**Figure 7.3B-C**), as determined by half maximal inhibitory concentration (IC_{50}) (**Figure 7.3D**). However, when R3 was incorporated into mixed micelles with

melittin, the toxicity was amplified above that of CP-R3 alone. To optimize the ratio of CP-R3:CP-melittin in mixed micelles, we assessed toxicity of mixed micelles with differing amounts of each polymer-peptide conjugate (5:1, 2.5:1, and 1:1) against RAW macrophages, and based on the lowest IC_{50}, determined that a ratio of 1:1 CP-R3:CP-melittin maximized toxicity (**Figure 7.3E, G**). This formulation of VIPER-D-R3 at a 1:1 ratio of R3:melittin retained robust activity against tumor cells, evidenced by an IC_{50} of 8.9 μM against CT26 cells (**Figure 7.3F**).

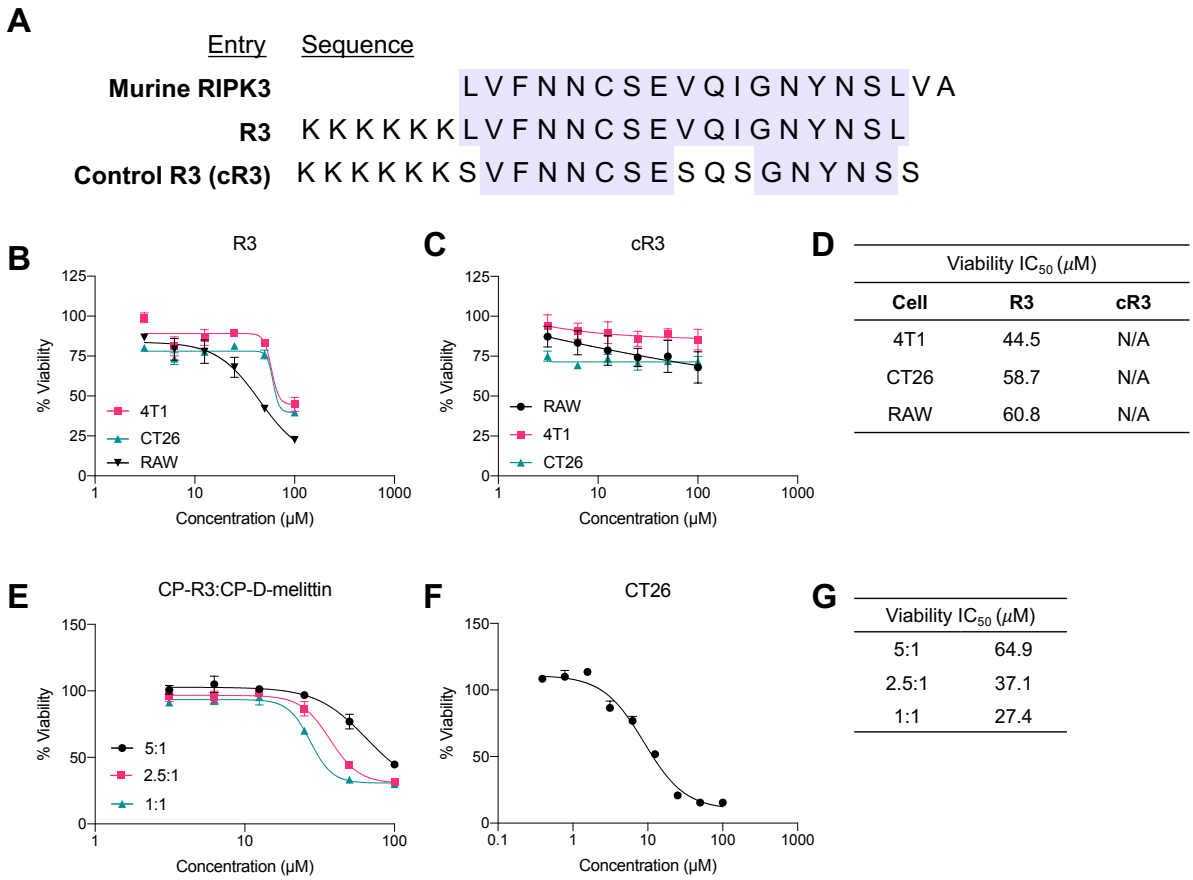

Figure 7.4: *Cytotoxicity of R3 peptide and micelles. A) Sequence alignment of murine RIPK3, R3, and control R3 (cR3). Conserved sequences are highlighted in purple. B-C) Toxicity of R3 (B) and cR3 (C) against 4T1, CT26, and RAW cells. D) IC_{50} concentrations of R3 and cR3. E) Toxicity of mixed micelles with varying ratios of CP-R3 and CP-melittin. F) Toxicity of VIPER-D-R3 micelles (1:1) against CT26 cells. G) IC_{50} concentrations of VIPER-D-R3 with varying ratios of CP-R3 and CP-melittin.*

7.3.3 Lytic activity in vitro

We next confirmed the lytic activity of VIPER-D-R3 based on hemolytic activity against red blood cells (RBCs) and ability to disrupt endosomes. Free peptide had no hemolytic activity (**Figure 7.5A**), while micelles were hemolytic in a pH-dependent manner (**Figure 7.5B**). At pH 7.4, micelles were not hemolytic, demonstrating safe encapsulation of the peptides melittin and R3. Some activity was observed at pH 6.4, but this can be attributed to pH transition point (pH 6.3); at this pH, the polymers transition between micelles and unimers, which are lytic due to the melittin content. At pH 5.4, the micelles are extremely lytic, evidenced by the half maximal hemolysis concentration (HC_{50}) of 0.55 μM. Furthermore, micelles were capable of disrupting endosomes after cellular uptake, as observed in a Gal8-GFP-RAW 264.7 reporter cell line. Cells constitutively express the fusion protein Gal8-GFP throughout the cell, and upon endosomal disruption, the Gal8-GFP binds to the inner face of disrupted endosomes. Thus, events of endosomal rupture are expressed as GFP^+ punctae (green) in the cell (**Figure 7.5D**). We additionally stained cell nuclei (Hoechst, blue) and cell viability (propidium iodide (PI), red) and compared the percent of live cells that expressed punctae (**Figure 7.5C**). While CP, free R3, and CP-R3 induced some endosomal disruption, this occurred in less than 1% of all live cells; as observed from RBC hemolysis, R3 has no lytic activity, so this was expected. In contrast, melittin-containing micelles induced higher rates of endosomal disruption. About 1.48% and 4.25% of cells treated with CP-melittin and VIPER-D-R3, respectively, expressed GFP^+ punctae, which is consistent with expected results based on the lytic behavior of melittin.

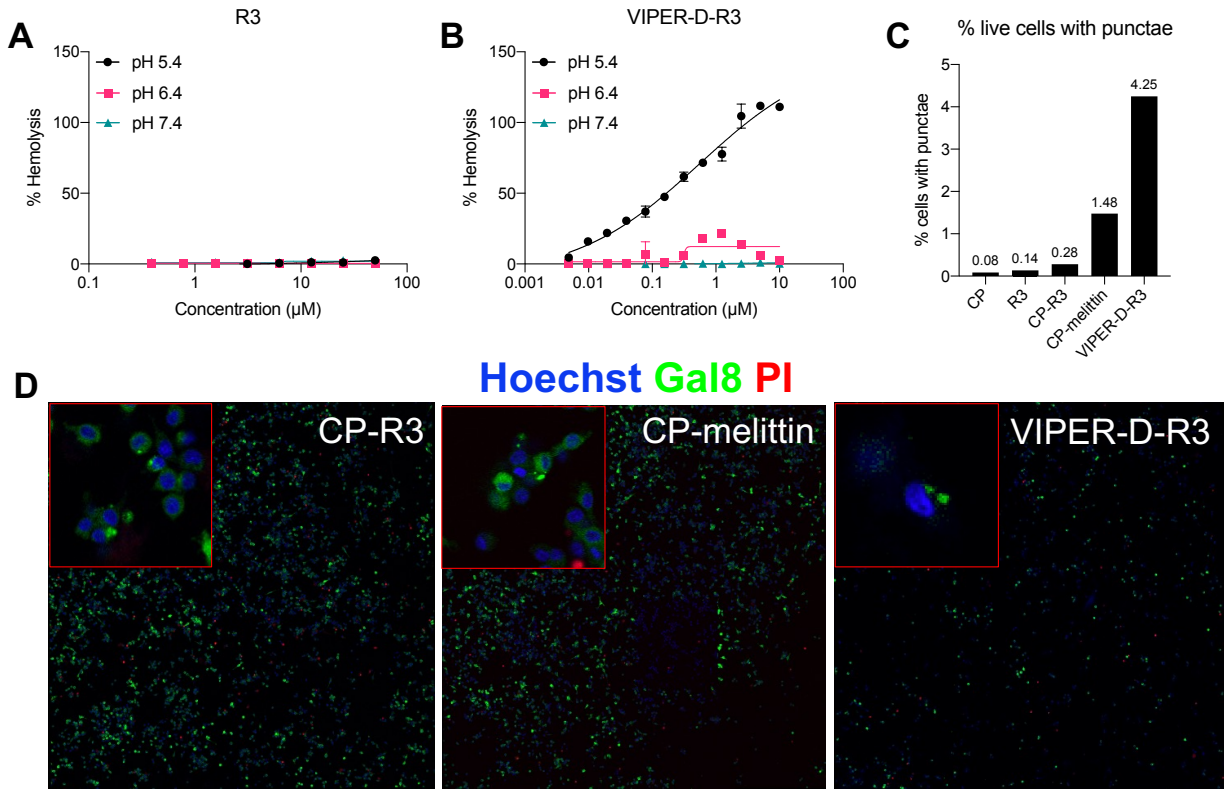

Figure 7.5*: Lytic activity of micelles in vitro. A-B) Peptide R3 (A) and VIPER-D-R3 (B) micelles were incubated with RBCs and the half maximal hemolysis concentration (HC_{50}) was determined. C) Capacity for endosomal disruption was evaluated in a Gal8-GFP-RAW reporter cell line, in which events of endosomal rupture are expressed as GFP^+ punctae. The percent of live cells (determined via PI staining) expressing punctae are reported. D) Visualization of cell staining with Hoechst (blue) and PI (red); Gal8-GFP is constitutively expressed (green). Single cell expression of punctae are outlined in red.*

7.3.4 Immunogenic cell death

Based on the role of RIPK3 in mediating necroptosis, a form of immunogenic cell death (ICD), we evaluated the extent of ICD based on calreticulin (CRT) surface expression and release of ATP and HMGB1.[6,11,12] These events occur during (CRT, ATP release) and after (HMGB1) cellular necroptosis, and thus were evaluated at appropriate time points.[13] To assess CRT translocation to the cell surface, CT26 cells were incubated with micelles for 6, 24, and 48h, and stained with anti-CRT antibody (**Figure 7.6A**). At all time points, micelles induced significantly higher expression (****$p < 0.0001$) compared to untreated cells. However, this trend was not consistent with what

was observed with HMGB1 release; micelles (CP-R3, VIPER-D-R) induced minimal HMGB1 release at concentrations below that of untreated cells (**Figure 7.6B**). cR3 and CP induced the highest amount of HMGB1, slightly above that of untreated cells. ATP release in the supernatant was evaluated after 24 hour incubation with peptide and micelles and was determined to be concentration dependent for R3 and CP-R3 (**Figure 7.6C**). In contrast, all concentrations of VIPER-D-R3 induced robust ATP production, comparable to that of only the highest concentrations of R3 and CP-R3. Despite variable HMGB1 results, VIPER-D-R3 likely induces ICD to some extent, based on CRT expression and ATP release.

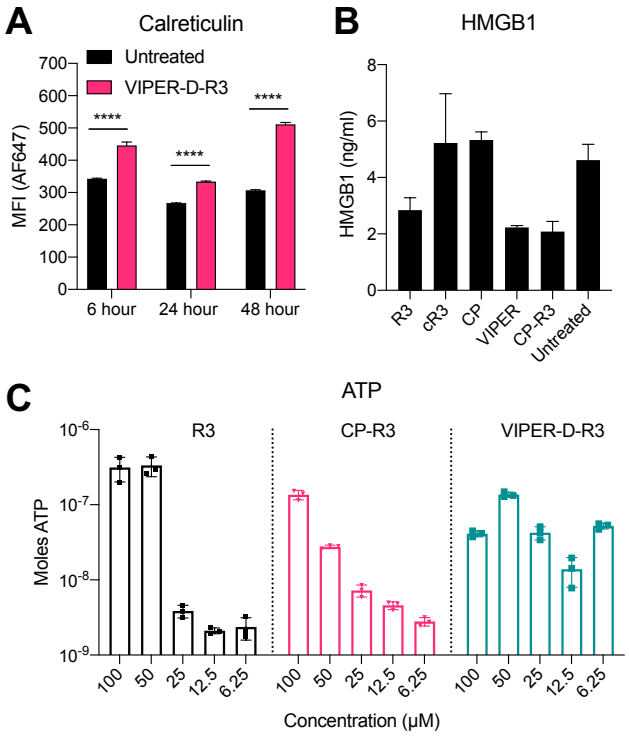

Figure 7.6: *Immunogenic cell death. A) Calreticulin expression on the surface of CT26 cells after 6, 24, and 48 hour treatment with micelles. B) HMGB1 release from CT26 cells after 48 hour incubation with peptide and micelles. C) ATP release from CT26 cells after 24 hour incubation with peptide and micelles.*

7.3.5 Anti-tumor efficacy in vivo

Finally, we evaluated the anti-tumor efficacy of VIPER-D-R3 *in vivo*. Based on prior reports, we employed a 4T1 (triple negative breast cancer) model, as this model is more resistant to immune checkpoint blockade (ICB) therapy and has high immune infiltration.[14,15] We have previously

established that free peptide, polymer with peptide (CP), and micelle formulations with control R3 (VIPER-D-cR3) have no anti-tumor efficacy, so they were not included in these studies (**Figure S7.8**). In a pilot study, we compared efficacy of (*i*) PBS, (*ii*) ICB (anti-PD-1 and anti-CTLA4 antibodies, 100 μg/mouse), (*iii*) CP-melittin 5 mg peptide/kg+ICB, (*iv*) VIPER-D-R3 at 5 mg melittin/kg + 5 mg R3/kg, and (*v*) VIPER-D-R3+ICB (**Figure 7.7A**). Eight days after tumor inoculation, mice were injected IV every 2nd day with micelles, and with ICB every day following treatment, for a total of 3 injections of micelles and 3 injections of ICB. In this initial study, VIPER-D-R3 synergized with ICB to completely inhibit tumor growth. After completion of treatment, tumors on ICB-treated mice started to grow, while VIPER-D-R3+ICB tumors remained < 100 mm^3. VIPER-D-R3 mice had significantly smaller tumors than ICB (***p = 0.0011*) and CP-melittin+ICB (****p = 0.0005*) treated mice. However, when we repeated this study, there was no significant reduction in tumor growth after VIPER-D-R3+ICB treatment, even after a 4th injection of micelles and ICB (**Figure 7.7B**).

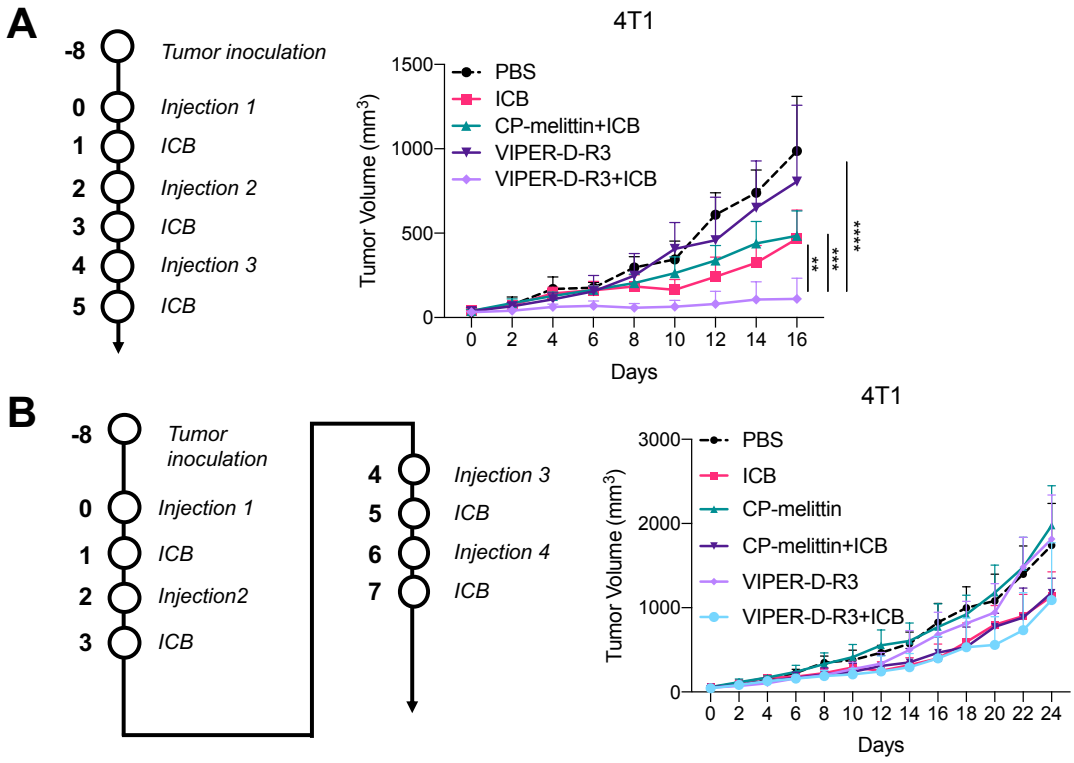

Figure 7.7: *Tumor inhibition in vivo. A) 4T1-tumor bearing mice were treated with (i) PBS, (ii) ICB (100 μg/mouse), (iii) CP-melittin 5 mg peptide/kg+ICB, (iv) VIPER-D-R3 at 5 mg melittin/kg + 5 mg R3/kg, and (v) VIPER-D-R3+ICB. Mice were injected every 2nd day with micelles, and*

with ICB every day following treatment, for a total of 3 injections of each. (n=4 mice/group) B) Treatment groups were the same as above, plus an additional cohort treated with CP-melittin (5 mg peptide/kg). Mice were injected with micelles and ICB as indicated, for a total of 4 injections of each. (n=8 mice/group)

7.4 Discussion

Here, we present the first study delivering peptide R3 to tumors. In prior work, we developed D-melittin micelles for systemic delivery of melittin. While these formulations synergized with immune checkpoint blockade (ICB) therapy, efficacy was modest in 4T1 tumors, which are resistant to ICB therapy (Chapter 5).[15] Furthermore, no differences in tumor infiltrating leukocyte population were detected between treatment groups. Similar to results observed with the CP-Candidalysin platform (Chapter 6), the predominately cytolytic activity of D-melittin was unable to elicit an inflammatory response sufficient for tumor clearance. Thus, we investigated the effect of delivering a more immunogenic peptide R3 with the goal of initiating necroptosis to alter the TME and inhibit solid tumor growth. The R3 sequence comprises residues from the 17 amino acid truncated RHIM motif of murine RIPK3 and RIPK1; this motif emerges when murine RIPK1 and RIPK3 are aligned.[16] Prior work from our group confirmed that peptide R3-KKK-TAT (Trans-Activator of Transcription) was capable of forming amyloid scaffolds that activate NF-kB and engage the NLRP3 inflammasome, triggering cell death and IL-1β and IL-6 secretion *in vitro* (data not shown). Here, we confirmed the cytotoxicity of R3 (no TAT), but observed poor lytic activity, which could prevent sufficient R3 accumulation in cells to initiate ICD. Thus, we incorporated R3 into the VIPER platform, in which D-melittin facilitates endosomal release of R3 into the cytosol, delivering R3 more efficiently to the cell cytosol where it can activate downstream necroptotic machinery.

We demonstrate the enhanced cytotoxicity and hemolytic activity of VIPER-D-R3 constructs compared to free peptide or micelles containing melittin or R3 alone. Mixed micelles exhibited enhanced cytotoxicity that cannot be attributed to melittin alone, implicating R3 in mediating cell death (**Figure S7.5**). Specifically, mixed micelles of CP-R3 and CP-melittin were toxic to RAW cells; but when the CP-R3 was replaced with CP, micelles (comprising CP and CP-melittin) had no toxicity. Thus, R3 plays a role in potentiating cell death. Additionally, mixed micelles were

more lytic than micelles with melittin or R3 alone. This was surprising since R3 has no hemolytic activity on its own, so we expected complexed micelles with melittin and R3 to be as hemolytic as melittin micelles. We also observed some lytic activity by CP-R3 at pH 5.4, although CP and R3 had no lytic activity at any pH (**Figure S7.6**). This could perhaps be explained by the hydrophobicity of the R3 sequence which could contribute to RBC lysis.[17] Together, this implies that polymer conjugation of R3 bolsters its lytic activity at acidic pH 5.4. This trend is consistent with events of endosomal disruption: VIPER-D-R3 micelles induced endosomal disruption in 4.25% of live cells, whereas only 1.48% and 0.28% of cells treated with CP-melittin or CP-R3 micelles, respectively, had identified events. Both formulations of VIPER-D-R3 and CP-melittin had equivalent concentrations of melittin (12.5 μM) or R3 (in VIPER-D-R3 and CP-R3 micelles), so the enhanced endosomal disruption can be attributed to the synergistic activity CP-R3 and melittin. Overall, these results align with prior observations that polymer conjugation enhances peptide activity, demonstrated here and with D-melittin micelles (Chapter 5).

After characterizing behavior *in vitro,* we next evaluated anti-tumor efficacy of constructs in tumor-bearing mice. However, this effect was inconsistent *in vivo*, as demonstrated by the variable efficacy in two separate studies. When investigating the efficacy of CP-melittin *in vivo*, we realized that this formulation, particularly when combined with ICB, was extremely effective against CT26 tumors and that we would only be able to differentiate efficacy between micelles and ICB cohorts in a 4T1 tumors, as 4T1 tumors are largely resistant to ICB therapy. We additionally increased the frequency of the dosing schedule, transitioning to injecting treatments every 2nd day instead of every 4th day. In our initial study, we believed that these changes enabled the robust anti-tumor efficacy observed. Yet when we repeated this treatment regimen in a larger cohort of animals, we realized that this efficacy was not reproducible, as VIPER-D-R3+ICB had the same efficacy as CP-melittin+ICB and ICB alone. In this second study, any anti-tumor efficacy can be attributed to ICB therapy alone, as all cohorts receiving ICB experienced similar trends of tumor growth. Tumor inhibition may have inconsistent due to several factors, including (1) variability of ICB therapy based on external influences; (2) poor immunogenicity from VIPER-D-R3; or (3) poor uptake by cells. Indeed, Jin et. al. recently reported how drinking water pH could attenuate anti-PD-1 efficacy in syngeneic mouse models.[18] When anti-PD-1 treated mice were given acidic drinking water (pH 3), tumors were larger compared to mice given neutral or alkaline water (pH 7 or 8.5). While this

impact was less pronounced in Balb/c mice, other external conditions like this could perhaps influence ICB and its ability to synergize with other treatments. However, this factor is unlikely, as all ICB-treated mice had similar tumor growth patterns, suggesting that ICB therapy had some influence on tumor growth. Instead, it is likely that CP-melittin and VIPER-D-R3 micelles were ineffective.

Thus, another contributing factor to the lack of observed efficacy could be suboptimal immunogenicity of R3. When evaluating ICD *in vitro*, we noted that VIPER-D-R3 induced CRT surface expression and ATP release, but was a poor inducer of HMGB1 release. While this could be the result of an ineffective ELISA kit, it more likely suggests that R3 and polymer derivatives are not inducing ICD. This could be attributed to poor release of R3 from VIPER-D-R3; while we hypothesized that lysosomal thiol reductase should reduce the disulfide bond conjugating R3 to VIPER, this process may be inefficient or incomplete, preventing R3 from diffusing to the cytosol. Or, R3 could be associating with endosomal membranes due to the hydrophobicity of the sequence; in cells incubated with VIPER-D-R3-Cy5, we observed high colocalization of peptide in endosomes, and did not observe high dispersal throughout the cell (data not shown). Other factors could be delivery of an insufficient peptide concentration to cells. We have not determined the maximum tolerated dose (MTD) of micelles, so we could be dosing below the therapeutic index. Furthermore, delivery barriers could be preventing sufficient micelles accumulation in tumors and subsequent inefficient R3 delivery to cells. Indeed, we assessed the serum concentrations of IL-1β, an inflammatory cytokine released after NLRP3 inflammasome activation, and did not detect a significant increase in VIPER-treated mice above PBS-treated mice (**Figure S7.9**). Furthermore, we assessed populations of tumor infiltrating leukocytes (TILs) and did not detect differences between PBS and VIPER-D-R3 treated mice (**Figure S7.9**). Together, these results suggest that VIPER-D-R3 does not induce robust changes in the TME *in vivo*. Alternative delivery methods such as direct intratumoral (IT) injections could help identify if lack of efficacy is caused by poor micelle delivery to tumors. However, this would not overcome the challenge of poor cellular uptake by tumor cells and phagocytes. The micelles may be accumulating in tumors, but may suffer from poor cellular uptake due to the PEG corona, originally intended to enhance circulation and reduce nonspecific uptake. But, this PEG block could actually prevent efficient uptake in tumors. To identify if micelles are being uptaken, we could inject Cy5-labeled micelles (IV or IT)

into tumor-bearing mice, resect and section tumors, and stain for macrophages and tumor cells in order to identify if micelles colocalize with cells.

Conversely, perhaps inducing necroptosis is not an effective anti-cancer strategy. Indeed, some groups have reported a tumor-promoting role of RIPK3 signaling in tumors. Seifert et. al. showed that RIPK1 and RIPK3 were highly upregulated in pancreatic ductal adenocarcinoma samples and that Ripk3 knockout mice were protected from oncogenic progression.[21] Inhibitory macrophages lose their immune-suppressive effects when RIP3 is deleted, and T cells are reprogrammed to mediate tumor clearance. This trend was also reflected in a report by Lin et. al., who noted RIPK3 upregulation in recurrent breast tumor cells, establishing a role of RIPK3 in breast tumor proliferation.[22] Adverse outcomes have also been associated with lytic cell death and release of danger associated molecular patterns (DAMPs). For example, stimulator of interferon (STING)-inducers can interact with immune cells and elicit inflammatory cytokine, and ultimately promote inflammation-driven tumorigenesis.[23] Clearly, these studies demonstrate the complex roles of inflammation and necroptosis in cancer.[8] While the tumor microenvironment is largely immunosuppressive, the specific combinations of inflammatory signals from necroptotic cells can either drive or suppress an anti-tumor immune response. There remains a need for a better understanding how these signals interact with the immune system at different stages of cancer progression in order to design therapies that can elicit the necessary inflammatory signals for a potent oncogenic response. Overall, we demonstrate the potential of R3 for cancer applications, but additional work is needed to establish the exact pathway of cell death and how this influences bystander cells and the immune system.

7.5 Methods & Materials

Peptide synthesis. Peptides (R3 KKKKKKLVFNNCSEVQIGNYNSL; control R3 (cR3) KKKKKKSVFNNCSESQSGNYNSS; and D-melittin gigavlkvlttglpaliswikrkrqqc) were synthesized using a solid phase peptide synthesizer (Liberty Blue CEM) on a rink amide resin. Peptides were cleaved from the resin in a trifluoroacetic acid (TFA) cocktail with 5% dimethoxybenzene 2.5% triisopropylsilane and 2.5% ethanedithiol; water was included at 2.5% for peptides containing arginine. Peptides were precipitated in cold diethyl ether AND purified by reverse-phase high performance liquid chromatography (HPLC). Peptide molecular weight was

confirmed using Matrix-Assisted Laser Desorption/Ionization-Time of Flight Mass spectrometry (MALDI-TOF) in a CHCA:DHB 2:1 matrix. Cy5 labeled peptides were generated by reaction of Cy5-NHS with Fmoc-deprotected peptide N-terminal amines through EDC/NHS chemistry on the resin, followed by cleavage and purification.

Materials, polymer synthesis, and characterization. Chemicals were purchased from Sigma and used as received. Polymer was prepared with RAFT polymerization. In brief, PEG-CTA, DIPAMA, PDSEMA and azobisisobutyronitrile (AIBN) were dissolved in dimethylacetamide (DMAc), purged in argon, and immersed in an oil bath at 70°C.[10] After 24h, the polymerization was quenched with liquid nitrogen and the resultant polymer p(PEG_{113})-*b*-p($DIPAMA_{40}$-*co*-$PDSEMA_2$) was purified by dialysis against methanol for 2 days. Synthesized peptides were conjugated to the PDSEMA monomer via disulfide exchange reaction in a mixture of methanol and water at a polymer:peptide feeding ratio of 5:1. After 8h, the polymer-peptide conjugates were purified by dialysis against DI water for 2 days. To prepare the micelles, the polymers or polymer-peptide conjugates were first dissolved in acidic phosphate buffer (pH 4.0), and the pH was adjusted to pH 7-8. Mixed micelles were formed by combining CP, CP-melittin, CP-R3, or CP-cR3 at indicated ratios using similar methods. All micelles were sterile filtered using a 0.22 mm pore filter. Polymer was characterized by ^{1}H NMR on a Bruker AV 300 in deuterated chloroform ($CDCl_3$). Peptide conjugation with PDSEMA was monitored by UV at 353 nm for the release of 2-thiopyridine. Micelle size was assessed by dynamic light scattering (DLS) at 0.5 mg/ml in PBS 7.4, and critical micellar concentration (CMC) was determined via Nile red method (ex/em 557/625 nm) with 0.5 mg/mL dye. The transition point of micelles was determined using a Nile Red method, as previously described.

Cell culture. RAW 264.7, CT26, and 4T1 cells were obtained from ATCC and cultured in RPMI supplemented with 10% FBS and 1% Pen-Strep. For viability studies, cell were plated at 15-20k cells/well in a 96-well plate overnight. Cells were incubated with peptide or micelles for 24 hours and viability was determined by MTS/PMS (Promega). The Gal8-RAW 264.7 cell line was generated as previously described.[24] Briefly, RAW cells were transfected with plasmids containing a transposable Gal8-GFP construct and PiggyBac transposon (generous gift of Jordan Green) using

Lipofectamine 2000. Cells were sorted for the top 5% brightest GFP^+ singlet cell events, expanded, and sorted three more time to yield a population of Gal8-GFP^{high} cells.

Hemolysis. Hemolysis assays were conducted as described.[25] Human blood was obtained in accordance with University of Washington Institutional Review Board (IRB) guidelines. Briefly, blood was washed in 150 mM NaCl and washed 2X. Blood was transferred to PBS pH 7.4 and washed, and resuspended in PBS at each pH to be tested (pH 5.4, 6.4, 7.4). Blood was diluted 1:50 and 190 μl of diluted blood was plated in a V-bottom 96 well plate. Samples were incubated with peptide in appropriate pH at 37°C for 1h and centrifuged. Supernatant was transferred to a clear, flat bottom 96-well plate and absorbance (541 nm) was detected on a plate reader. Triton X-100 1% (w/v) was used as a positive control, and PBS at appropriate pH was used as a negative control.

Imaging. Confocal imaging of endosomal escape was conducted as previously described.[24] Gal8-GFP-RAW 264.7 macrophages were plated (20k) in a 96-well half-area plate overnight and incubated with peptide or micelles for 16 hours. Media was replaced with FluoroBrite RPMI supplemented with 25 mM HEPES, 10% FBES, Hoechst 33342, and PI, and imaged on a confocal at 20X (Leica SP8X).

Immunogenic cell death (ICD) characterization. ICD was characterized by surface calreticulin expression and ATP and HMGB1 secretion in cell supernatant. *Calreticulin staining.* CT26 cells were incubated with micelles (50 μM) for 24 hours, lifted with Accutase, and stained with anti-calreticulin primary antibody (1:20, Abcam) followed by an anti-mouse secondary antibody (1:750), and analyzed on an Attune NxT (Invitrogen) flow cytometer. *ATP release.* CT26 cells were incubated with peptide or micelles at indicated concentrations for 24 hours and supernatant was collected and assessed for ATP concentration via the ENLITEN ATP Assay (Promega) according to manufacturer instructions. *HMGB1 release.* CT26 cells were incubated with peptide or micelles (50 μM peptide concentration in both) for 48 hours and supernatant was collected. Insoluble lipids were removed via centrifugation. HMGB1 concentration was assessed via ELISA (Chondrex) according to manufacturer instructions.

IL-1β assays. Non-terminal blood draws were performed via submental pricks with a 4 mm lancet. Blood (100-200 ml) was collected in serum separator tubes (BD) and allowed to coagulate for 30 minutes at room temperature, followed by centrifugation at 1000xg for 10 minutes at 4°C. Serum was collected and IL-1β was detected using the Mouse IL-1β ELISA MAX kit (BioLegend) per manufacturer instructions.

Tumor reduction studies. All animal experiments were approved by the Institutional Animal Care and Use Committee at the University of Washington and were conducted in accordance with use and regulations. For both 4T1 and CT26 tumor models, cells (1M) were injected subcutaneously in the right flank of 6-8 week old female balb/c mice (Charles River Laboratories) and tumors were measured by calipers. Mice were humanely euthanized when euthanasia criteria were met (tumor volume > 2000 mm^3 of body weight; weight loss > 20%; etc.). For tumor dissociation studies, mice were sacrificed and perfused. Tumors were collected and dissociated in RPMI supplemented with DNase (125 U/mL) and Collagenase IV (20 U/mL) using a gentleMACS dissociator. Cells were stained with the following antibodies (BioLegend): CD45-APC/Cy7, CD3-AF647, CD4-PE, CD8-FITC, CD11b-FITC, F4/80-APC, CD80-PE, CD206-BV605, CD11c-FITC, and MHCII-PE/Cy5. T-cells, macrophages, and dendritic cells were stained separately. For NLRP3 inhibition studies, mice were injected IP daily for 6 days with MMC950 (10 mg/kg).

Statistical analysis. Flow data was analyzed using FlowJo. Statistical analysis was calculated using a two-way ANOVA in Graphpad Prism 8.0.

7.6 Acknowledgments

This work was supported by NIH (R01CA17727, R01CA257563, and U54CA199090). We thank Nathanial Peters and W. M. Keck Microscopy Center (S10 OD016240) for confocal microscopy support. We thank Kim Woodrow (University of Washington) for use of her plate reader. We thank Jordan Green (Johns Hopkins University) for kindly providing the Gal8-GFP and PiggyBac transposon plasmids.

7.7 Conflicting Interests

S.H.P. has submitted a patent with the U.S. Patent and Trademark Office (WO2018027164A1) related to VIPER. S.H.P., S.L., and M.S. have filed a provisional patent on the DMM technology. S.M., J.V., and S.H.P. are co-inventors on a provisional patent on the R3 peptide.

7.8 Supplemental Information

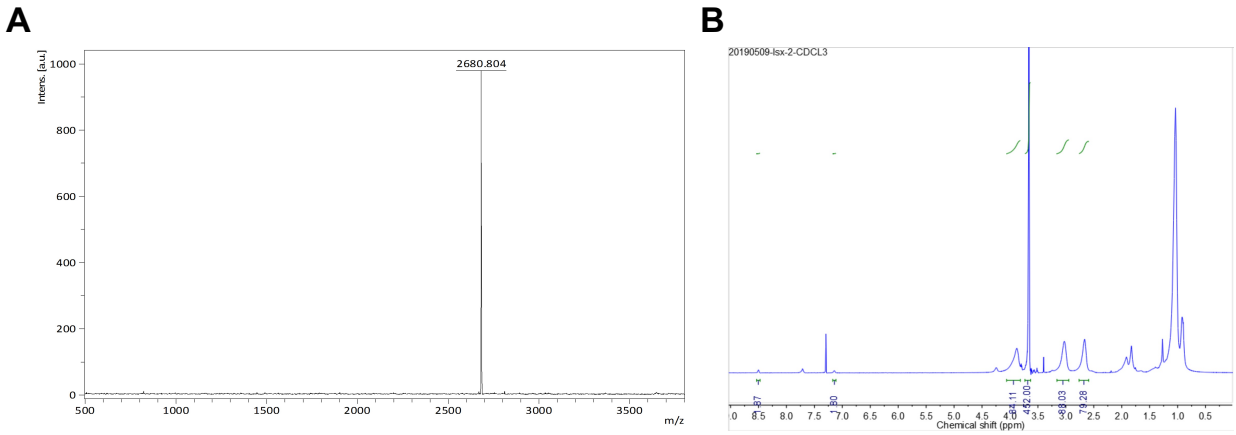

Figure S7.1: *Confirmation of peptide and polymer composition. A) MALDI of peptide sequence. B) ^{1}H NMR of CP polymer.*

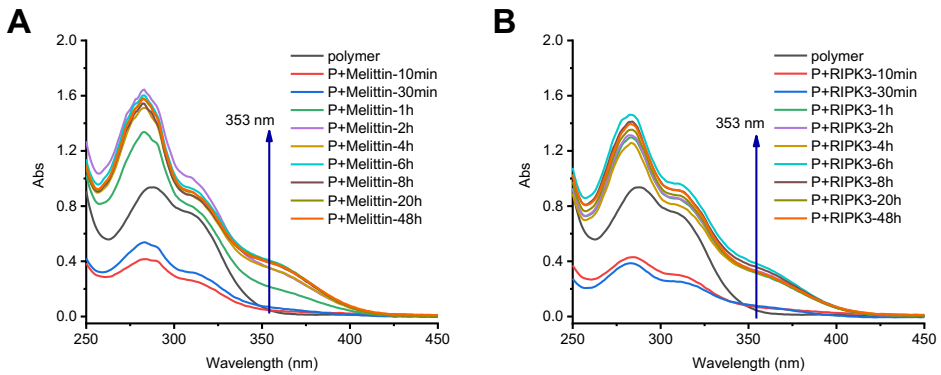

Figure S7.2: *Kinetics of peptide conjugation to CP. A) Melittin conjugation to CP. B) R3 peptide conjugation to polymer.*

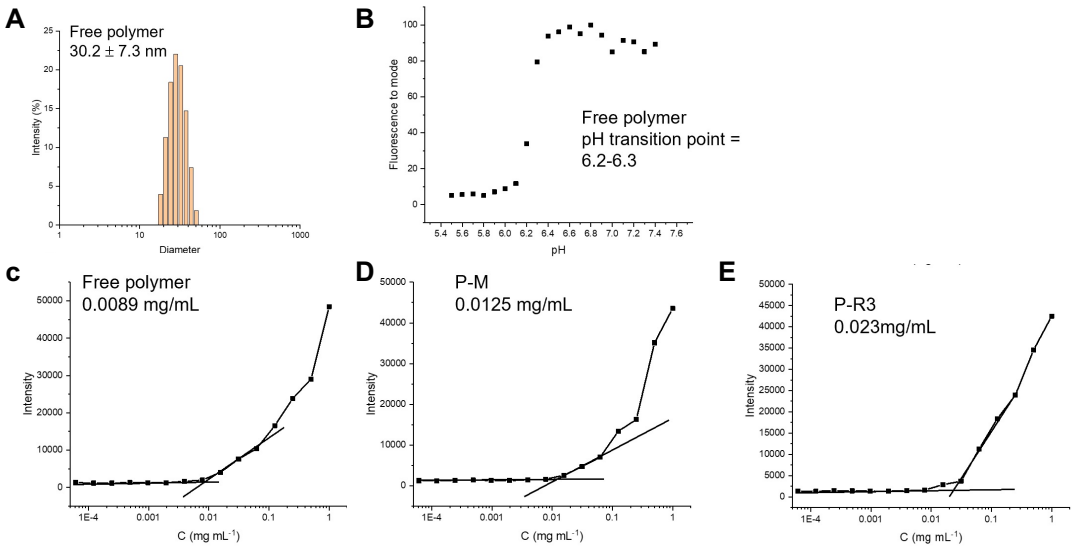

Figure S7.3: *Characterization of CP and critical micelle concentration (CMC). A-B) Diameter (A) and pH transition point (B) of CP. C-E) Calculation of CMC for CP (C), CP-melittin (D), and CP-R3 (E).*

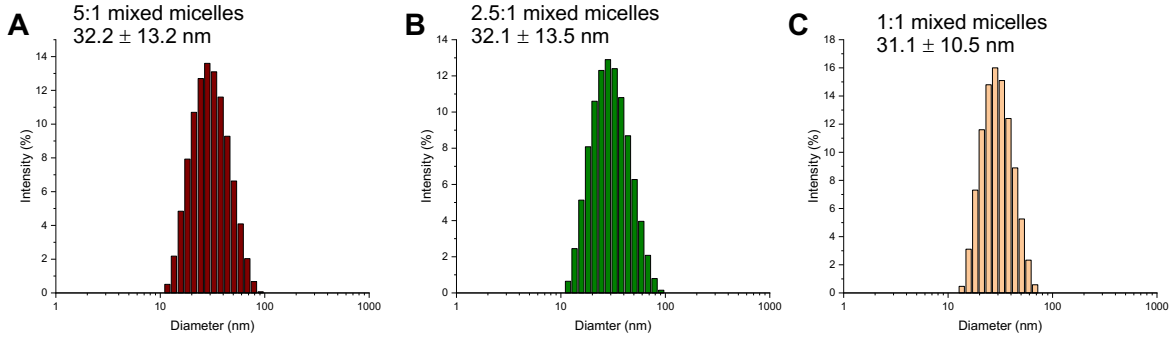

Figure S7.4*: Diameters of mixed micelles at 5:1 (A), 2.5:1 (B), and 1:1 (C) ratio of CP-R3:CP-melittin.*

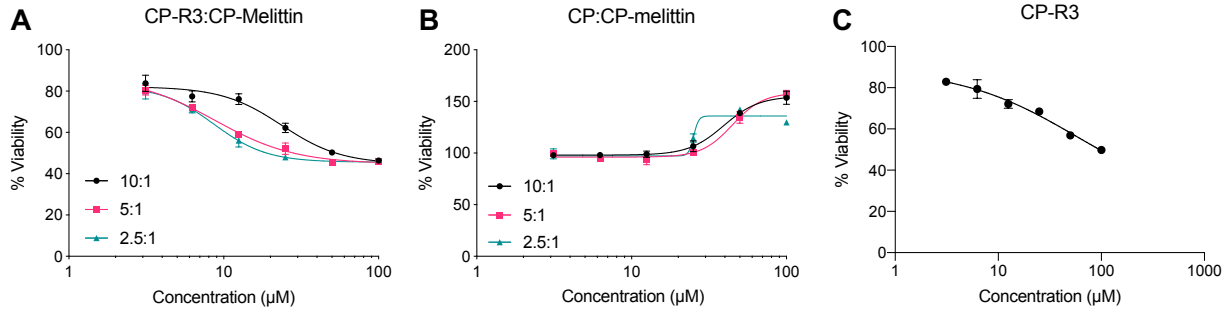

Figure S7.5*: Toxicity of micelles against RAW macrophages. A) Viability of cells after treatment with mixed micelles at ratios of 10, 5, and 2.5:1 of CP-R3:CP-melittin. B) Viability of cells after treatment with mixed at ratios of 10, 5, and 2.5:1 of CP:CP-melittin. C) Toxicity of CP-R3.*

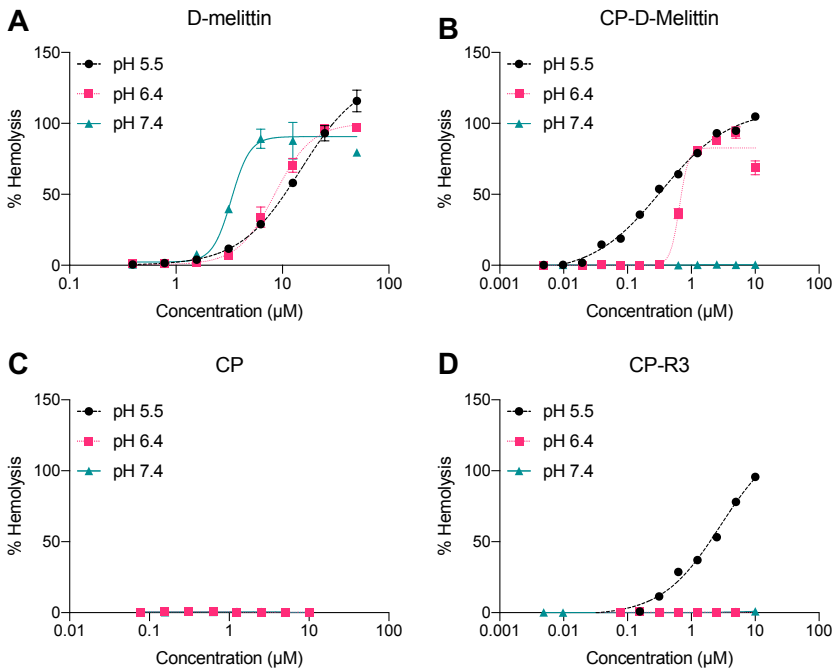

Figure S7.6: *Hemolytic activity of micelles against RBCs. Hemolysis of free peptide D-melittin (A), CP-D-melittin micelles (B), CP (C), and CP-R3 micelles (D).*

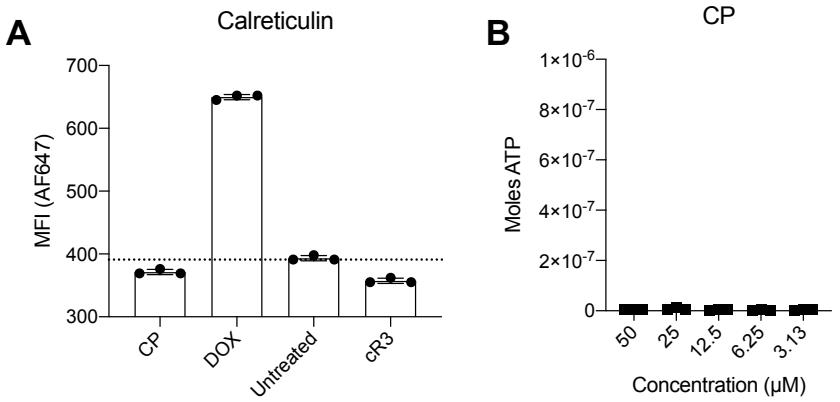

Figure S7.7*: Immunogenic cell death of controls. A) Calreticulin expression induced by CP, cR3, and doxorubicin (DOX). DOX is used as a positive control. B) ATP release induced by CP.*

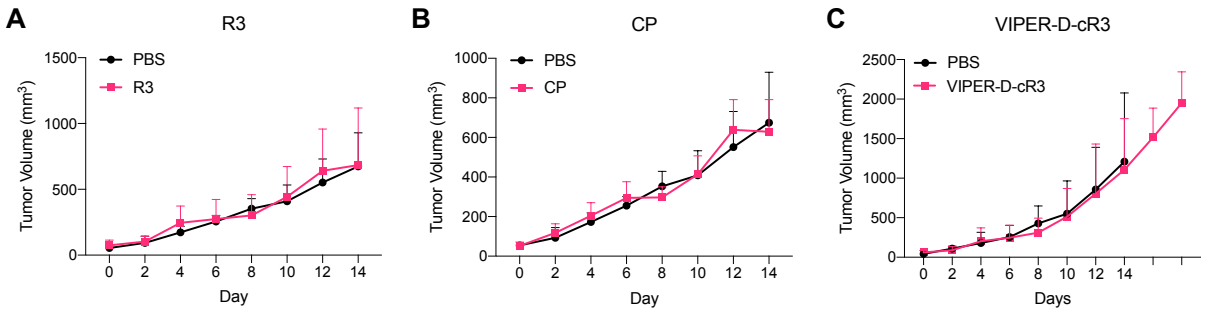

Figure S7.8*: Tumor reduction of controls. Mice were treated with R3 (A), CP (B), or VIPER-D-cR3 (C).*

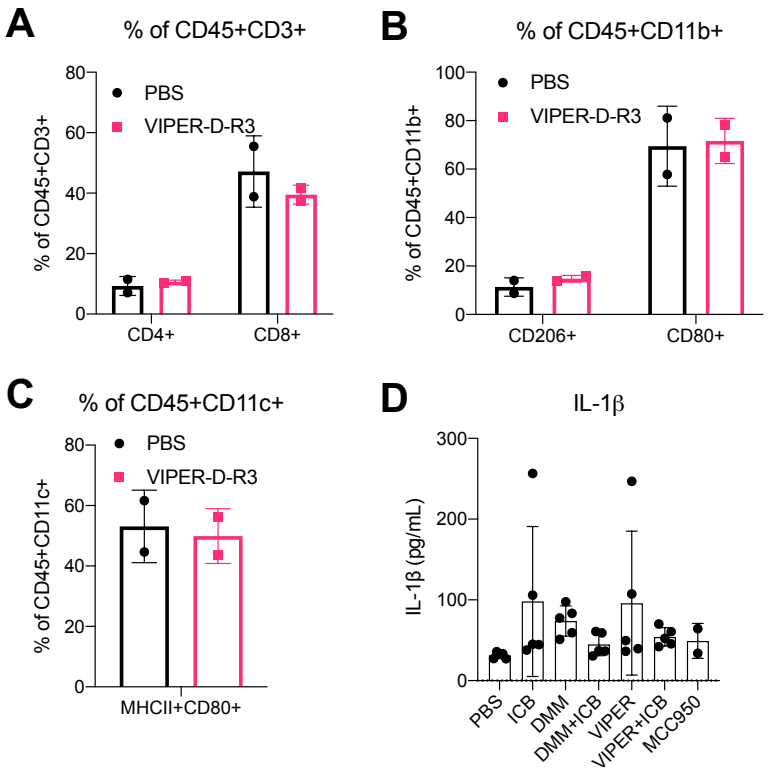

Figure S7.9*: TIL populations and IL-1β levels after 3-4 IV treatments with VIPER-D-R3. Populations of T-cells (A), macrophages (B), and dendritic cells (C) were evaluated after 3 treatments with VIPER-D-R3. D) Serum IL-1β levels in mice after 4 treatments with conjugates.*

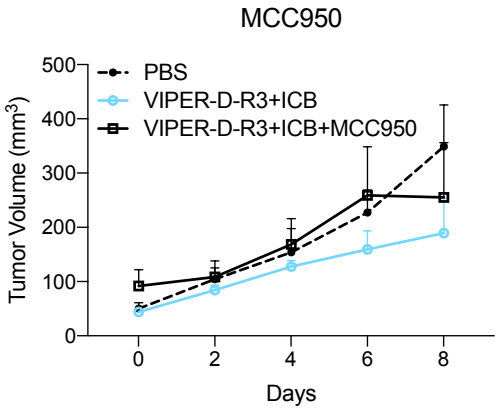

Figure S7.10*: Tumor growth after treatment with NLRP3 inhibitor MCC950 and VIPER-D-R3+ICB. VIPER-D-R3 was administered on days 0, 2, 4, and 6; ICB was administered on days 1, 3, 5, and 7. MCC950 was injected IP daily from days 0 to 5.*

References

1 Galluzzi, L., Buque, A., Kepp, O., Zitvogel, L. & Kroemer, G. Immunogenic cell death in cancer and infectious disease. *Nat Rev Immunol* **17**, 97-111, doi:10.1038/nri.2016.107 (2017).

2 Fucikova, J. *et al.* Detection of immunogenic cell death and its relevance for cancer therapy. *Cell Death Dis* **11**, 1013, doi:10.1038/s41419-020-03221-2 (2020).
3 Krysko, D. V. *et al.* Immunogenic cell death and DAMPs in cancer therapy. *Nat Rev Cancer* **12**, 860-875, doi:10.1038/nrc3380 (2012).
4 Kroemer, G., Galluzzi, L., Kepp, O. & Zitvogel, L. Immunogenic cell death in cancer therapy. *Annu Rev Immunol* **31**, 51-72, doi:10.1146/annurev-immunol-032712-100008 (2013).
5 Gong, Y. *et al.* The role of necroptosis in cancer biology and therapy. *Mol Cancer* **18**, 100, doi:10.1186/s12943-019-1029-8 (2019).
6 Dhuriya, Y. K. & Sharma, D. Necroptosis: a regulated inflammatory mode of cell death. *J Neuroinflammation* **15**, 199, doi:10.1186/s12974-018-1235-0 (2018).
7 Kaczmarek, A., Vandenabeele, P. & Krysko, D. V. Necroptosis: the release of damage-associated molecular patterns and its physiological relevance. *Immunity* **38**, 209-223, doi:10.1016/j.immuni.2013.02.003 (2013).
8 Messmer, M. N., Snyder, A. G. & Oberst, A. Comparing the effects of different cell death programs in tumor progression and immunotherapy. *Cell Death Differ* **26**, 115-129, doi:10.1038/s41418-018-0214-4 (2019).
9 Sylvestre, M. *et al.* Replacement of L-amino acid peptides with D-amino acid peptides mitigates anti-PEG antibody generation against polymer-peptide conjugates in mice. *J Control Release* **331**, 142-153, doi:10.1016/j.jconrel.2021.01.015 (2021).
10 Cheng, Y., Yumul, R. C. & Pun, S. H. Virus-Inspired Polymer for Efficient In Vitro and In Vivo Gene Delivery. *Angew Chem Int Ed Engl* **55**, 12013-12017, doi:10.1002/anie.201605958 (2016).
11 Orozco, S. & Oberst, A. RIPK3 in cell death and inflammation: the good, the bad, and the ugly. *Immunol Rev* **277**, 102-112, doi:10.1111/imr.12536 (2017).
12 Snyder, A. G. *et al.* Intratumoral activation of the necroptotic pathway components RIPK1 and RIPK3 potentiates antitumor immunity. *Sci Immunol* **4**, doi:10.1126/sciimmunol.aaw2004 (2019).
13 Menger, L. *et al.* Cardiac glycosides exert anticancer effects by inducing immunogenic cell death. *Sci Transl Med* **4**, 143ra199, doi:10.1126/scitranslmed.3003807 (2012).
14 Kim, K. *et al.* Eradication of metastatic mouse cancers resistant to immune checkpoint blockade by suppression of myeloid-derived cells. *Proc Natl Acad Sci U S A* **111**, 11774-11779, doi:10.1073/pnas.1410626111 (2014).
15 DuPre, S. A., Redelman, D. & Hunter, K. W., Jr. The mouse mammary carcinoma 4T1: characterization of the cellular landscape of primary tumours and metastatic tumour foci. *Int J Exp Pathol* **88**, 351-360, doi:10.1111/j.1365-2613.2007.00539.x (2007).
16 Murphy, J. M. & Silke, J. Ars Moriendi; the art of dying well - new insights into the molecular pathways of necroptotic cell death. *EMBO Rep* **15**, 155-164, doi:10.1002/embr.201337970 (2014).
17 Chen, Y. *et al.* Role of peptide hydrophobicity in the mechanism of action of alpha-helical antimicrobial peptides. *Antimicrob Agents Chemother* **51**, 1398-1406, doi:10.1128/AAC.00925-06 (2007).
18 Jin, Y. *et al.* in *American Association for Cancer Research.*
19 Sylvestre, M., Crane, C. A. & Pun, S. H. Progress on Modulating Tumor-Associated Macrophages with Biomaterials. *Adv Mater*, e1902007, doi:10.1002/adma.201902007 (2019).
20 Ngambenjawong, C., Gustafson, H. H. & Pun, S. H. Progress in tumor-associated macrophage (TAM)-targeted therapeutics. *Adv Drug Deliv Rev* **114**, 206-221, doi:10.1016/j.addr.2017.04.010 (2017).
21 Seifert, L. *et al.* The necrosome promotes pancreatic oncogenesis via CXCL1 and Mincle-induced immune suppression. *Nature* **532**, 245-249, doi:10.1038/nature17403 (2016).
22 Lin, C. C. *et al.* RIPK3 upregulation confers robust proliferation and collateral cystine-dependence on breast cancer recurrence. *Cell Death Differ* **27**, 2234-2247, doi:10.1038/s41418-020-0499-y (2020).
23 Ahn, J. *et al.* Inflammation-driven carcinogenesis is mediated through STING. *Nat Commun* **5**, 5166, doi:10.1038/ncomms6166 (2014).
24 Kilchrist, K. V. *et al.* Gal8 Visualization of Endosome Disruption Predicts Carrier-Mediated Biologic Drug Intracellular Bioavailability. *ACS Nano* **13**, 1136-1152, doi:10.1021/acsnano.8b05482 (2019).
25 Evans, B. C. *et al.* Ex vivo red blood cell hemolysis assay for the evaluation of pH-responsive endosomolytic agents for cytosolic delivery of biomacromolecular drugs. *J Vis Exp*, e50166, doi:10.3791/50166 (2013).

Part III

Crossing the blood-brain barrier

Chapter 8

Challenges in crossing the blood-brain barrier in cancer treatment

8.1 Abstract

The blood-brain barrier (BBB) remains a critical hurdle in delivering therapeutics to the brain, as it excludes > 98% of small molecules and nearly 100% of macromolecules. Current strategies to bypass the BBB involve (1) physical disruption, (2) transient disruption, or (3) receptor mediated transcytosis (RMT). Of these, RMT has emerged as a promising strategy to cross the BBB as it is noninvasive and exploits endogenous transport pathways. Specifically, the transferrin pathway has been extensively investigated for drug delivery to the brain. Recent studies have elucidated how transferrin binding to its receptor governs intracellular sorting patterns and subsequent delivery or degradation. As a result, transferrin-targeted therapies have improved accumulation and delivery into the brain.

8.2 Need for new therapies

Despite the high incidence and devastating prognosis of brain cancer, therapies are limited to only 4 FDA approved drugs and 1 device, with only marginal improvements in survival.[1] The development of effective brain cancer therapies is thwarted by the blood brain barrier (BBB), which effectively excludes > 98% of small molecules and nearly all large molecules from the central nervous system (CNS).[2] Brain tumors present the greatest clinical challenge because they are located behind this barrier, beyond the reach of most skilled surgeons and therapies.[3] Current therapies suffer from systemic toxicity and insignificant drug penetration due to an inability to successfully traverse cells of the BBB. Significantly, less than 1% of the injected dose is delivered to brain tumors.[4] As such, there remains a critical need to develop new drug delivery systems that can overcome the biological challenges imposed by the blood-blood barrier.

8.3 Blood-brain barrier biology

The blood-brain barrier (BBB) is a physiological barrier that tightly controls the interface between the blood and neural tissues. It maintains homeostasis and regulates influx and efflux of nutrients

and waste. In disease, this neuroprotective role is a major hurdle in delivering therapeutics to diseased tissue, as the BBB prevents entry and distribution to the brain. Thus, significant effort has been directed toward understanding transport across the BBB and developing strategies that can exploit these mechanisms.

8.3.1 Anatomical composition

The BBB comprises many cell types, mainly endothelial cells, pericytes, and astrocyte end foot processes, which tightly control the movement of ions, molecules, and cells between the blood and the brain (**Figure 8.1**).[5,6] Cerebral endothelial cells form tight junctions at their margins, barring the paracellular diffusional pathway between cells. These junctions consist of proteins spanning the intercellular cleft, such as transmembrane proteins (e.g. occludins, claudins).[7] The expression of these proteins is associated with the integrity of the BBB, and some drugs target these proteins to influence BBB permeability. Pericytes, multi-functional mural cells, periodically wrap about the endothelial cells. Together, the endothelium and pericytes contribute to the local basement membrane. Astrocyte foot processes also partially surround the capillaries, forming tight junctions which are critical for communication and maintenance of the barrier. Vascular smooth muscle cells are also embedded in the endothelium and interface with neuronal axon projections, which can release neurotransmitters and peptides that help regulate BBB permeability. Together, these barriers maintain homeostasis in the CNS by regulating selective transport of nutrients, hormones, and removal of waste.

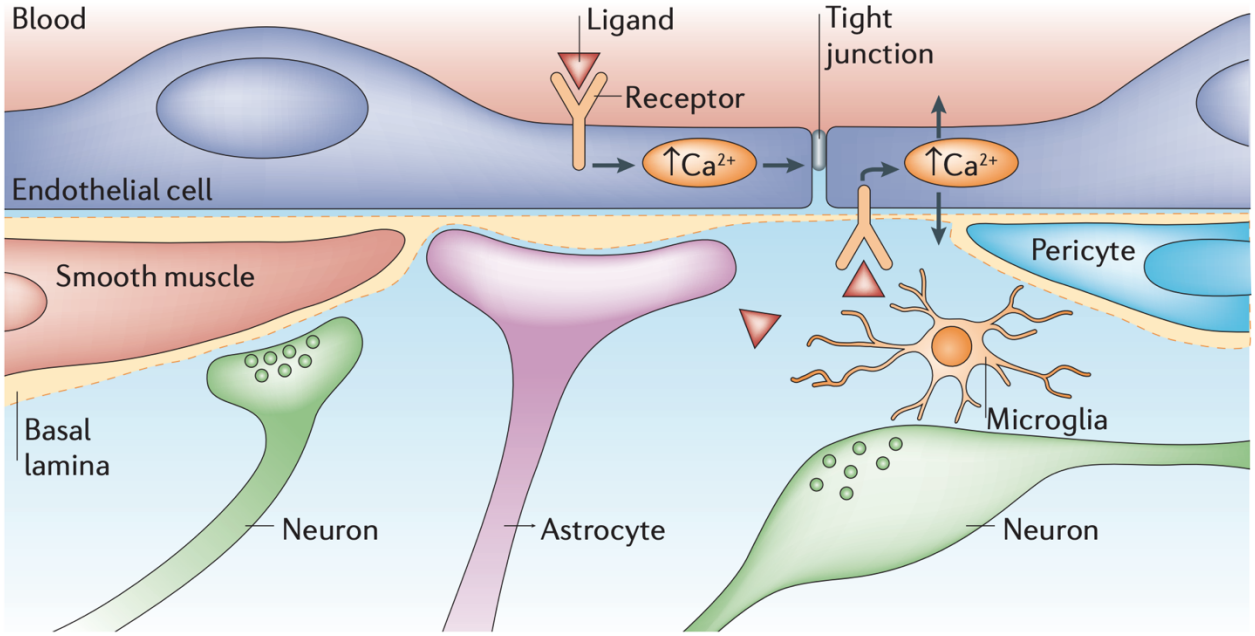

Figure 8.1: Anatomical composition of the blood brain barrier. The blood-brain barrier comprises many cells that tightly regulate the movement of ions, nutrients, and waste. Endothelial cells form tight junctions between adjacent cells, barring paracellular transport of the majority of small and large molecules. Pericytes wrap around endothelial cells and form close associations. Astrocyte foot projects interface with endothelium, as well as smooth muscle cells and neurons. Reprinted with permission from Nature Reviews Neuroscience, Volume 7:41-53, copyright 2006 Nature Reviews.[8]

8.3.2 Transport across the BBB

Substances cross the BBB through (*i*) paracellular transport, passing between endothelial cells, or through (*ii*) transcellular transport, which involves passing from the luminal (blood) side through the cytoplasm of the endothelial cells, and into the abluminal (brain) side (**Figure 8.2**).[2,9] For the majority of small molecules (> 98%) and nearly all large molecules, the tight junctions prevent paracellular transport from occurring. Only small, gaseous molecules (e.g. O_2, CO_2) and small, lipophilic agents (e.g. barbiturates, ethanol) can diffuse freely. Generally, small molecules can cross the BBB in physiologically relevant amounts if their molecular mass is < 400-500 Daltons, and the molecule forms fewer than 8-10 hydrogen bonds with water; BBB permeation decreases exponentially with each additional pair of hydrogen bonds in the drug structure.[10] Otherwise,

specific transport systems and enzymes regulate transcellular transport of small and large molecules, including peptides, proteins, and cell waste.[8] In this process, events on the luminal (blood) side of the BBB trigger the formation of a endocytic vesicle that encapsulates the macromolecule, where it is then routed across the cell, and fuses with the abluminal (brain) side of the endothelium, releasing the macromolecule into the brain. In receptor mediated transcytosis, ligand:receptor binding triggers internalization and subsequent transport. In contrast, adsorptive-mediated transcytosis is nonspecific and transport is dependent on protein charge.[11] Interaction with cationic proteins facilitates endocytosis and movement through the endothelial cytoplasm.

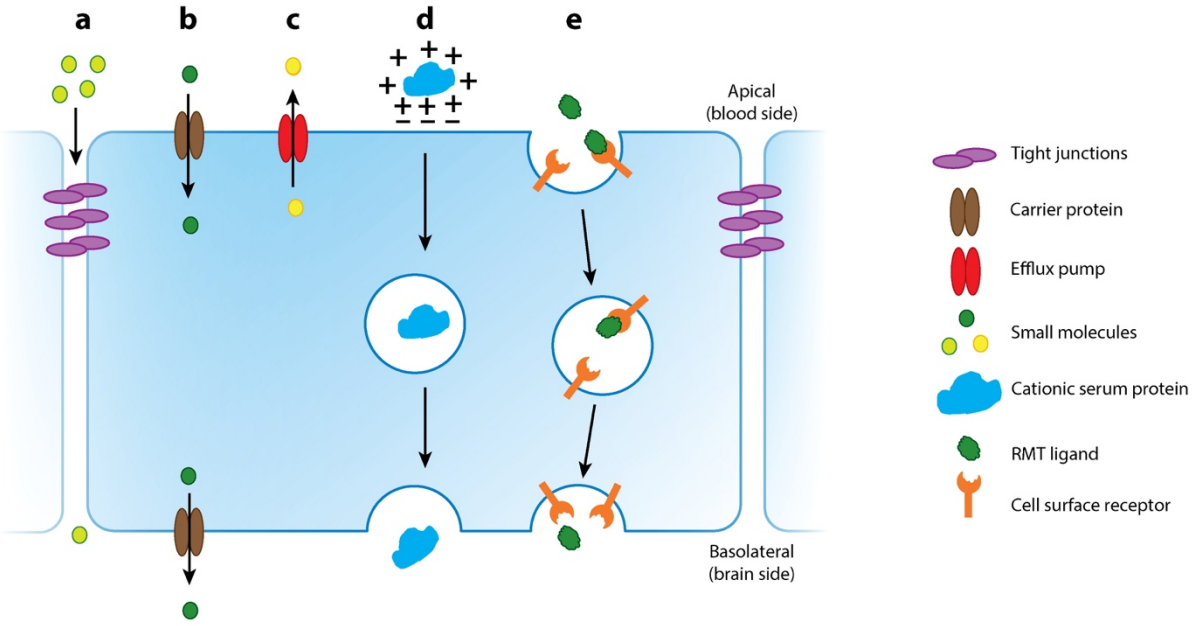

Lajoie JM, Shusta EV. 2015.
Annu. Rev. Pharmacol. Toxicol. 55:613–31

Figure 8.2: Transport routes across the endothelial cells of the BBB. (a) Paracellular diffusion is restricted by the tight junctions between adjacent cells. (b) Carrier proteins can facilitate the transport of small molecules such as amino acids and glucose. (c) Efflux pumps can recognize and remove substances from endothelial cells and transport them to the luminal (blood) side. (d) Adsorptive mediated transcytosis nonspecifically transports cationic molecules. These positively charged molecules interact with the negative domains on the endothelial cells and are shuttled across the cell. (e) Receptor mediated transcytosis involves specific ligand:receptor binding which triggers internalization and subsequent transcytosis. Reprinted with permission from Annual Review of Pharmacology and Toxicology, Volume 55:613-31, copyright 2015 Annual Reviews.[12]

8.3.3 Macromolecule exclusion and implications for therapy

The BBB is the fundamental biological mechanism that protects the central nervous system from vascularly injected agents.[2] This is best illustrated by intravenous (i.v.) injection of radiolabeled histamine, which readily enters all organs except the brain and spinal cord.[10] As discussed, this lack of CNS transport can be attributed to the BBB, which forces most molecular traffic to cross transcellularly rather than paracellularly through the junctions, as in most endothelia.[8] Additionally, brain transport is further limited by the decreased endocytosis/transcytosis activity of brain endothelium compared to peripheral endothelium, contributing to the transport-barrier of the BBB.[5] Drugs that are capable of traversing the BBB may be actively exported back out via efflux transporters (e.g. P-glycoprotein 1).[9] Lastly, drugs still face biological hurdles seen elsewhere, such as metabolic degradation and poor pharmacokinetics. Overall, the majority of neurotherapeutics are unable to cross the BBB alone, necessitating novel strategies to facilitate CNS entry and diffusion.

8.4 Current strategies to cross the BBB

Several strategies have been investigated to bypass the BBB. Generally, these strategies seek to (*1*) physically bypass the BBB and inject therapeutics directly into the CNS, (*2*) transiently open the BBB to facilitate entry of intravenously injected therapies, or (*3*) exploit endogenous transport mechanisms on the luminal (blood) side of the BBB to deliver therapeutics into the brain. While several platforms have been utilized in the clinic, improvements are unclear or modest.

8.4.1 Physical disruption

One strategy to bypass the BBB is to physically disrupt it and introduce drugs into the brain through intracerebral implantation, intracerebroventricular infusion, or convection-enhanced diffusion. Intracerebral implantation involves direct introduction of drugs into the parenchyma, with the goal of facilitating drug diffusion to tumor cells. This was the premise behind the Gliadel® wafer, a drug-polymer implanted into the cavity of resected brain tumors to deliver the chemotherapeutic carmustine.[13] While modest efficacy was demonstrated, implantation was associated with significant complications, including brain edema, cerebral spinal fluid leak, and intracranial infection.[14,15] Furthermore, no study compared efficacy of Gliadel® with systemic

therapy. Ultimately, it is still unclear if the risks balance the potential benefits. Similarly, intracerebroventricular infusion seeks to bypass the BBB by injecting drugs directly into the ventricles of the brain, introducing physiologically relevant drug concentrations into the brain.[16] This must be performed carefully, as the risk of infection and adverse events (e.g. cutaneous-CSF fistula, injured nerve roots, intraspinal hemorrhage) is high. However, efficacy is unclear and dosing regimens vary considerably based on the drug and patient. Significantly, while both methods can introduce high drug concentrations into the CNS, their efficacy is dependent on diffusion through the parenchyma, which is highly limited.[17] Diffusion through the parenchyma is too slow to transfer materials more than several hundred microns within 1-2 hours; thus, drug concentration drops off exponentially from the site of initial implantation. Lastly, convection-enhanced delivery generates a pressure gradient at the tip of the infusion catheter in order to deliver therapeutics through the interstitial spaces of the CNS.[18] This method facilitates predictable and homogenous drug distribution, compared to diffusive therapies. While initial clinical investigations hold promise, this technique faces technical limitations in catheter design and unpredictable flow patterns. Continued work focuses on improving catheter design and developing a model for sustained infusion.

8.4.2 Transient disruption

Another strategy to facilitate transport of drugs past the BBB is to transiently disrupt the BBB. Arterial injection of hypertonic solutions can widen the interendothelial tight junctions by (*1*) drawing water out of the endothelial cell and into the blood vessel, causing the endothelial cell to shrink, (*2*) increasing water flow out of the brain, causing vasodilation and endothelial cell membrane stretching, and (*3*) contracting the endothelial cytoskeleton via a calcium-dependent mechanism.[9,19] Osmotic agents that have been investigated include arabinose, urea, and mannitol. Chemical disruption can be mediated by vasoactive agents that induce a temporary inflammatory reaction in the BBB, such as alkylglycerols and bradykinin. However, while these methods can increase drug concentrations in the brain, they can also result in some drugs reaching neurotoxic levels. Additionally, these methods have been associated with adverse events such as transient cerebral edema and seizures. Lastly, BBB disruption by these methods is non-specific and takes place throughout normal brain tissue as well, resulting in unregulated accumulation of proteins in

the brain that can be toxic to normal tissue. In cancer, there is an additional concern that BBB disruption enables circulating cancer cells to more readily access the brain and form new lesions.

Recently, focused ultrasound (FUS) has been investigated as a non-invasive method to disrupt the BBB in a controlled manner.[20,21] In this technique, gas filled microbubbles expand and contract in response to acoustic pressure waves, pushing and pulling on the endothelial cell tight junctions to enhance paracellular transport. This modality has successfully mediated the delivery of a variety of therapeutic agents, including antibodies, proteins, and nanoparticles. Significantly, this technique was well-tolerated by all patients with glioblastoma in a Phase I clinical trial.[22] However, recent reports have implicated BBB opening by FUS with an acute sterile inflammatory response in the brain, which is undesirable in gene therapy or neurological conditions that already suffer from chronic inflammation.[23]

8.4.3 Receptor mediated transcytosis

Receptor mediated transcytosis (RMT) has emerged as a promising drug delivery strategy to cross the BBB because it takes advantage of endogenous uptake pathways in the brain while leaving the BBB intact.[24] RMT involves the interaction between a ligand and its cognate receptor in order to trigger internalization and subsequent transcytosis (**Figure 8.3**).[25] Upon transport to the abluminal (brain) side, the drug is released and diffuses into the parenchyma. RMT is also called the "Trojan Horse" approach, as it smuggles its payload into the brain under the guise of an acceptable molecule.[26] This strategy has been investigated to deliver a broad variety of payloads, such as protein-drug conjugates, therapeutic antibodies, liposomes, and nanoparticles. Commonly leveraged receptors of RMT include transferrin (Tf), low-density lipoprotein (LDL), and insulin receptor. The Tf receptor (TfR) is an attractive receptor because it is highly expressed on the luminal side of the BBB endothelium and facilitates one-way transport from the blood to brain, unlike the LRP lipoprotein receptor which is highly expressed on both BBB endothelium and in the brain.[2] Insulin-targeting can dysregulate insulin metabolism and risks inducing hypoglycemia.[25] Importantly, transferrin-conjugates have an established track-record to deliver therapeutic payloads and achieve improved drug delivery and survival in animals.[25,27,28]

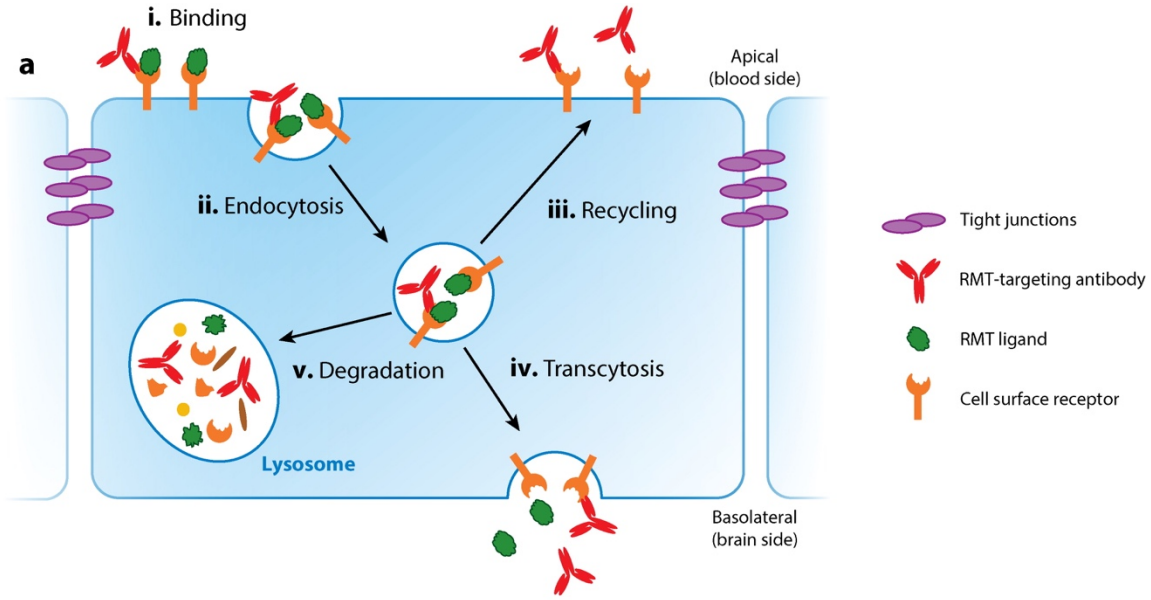

Figure 8.3: Schematic of RMT mechanism. (i) On the apical (blood) side of the BBB, the ligand binds to its receptor, trigger (ii) endocytosis of the ligand:receptor complex. This vesicle can be trafficked through several pathways, mainly (iii) recycling, (iv) transcytosis, or (v) degradation. (iii) Complexes that are recycled are returned to the apical (blood) side of the BBB. (iv) Complexes that undergo transcytosis are shuttled to the basal (brain) side of the cell, where they fuse with the membrane and release its cargo. (v) Some vesicles are fused with lysosomes, degrading the vesicle's contents. Recent studies have shown that engineering ligand:receptor binding kinetics can direct the pathway that the vesicles undergo following internalization. Reprinted with permission from Annual Review of Pharmacology and Toxicology, Volume 55:613-31, copyright 2015 Annual Reviews.[12]

8.5 Transferrin targeted delivery across the BBB

The transferrin receptor is the most widely exploited receptor for RMT. Recent studies have explored how binding kinetics to the receptor impact intracellular sorting and ultimately determine carrier fate. Even the iron release rate of transferrin influences the degree of receptor association and subsequent trafficking patterns.[29] Overall, understanding the role of transferrin:receptor binding is crucial for developing therapies that can effectively cross the BBB.

8.5.1 Transferrin and transferrin receptor binding

Transferrin (Tf) is a plasma glycoprotein that controls the levels of free iron in the blood and delivers iron into cells.[12] The transferrin receptor (TfR) is highly expressed on the apical side of the BBB, making it an attractive target for RMT into the brain (**Figure 8.4**).[30] Iron-bound transferrin (holo-Tf) has higher affinity for the TfR compared to iron-free transferrin (apo-Tf). Upon holo-Tf binding to the TfR, the holo-Tf:TfR complex is rapidly internalized via clathrin-mediated endocytosis. As endosomal pH drops (~ pH 5.5), holo-Tf undergoes conformational changes that releases its iron cargo, and the endosome recycles iron-free apo-Tf to the cell surface. The decreased apo-Tf:TfR affinity at extracellular pH releases Tf from the receptor.

Both Tf and anti-TfR antibodies have been used as targeting ligands for BBB delivery, and both have associated advantage and disadvantages.[12] Tf lends its well toward pre-clinical studies because there is high homology between human and murine Tf, enabling species cross-reactivity. However, Tf is also present in high concentrations in the bloodstream, requiring the injected Tf-carrier to compete with endogenous Tf for TfR binding. Alternatively, anti-TfR antibodies can exploit distal binding sites to avoid Tf binding competition, and can be engineered to bind the TfR with higher affinity than endogenous Tf.[31] Yet, recent studies have demonstrated that Tf:TfR binding interactions must be precisely engineered, else complexes could instead be preferentially sorted for degradation; this is further discussed in the section 5.2.[32] Furthermore, antibody cross-reactivity (or lack of) necessitates further ligand optimization to bypass immune events or enable use across multiple species, limiting clinical applicability.[33]

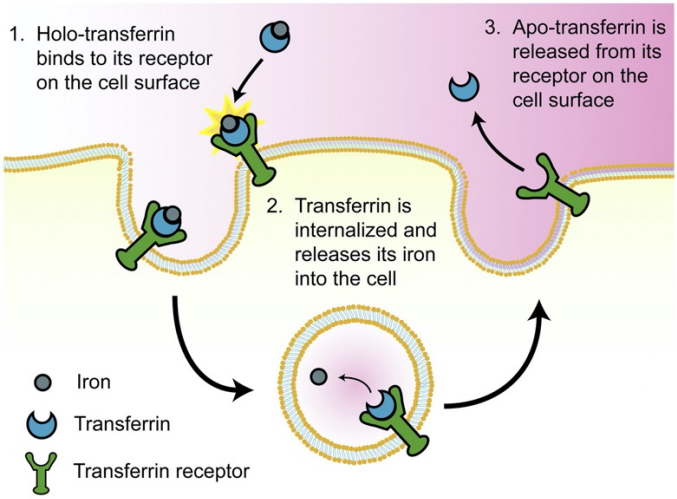

Figure 8.4: *Endocytic recycling of Tf. Iron-bound holo-Tf binds the TfR on the apical side, triggering endocytosis. Endosomal acidification (~pH 5.5) leads to a conformational change in holo-Tf, release iron. The endosome is recycled back to the apical side of the cell, and the now iron-free apo-Tf is released from the receptor. Reprinted with permission from Journal of Controlled Release, Volume 117:403-412, copyright 2007 JCR.*[29].

8.5.2 Influence of binding affinity and avidity on Tf-targeted transcytosis

Pioneering studies engineered high-affinity anti-TfR antibodies in order to increase carrier transport into the brain and necessitate lower dosing compared to low-affinity variants. In particular, the monoclonal OX26 antibody was demonstrated to bind a conserved TfR epitope and was detectable in the parenchyma.[34] However, when compared to an antibody control, OX26 was cleared more rapidly and primarily accumulated in the BBB endothelium rather than crossing into the brain.[31] This was later attributed to high affinity antibody:receptor binding kinetics that prevented the release of OX26 from the TfR.[33] Thus, it was discovered that ligand:receptor kinetics play a fundamental role in Tf-mediated drug delivery. Mainly, binding affinity and avidity constrain uptake and transport into the brain.

In the context of the BBB, binding affinity is inversely correlated to transport.[35] Yu, et. al. demonstrated that reducing the affinity of anti-TfR antibodies enhanced RMT compared to high-affinity variants. While high affinity variants can ensure TfR binding, they are unable to release from the TfR once on the abluminal (brain) side, preventing effective accumulation in the parenchyma. Furthermore, high affinity binding alters trafficking routes from recycling to degradation, whereas low affinity binding is more capable of transcytosis.[36] Similarly, avidity is inversely correlated with transport, which has been demonstrated with both anti-TfR antibodies and Tf ligands.[37,38] Niewoehner, et. al. decorated shuttles with anti-TfR antibodies as a single (monovalent) or double (bivalent) formulation.[37] Carriers with monovalent TfR binding underwent successful transcytosis *in vitro* and *in vivo*, whereas carriers with bivalent binding induced lysosomal sorting and subsequent degradation. In agreement, Wiley, et. al. varied the Tf content on gold nanoparticles and showed that high Tf-content (high avidity) nanoparticles were unable to detach from the TfR on the abluminal (brain) side of the BBB.[38]

8.5.3 Acid-labile transferrin targeted particles

Motivated by studies investigating how affinity and avidity influence transcytosis, Clark and Davis engineering transferrin-targeted nanoparticles with acid-cleavable linkers between transferrin and the nanoparticle core, facilitating release of the nanoparticle from the TfR to promote entry into the brain (**Figure 8.5**).[39] Following TfR binding and internalization, the drop in pH in the endosome triggered cleavage of the linker between Tf and the nanoparticle core. Thus, upon fusion of the endosome with the abluminal (brain) side of the cell, the nanoparticles are unbound and free to diffuse into the parenchyma. Together, this design retains high affinity TfR binding but also facilitates subsequent release. Significantly, the pH-labile linker enhanced the ability of Tf-containing nanoparticles to enter the brain, but did not affect particles employing anti-Tfr antibodies. This emphasizes the sensitivity of Tf:TfR interactions and how they direct intracellular trafficking. This work was further supported by Wyatt, who employed a pH-dependent boronic acid-diol linker in polymeric nanoparticles for camptothecin delivery to brain metastases.[40] Building on these studies, Ruan, et. al. incorporated detachable ligands and influx transporter substrates to enhance subsequent exocytosis.[41] Specifically, following acid-mediated cleavage of Tf, a glucose analog was exposed, which bound to glucose transporters and accelerated exocytosis from the endosome into brain parenchyma. Together, these results underscore how pH-sensitive, transferrin-targeted nanoparticles can be successfully employed for brain cancer applications.

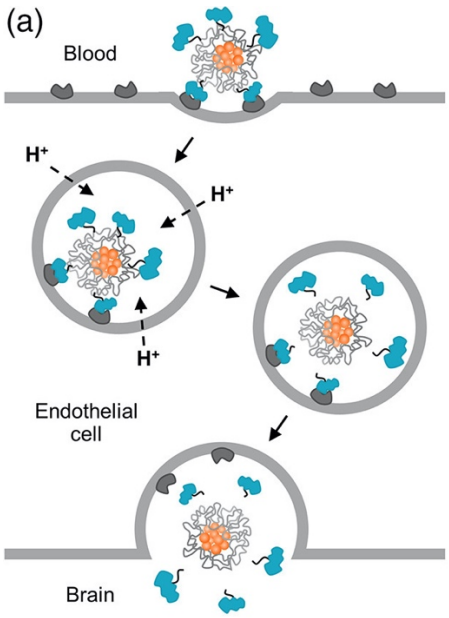

Figure 8.5: *Schematic of acid-cleavable decoupling of Tf. Binding of the Tf-coated nanoparticle to the TfR triggers internalization. Endosomal acidification cleaves the acid-labile bond, separating the Tf ligands from the nanoparticle core. Upon endosomal fusion with the abluminal (brain) side of the cell, the nanoparticle can diffuse into the brain parenchyma. Reprinted with permission under the Creative Commons license (https://creativecommons.org/licenses/by/4.0/) from Bioeng Transl Med Volume 4:30-37 2018.*[40]

References

1 *Current Treatments for Brain Tumors*, 2017.

2 Furtado, D. *et al.* Overcoming the Blood-Brain Barrier: The Role of Nanomaterials in Treating Neurological Diseases. *Adv Mater* **30**, e1801362, doi:10.1002/adma.201801362 (2018).

3 Aldape, K. *et al.* Challenges to curing primary brain tumours. *Nat Rev Clin Oncol* **16**, 509-520, doi:10.1038/s41571-019-0177-5 (2019).

4 Wilhelm, S. *et al.* Analysis of nanoparticle delivery to tumours. *Nature Reviews Materials* **1**, doi:10.1038/natrevmats.2016.14 (2016).

5 Daneman, R. & Prat, A. The blood-brain barrier. *Cold Spring Harb Perspect Biol* **7**, a020412, doi:10.1101/cshperspect.a020412 (2015).

6 Abbott, N. J., Patabendige, A. A., Dolman, D. E., Yusof, S. R. & Begley, D. J. Structure and function of the blood-brain barrier. *Neurobiol Dis* **37**, 13-25, doi:10.1016/j.nbd.2009.07.030 (2010).

7 Chiba, H., Osanai, M., Murata, M., Kojima, T. & Sawada, N. Transmembrane proteins of tight junctions. *Biochim Biophys Acta* **1778**, 588-600, doi:10.1016/j.bbamem.2007.08.017 (2008).

8 Abbott, N. J., Ronnback, L. & Hansson, E. Astrocyte-endothelial interactions at the blood-brain barrier. *Nat Rev Neurosci* **7**, 41-53, doi:10.1038/nrn1824 (2006).

9 Hersh, D. S. *et al.* Evolving Drug Delivery Strategies to Overcome the Blood Brain Barrier. *Curr Pharm Des* **22**, 1177-1193, doi:10.2174/1381612822666151221150733 (2016).

10 Pardridge, W. M. The blood-brain barrier: bottleneck in brain drug development. *NeuroRx* **2**, 3-14, doi:10.1602/neurorx.2.1.3 (2005).

11 Herve, F., Ghinea, N. & Scherrmann, J. M. CNS delivery via adsorptive transcytosis. *AAPS J* **10**, 455-472, doi:10.1208/s12248-008-9055-2 (2008).

12 Lajoie, J. M. & Shusta, E. V. Targeting receptor-mediated transport for delivery of biologics across the blood-brain barrier. *Annu Rev Pharmacol Toxicol* **55**, 613-631, doi:10.1146/annurev-pharmtox-010814-124852 (2015).

13 Guerin, C., Olivi, A., Weingart, J. D., Lawson, H. C. & Brem, H. Recent advances in brain tumor therapy: local intracerebral drug delivery by polymers. *Invest New Drugs* **22**, 27-37, doi:10.1023/b:drug.0000006172.65135.3e (2004).

14 Perry, J., Chambers, A., Spithoff, K. & Laperriere, N. Gliadel wafers in the treatment of malignant glioma: a systematic review. *Curr Oncol* **14**, 189-194, doi:10.3747/co.2007.147 (2007).

15 Kuramitsu, S., Motomura, K., Natsume, A. & Wakabayashi, T. Double-edged Sword in the Placement of Carmustine (BCNU) Wafers along the Eloquent Area: A Case Report. *NMC Case Rep J* **2**, 40-45, doi:10.2176/nmccrj.2014-0025 (2015).

16 Cook, A. M., Mieure, K. D., Owen, R. D., Pesaturo, A. B. & Hatton, J. Intracerebroventricular administration of drugs. *Pharmacotherapy* **29**, 832-845, doi:10.1592/phco.29.7.832 (2009).

17 Hladky, S. B. & Barrand, M. A. Elimination of substances from the brain parenchyma: efflux via perivascular pathways and via the blood-brain barrier. *Fluids Barriers CNS* **15**, 30, doi:10.1186/s12987-018-0113-6 (2018).

18 Mehta, A. M., Sonabend, A. M. & Bruce, J. N. Convection-Enhanced Delivery. *Neurotherapeutics* **14**, 358-371, doi:10.1007/s13311-017-0520-4 (2017).

19 Rapoport, S. I. Osmotic opening of the blood-brain barrier: principles, mechanism, and therapeutic applications. *Cell Mol Neurobiol* **20**, 217-230, doi:10.1023/a:1007049806660 (2000).

20 Piper, R. J., Hughes, M. A., Moran, C. M. & Kandasamy, J. Focused ultrasound as a non-invasive intervention for neurological disease: a review. *Br J Neurosurg* **30**, 286-293, doi:10.3109/02688697.2016.1173189 (2016).
21 Gorick, C. M. *et al.* Sonoselective transfection of cerebral vasculature without blood-brain barrier disruption. *Proc Natl Acad Sci U S A* **117**, 5644-5654, doi:10.1073/pnas.1914595117 (2020).
22 Mainprize, T. *et al.* Blood-Brain Barrier Opening in Primary Brain Tumors with Non-invasive MR-Guided Focused Ultrasound: A Clinical Safety and Feasibility Study. *Sci Rep* **9**, 321, doi:10.1038/s41598-018-36340-0 (2019).
23 Kovacs, Z. I. *et al.* Disrupting the blood-brain barrier by focused ultrasound induces sterile inflammation. *Proc Natl Acad Sci U S A* **114**, E75-E84, doi:10.1073/pnas.1614777114 (2017).
24 Kievit, F. M. & Zhang, M. Cancer nanotheranostics: improving imaging and therapy by targeted delivery across biological barriers. *Adv Mater* **23**, H217-247, doi:10.1002/adma.201102313 (2011).
25 Pulgar, V. M. Transcytosis to Cross the Blood Brain Barrier, New Advancements and Challenges. *Front Neurosci* **12**, 1019, doi:10.3389/fnins.2018.01019 (2018).
26 Pardridge, W. M. Molecular Trojan horses for blood-brain barrier drug delivery. *Curr Opin Pharmacol* **6**, 494-500, doi:10.1016/j.coph.2006.06.001 (2006).
27 Staquicini, F. I. *et al.* Systemic combinatorial peptide selection yields a non-canonical iron-mimicry mechanism for targeting tumors in a mouse model of human glioblastoma. *J Clin Invest* **121**, 161-173, doi:10.1172/JCI44798 (2011).
28 Choudhury, H. *et al.* Transferrin receptors-targeting nanocarriers for efficient targeted delivery and transcytosis of drugs into the brain tumors: a review of recent advancements and emerging trends. *Drug Deliv Transl Res* **8**, 1545-1563, doi:10.1007/s13346-018-0552-2 (2018).
29 Lao, B. J. *et al.* Inhibition of transferrin iron release increases in vitro drug carrier efficacy. *J Control Release* **117**, 403-412, doi:10.1016/j.jconrel.2006.12.001 (2007).
30 Widera, A., Norouziyan, F. & Shen, W. C. Mechanisms of TfR-mediated transcytosis and sorting in epithelial cells and applications toward drug delivery. *Adv Drug Deliv Rev* **55**, 1439-1466, doi:10.1016/j.addr.2003.07.004 (2003).
31 Moos, T. & Morgan, E. H. Restricted transport of anti-transferrin receptor antibody (OX26) through the blood-brain barrier in the rat. *J Neurochem* **79**, 119-129, doi:10.1046/j.1471-4159.2001.00541.x (2001).
32 Haqqani, A. S. *et al.* Endosomal trafficking regulates receptor-mediated transcytosis of antibodies across the blood brain barrier. *J Cereb Blood Flow Metab* **38**, 727-740, doi:10.1177/0271678X17740031 (2018).
33 Paterson, J. & Webster, C. I. Exploiting transferrin receptor for delivering drugs across the blood-brain barrier. *Drug Discov Today Technol* **20**, 49-52, doi:10.1016/j.ddtec.2016.07.009 (2016).
34 Friden, P. M. *et al.* Anti-transferrin receptor antibody and antibody-drug conjugates cross the blood-brain barrier. *Proc Natl Acad Sci U S A* **88**, 4771-4775, doi:10.1073/pnas.88.11.4771 (1991).
35 Yu, Y. J. *et al.* Boosting brain uptake of a therapeutic antibody by reducing its affinity for a transcytosis target. *Sci Transl Med* **3**, 84ra44, doi:10.1126/scitranslmed.3002230 (2011).
36 Bien-Ly, N. *et al.* Transferrin receptor (TfR) trafficking determines brain uptake of TfR antibody affinity variants. *J Exp Med* **211**, 233-244, doi:10.1084/jem.20131660 (2014).
37 Niewoehner, J. *et al.* Increased brain penetration and potency of a therapeutic antibody using a monovalent molecular shuttle. *Neuron* **81**, 49-60, doi:10.1016/j.neuron.2013.10.061 (2014).
38 Wiley, D. T., Webster, P., Gale, A. & Davis, M. E. Transcytosis and brain uptake of transferrin-containing nanoparticles by tuning avidity to transferrin receptor. *P Natl Acad Sci USA* **110**, 8662-8667, doi:10.1073/pnas.1307152110 (2013).
39 Clark, A. J. & Davis, M. E. Increased brain uptake of targeted nanoparticles by adding an acid-cleavable linkage between transferrin and the nanoparticle core. *P Natl Acad Sci USA* **112**, 12486-12491, doi:10.1073/pnas.1517048112 (2015).
40 Wyatt, E. A. & Davis, M. E. Method of establishing breast cancer brain metastases affects brain uptake and efficacy of targeted, therapeutic nanoparticles. *Bioeng Transl Med* **4**, 30-37, doi:10.1002/btm2.10108 (2019).
41 Ruan, S. *et al.* Acid-Responsive Transferrin Dissociation and GLUT Mediated Exocytosis for Increased Blood-Brain Barrier Transcytosis and Programmed Glioma Targeting Delivery. *Advanced Functional Materials* **28**, doi:10.1002/adfm.201802227 (2018).

Chapter 9

Delivering nanodrugs across the blood-brain barrier for glioblastoma treatment

Meilyn Sylvestre, Shixian Lv, Anisa Ashraf, Drew Sellers, Alexander Prossnitz, and Suzie Pun

9.1 Abstract

Glioblastoma remains one of the most difficult cancers to treat and is largely uncurable. Treatment options are limited by the nearly impermeable blood brain barrier (BBB), the most critical obstacle for intravenous drug delivery to brain tumors. Receptor mediated transcytosis is an emerging strategy to cross the BBB as it is non-invasive and utilizes endogenous pathways. In particular, the transferrin pathway has been extensively investigated for drug delivery to the brain. Here, we sought to use pH-sensitive, transferrin-targeted nanoparticles to facilitate transcytosis across the BBB. Particles were engineered with acid-cleavable linkers between transferrin and the nanoparticle core, with the goal of enabling the nanoparticle to diffuse into the parenchyma. Instead, we demonstrated that targeted, non-labile nanoparticles showed the highest accumulation in brains, yet remained trapped in the vasculature. Thus, future work will iterate on this nanoparticle formulation to include (*i*) different targeting ligands or (*ii*) pH-buffering polymers to block endosomal acidification.

9.2 Introduction

Despite significant advances in cancer therapy, brain cancer patients still face a poor five-year survival rate of 33%.[1] Gliomas and glioblastomas have a particularly low survival rate due to their highly invasive nature, high rate of tumor recurrence, and the blood-brain barrier (BBB), a physical barrier that excludes virtually all (> 98%) molecular and macromolecular therapeutics from entering the brain. Crossing this barrier is the greatest clinical challenge to developing successful brain cancer therapies.[2] Brain tumors (primary and secondary) are nearly inaccessible because they exhibit minimal BBB disruption.[3] Strategies that physically disrupt the tight junctions of the BBB have minimal clinical utility due to the high risk of a burst influx of drug and toxins.[4] Direct intracerebroventricular injection into the cerebral spinal fluid (CSF) can bypass the BBB, but the

procedure poses a high risk for infection and 98-99% of the drug is lost to the blood because of rapid CSF bulk flow and CSF turnover.[5,6] As such, there is a desperate need to develop a non-invasive therapy that can actively traverse the BBB.[7]

Receptor-mediated transcytosis (RMT) has emerged as a promising drug delivery strategy to cross the BBB because it takes advantage of endogenous uptake pathways of the brain while leaving the integrity of the BBB intact.[3] In the brain, RMT enables the transport of macromolecules that would otherwise be excluded.[5] RMT is highly specific, and occurs when proteins engage with and are endocytosed by receptors on the luminal (blood) side of the BBB, move through endothelial cytoplasm, and are exocytosed on the abluminal (brain) side, where they diffuse through the parenchyma.[8] Commonly leveraged receptors of RMT are the transferrin receptor (TfR), LRP lipoprotein receptor, and insulin receptor.

TfR is an attractive receptor to mediate transcytosis through the BBB because it is highly expressed on the luminal side of the BBB endothelium and facilitates one-way transport from the blood to brain, unlike the LRP lipoprotein receptor which is highly expressed on both BBB endothelium and in the brain.[2] Insulin-targeting can dysregulate insulin metabolism and risks inducing hypoglycemia.[8,9] Importantly, transferrin-conjugates have an established track-record to deliver therapeutic payloads and achieve improved drug delivery and survival in animals.[10-12] In the context of the BBB, transferrin (Tf) can undergo three fates after binding to TfR: (*i*) recycling, (*ii*) degradation, or (*iii*) transcytosis into the brain parenchyma. In contrast, constructs that display multivalent Tf with high receptor binding avidity are primarily directed to lysosomal degradation.[13,14] Because of lysosomal sequestration, less than 1% of the injected dose is actually delivered to tumor cells.[15] Efforts to improve TfR-mediated delivery to the brain include engineered mouse or rat anti-TfR antibodies that undergo altered endocytic sorting; however, these modifications are highly species-dependent, limiting clinical translation in humans.[16,17] Furthermore, native transferrin has a greater ability to cross the BBB than antibody counterparts.[18] Because Tf-modified carriers with reduced avidity demonstrate the greatest ability to traverse the BBB, acid-cleavable Tf constructs have been synthesized, which enabled high-avidity particles to enter the brain followed by shedding of Tf from the carriers at endosomal pH, freeing the carrier

for diffusion into the parenchyma.[19] Despite these important discoveries, delivery across the BBB into the parenchyma remains a major limitation in developing effective brain therapies.

Given the pre-clinical success of transferrin to penetrate the BBB, we sought to direct intracellular sorting of Tf-functionalized drug carriers toward transcytosis across endothelial cells of the BBB. We report preliminary results investigating brain accumulation and transcytosis of acid-labile carriers. To our surprise, the non-labile carriers showed the highest brain accumulation. However, fluorescent microscopy revealed that these carriers remained trapped in the vasculature and did not cross the BBB. We also demonstrate preliminary results establishing a brain tumor model enabling non-invasive tumor burden monitoring.

9.3 Results

9.3.1 Synthesis of targeted pro-drug nanoparticles

We synthesized polyhydroxyethylmethacrylate (pHPMA) nanoparticles incorporating an acid-labile linker with both camptothecin (CPT) and transferrin through a beta-thiopropionate and boronic acid-diol complexation, respectively. These micelles self-assembled with a hydrophobic CPT core and vicinal diols on the surface. CPT was chosen to validate particle efficacy, compared to studies by Wyatt and Davis.[19] The acid-cleavable moiety between Tf and the nanoparticle core has been shown to facilitate transcytosis and diffusion through the brain parenchyma (**Figure 9.1**). We employed transferrin as targeting ligands to increase likelihood of transcytosis, as it has an enhanced likelihood of transcytosis compared to anti-transferrin receptor antibodies. Moreover, using the native transferrin protein avoids the anti-drug antibody response generated against the Fc-region of antibodies. Unlike anti-transferrin receptor antibodies, the human transferrin protein demonstrates species cross-reactivity in mice and non-human primates, lending this technology toward clinical applications.

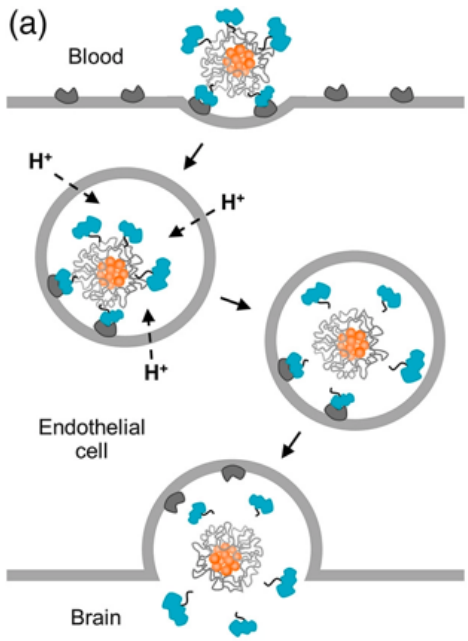

***Figure 9.1**: Schematic of acid-cleavable transferrin nanoparticles. Tf-targeted nanoparticles bind to the TfR and trigger internalization. As endosomal pH drops, Tf is cleaved from the nanoparticle core. Upon fusion of the endosome with the abluminal (brain) side of the cell, the nanoparticles are unbound and free to diffuse into the parenchyma. Reprinted with permission under the Creative Commons license (https://creativecommons.org/licenses/by/4.0/) from Bioeng Transl Med Volume 4:30-37 2018.*[19]

First, the CPT pro-drugs were synthesized by conjugating CPT with a beta-thiopropionate linkage (SCPT). This pH-sensitive linker degrades at low pH in order to rapidly release its chemotherapeutic payload.[21,22] SCPT was then conjugated to the pHPMA polymer. pHPMA-CPT was then reacted with succinic anhydride to induce carboxyl group formation for further dopamine conjugation (P-CPT-SA) (**Figure 9.2**). Human holo-transferrin was coupled with PBA via EDC NHS (Tf-PBA) and was then reacted with the catechol groups on pHPMA-CPT, forming a boronic ester linker. The resulting boronic esters are pH-sensitive, enabling transferrin to decouple from the nanoparticle at endosomal pH 5-6.[19,23] Additionally, boronic esters are readily reacted with diols and are stable in aqueous conditions. Control particles were synthesized through direct Tf conjugation with P-CPT-SA via EDC NHS (Tf-amide) (**Figure S9.1**). Untargeted particles with (non-Tf-Dop) and without (non-Tf-COOH) dopamine were allowed to self-assemble directly in aqueous conditions. Nanoparticles were fluorescently labeled with a Cy5 fluorophore via EDC

NHS reaction. Polymer structure was validated by ^{1}H NMR (**Figure S9.2**). Drug loading (16%) was evaluated by UV spectroscopy (**Figure S9.3**) and nanoparticle size, measured by dynamic light scattering, was determined to be around 60 nm (**Figure S9.4**).

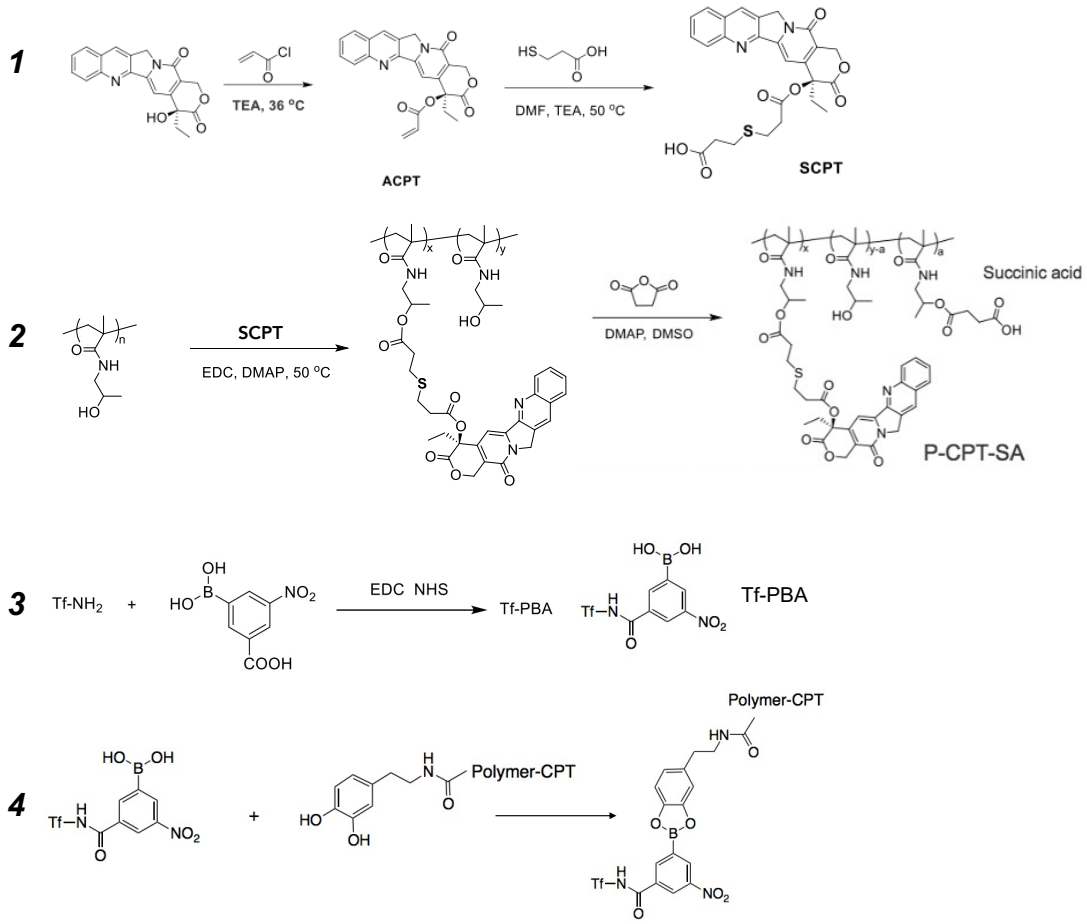

Figure 9.2: *Schematic of synthesis of particles. An acid-labile beta-thiopropionate bond was introduced to CPT (SCPT). This CPT pro-drug was then reacted with pHPMA, succinic acid, and dopamine for subsequent conjugation with Tf-PBA. The resulting nanoparticles employed two pH-sensitive chemistries to facilitate drug release and Tf-decoupling at endosomal pH.*

9.3.2 Development of transcytosis assay

We screened nanoparticle transcytosis *in vitro* using a transwell assay, an artificial model of the BBB, either as a single-cell culture or dual co-culture. In this model, cells are grown into monolayers on a membrane insert; here, we used a murine brain endothelial bEnd.3 cell line. Cells were cultured until monolayers formed, as indicated by tight junction integrity reaching a transepithelial/transendothelial electrical resistance (TEER) value above 30 Ωcm^2. Fluorescently-

labeled substrates are then added to the top (apical) compartment of the model and transport into the bottom (basal) compartment is evaluated. First, we optimized the assay using only bEnd.3 cells to ensure we could reproducibly make a model with tight junctions (**Figure 9.3Ai**). We plated bEnd.3 at indicated cell number, monitored TEER growth over time, and determined that a number of 75k or more cells are necessary to achieve a TEER of 30 $\Omega*cm^2$ (**Figure 9.3B**). The model was validated by assessing transcytosis of holo-Tf, apo-Tf, and BSA (**Figure S9.5A**). As expected, iron-bound holo-Tf crossed the monolayer, while iron-deficient apo-Tf and BSA had minimal transport. Next, we developed a co-culture model using bEnd.3 cells and primary murine astrocytes (**Figure 9.3Aii-iii**). Compared to a single cell mode, a two cell co-culture models offers greater barrier strength, exhibited by higher TEER and lower permeability, contributing toward a more robust model of the BBB.[24] We then incorporated astrocytes into our transwell model as they play a role in inducing and maintaining endothelial BBB properties and closely associate with endothelial cells.[25] Furthermore, astrocytes are the most abundant glial cell in the brain and have been positively correlated with BBB integrity *in vivo*.[26] Neural progenitor cells (NPCs) were plated on laminin-coated transwells for 4 days in astrocyte-differentiation media. NPCs were plated on either the apical or basal compartment at varied cell density. On day 5, bEnd.3 cells were plated onto the apical compartment, and TEER value was measured on days 11, 14, and 17 (**Figure 9.3C)**. From this study, we determined that astrocytes cultured on the basal-facing compartment at a density of 90-100k were able to achieve barrier integrity.

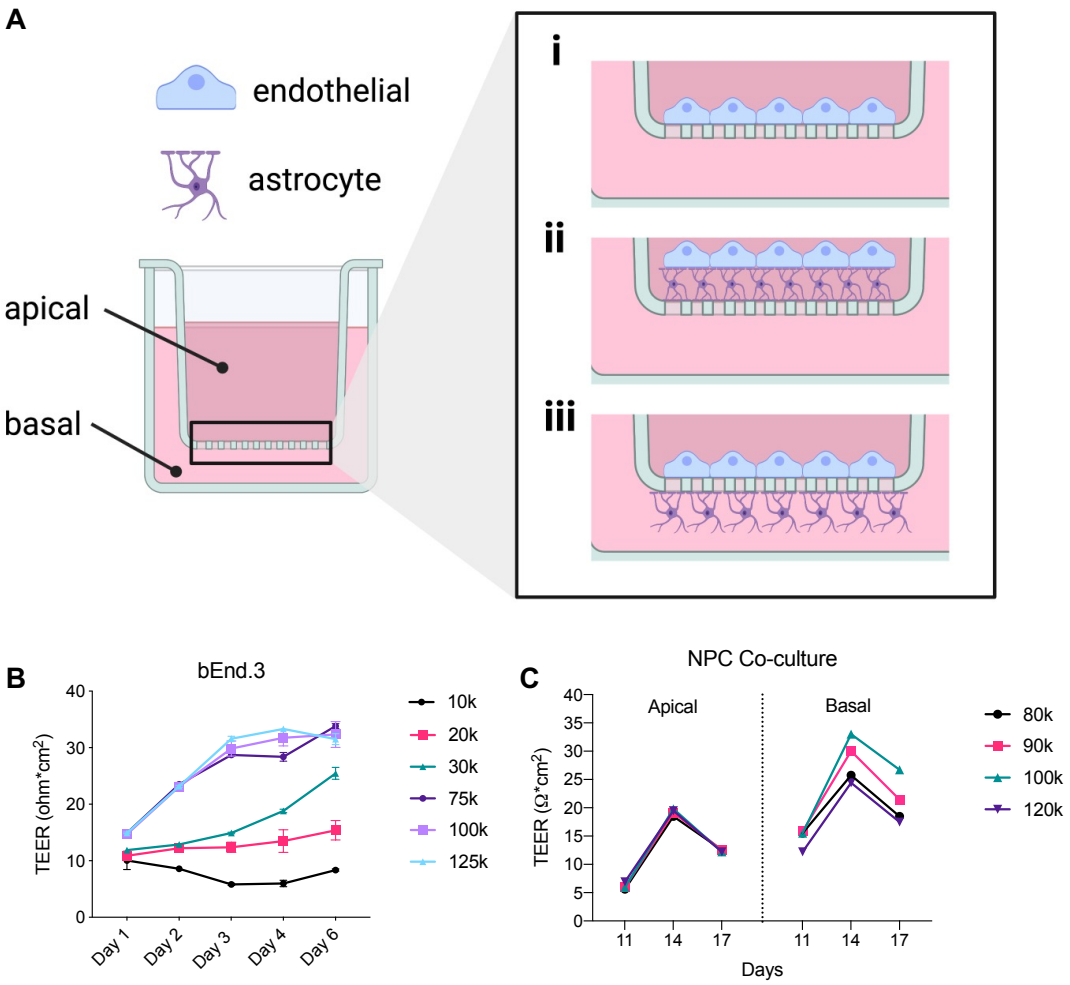

Figure 9.3*: Development of a transwell assay. A) Schematic of the transwells used to model the BBB, as either (i) a single bEnd.3 monolayer culture, or a co-culture of astrocytes and bEnd.3 cells, with astrocytes plated on the (ii) apical compartment or (iii) basal compartments. B) bEnd.3 cells were cultured at different densities (10, 20, 30, 75, 100, and 125k) on transwell membranes and TEER was monitored. Monolayer integrity was determined when TEER > 30 Ω*cm². C) To develop a co-culture model of bEnd.3 and astrocytes, astrocytes were cultured at different densities (80, 90, 100, or 120k) on either the apical or basal-facing side of the transwell.*

9.3.3 Brain accumulation of nanoparticles

We compared the accumulation of targeted, acid-labile nanoparticles with untargeted and non-labile particle in the brains of normal mice. We used normal mice to assess accumulation and transcytosis due to the retained integrity of the blood-brain barrier; if particles could efficiently

cross into the parenchyma of normal mice, we posited that they would also be effective in tumor-bearing mice. Mice were injected intravenously (IV) with targeted acid labile (Tf-PBA), targeted non-labile (Tf-amide), and untargeted control particles (non-Tf-Dop and non-Tf-COOH, respectively) at 5 mg CPT/kg. After 1 and 2 hours, mice were perfused with PBS and major organs were imaged for fluorescence. Brains were homogenized in RIPA buffer and supernatant was assessed for nanoparticle content on a fluorescent plate reader; fluorescence was normalized to protein content. The targeted, non-labile particles (Tf-amide) demonstrated the highest brain accumulation over acid-labile (Tf-PBA) and untargeted controls (non-Tf-COOH) (**Figure 9.4A-B**). As expected, all particles showed high accumulation in the lungs, liver, and kidneys. Because targeted, non-labile particles showed the most accumulation, we characterized transport of these formulations. We assessed nanoparticle persistence by injecting mice with particles (5 mg/kg) and assessing nanoparticle content at 2, 4, 8, 12, and 24 hours after injection (**Figure 9.4C**). Particles rapidly accumulated in the brain in the first two hours after injection and persisted for over 24 hours. We next repeated the study in biological triplicate at 1, 2 and 4 hours after injection (**Figure 9.4D**). However, we obtained inconsistent results with unexpectedly high accumulation by non-targeted controls. One possible explanation for the high variability is instability of the particulate formulations. Future work will assess nanoparticle stability over time. Lastly, we sought to visualize nanoparticle transport in the brain with fluorescent microscopy (**Figure 9.3E**). Cy5-labeled Tf-amide nanoparticles were injected IV and after 2 hours, mice were perfused and brains were removed. Brains were stained for endothelial cells and astrocytes with anti-CD31 and anti-GFAP antibodies, respectively. We stained for endothelial cells to locate blood vessels and assessed astrocyte staining in the parenchyma. Overall, nanoparticles accumulated in the blood vessels but were not transported across the BBB.

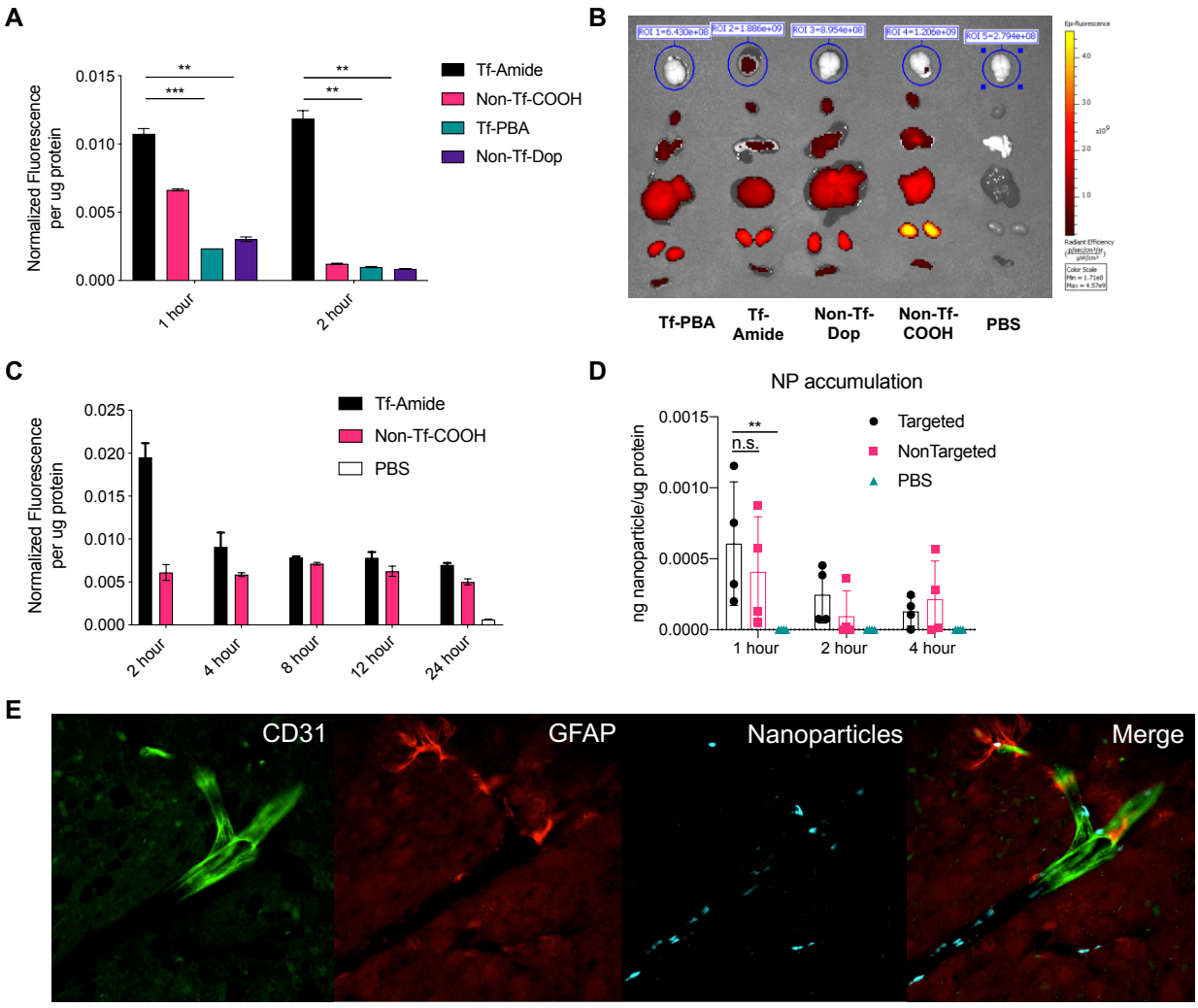

Figure 9.4: Nanoparticle accumulation in normal mice. A) Nanoparticles (5 mg/kg) were injected and brains were removed after 1 and 2 hours. Brains were homogenized and nanoparticle fluorescence was normalized to protein content. B) Brains and organs were imaged on an IVIS Xenogen to qualitatively assess fluorescent nanoparticle accumulation. C) Nanoparticle persistence was at 2, 4, 8, 12, and 24 hours after injection. D) Nanoparticle accumulation was assessed in biological triplicate. E) Mice were injected with Cy5-labeled nanoparticles and brains were sectioned and stained for endothelial cells (anti-CD31) and astrocytes (anti-GFAP).

9.3.4 Development of brain tumor model

To assess tumor reduction of our nanoparticles, we sought to develop a brain model that would enable us to monitor tumor burden continuously and non-invasively. Thus, we transduced DBTRG-05MG cells, immortalized human glioblastoma cells, to express GFP and luciferase

(**Figure 9.5A-C**). GFP expression enables easy differentiation of tumor (GFP^+) from healthy (GFP^-) cells in the brain to visualize tumor burden via fluorescent imaging. Luciferase processes its substrate, D-luciferin, to produce a sensitive, bright signal that is only emitted by cells that express luciferase.[27] Furthermore, D-luciferin readily crosses the BBB. After implanting mouse brains with luciferase-expressing cells, tumor burden was monitored by bioluminescent live-animal imaging (Xenogen). As Xenogen is mostly semi-quantitative, we also quantified tumor burden in brains *ex vivo* by luciferase reporter assay. We used nonobese diabetic-severe combined immunodeficient (NOD-SCID) mice because of their defects in innate and adaptive immunity, which make them better recipients for human tumor transplantation.[28] Tumor cells were implanted in the striatum (1 mm anterior to bregma, 1 mm lateral to midline, 2 mm depth) and tumor burden was monitored weekly by live-animal bioluminescent imaging. Tumor-bearing mice exhibited increased luciferase activity over time, suggesting tumor burden was increasing (**Figure 9.5D**). Next, we quantified tumor burden in the ipsilateral (tumor-implanted) and contra-lateral (opposite) hemispheres of brains from mice each week to assess luciferase activity per μg of tissue (**Figure 9.5E**). We demonstrate that all implanted mice exhibited increasing tumor burden over time, as evidenced by both Xenogen and luciferase assay. Tumors primary stayed within the implanted ipsilateral hemisphere, but by week 4, some tumors expanded into the contralateral hemisphere. Finally, we visualized tumor growth by fluorescent microscopy, staining for cell nuclei (DAPI, blue), blood vessels (CD31, cyan), and microglia (Iba1, red); tumors cell expressed GFP (green) (**Figure 9.5F**). We observed the tumor increasing in area, as well as increasing microglia (macrophage) infiltration. At later time points, we also observed tumor cell migration to the edges of brain slices, suggesting the start of tumor metastasis.

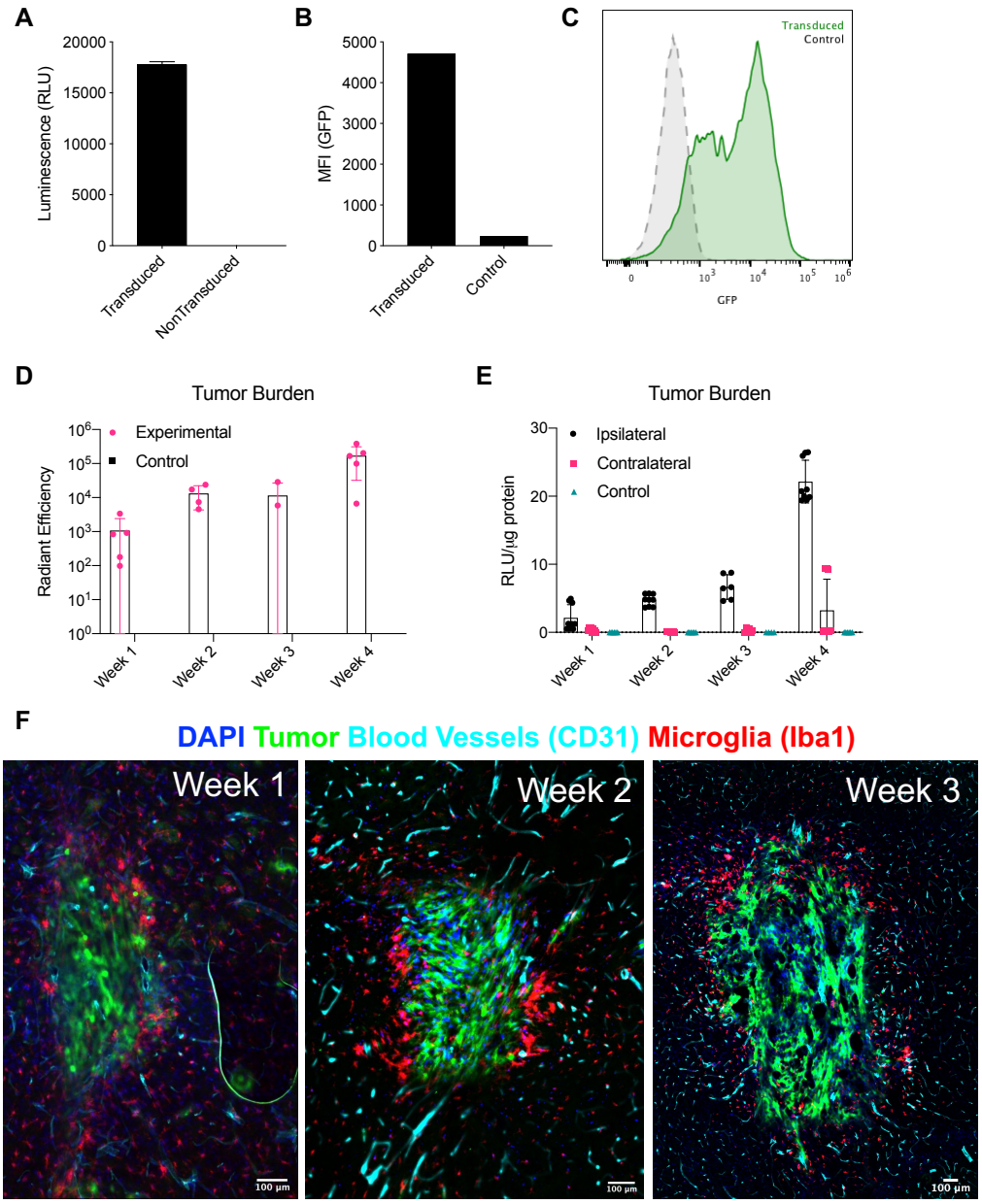

Figure 9.5*: Measuring tumor burden in vivo. A-C) Transformed DBTRG cells express luciferase (A) and GFP (B-C). D) Quantification of tumor burden via live animal imaging (Xenogen) over 4 weeks after implantation. E) Quantification of luciferase activity in ipsilateral and contralateral hemispheres of the brain. F) Fluorescent microscopy of brains from tumor-bearing mice.*

9.3.5 Tumor reduction with targeted nanoparticles

After developing the tumor model, we investigated the anti-tumor efficacy of targeted and non-targeted nanoparticles *in vivo*. Although there was some variability with brain accumulation of

particles, we decided to pursue these particles based on observed trends, although not statistically significant. Furthermore, despite lack of transcytosis into the parenchyma, we hypothesized that particles could accumulate in the vasculature near the tumor and release drug that could subsequently cross the BBB and enter the tumor. This has been previously reported with transferrin-targeted liposomes, which increased cargo uptake in the endothelium and subsequent cargo transport into the brain.[20] Brain tumors were implanted in NSG mice and mice were injected IV with (*i*) PBS, (*ii*) irinotecan 10 mg/kg, (*iii*) non-targeted NPs at 10 mg CPT/kg, or (*iv*) targeted NPs at 10 mg CPT/kg for 3 injections (**Figure 9.6A**). Irinotecan is the soluble analogue of camptothecin and was used as a free drug control. During this round of implantations, 9 mice died before the initial treatment. Mice exhibited severe bloating and constipation; upon autopsy, we confirmed that the mouse intestines were full of feces. We posited that the brain tumors could be interfering with the autonomic nervous system and ability to defecate, but this was not validated. This issue continued to affect all mice throughout the first two weeks following implantation, but surviving mice recovered after this time period.

Tumor burden was monitored throughout the study via bioluminescence (**Figure 9.6B**) and final tumor burden at the end of the study (day 35 post-implantation) was quantified by homogenizing brains and assessing luciferase activity (**Figure 9.6C**). While cohorts receiving targeted NPs had the lowest average tumor burden compared to PBS and irinotecan cohorts, this was not statistically significant. Furthermore, no mice from the nontargeted NP group survived (**Figure 9.6D**); this formulation was significantly more toxic than free drug or targeted NPs, as exhibited by severe weight loss of mice in this group (**Figure 9.6E**). Overall, targeted nanoparticles did not extend survival compared to irinotecan or PBS treatment.

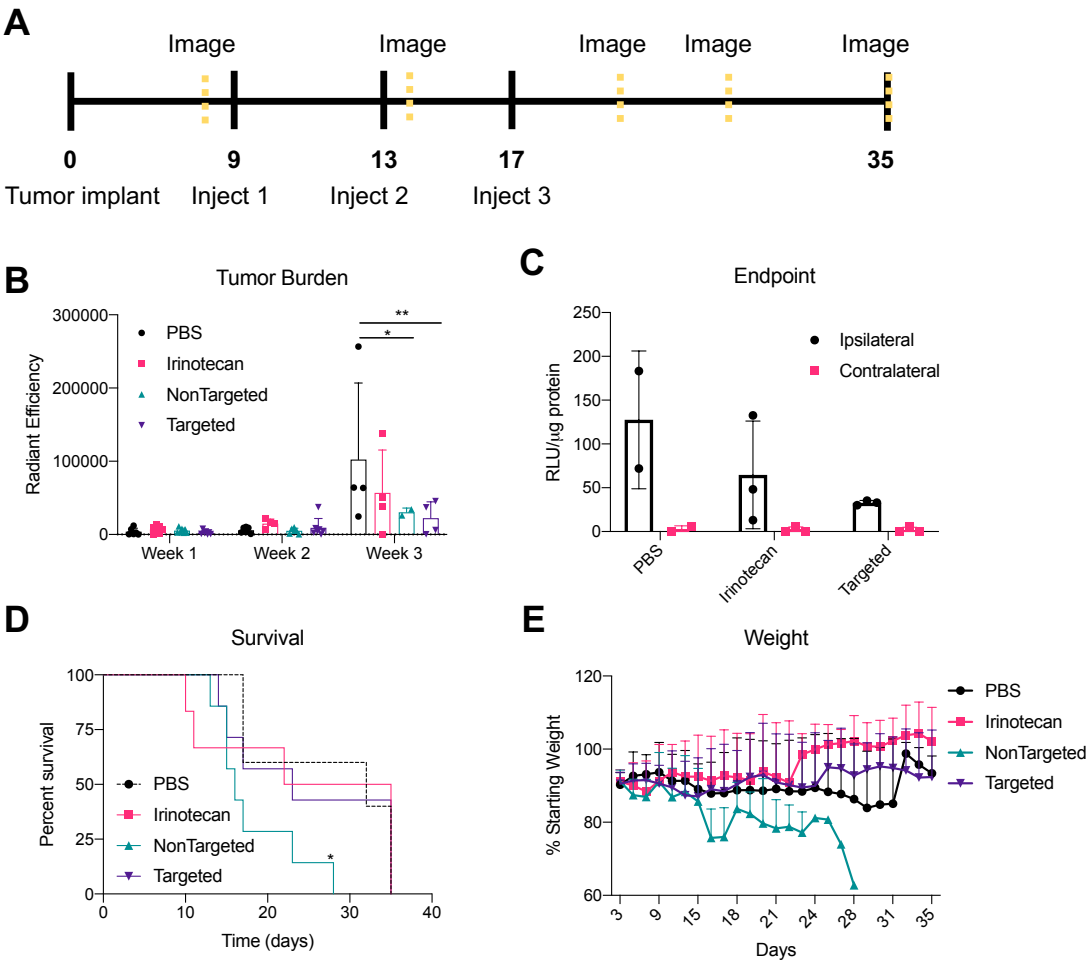

Figure 9.6: Anti-tumor efficacy of particles in vivo. A) Overview of study design. B) Tumor burden evaluated by live animal bioluminescent imaging. C) Tumor burden quantified in ipsilateral and contralateral hemispheres of homogenized brains. D) Survival of mice treated with PBS, irinotecan, nontargeted, or targeted nanoparticles. E) Weight of mice throughout the duration of the study. (n = 5-7 mice/group)

9.4 Discussion

Here, we developed nanoparticles with a Tf-targeting ligand and CPT payload with the goal of transporting therapeutics past the BBB. We incorporated an acid-labile linker between Tf and the nanoparticle core based on prior research suggesting that cleavage at endosomal pH facilitates transport through the BBB and into the brain.[18,19] We first developed a single-cell transwell model to simulate the BBB, and are working on developing a two-cell transwell model to include astrocytes. Preliminary assessment of nanoparticle biodistribution demonstrated that targeted, non-

labile particles had higher accumulation than targeted, acid-labile particles, but this work was not able to be replicated. Furthermore, fluorescent microscopy revelated that these particles remained trapped in the vasculature and did not cross into the parenchyma. Despite this lack of transport into the brain, we hypothesized that particle accumulation in the brain vasculature could enhance drug transport into the brain. When applied to an *in vivo* glioblastoma model, mice treated with targeted nanoparticles had a slight reduction in tumor burden, but this was not statistically significant; additionally, there was no difference in survival between treated and untreated mice.

We initially detected significantly increased accumulation of Tf-amide nanoparticles, but when we sought to reproduce this study, we were not able to replicate our pilot results. We initially assumed that Tf instability prevented us from reproducing this study; however, when we repeated the accumulation studies again with freshly prepared particles, we were still unable to detect significantly higher Tf-amide brain accumulation. Non-targeted particles had a higher amount of accumulation, particularly at later time points, but targeted particles also had lower than expected accumulation. While we determined that particle stability was not the cause of decreased accumulation, we still have not identified the cause of our inconsistent results. The initial studies may have been an anomaly, but we observe that targeted particles follow trends suggesting they may have increased accumulation. Small differences between studies could precipitate these differences, such as variability in protein stock that result in variable Tf conjugation and valency. If the Tf valency is too high, then particle binding and uptake could be decreased due to steric hindrance.[7] Tuning the degree of protein attachment to the polymer could help overcome this issue, but we have not quantified the degree protein conjugation to the polymer, as this process is quite complex. Determining the polymer-to-protein ratio (PPR) is challenged by the large size and complexity of these conjugates, including the heterogeneity of the conjugates based on polymer polydispersity; multiplicity of conjugation sites; and randomness of protein conjugation to the polymer.[29] While several methods (e.g. size exclusion chromatography or mass spectroscopy) can provide some information of the PPR, these modes limited by biased ionization of conjugates with different PPRs and by the challenge of preserving noncovalent higher-order aggregates in a vacuum. A recent paper by Clardy et al. identified a method using multisignal sedimentation velocity analytical ultracentrifugation to quantify PPR.[29] In the future, we could apply a method such as this to determine and fine-tune PPR in order to enhance particle avidity and binding.

For targeted nanoparticles that showed enhanced brain accumulation, fluorescent microscopy revealed that particles remained trapped in the vasculature and did not enter the brain. This entrapment could be due to the lack of Tf dissociation in the endosome, preventing release of the nanoparticle from intracellular compartment. We did not section brains injected with the acid-labile particles. However, this study could be useful in the future to inform if the acid-labile Tf-conjugation improved transport into the brain. Perhaps the non-labile chemistry increased particle accumulation in the brain, but only the acid-labile particles possessed the ability to transcytose. These differences in accumulation could be attributed to differences in Tf conjugation, but we have not quantified Tf-conjugation, as discussed above.

Despite these inconsistencies, we evaluated the potential of these particles to reduce tumor burden *in vivo*. However, the study was complicated by both the unexpected toxicity of the brain tumors and the non-targeted nanoparticles. In the pilot tumor implant study, we characterized tumor growth over time and determined that mice experienced some intestinal blockage, but this occurred around week 3, when the tumor had progressed further. When we scaled up the study to compare efficacy of our particles, mice experienced these issues by the end of week one, post implantation. We were not able to find any reports documenting the symptoms mice presented after brain tumor implantation; but we hypothesized that mice were experiencing colonic dysmotility based on presentations of distended abdomen (severe bloating) and significantly reduced feces excretion. Correlation between traumatic brain injury and intestinal dysfunction has been established, although this does not explain why this dysfunction presented at different times (1 vs. 3 week post-implant) between studies.[30,31] Due to the accelerated disease progression in the second study, mice were treated with particles at an earlier time. Unfortunately, we did not detect any significant difference in survival between the targeted nanoparticle, free drug, or PBS-treated groups. The lack of efficacy of irinotecan suggests that the drug dose was insufficient, as irinotecan is currently administered for glioblastoma treatment.[32] Furthermore, the DBTRG tumor model may have been too aggressive for this drug to exert any detectable anti-tumor efficacy, and the use of an immunodeficient mouse model without functional T or B cells may have also hindered detectable efficacy. Irinotecan can induce immunogenic cell death (ICD) which can activate and recruit cytotoxic T cells; but NSG mice lack a functional adaptive immune responsive, further dampening any anti-tumor effects.[33] Lastly, nontargeted CPT nanoparticles were significantly more toxic than

other treatments, and no mice in this treatment cohort survived past week 4 post implantation and all mice exhibited extreme weight loss. This toxicity was unexpected, as we expected less uptake of particles without Tf and thus less off-target delivery of CPT. The lack of a targeting moiety left a free carboxylic acid that may contribute to increased toxicity, as carboxylic acid-containing drugs have been linked with idiosyncratic drug toxicity. Biodistribution studies could help explain the reason for increased toxicity, although the enhanced uptake and toxicity of nontargeted particles has been noted *in vitro* as well (**Figure S9.6**).

9.5 Methods

Nanoparticle synthesis. CPT prodrug was synthesized in two steps. In brief, CPT and triethylamine were mixed in dichloromethane (DCM) in an ice bath. Acryloyl chloride was added dropwise and the reaction mixture was stirred overnight. The intermediate CPT acrylate was purified by chromatography using pure ethyl acetate (yield 85%). CPT acrylate, mercaptopropionic acid, and triethylamine were mixed in tetrahydrofuran. After stirring at 50 ^{o}C for 14 h, SCPT was obtained and purified by chromatography in DCM/methanol (20:1) (yield 50%). The pHPMA (M_n 36 kDa, PDI 1.01) was synthesized via RAFT using 4-((((2-Carboxyethyl)thio)carbonothioyl)thio)-4-cyanopentanoic acid as a chain transfer agent (CTA).

SCPT was conjugated to pHPMA using EDC 4-dimethylaminopyridine (DMAP) agents. In brief, pHPMA, SCPT, EDC, and DMAP were dissolved in dry DMF, and the reaction was stirred overnight and then precipitated into dimethyl ether. The conjugate was purified by dialysis against DI water. SCPT, succinic anhydride, and DMAP were mixed in DMSO at 50 ^{o}C for 18 h to introduce the carboxyl groups on the side chain, and the obtained polymer-drug conjugate was further functionalized with dopamine using a typical EDC NHS reaction at a feeding ratio of polymer:dopamine of 1:100. The final polymer-drug conjugate was purified by dialysis against DI water to remove unconjugated dopamine.

Tf was modified with PBA following the reaction schematic shown in Figure 9.1. Targeted, acid-labile nanoparticles were prepared by complexation of Tf-PBA and dopamine-functionalized polymer-drug conjugate at the mass ratio of 1:10. Targeted, non-labile nanoparticles were prepared by reacting Tf with polymer-drug conjugates (modified with succinic acid on the side chain) via

EDC NHS at a mass ratio of Tf:polymer-drug conjugate of 1:10. Nanoparticles were purified by ultrafiltration against PBS.

Nanoparticle characterization. Polymers were characterized by ^{1}H NMR and UV spectroscopy. ^{1}H NMR spectra were recorded on a Bruker AV 300 in DMSO-d6. Drug loading was monitored by UV spectroscopy at 367 nm. Nanoparticle size was assessed via DLS.

Cell culture. bEnd.3 and DBTRG-05MG cells were obtained from ATCC and cultured in DMEM supplemented with 10% FBS and RPMI supplemented with 10% FBS and 1% PenStrep, respectively. DBTRG-05MG cells were transduced with recombinant luciferase (rFluc)-GFP lentivirus (System Biosciences) under Puromycin selection. rFluc expression was quantified via Luciferase Assay System (Promega) and GFP^+ expression was quantified via flow cytometry.

Transcytosis assay. bEnd.3 cells were cultured for 30 days prior to use. Cells (80k/well) were seeded in a 6.5 mm transwell insert (Corning) in a 24-well plate for 7 days. Transepithelial/transendothelial electrical resistance (TEER) was measured using an EndOhm Chamber with an EVOM2 (World Precision Instruments) to confirm monolayer integrity. Monolayer confluency was reached when TEER exceeded 30 Ω*cm^2. Particles were added to the apical well and concentration in the basal well was evaluated after 24 hours.

Animal studies. All animal studies were conducted in accordance with UW animal care guidelines and protocols approved by IACUC. Female Balb/c mice (6-8 weeks) were ordered from Charles River Laboratories. Particles were injected intravenous IV via tail vein injection at 5 mg CPT/kg. At indicated time points, mice were euthanized by drug overdose and perfused with 20 ml PBS. Brain, heart, lung, liver, spleen, and kidney were imaged on a IVIS Xenogen at ex/em 640/700 nm. For brain tumor studies, female NSG mice were anesthetized by intraperitoneal (IP) injection of Avertin (500 mg/kg). After craniotomy, a burr hole (1 mm diameter) was created on the right side of the skull and 2 ml of cells (50k in HBSS supplemented with 5% glucose and 5 mM EDTA) were injected (1 mm lateral midline, 1 mm anterior bregma, at 2 mm depth) using a 33 gauge Hamilton syringe.

Brain tissue processing. Brains were homogenized with a TissueRuptor II (Qiagen) in RIPA buffer (Fisher) supplemented with 150 U/ml DNAse-I (Fisher). Supernatant was collected and assessed for nanoparticles via fluorescent spectrophotometer (ex/em 633/666). Protein content was assessed using a Pierce BCA kit (Thermo), as indicated.

Imaging. Brains were fixed in 4% PFA and dehydrated in a sucrose gradient up to 30%. Brains were mounted in OCT and frozen at -80°C, prior to sectioning (Leica CM1850) into 30 mm slices at -19°C as floating sections. Sections were washed in TBS and blocked and permeabilized in 2% DKS + 2% BSA + 0.3% Triton-X in TBS for 1 hour. Sections were stained with anti-GFAP (1:500) and anti-CD31 (1:500) primary antibodies, washed in TBS-Tween 0.1%, and incubated with secondary antibodies (1:500) and DAPI (300 nM) for 1 hour. Sections were washed in TBS-Tween 0.1%, mounted onto slides, covered, and imaged with a Nikon Eclipse TI.

9.6 Acknowledgements.

This work was supported by NCI U54CA199090 and DOD W81XWH2010782. We thank Dr. Kim Woodrow for use of her microplate reader.

9.7 Conflicting Interests

The authors declare no competing interest

9.8 Supplemental Information

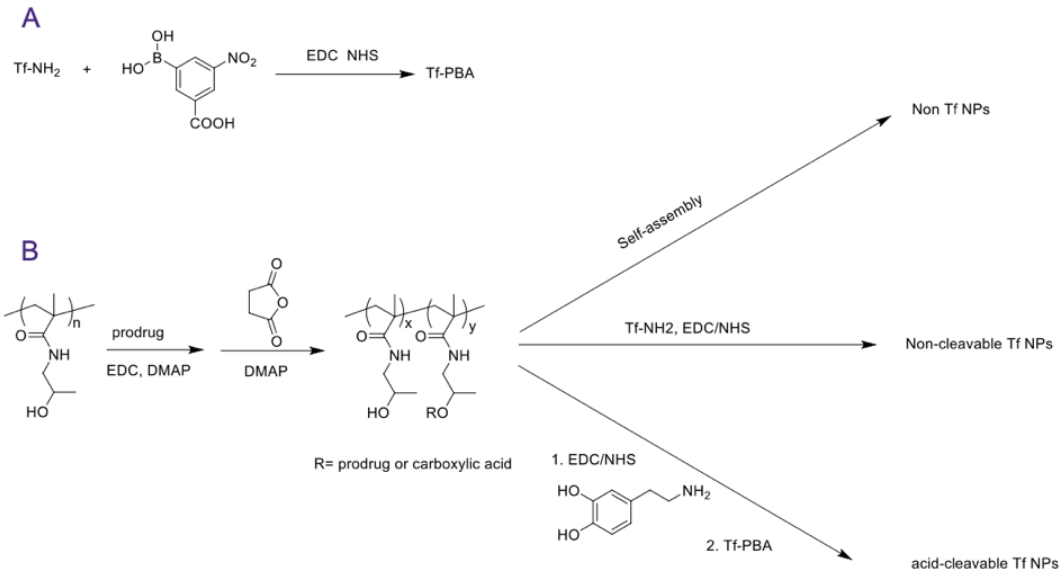

Figure S9.1: Schematic of targeted, acid-labile nanoparticle formulation and controls.

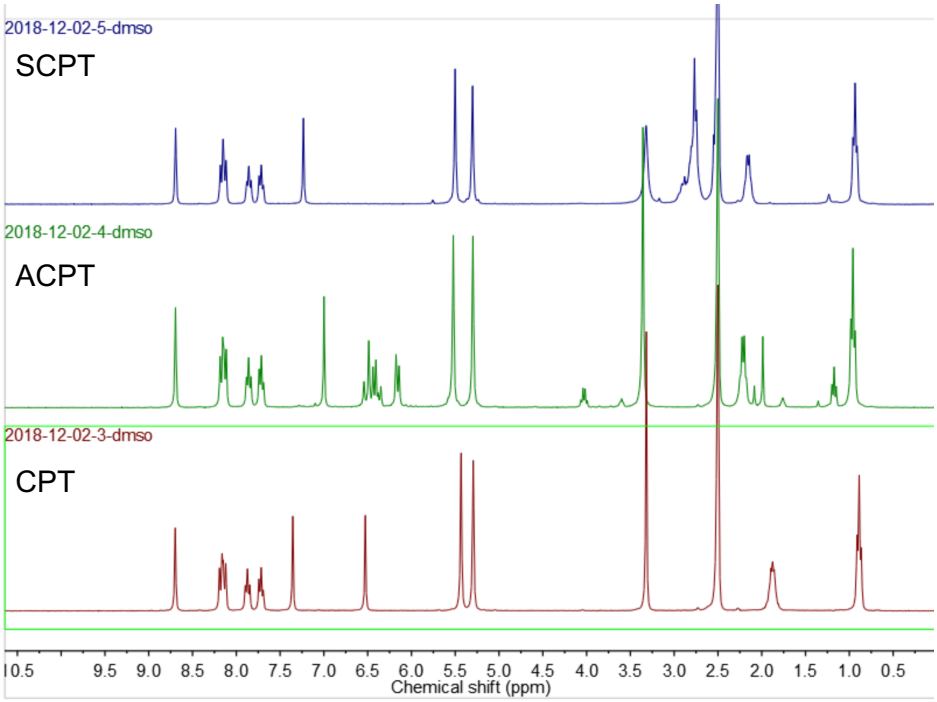

Figure S9.2: ^{1}H NMR spectra of SCTP, ACPT, and CPT in DMSO-d6.

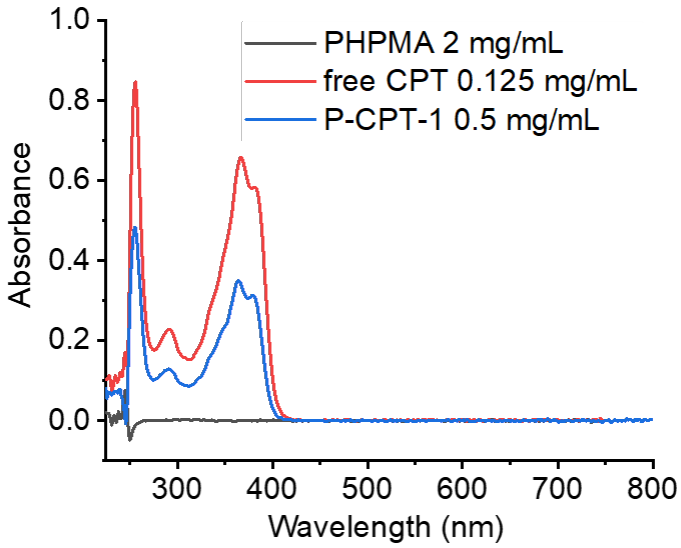

Prodrug feeding ratio	Obtained DLC%	Conjugation efficiency	PDI
20%	16.0	85.6%	0.34

Figure S9.3: UV spectroscopy was used to monitor CPT drug loading onto HPMA polymers.

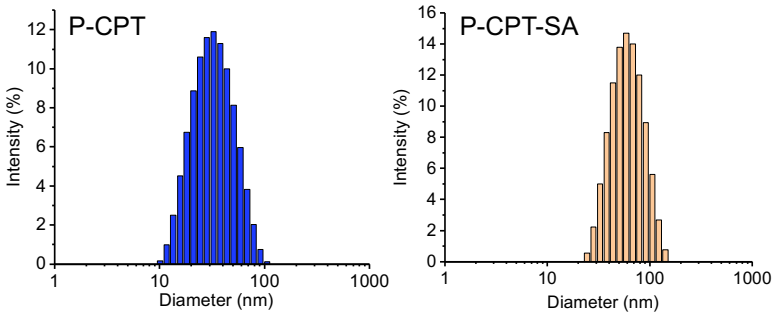

Polymer	Diameter (nm)	Zeta potential (mV)
P-CPT	29.2	-0.37
P-CPT-SA	60.7	-29.9

Figure S9.4: Nanoparticle size was assessed via DLS.

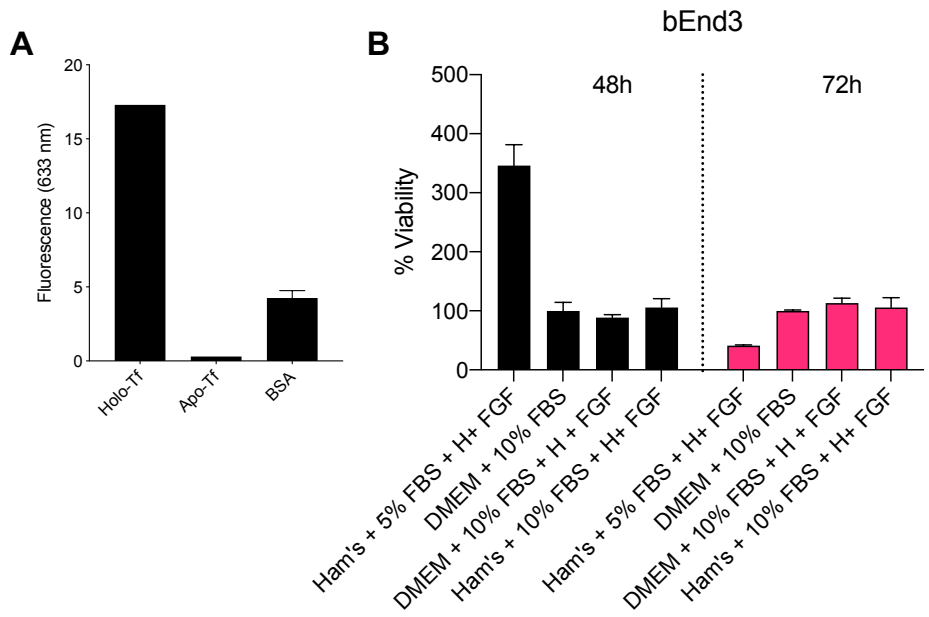

Figure S9.5: A) Confirmation of monolayer. Holo-tf should have increased transcytosis compared to apo-Tf or BSA. B) viability of bEnd3 cells in different medias at 48 and 72h timepoint.

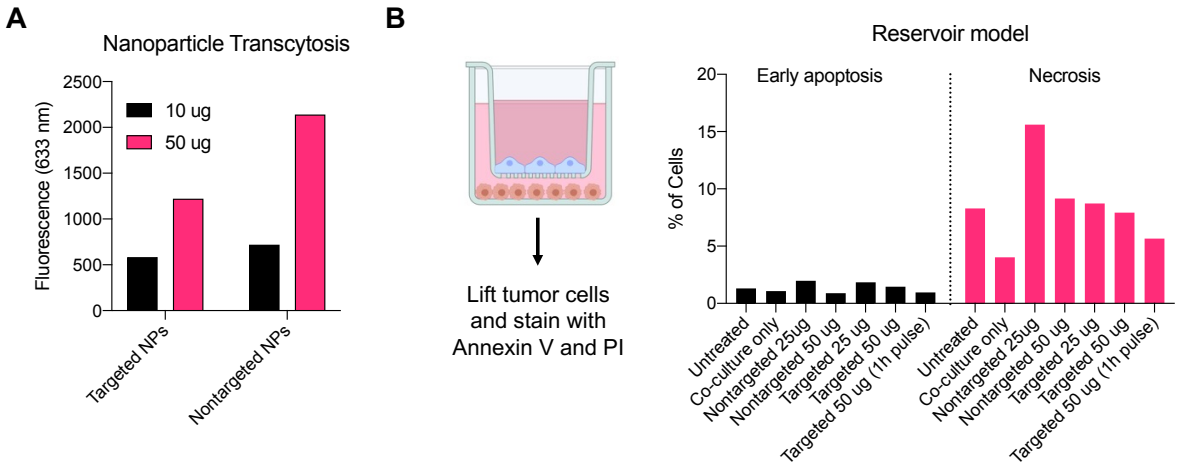

Figure S9.6: A) Transcytosis of Tf- and nontargeted nanoparticles. B) Testing the capacity of the bEnd.3 monolayer to act as a reservoir for nanoparticles. Particles were incubated with the monolayer for 1-2 hours, washed, and incubated with tumor cells for 24 hours. Tumor cells were lifted and stained for early apoptosis (Annexin V) and viability (PI).

References

1 Institute, N. N. C. *Cancer Stat Facts: Brain and Other Nervous System Cancer*, <https://seer.cancer.gov/statfacts/html/brain.html> (

2 Furtado, D. *et al.* Overcoming the Blood-Brain Barrier: The Role of Nanomaterials in Treating Neurological Diseases. *Adv Mater* **30**, e1801362, doi:10.1002/adma.201801362 (2018).

3 Kievit, F. M. & Zhang, M. Cancer nanotheranostics: improving imaging and therapy by targeted delivery across biological barriers. *Adv Mater* **23**, H217-247, doi:10.1002/adma.201102313 (2011).

4 Zhou, Y., Peng, Z., Seven, E. S. & Leblanc, R. M. Crossing the blood-brain barrier with nanoparticles. *J Control Release* **270**, 290-303, doi:10.1016/j.jconrel.2017.12.015 (2018).
5 Mager, I. *et al.* Targeting blood-brain-barrier transcytosis - perspectives for drug delivery. *Neuropharmacology* **120**, 4-7, doi:10.1016/j.neuropharm.2016.08.025 (2017).
6 Zhang, Y. & Pardridge, W. M. Mediated efflux of IgG molecules from brain to blood across the blood–brain barrier. *Journal of Neuroimmunology* **114**, 168-172, doi:10.1016/s0165-5728(01)00242-9 (2001).
7 Wiley, D. T., Webster, P., Gale, A. & Davis, M. E. Transcytosis and brain uptake of transferrin-containing nanoparticles by tuning avidity to transferrin receptor. *P Natl Acad Sci USA* **110**, 8662-8667, doi:10.1073/pnas.1307152110 (2013).
8 Chen, Y. & Liu, L. Modern methods for delivery of drugs across the blood-brain barrier. *Adv Drug Deliv Rev* **64**, 640-665, doi:10.1016/j.addr.2011.11.010 (2012).
9 Pulgar, V. M. Transcytosis to Cross the Blood Brain Barrier, New Advancements and Challenges. *Front Neurosci* **12**, 1019, doi:10.3389/fnins.2018.01019 (2018).
10 Choudhury, H. *et al.* Transferrin receptors-targeting nanocarriers for efficient targeted delivery and transcytosis of drugs into the brain tumors: a review of recent advancements and emerging trends. *Drug Deliv Transl Res* **8**, 1545-1563, doi:10.1007/s13346-018-0552-2 (2018).
11 Lajoie, J. M. & Shusta, E. V. Targeting receptor-mediated transport for delivery of biologics across the blood-brain barrier. *Annu Rev Pharmacol Toxicol* **55**, 613-631, doi:10.1146/annurev-pharmtox-010814-124852 (2015).
12 Staquicini, F. I. *et al.* Systemic combinatorial peptide selection yields a non-canonical iron-mimicry mechanism for targeting tumors in a mouse model of human glioblastoma. *J Clin Invest* **121**, 161-173, doi:10.1172/JCI44798 (2011).
13 Ohtsuki, S. *et al.* Quantitative targeted absolute proteomic analysis of transporters, receptors and junction proteins for validation of human cerebral microvascular endothelial cell line hCMEC/D3 as a human blood-brain barrier model. *Mol Pharm* **10**, 289-296, doi:10.1021/mp3004308 (2013).
14 Yoon, D. J., Liu, C. T., Quinlan, D. S., Nafisi, P. M. & Kamei, D. T. Intracellular trafficking considerations in the development of natural ligand-drug molecular conjugates for cancer. *Ann Biomed Eng* **39**, 1235-1251, doi:10.1007/s10439-011-0280-y (2011).
15 Wilhelm, S. *et al.* Analysis of nanoparticle delivery to tumours. *Nature Reviews Materials* **1**, doi:10.1038/natrevmats.2016.14 (2016).
16 Haqqani, A. S. *et al.* Endosomal trafficking regulates receptor-mediated transcytosis of antibodies across the blood brain barrier. *J Cereb Blood Flow Metab* **38**, 727-740, doi:10.1177/0271678X17740031 (2018).
17 Paterson, J. & Webster, C. I. Exploiting transferrin receptor for delivering drugs across the blood-brain barrier. *Drug Discov Today Technol* **20**, 49-52, doi:10.1016/j.ddtec.2016.07.009 (2016).
18 Clark, A. J. & Davis, M. E. Increased brain uptake of targeted nanoparticles by adding an acid-cleavable linkage between transferrin and the nanoparticle core. *P Natl Acad Sci USA* **112**, 12486-12491, doi:10.1073/pnas.1517048112 (2015).
19 Wyatt, E. A. & Davis, M. E. Method of establishing breast cancer brain metastases affects brain uptake and efficacy of targeted, therapeutic nanoparticles. *Bioeng Transl Med* **4**, 30-37, doi:10.1002/btm2.10108 (2019).
20 Johnsen, K. B. *et al.* Targeting transferrin receptors at the blood-brain barrier improves the uptake of immunoliposomes and subsequent cargo transport into the brain parenchyma. *Sci Rep* **7**, 10396, doi:10.1038/s41598-017-11220-1 (2017).
21 Dararatana, N., Seidi, F. & Crespy, D. pH-Sensitive Polymer Conjugates for Anticorrosion and Corrosion Sensing. *ACS Appl Mater Interfaces* **10**, 20876-20883, doi:10.1021/acsami.8b05775 (2018).
22 Xu, C. R., Qiu, L., Pan, C. Y., Hong, C. Y. & Hao, Z. Y. Efficient Synthesis of Polymer Prodrug by Thiol-Acrylate Michael Addition Reaction and Fabrication of pH-Responsive Prodrug Nanoparticles. *Bioconjug Chem* **29**, 3203-3212, doi:10.1021/acs.bioconjchem.8b00531 (2018).
23 Antonio, J. P. M., Russo, R., Carvalho, C. P., Cal, P. & Gois, P. M. P. Boronic acids as building blocks for the construction of therapeutically useful bioconjugates. *Chem Soc Rev* **48**, 3513-3536, doi:10.1039/c9cs00184k (2019).
24 Stone, N. L., England, T. J. & O'Sullivan, S. E. A Novel Transwell Blood Brain Barrier Model Using Primary Human Cells. *Front Cell Neurosci* **13**, 230, doi:10.3389/fncel.2019.00230 (2019).
25 Gastfriend, B. D., Palecek, S. P. & Shusta, E. V. Modeling the blood-brain barrier: Beyond the endothelial cells. *Curr Opin Biomed Eng* **5**, 6-12, doi:10.1016/j.cobme.2017.11.002 (2018).
26 He, Y., Yao, Y., Tsirka, S. E. & Cao, Y. Cell-culture models of the blood-brain barrier. *Stroke* **45**, 2514-2526, doi:10.1161/STROKEAHA.114.005427 (2014).

27 Zinn, K. R. *et al.* Noninvasive bioluminescence imaging in small animals. *ILAR J* **49**, 103-115, doi:10.1093/ilar.49.1.103 (2008).
28 Morton, J. J., Bird, G., Refaeli, Y. & Jimeno, A. Humanized Mouse Xenograft Models: Narrowing the Tumor-Microenvironment Gap. *Cancer Res* **76**, 6153-6158, doi:10.1158/0008-5472.CAN-16-1260 (2016).
29 Clardy, S. M., Lee, D. H. & Schuck, P. Determining the Stoichiometry of a Protein-Polymer Conjugate Using Multisignal Sedimentation Velocity Analytical Ultracentrifugation. *Bioconjug Chem* **32**, 942-949, doi:10.1021/acs.bioconjchem.1c00095 (2021).
30 Bansal, V. *et al.* Traumatic brain injury and intestinal dysfunction: uncovering the neuro-enteric axis. *J Neurotrauma* **26**, 1353-1359, doi:10.1089/neu.2008-085810.1089/neu.2008.0858 (2009).
31 Lim, Y. H., Kim, D. H., Lee, M. Y. & Joo, M. C. Bowel dysfunction and colon transit time in brain-injured patients. *Ann Rehabil Med* **36**, 371-378, doi:10.5535/arm.2012.36.3.371 (2012).
32 Vredenburgh, J. J., Desjardins, A., Reardon, D. A. & Friedman, H. S. Experience with irinotecan for the treatment of malignant glioma. *Neuro Oncol* **11**, 80-91, doi:10.1215/15228517-2008-075 (2009).
33 Liu, X. *et al.* Combination Chemo-Immunotherapy for Pancreatic Cancer Using the Immunogenic Effects of an Irinotecan Silicasome Nanocarrier Plus Anti-PD-1. *Adv Sci (Weinh)* **8**, 2002147, doi:10.1002/advs.202002147 (2021).

Chapter 10

Future directions

10.1 VIPER-D-R3 for peptide delivery to solid tumors

In **Chapter 7**, we developed peptide-polymer conjugates to deliver the peptide R3 to the cytosol of cells. While the *in vitro* efficacy was promising, we faced issues detecting HMGB1 release *in vitro*, as well as inconsistent tumor inhibition *in vivo*. Future directions with this project include verifying pathway specific immunogenic cell death; incorporating targeting ligands; investigating efficacy via different delivery routes; and perhaps pursuing alternative peptide cargos.

10.1.1 Pathway specific cell death

The three hallmarks of immunogenic cell death are calreticulin translocation to the cell surface, and release of ATP and HMBG1.[1,2] While we successfully characterized calreticulin surface expression and ATP release induced by R3 conjugates, we are unable to detect HMGB1 release *in vitro*. This is particularly confusing, as we successfully detected release of this DAMP with D-melittin peptide-polymer conjugates (**Chapter 6**), suggesting that the polymer permits HMGB1 detection. One possible explanation for this difference is that HMBG1 and peptide R3 form a complex, impeding extracellular HMBG1 detection. While there are no reports suggesting this, we could investigate this phenomenon by doping in various HMGB1 concentrations with peptide treated cells, and measuring resultant HMGB1 concentration after 3 hours, the half-life of HMBG1 in cell culture media.[3] Additionally, we could investigate HMGB1 release via confocal microscopy, or co-culture of peptide-treated tumor cells and macrophages, and assess macrophage activation.

We will also need to verify that formulations of R3 (CP-R3 and VIPER-D-R3) induce necroptosis, either by inhibiting MLKL (e.g. necrosulfonamide) and assessing toxicity; confirming MLKL phosphorylation by Western blot; or evaluating toxicity in MLKL or NLRP3 inflammasome knockout cell lines. This can also be investigated *in vivo* by investigating anti-tumor efficacy when co-treating mice with a pathway inhibitor, such as MCC950, a small molecule inhibitor of the NLRP3 inflammasome. If R3 is inducing necroptosis, then administration of MCC950 should

inhibit NLRP3 activation and ICD and thus result in tumor progression, despite VIPER-D-R3+ICB treatment. In our initial attempt to investigate how MCC950 affected tumor growth, we noted inhibition while MCC950 was administered concurrently with treatment (**Figure S7.10**). However, due to toxicity of the inhibitor (soluble in 15% DMSO), we halted treatment early due to poor mouse condition. After halting MCC950 treatment, tumor growth slowed and overlapped with the growth trend of mice receiving just VIPER-D-R3+ICB without MCC950. Thus, we will repeat this study using either a different inflammasome inhibitor or a water soluble iteration of it.

10.1.2 Incorporation of targeting ligands

The mannose receptor (CD206) is highly expressed by macrophages. We hypothesize that adding a targeting ligand could improve uptake by tumor associated macrophages (TAMs), cells that are implicated in potentiating tumor progression.[4,5] Targeting would have the dual benefit of killing TAMs while also activating inflammatory pathways in the tumor. Initial investigation with mannose-VIPER-D-R3 revealed that this formulation is extremely toxic (4/5 mice dead) when dosed at the same peptide concentration of PEG-VIPER-D-R3, implying increased cellular uptake and toxicity. We determined that a slightly lower dose of mannose-VIPER-D-R3 ((3 mg D-melittin + 3 mg R3)/kg) was safe for repeat dosing, but were unable to observe tumor inhibition compared to PBS-treated mice. However, anti-tumor efficacy may be pronounced when combined with ICB treatment.

10.1.3 Investigation of different delivery routes

As we observed inconsistent efficacy with VIPER-D-R3+ICB treatment via IV injection, we could determine if this is caused by poor tumor delivery by comparing anti-tumor efficacy following IV and direct intratumoral (IT) injection. Direct IT injection removes delivery barriers and will reveal if poor efficacy is due to poor tumor delivery, or due to poor immunogenicity of the conjugate. This method also permits higher dosing, as dose is not limited by systemic toxicity.

10.1.4 Incorporation of alternative immunogenic peptide cargos

Alternative platform designs could incorporate other immunogenic peptides with different targets. Free peptide R3 has poor cytotoxicity *in vitro*, and is a very hydrophobic sequence that may prevent efficient cytosolic delivery. Initial fluorescent microscopy using Cy5-labeled R3 revealed

high overlap between the peptide and endosomes, perhaps suggesting peptide association with endosomal membranes. The obvious alternative peptide to investigate would be R1 (derived from conserved RHIM motif of RIPK1). We initially investigated RIPK3 as overexpression of this protein alone can drive necroptosis.[6] However, RIPK3 associates with RIPK1 to form the necrosome, which activates downstream signaling; both kinases are critical for necroptosis.

We could also investigate more upstream activators. While RIPK1 and RIPK3 form the machinery of necroptosis, we could also deliver peptide inducers of this process. For example, ER stress is a key inducer of necroptosis. Pharmaceutical inducers (i.e. tunicamycin, thapsigargan) can cause ER stress after 5 hours of treatment.[7] The peptide PFR (PFWRIRIRR-NH_2) is an antimicrobial peptide that induces necroptosis by inducing ER stress (expression of GRP78, ER stress marker), elevating mitochondrial ORS production, and increasing levels of phosphorylated RIPK1, RIPK3, and MLKL.[8] This peptide was used to treat acute myeloid leukemia and would perhaps have similar efficacy in solid tumors.

LTX-315 is another potential peptide of interest. While its ability to induce immunogenic cell death has been well characterized *in vitro* and its anti-tumor effect and changes to local immune populations have been demonstrated *in vivo*, the route of administration of LTX-315 seems to be limited to direct intratumoral injection.[9,10] VIPER could be an excellent platform to enable systemic dosing.

10.2 Targeted nanoparticles for chemotherapeutic delivery to brain tumors

In **Chapter 9,** we developed transferrin-decorated polymeric nanoparticles to deliver camptothecin (CPT) past the blood-brain barrier (BBB). However, this system demonstrated inconsistent brain accumulation *in vivo*, did not significantly reduce tumor burden compared to free drug, or extend survival in tumor-bearing mice. Furthermore, non-targeted formulations were transported across monolayers to a higher extent than targeted formulations. Future work on this project requires designing a new generation of nanoparticles. We are investigating both additional targeting ligands and alternative core nanoparticle chemistry.

10.2.1 Incorporation of alternative targeting ligands

The original generation of nanoparticles were conjugated to transferrin, enabling transferrin-mediated transcytosis. Due to lack of observed transport *in vitro* and *in vivo*, we are pursuing alternative ligands, such as apolipoprotein E (ApoE) and angiopep-2, ligands for the lipoprotein receptor pathway (LRP) receptor, and comparing transport to that of transferrin-decorated particles. Several studies have demonstrated that ApoE enables nanoparticles to enter the BBB *in vivo*, as it is recognized by LRP receptors on endothelial cells.[11-13] Similarly, the synthetic LRP1 peptide ligand, Angiopep-2, is also employed to shuttle nanodrugs across the BBB.[14,15] And in comparison to transferrin peptide ligands, Angiopep-2 demonstrated superior trafficking into the brain parenchyma, particularly when synthesized with a trileucine (LLL) residue, which facilitates intracellular endosomal escape.[16]

10.2.2 Incorporation of alternative core chemistries

We are also investigating the use of pH-buffering polymers to enhance transcytosis. In the original iteration of particles, we hypothesized that acid-labile decoupling of transferrin from the nanoparticle core would facilitate transcytosis.[17,18] However, we determined that non-acid-labile particles experienced greater brain accumulation than acid-labile formulations, and hypothesized that the increased brain accumulation would increase drug diffusion to brain tumors.[19] This trend was not statistically significant in tumor bearing mice, so future particles should be designed for enhanced transcytosis. To this end, we are designing nanoparticles with pH-buffering polymers to attenuate endosomal acidification, with the hypothesis that this will increase transcytosis of drug carriers through the BBB. Following cellular uptake and endosomal acidification, pH-buffering polymers will be protonated, neutralizing endosomal acidification and preventing lysosomal sorting. Endosomal pH modulation has been shown to alter intracellular sorting, resulting in increased transcytosis *in vitro* by up to 24-fold and significantly increasing brain accumulation *in vivo*.[20,21] To do this, we are incorporating hydroxychloroquine (HCQ) monomers into the nanoparticle design.[22] We are now comparing the effect of these targeting ligands (transferrin, ApoE, and Angiopep-2) and nanoparticle cores (HPMA or HCQ) on transcytosis across a monolayer, and on tight junction permeability (claudin-5, ZO-1 tight junction proteins). Additionally, we will assess how these nanoparticles are trafficked *in vitro* by staining early and late endosomes (EEA-1 and Rab7 antibodies, respectively) and if endosomal buffering can reduce

endosomal maturation into lysosomes. Preliminary results suggest that targeted iterations of HCQ particles have enhanced uptake compared to non-targeted particles. Future work on this project will identify the optimal targeting ligand and core chemistry for increased transcytosis and investigate if these modifications enhance brain accumulation and transport into the parenchyma.

References

1 Fucikova, J., Kepp, O., Kasikova, L., Petroni, G., Yamazaki, T., Liu, P., Zhao, L., Spisek, R., Kroemer, G. & Galluzzi, L. Detection of immunogenic cell death and its relevance for cancer therapy. *Cell Death Dis* **11**, 1013, doi:10.1038/s41419-020-03221-2 (2020).

2 Krysko, D. V., Garg, A. D., Kaczmarek, A., Krysko, O., Agostinis, P. & Vandenabeele, P. Immunogenic cell death and DAMPs in cancer therapy. *Nat Rev Cancer* **12**, 860-875, doi:10.1038/nrc3380 (2012).

3 Zandarashvili, L., Sahu, D., Lee, K., Lee, Y. S., Singh, P., Rajarathnam, K. & Iwahara, J. Real-time kinetics of high-mobility group box 1 (HMGB1) oxidation in extracellular fluids studied by in situ protein NMR spectroscopy. *J Biol Chem* **288**, 11621-11627, doi:10.1074/jbc.M113.449942 (2013).

4 Sylvestre, M., Crane, C. A. & Pun, S. H. Progress on Modulating Tumor-Associated Macrophages with Biomaterials. *Adv Mater*, e1902007, doi:10.1002/adma.201902007 (2019).

5 Ngambenjawong, C., Gustafson, H. H. & Pun, S. H. Progress in tumor-associated macrophage (TAM)-targeted therapeutics. *Adv Drug Deliv Rev* **114**, 206-221, doi:10.1016/j.addr.2017.04.010 (2017).

6 Dhuriya, Y. K. & Sharma, D. Necroptosis: a regulated inflammatory mode of cell death. *J Neuroinflammation* **15**, 199, doi:10.1186/s12974-018-1235-0 (2018).

7 Oslowski, C. M. & Urano, F. Measuring ER stress and the unfolded protein response using mammalian tissue culture system. *Methods Enzymol* **490**, 71-92, doi:10.1016/B978-0-12-385114-7.00004-0 (2011).

8 Lv, Y., Shao, G., Zhang, Q., Wang, X., Meng, Y., Wang, L., Huang, F., Yang, T., Jin, Y. & Fu, C. The antimicrobial peptide PFR induces necroptosis mediated by ER stress and elevated cytoplasmic calcium and mitochondrial ROS levels: cooperation with Ara-C to act against acute myeloid leukemia. *Signal Transduct Target Ther* **4**, 38, doi:10.1038/s41392-019-0073-6 (2019).

9 Zhou, H., Forveille, S., Sauvat, A., Yamazaki, T., Senovilla, L., Ma, Y., Liu, P., Yang, H., Bezu, L., Muller, K., Zitvogel, L., Rekdal, O., Kepp, O. & Kroemer, G. The oncolytic peptide LTX-315 triggers immunogenic cell death. *Cell Death Dis* **7**, e2134, doi:10.1038/cddis.2016.47 (2016).

10 Camilio, K. A., Wang, M. Y., Mauseth, B., Waagene, S., Kvalheim, G., Rekdal, O., Sveinbjornsson, B. & Maelandsmo, G. M. Combining the oncolytic peptide LTX-315 with doxorubicin demonstrates therapeutic potential in a triple-negative breast cancer model. *Breast Cancer Res* **21**, 9, doi:10.1186/s13058-018-1092-x (2019).

11 Wagner, S., Zensi, A., Wien, S. L., Tschickardt, S. E., Maier, W., Vogel, T., Worek, F., Pietrzik, C. U., Kreuter, J. & von Briesen, H. Uptake mechanism of ApoE-modified nanoparticles on brain capillary endothelial cells as a blood-brain barrier model. *PLoS One* **7**, e32568, doi:10.1371/journal.pone.0032568 (2012).

12 Kreuter, J., Shamenkov, D., Petrov, V., Ramge, P., Cychutek, K., Koch-Brandt, C. & Alyautdin, R. Apolipoprotein-mediated transport of nanoparticle-bound drugs across the blood-brain barrier. *J Drug Target* **10**, 317-325, doi:10.1080/10611860290031877 (2002).

13 Wunsch, A., Mulac, D. & Langer, K. Lipoprotein imitating nanoparticles: Lecithin coating binds ApoE and mediates non-lysosomal uptake leading to transcytosis over the blood-brain barrier. *Int J Pharm* **589**, 119821, doi:10.1016/j.ijpharm.2020.119821 (2020).

14 Demeule, M., Regina, A., Che, C., Poirier, J., Nguyen, T., Gabathuler, R., Castaigne, J. P. & Beliveau, R. Identification and design of peptides as a new drug delivery system for the brain. *J Pharmacol Exp Ther* **324**, 1064-1072, doi:10.1124/jpet.107.131318 (2008).

15 Wang, X., Liu, G., Chen, N., Wu, J., Zhang, J., Qian, Y., Zhang, L., Zhou, D. & Yu, Y. Angiopep2-Conjugated Star-Shaped Polyprodrug Amphiphiles for Simultaneous Glioma-Targeting Therapy and MR Imaging. *ACS Appl Mater Interfaces* **12**, 12143-12154, doi:10.1021/acsami.0c00509 (2020).

16 Israel, L. L., Braubach, O., Galstyan, A., Chiechi, A., Shatalova, E. S., Grodzinski, Z., Ding, H., Black, K. L., Ljubimova, J. Y. & Holler, E. A Combination of Tri-Leucine and Angiopep-2 Drives a Polyanionic

Polymalic Acid Nanodrug Platform Across the Blood-Brain Barrier. *ACS Nano* **13**, 1253-1271, doi:10.1021/acsnano.8b06437 (2019).

17 Wyatt, E. A. & Davis, M. E. Method of establishing breast cancer brain metastases affects brain uptake and efficacy of targeted, therapeutic nanoparticles. *Bioeng Transl Med* **4**, 30-37, doi:10.1002/btm2.10108 (2019).

18 Clark, A. J. & Davis, M. E. Increased brain uptake of targeted nanoparticles by adding an acid-cleavable linkage between transferrin and the nanoparticle core. *P Natl Acad Sci USA* **112**, 12486-12491, doi:10.1073/pnas.1517048112 (2015).

19 Johnsen, K. B., Burkhart, A., Melander, F., Kempen, P. J., Vejlebo, J. B., Siupka, P., Nielsen, M. S., Andresen, T. L. & Moos, T. Targeting transferrin receptors at the blood-brain barrier improves the uptake of immunoliposomes and subsequent cargo transport into the brain parenchyma. *Sci Rep* **7**, 10396, doi:10.1038/s41598-017-11220-1 (2017).

20 Cui, Y., Shan, W., Zhou, R., Liu, M., Wu, L., Guo, Q., Zheng, Y., Wu, J. & Huang, Y. The combination of endolysosomal escape and basolateral stimulation to overcome the difficulties of "easy uptake hard transcytosis" of ligand-modified nanoparticles in oral drug delivery. *Nanoscale* **10**, 1494-1507, doi:10.1039/c7nr06063g (2018).

21 Widera, A., Norouziyan, F. & Shen, W. C. Mechanisms of TfR-mediated transcytosis and sorting in epithelial cells and applications toward drug delivery. *Adv Drug Deliv Rev* **55**, 1439-1466, doi:10.1016/j.addr.2003.07.004 (2003).

22 Yu, F., Xie, Y., Wang, Y., Peng, Z. H., Li, J. & Oupicky, D. Chloroquine-Containing HPMA Copolymers as Polymeric Inhibitors of Cancer Cell Migration Mediated by the CXCR4/SDF-1 Chemokine Axis. *ACS Macro Lett* **5**, 342-345, doi:10.1021/acsmacrolett.5b00857 (2016).